Spatio–temporal assessment of dynamics in discontinuous mountain permafrost —

Investigation of small-scale influences on the ground thermal regime and on active layer processes during snow melt

Dissertation zur Erlangung des

naturwissenschaftlichen Doktorgrades

der Bayerischen Julius-Maximilians-Universität Würzburg

vorgelegt von

Tobias Rödder

aus

Hachenburg

Würzburg

Eingereicht am: 12.09.2012

1. Gutachter: PD Dr. Christof Kneisel

2. Gutachter: Prof. Dr. Christian Hauck

der Dissertation

1. Prüfer: PD Dr. Christof Kneisel

2. Prüfer: Prof. Dr. Jürgen Rauh

der mündlichen Prüfung

Tag der mündlichen Prüfung: 08.05.2013

Doktorurkunde ausgehändigt am:

Contents

List of Figures

List of Tables

List of Acronyms and Symbols

AL	active layer
a.s.l.	above sea level
BH	borehole
BTS	Basistemperatur der Schneedecke – bottom temperature of the winter snow cover
DC	direct current
DDF	freezing degree-day
DDT	thawing degree-day
DGPS	differential global positioning system
DMI	Danish Meteorological Institute
DWD	Deutscher Wetterdienst – German Meteorological Service
ERT(M)	electrical resistivity tomography (monitoring)
GST	ground surface temperature
IPA	International Permafrost Association
LIA	Little Ice Age
MAAT	mean annual air temperature
MAGST	mean annual ground surface temperature
MPI	Max-Planck-Institute, Hamburg
Mrg	investigation site Muragl
Mrt	investigation site Murtèl
PACE	Permafrost and Climate in Europe
PERMOS	Swiss Permafrost Monitoring Network
RCM	Regional Climate Model
RST	refraction seismic tomography
SPCC	Sensitivity of Permafrost to Climate Change
TTOP	temperature at the permafrost table
UFS	Umweltforschungsstation Schneefernerhaus – research station Schneefernerhaus

Zug	investigation site Zugspitzplatt
a	constant of proportionality (empirical constant: $0.5 \leq a \geq 2.5$)
E	Young's modulus
k	bulk modulus
m, n	empirical constants ($1.3 \leq m \geq 2.5$ and $n \approx 2$)
P	volume stress
s	volume fraction of pores with water
V	volume strain
ϵ	strain (longitudinal or shear strain)
λ	damping factor
μ	shear modulus
π	ratio of a circle's circumference to its diameter
ρ	specific resistivity/density
ρ_a	apparent resistivity
ρ_w	resistivity of water
σ	longitudinal stress $\delta F/A$
τ	shear stress
ϕ	fractional pore volume (porosity)

Abstract

The discontinuous mountain permafrost zone is characterized by its heterogeneous distribution of frozen ground and a small-scale variability of the ground thermal regime. Large parts of these areas are covered by glacial till and sediments that were exposed after the recession of the glaciers since the 19th century. As response to changed climatic conditions permafrost-affected areas will lose their ability as sediment storage and on the contrary, they will act as source areas for unconsolidated debris. Along with modified precipitation patterns the degradation of the discontinuous mountain permafrost zone will (temporarily) increase its predisposition for mass movement processes and thus has to be monitored in a differentiated way.

Therefore, the spatio-temporal dynamics of frozen ground are assessed in this study based on results obtained in three glacier forefields in the Engadin (Swiss Alps) and at the Zugspitze (German Alps). Sophisticated techniques are required to uncover structural differences in the subsurface. Thus, the applicability of advanced geophysical methods is tested for alpine environments and proved by the good 3D-delineation of a permafrost body and by the detection of detailed processes in the active layer during snow melt.

Electrical resistivity tomography (ERT) approaches (quasi-3D, daily monitoring) reveal their capabilities to detect subsurface resistivity changes both, in space and time. Processes and changes in regard to liquid water content and ice content are observed to exist at short distances even though the active layer is not subject to a considerable thickening over the past 7 years.

The stability of the active layer is verified by borehole temperature data. No synchronous trend is recognized in permafrost temperatures and together with multi-annual electrical resistivity data they indicate degradation and aggradation processes to occur at the same time.

Different heat transfer mechanisms, especially during winter, are recognized by means of temperature sensors above, at, and beneath the surface. Based on surface and borehole temperature data the snow cover is assessed as the major controlling factor for the thermal regime on a local scale. Beyond that, the debris size of the substrate, which modifies the

snow cover and regulates air exchange processes above the ground, plays a crucial role as an additional buffer layer.

A fundamental control over the stability of local permafrost patches is attributed to the ice-rich transient layer at the base of the active layer. The refreezing of melt water in spring is illustrated with diurnal ERT monitoring data from glacier forefield Murtèl. Based on these ERT and borehole temperature data a conceptual model of active layer processes between autumn and spring is developed. The latent heat that is inherent in the transient layer protects the permafrost beneath from additional energy input from the surface as long as the refreezing of melt water in spring prevails and sufficient ice is build up each spring. Permafrost sites without a transient layer show considerably higher temperatures at their table and are more prone to degradation in the years and decades ahead.

As main investigation area a glacier forefield beneath the summits of Piz Murtèl and Piz Corvatsch in the Swiss Engadin was chosen. It is located west of the well-known rock glacier Murtèl. Here, a permafrost body inside and adjacent to the lateral moraine was investigated and could be delineated very well. In the surrounding glacier forefield no further indications of permafrost occurrence could be made. Geophysical data and temperature values from the surface and from a permafrost borehole were compared with long-term data from proximate glacier forefield Muragl (Engadin). Results from both sites show a considerable stability of the active layer depth in summer while at the same time geophysical data demonstrate annual changes in the amount of liquid water content and ice content in the course of years.

A third investigation area is located in the German Alps. The Zugspitzplatt is a high mountain valley with considerably more precipitation and thicker snow cover compared to both Swiss sites. In close proximity to the present glacier and at a large talus slope beneath the summit crest ground ice could be observed. The high subsurface resistivity values and comparable data from existing studies at the Zugspitze may indicate the presence of sedimentary ice in the subsurface of the karstified Zugspitzplatt.

Based on these complementary data from geophysical and temperature measurements as well as geomorphological field mapping the development of permafrost in glacier forefields under climate change conditions is analyzed with cooperation partners from the SPCC project. Ground temperature simulations forced with long-term climatological data are

modeled to assess future permafrost development in glacier forefield Murtèl. Results suggest that permafrost is stable as long as the ice-rich layer between the active layer and the permafrost table exists. After a tipping point is reached, the disintegration of frozen ground starts to proceed rapidly from the top.

Zusammenfassung

Die Zone des diskontinuierlichen Gebirgspermafrosts in den Europäischen Alpen ist durch das kleinräumige Auftreten von gefrorenem Untergrund und eine hohe Variabilität des thermischen Regimes gekennzeichnet. Weite Bereiche dieser Zone sind mit glazialen Sedimenten und Felsschutt bedeckt, die mit dem Abschmelzen der Gletscher seit Mitte des 19. Jahrhunderts freigelegt wurden. Im Zuge von klimatischen Veränderungen werden Gebiete, in denen Permafrost auftritt, ihre Funktion als Sedimentspeicher verlieren und stattdessen als Sedimentquelle für Lockermaterial wirken. Zusammen mit Änderungen im Niederschlagsregime kann sich dadurch die Disposition für Massenbewegungen (zeitweilig) erhöhen, so dass differenzierte Beobachtungsstrategien dieser lokalen Permafrostvorkommen erforderlich sind.

Im Rahmen dieser Arbeit wurde die raum-zeitliche Dynamik von Permafrost in drei Gletschervorfeldern im Engadin (Schweizer Alpen) und an der Zugspitze (Deutsche Alpen) untersucht. Um strukturelle Unterschiede im Untergrund zu erkennen ist der Einsatz von modernen, sich ergänzenden Techniken und Methoden unbedingt erforderlich. Mit der genauen dreidimensionalen Abgrenzung eines Permafrostkörpers sowie der Beobachtung von aktiven Prozessen während der Schneeschmelze in der Auftauschicht, konnte die Anwendbarkeit der geophysikalischen Methoden in unzugänglichem alpinen Gelände unter Beweis gestellt werden. Insbesondere die elektrische Widerstandstomographie (ERT), basierend auf einem quasi-3D Ansatz und einem täglichen Monitoring, erlaubt eine detaillierte Untersuchung von Widerstandsveränderungen (räumlich und zeitlich). Obwohl die Mächtigkeit der Auftauschicht über die letzten 7 Jahren kaum variierte, konnten Prozesse und Veränderungen im Permafrost beobachtet werden.

Die Stabilität der Auftauschicht im Untersuchungszeitraum wird durch Temperaturmessungen in den Bohrlöchern bestätigt. Die Permafrosttemperaturen zeigen einen gleichlaufenden Trend. Zusammen mit den mehrjährigen ERT-Daten unterstreicht dies die Variabilität in der Zusammensetzung des Untergrunds in Bezug auf den jeweiligen Anteil von flüssigem bzw. gefrorenem Wasser.

Mit Hilfe von Temperatursensoren oberhalb, auf und unterhalb der Erdoberfläche kon-

nten verschiedene Wärmetransportprozesse, insbesondere im Winter, beobachtet werden. Auf Grundlage dieser Temperaturdaten wird die Schneedecke als der größte Einflussfaktor auf das thermische Regime des Untergrundes auf lokaler Ebene angesehen. Zusätzlich spielt die Größe des vorhandenen Schuttmaterials eine wesentliche Rolle, da zum einen die Schneedecke verändert und zum anderen die Luftaustauschprozesse an der Oberfläche stark reguliert werden. Dies bestätigt die bereits bekannte mikroklimatische Wirkung von grobem Blockschutt.

Maßgeblich für die Stabilität der Auftauschicht ist der eisreiche Übergangsbereich zwischen Auftauschicht und Permafrost. Tägliche ERT-Daten aus dem Gletschervorfeld Murtèl zeigen das Wiedergefrieren von Schmelzwasser in diesem Bereich im Frühjahr. Auf Grundlage von Bohrlochtemperaturen und ERT-Daten wurde ein konzeptionelles Modell der Prozesse innerhalb der Auftauschicht für den Zeitraum Herbst bis Frühjahr erstellt. So lange der Eiszuwachs im Frühjahr dominiert, schützt die eisreiche Schicht durch die gespeicherte latente Wärme den Permafrost vor zusätzlichem Wärmeeintrag. Standorte mit einem niedrigen Eisgehalt an der Permafrosttafel unterliegen damit in größerem Maße dem Einfluss des Wärmetransports und sind in den kommenden Jahren und Jahrzehnten stärker anfällig für Degradationserscheinungen.

Hauptuntersuchungsgebiet ist ein Gletschervorfeld unterhalb der Gipfel von Piz Murtèl und Piz Corvatsch im Schweizer Engadin westlich des gut untersuchten Blockgletscher Murtèl. Hier wurde ein Permafrostkörper am Rande bzw. innerhalb der Lateralmoräne untersucht und die Abgrenzung des Untergrundeises detektiert. Im übrigen Gletschervorfeld konnte Permafrost nicht nachgewiesen werden. Die geophysikalischen Daten und Temperaturdaten von der Oberfläche bzw. aus einem Permafrostbohrloch wurden mit langjährigen Messreihen aus dem Gletschervorfeld Muragl (ebenfalls im Engadin) verglichen. Die Ergebnisse an beiden Standorten zeigen eine gewisse Stabilität der jährlichen Auftauschicht. Zur gleichen Zeit zeigen die geophysikalischen Ergebnisse Veränderungen im Verhältnis von flüssigen Wasser zu gefrorenem Eis im Untergrund an.

Als drittes Untersuchungsgebiet wurde das Zugspitzplateau ausgewählt, ein alpines Hochtal mit deutlich mehr Niederschlag und größerer Schneedecke als an den beiden Standorten im Engadin. Hier konnten in unmittelbarer Nähe zum heutigen Gletscherrand und unter steilen Hangschuttkegeln durch Widerstandstomographie deutliche Hinweise auf Untergrundeis gegeben werden. Feldbeobachtungen und die bekannt hohen Wider-

standswerte aus vergleichbaren Untersuchungen am Zugspitzgipfel lassen auf sedimentäres Eis im verkarsteten Untergrund schließen.

Abschließend wurde die zukünftige Entwicklung am Standort Murtèl anhand von Simulationsläufen, die auf langfristigen Energiebilanzdaten von regionalen Klimamodellen beruhen, abgeschätzt. Auf Basis der umfangreichen Daten aus den Geländemessungen und der geomorphologischen Kartierung, wurde mit Hilfe einer Sensivitätsanalyse mit Partnern aus dem SPCC-Projekt die Termperaturentwicklung im Permafrost modelliert. Die Ergebnisse zeigen eine kurzfristige Stabilität des Permafrosts bis ein kritischer Schwellenwert erreicht ist, der vermutlich mit dem Tauen der eisreichen Zone verbunden ist. Nachdem dieser Zeitpunkt überschritten ist, setzt sich die Permafrostdegradation rasch in die Tiefe fort.

Acknowledgements

1. Introduction

The introduction starts with a general background on recent climatic change and its consequences on the cryosphere in the European Alps (1.1). A short summary of findings and observations in research on the alpine cryosphere follows addressing mountain glaciers and permafrost. Thereafter the focus is placed on mountain permafrost in general supplemented with a synoptic literature overview (1.2). Section 1.3 gives a more in-depth description of the alpine permafrost environment and its modulating external factors before the framework of this study and the SPCC-project are presented (1.4). In the last section of this introduction (1.5) the main research goals and the structure of the thesis are given.

1.1. General climatic background

A positive trend in mean air temperatures has been observed in the European Alps since the 19th century, albeit interrupted by short periods of cooling or constant mean temperatures in the 1930s and between 1950 and 1970. Analyses of homogenized long-term meteorological data of almost 100 instrumental series from the European Alps indicate a secular warming trend of about 1.1°C since 1890 (Böhm et al., 2001). Similarly, Haeberli and Beniston (1998) showed that the average of mean temperatures at eight alpine stations in Switzerland increased by almost 1°C during the past century. This warming is of greater amplitude than the global average (Beniston, 2004) and compared with results derived from the global data set of Jones et al. (1999). Profound effects on glacial and periglacial systems in response to higher air temperatures are already recognized (e.g. Harris et al., 2009).

In the European Alps, climate-induced changes in environmental conditions can be directly observed at numerous mountain glaciers. Mountain glaciers adapt rapidly to climatic changes by area and volume loss or even total disintegration. For the entire Alps a glacier inventory of 5422 glaciers derived from satellite data shows that changes in glacier area amount to about -22 % between 1973 and 1999 (Paul et al., 2004). Analyses

of 938 glaciers in the Swiss Alps (1973 glacier inventory) have shown that the rate of change has increased within the last decades. Between 1850 and 1973, the area change was about -2.2 % per decade, has increased to -6.4 % from 1973 to 1999, and to -14.0 % from 1985 to 1999. The increased speed of glacier area loss in recent decades is attributed to positive feedbacks caused by enhanced thermal radiation from newly exposed ice-free surfaces and by a massive downwasting of the ice that leads to emerging bedrock outcrops and disintegration in dependence of the geometry of the glacier and the underlying surface (Paul et al., 2004). Summarizing the whole period since the Little Ice Age (LIA) maximum extent the area reduction amounts to about 50 % (Zemp et al., 2006). Model simulations have predicted that it is probable for several Alpine glaciers to disappear within the upcoming decades (Zemp et al., 2006).

Beside glaciers, as the most apparent component of the alpine cryosphere, permafrost is a second component that acts to average out short-term climatic variability and hence, can be used as a sensitive indicator of climate change (Lemke et al., 2007).

Permafrost is less obvious at the earth's surface and changes in frozen ground conditions cannot be directly observed by visual documentation. It is defined as thermal phenomenon, comprising ground or bedrock that has temperatures at or below 0°C for at least two consecutive years (van Everdingen, 2005). Because of the generally moist air of the alpine climate and the presence of moisture in the near-surface, mountain permafrost generally contains a certain amount of ice. Ice-supersaturated mountain permafrost is affected by creep processes caused by ice crystal deformation, overburden pressure, and gravity leading to the typical landform of a rock glacier (Barsch, 1996; Berthling, 2011). The response time of permafrost to climatic change occurs on different time scales as proposed by Haeberli and Beniston (1998): a direct response to a warming of mean temperatures is the melt of ice at the permafrost table that can be associated with or without changes in active layer thickness and happens within a few years. Over decades to centuries, a modification of the ground temperature profile is expected, until finally the permafrost base adjusts to the new thermal conditions (centuries to millennia). Generally, the temperature regime of frozen ground is in a transient state: it constantly adjusts to modified thermal boundary conditions at the ground surface (Harris et al., 2009). Beside the climate control, the ground thermal regime is highly influenced by local site characteristics that include vegetation, organic layers, snow cover, soil properties, and running

water at the surface.

Research on climate-induced changes in permafrost characteristics and adaption of ground temperatures has developed in the European Alps only since the 1970s, much later than observations and mapping of glacier changes have started. The longest record of borehole temperature data in the European Alps exists at the rock glacier Murtèl, southeastern Switzerland (Vonder Muehll and Haeberli, 1990). Temperatures from a 59 m deep borehole show a warming trend of about 0.5°C at 11.6 m depth and of about 0.3°C below the depth of zero annual amplitude in 21.6 m depth between 1987 and 2005 (Harris et al., 2009), which was mainly caused by an especially rapid warming until 1995. No clear trend is obvious for the first decade of the 20th century (PERMOS, 2010). Haeberli and Beniston (1998) already caution that the representativity of single signals remains uncertain and requires further monitorings at various sites for a meaningful regional or even alpine-wide assessment of the state of permafrost. The Swiss permafrost monitoring network PERMOS (www.permos.ch) has been set up for this task and addresses questions concerning the distribution and dynamics of alpine permafrost since 2000.

Despite these efforts, little is known about the spatial and temporal behavior of permafrost in areas that are deglaciated since the LIA and the processes that occur during active layer freeze and thaw. The proximity and coexistence of glaciers and permafrost in mountain environments necessitate investigations to increase the knowledge of the interaction of both cryospheric components and their influence on processes and landforms. First studies on this coexistence in the Swiss Alps were conducted by Kneisel (1998) who investigated ground ice of polygenetic origin (sedimentary ice from snow-ice metamorphism and congelation ice from ground freezing) in two glacier forefields (including Muragl). Ground temperature trends, changes in the amount of ground ice, and the response time of permafrost on changing environmental conditions in regions where both parts of the alpine cryosphere occur side by side and have influenced each other in the past are yet to be investigated in detail. Possible consequences of glacier-permafrost interaction were recently addressed by Harris et al. (2009): "...permafrost may aggrade in recently deglaciated glacier forefields, thereby altering the thermal, hydrological and dynamic conditions of glacial deposits, and influencing related hazards. These effects are of increasing importance in the light of the current pronounced worldwide glacier retreat (p. 42)". Similarly, Haeberli and Beniston (1998) see a holistic understanding

of permafrost and its role in mountain landscapes as the most important goal with, for instance, the complex interaction between glaciers and permafrost as fascinating and important research avenue. This topic has been also discussed in other mountain areas such as Norway and Svalbard (Etzelmüller and Hagen, 2005) or lowland regions (Waller et al., 2012).

The present thesis seeks to narrow this research gap by the application of sophisticated methods and monitoring systems. It aims for an increased understanding of the spatial distribution of permafrost and of the processes occurring within the active layer and permafrost bodies in sediments of recently deglaciated glacier forefields.

1.2. Synoptic literature overview

Compared to other scientific fields that study components of the global cryosphere (in particular glaciology) mountain permafrost research has evolved relatively late in the second half of the 20th century. In Europe the interest in frozen ground and its geomorphological expressions such as rock glaciers and ice-cored moraines arose in a time of increasing air temperature and a postulated coupling between degradation and increased slope instabilities (geohazards) in permafrost environments (e.g. Gruber and Haeberli, 2007; Harris et al., 2009). The first international conference on permafrost in Europe was held in Trondheim in 1988 following a series of four precursory conferences in North America (USA and Canada) and Russia since 1963.

The interest in mountain permafrost research can be mainly categorized in three general topics: permafrost monitoring, permafrost mapping and characterization, and permafrost modeling, both, in space (regional modeling) and time (prediction). These fundamental targets in mountain permafrost research have evolved simultaneously since the 1970ies and were progressively pushed forward by modern observational and computational techniques (Etzelmüller, 2013). Two major review articles that cover the evolution in research on mountain permafrost were given lately by Harris et al. (2009) and Haeberli et al. (2010). The following three subsections focus on recent findings and research articles dealing with permafrost topics of relevance for mountain permafrost in the European Alps.

Permafrost monitoring

Starting in 1987 a subsequently growing network of boreholes drilled in mountain permafrost was initialized by realizing a 58 m deep borehole in rock glacier Murtèl (e.g. Haeberli and Hölzle 1998). This borehole was part of the EU project Permafrost and Climate in Europe (PACE, e.g. Harris et al., 2001, 2009) that included a transect of instrumented permafrost boreholes across the higher mountains of Europe ranging from Janssonhaugen, Svalbard (Norway) to Veleta Peak, Sierra Nevada (Spain). Today, the most extensive number of boreholes is maintained in Switzerland were the PERMOS network operates since 2000 as a systematic long-term observational network. In 2010 PERMOS registered 25 permafrost boreholes at 15 sites (PERMOS, 2010). In recent years boreholes were also drilled at permafrost sites in Germany (Zugspitze) (Krautblatter, 2010a) and in Austria (Hoher Sonnblick, Kitzsteinhorn) (Hartmeyer et al., 2012).

These time series document changes in permafrost temperatures mainly dependent on the ice content in the subsurface. Locations with high ice content are influenced by a latent heat effect that delays sensible heating during the melt of ice. Contrary, locations with low ice content (e.g. Schilthorn, Switzerland) react short-dated to atmospheric warming and heat waves such as in 2003 (PERMOS, 2007). As response to technical progress miniature temperature dataloggers are more and more used as proxy for ground thermal conditions. Several studies in the European Alps have shown the value of these loggers for estimating the conditions in the subsurface and have highlighted the strong spatial heterogeneity of ground temperatures that finally govern the distribution of mountain permafrost (e.g. Hoelzle et al., 1999; Gubler et al., 2011; Rödder and Kneisel, 2012a).

Permafrost mapping and characterization

On a local and regional scale temperature at the bottom of the snow cover in winter (Haeberli, 1973) can be used to predict the presence or absence of permafrost. This approach has been enlarged by the use of miniature temperature dataloggers that record year-round ground surface temperatures as mentioned in the previous subsection.

Early studies attempted to increase the knowledge on subsurface structure and characteristics (e.g. summarized in Barsch, 1996; Haeberli and Vonder Muehll, 1996) by indirect means such as seismic refraction or electrical resistivity. These studies investigated mainly the subsurface characteristics in rock glaciers representing typical permafrost-influenced

landforms. Overview articles on the progress in geophysical mapping and surveying are given by Vonder Muehll et al. (2001), Kneisel et al. (2008), and Hauck (2013). These reviews show the ongoing development in data acquisition and processing of geophysical techniques to investigate the presence and characteristics on mountain permafrost beyond the point scale of single boreholes or temperature loggers. The detailed description of the interior of single permafrost landforms have been provided by e.g. Hausmann et al. (2007); Kneisel and Schwindt (2008); Hilbich et al. (2009); Hauck et al. (2011); Scapozza et al. (2011); Rödder and Kneisel (2012b).

Through the interpretation of geophysical data series, i.e. multi-annual, seasonal, or even daily geoelectrical or seismic data sets the analyses of process rates and reaction of the subsurface to changed external forces have been made possible. Thus, the evolution of mountain permafrost is displayed by time-lapse tomograms (e.g. Hilbich et al., 2008b; Hilbich, 2010; Kneisel et al., 2014) showing anticipated changes in the content of liquid water or ice on varying temporal scales.

Permafrost modeling

The modeling of mountain permafrost enables the prediction on permafrost occurrence on a regional scale (spatial coverage) as well as the estimation on present and future developments (temporal coverage). Recent sensitivity analyses have investigated the influence of single parameters such as snow cover (Luetschg et al., 2008), atmospheric forcing parameters (Engelhardt et al., 2010), or meltwater infiltration (Scherler et al., 2010) on permafrost occurrence and its thermal state. Transient thermal effects could be modeled on simplified mountain topography and idealized mountain crests (Noetzli et al., 2007; Noetzli and Gruber, 2009) and showed the influence of multi-lateral warming in steep and complex topography.

On the spatial scale permafrost models are based on data sets of climate parameters (precipitation, air temperature, energy balance components) and topographic information (elevation, exposure, exposition). The performance of all models is dependent on the resolution of input parameters and its attempt to match the textured mountain topography. On the very local scale energy balance models give reasonable results on permafrost distribution and are able to predict ground temperature evolution under changed climatic conditions (Stocker-Mittaz et al., 2002; Gruber et al., 2004). Salzmann et al. (2007) tried

successfully to downscale regional climate models to drive an energy balance model and predict changes of ground surface temperatures in response to climate change.

Modeling permafrost distribution over larger areas such as the European Alps has been addressed with index maps based on a statistical model using mean annual air temperatures, potential incoming solar radiation, and precipitation as input variables (Boeckli et al., 2012b). The statistical model is calibrated using a rock glacier inventory and ground surface temperatures (Boeckli et al., 2012a).

A major task for upcoming attempts to model permafrost in mountain environments such as the European Alps is the high variability of topography compared to the size of the grid cells in common global or regional climate models (Etzelmüller, 2013).

1.3. The permafrost environment — a focus on alpine permafrost

As a consequence of cold climatic conditions and insufficient thaw in summer permafrost develops as a layer of the subsurface that does not totally thaw during summer. Following the official definition of the International Permafrost Association (IPA) permafrost is defined as ground that remains at or below 0°C for at least a period of two years (van Everdingen, 2005). Based on this thermal definition, the presence of ice is not a prerequisite for permafrost to exist.

On a global scale, about 24 % of the Earth's land area is underlain by permafrost (French, 2007), from which the predominant part lies in the lowlands of North America and Siberia, as well as in the high altitudes of the Tibetan Plateau. Only a small fraction of the global permafrost distribution is associated with mountain environments, both in polar and alpine areas. The controlling factors of mountain permafrost can be conceptualized on different scales (Haeberli et al., 2010): at a regional scale, climate determines the distribution of cold surface conditions. Key parameters are latitude and large scale circulation pattern. Topographic conditions further modify the fundamental climatic parameters temperature, precipitation, and solar radiation along an altitudinal transect and result in special microtopographic conditions (regional to local scale). Locally, vegetation, snow cover and redistribution, ground properties, and ice content ultimately determine

the ground surface and subsurface thermal conditions.

The climatic control makes permafrost a noteworthy phenomenon especially in the densely populated mountainous region of the European Alps. Here, systematic research has started as late as the second half of the 20th century (Haeberli et al., 2010). Today, permafrost research is increasingly related to topics such as natural hazards, constructional work, climatic and environmental changes, or impacts of atmospheric warming. But fundamental aspects of the ongoing processes and of the respective role of the above mentioned local factors on the small-scale distribution (1 m^2 to 100 m^2) of frozen ground are still unknown.

Because permafrost develops where the heat balance at the ground surface is negative, the radiation budget, i.e., the climate, is the most dominant factor for the existence of perennially frozen ground. The climate–permafrost system can be schematically described by boundary temperatures and offsets in-between (Smith and Riseborough, 2002, Fig. 1.1). In a qualitative way, a buffer layer at the ground surface (vegetation, substrate, snow cover) with a certain heat capacity and radiation property causes the mean annual ground surface temperature (MAGST) to be higher than the mean annual air temperature (MAAT). Depending on site-specific physical parameters of the subsurface (thermal conductivity, thermal diffusivity, and heat capacity) a thermal offset exists between the surface temperature and the temperature at the permafrost table (TTOP). In case of a negative thermal offset permafrost may be present even though the MAGST is at or above 0°C (Burn and Smith, 1988).

The interaction between the heat balance and the modification through buffer layers at the ground surface as well as within the uppermost part of the subsurface generates a heterogeneous pattern of permafrost occurrence in alpine environments. This is in accordance with the equally heterogeneous distribution of vegetation, surface substrate, and, influenced by the former factors, the annual snow cover. The latter varies spatially both in terms of absolute snow height and snow cover evolution during winter months. In general, mountain permafrost is relatively warm (temperatures close to the melting point) and shallow. A visual expression of creeping permafrost are rock glaciers that are frequently present in the less-glaciated areas of the Alps. But apart from this obvious phenomenon knowledge of the sporadic distribution of frozen ground within glacier forefields, talus slopes, and rock faces at the lower boundary of mountain permafrost (approx.
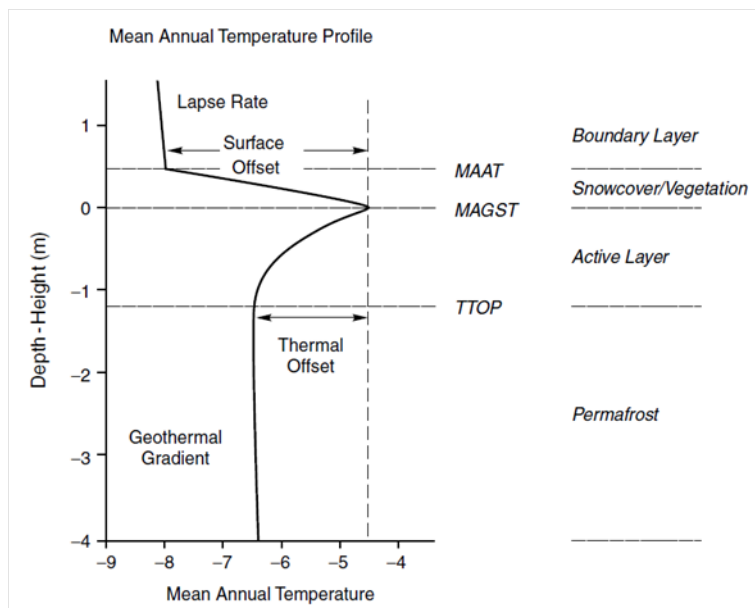
Figure 1.1: Schematic plot of the climate–permafrost system (from Smith and Riseborough, 2002).

2300–3000 m a.s.l.) is limited.

Attempts have been made to generate permafrost probability maps based on topoclimatological parameters to provide information for project planning in potentially permafrost-affected regions (Fig. 1.2). Similar approaches have been implemented in Norway (Etzelmüller et al., 2001), Austria (Ebohon and Schrott, 2008), and for the entire European Alps (Boeckli et al., 2012b) resulting in index maps, which give a certain degree of confidence for the existence of permafrost.

These empirical-statistical model approaches based on topoclimatological parameters and information on alpine-wide permafrost observations and landforms (e.g., rock glaciers) give an indication of the potential presence or absence of frozen ground on a regional scale (10–100 km^2). On a local scale (ca. 10 m^2), however, site characteristics such as snow cover, surface substrate, and if present, vegetation as well as the thermal properties of the soil/ground have a dominant influence on the radiation budget and the thermal offset. An accurate and careful validation of ground conditions, usually done by borehole temperature measurements or field work (applied geophysics, drilling, outcrops), is therefore necessary to finally evaluate the presence of permafrost.

As an alternative approach, process-oriented models focus on detailed process under-
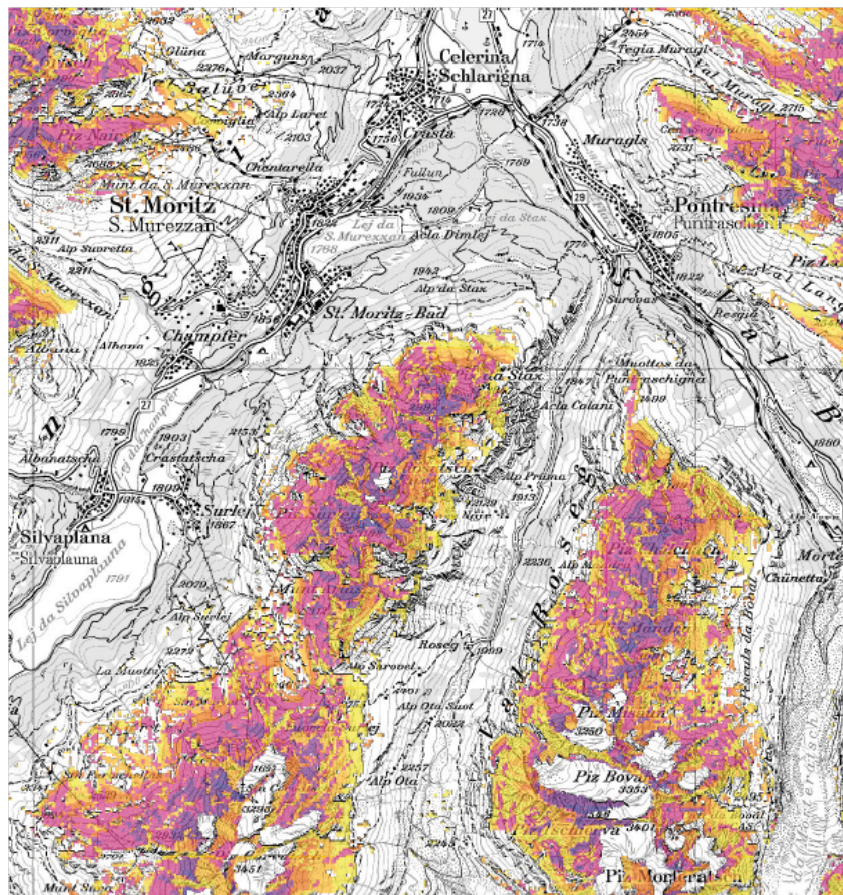
Figure 1.2: Potential permafrost distribution in the Upper Engadin (WebGIS BAFU, 1:100000).

Yellow tones = patchy permafrost possible, purple tones = permafrost extensively present, excerpt from www.bafu.ch.

standing and require an in-depth knowledge on the energy fluxes between the atmosphere, the ground surface, and the subsurface. Based on the parametrization of the single terms of the energy balance conclusions on the surface and/or the subsurface temperatures can be drawn. For this type of model, detailed energy balance measurements and knowledge of cryotic processes are crucial (Hoelzle et al., 2001; Stocker-Mittaz et al., 2002). Because of these requirements existing studies are limited to a few data sets and very local site conditions.

With regard to the typically medium- to coarse-grained surface layer of alpine environments large uncertainties of the thermal and hydrological processes exist. These processes are fundamental for heat transfer and the thermal regime of the ground. Vertical and lat-

eral water and vapour fluxes are closely connected to temperature conditions. Depending on seasonal temperatures and snow cover onset and melt, respectively, hydro-thermal processes undergo an annual cycle (Fig. 1.3). The presence of ice within the seasonally frozen active layer modifies the heat transfer because of latent heat effects that are associated with the phase change of water. Latent heat is taken up or liberated when water changes its state between liquid water, ice, and water vapour.
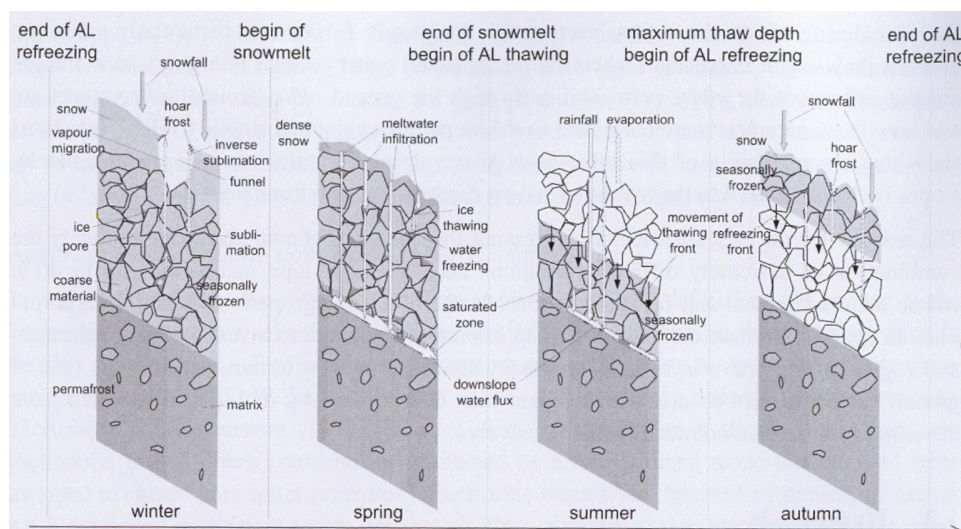
Figure 1.3: Temporal distribution of hydro-thermal processes in the active layer (AL) above permafrost on steep scree slopes (adopted from Rist, 2007).

1.4. The project cluster "Sensitivity of mountain Permafrost to Climate Change SPCC"

The project cluster "Sensitivity of mountain Permafrost to Climate Change SPCC" seeks to link atmosphere, surface, and subsurface in periglacial environments with the integration of all three spheres in a coupled way. Atmosphere, surface, and subsurface processes are investigated in a combined approach, therewith addressing current challenges in mountain permafrost research that were recently summarized in review articles by Harris et al. (2009) and Haeberli et al. (2010) on (mountain) permafrost in Europe in general and on permafrost creep and rock glacier dynamics (Haeberli et al., 2006). They comprise (i) the need for field measurements of processes within the main types of ground material

such as bedrock, fine-grained debris, and coarse, ice-rich debris, (ii) the consideration of the influence of the snow cover, (iii) the role of ice within fine and coarse debris and in bedrock, (iv) the mass and heat transfer by percolating water, (v) the transfer of energy through the blocky surface layer, as well as (vi) the interactions and feedbacks between snow, frozen scree, and glaciers in permafrost-affected areas to understand the dynamics of more complex landforms.

In the SPCC project, the sensitivity of permafrost dynamics is assessed to gain an integral system understanding. Therefore, different climate scenarios, spatio-temporal surface and subsurface processes, and kinematic reactions are studied. The term sensitivity is referred to as the degree of response of landforms to disturbance and includes both, types of disturbance (e.g., climate) as well as types of reaction (e.g., permafrost degradation). Figure 1.4 shows the five collaborating projects that cover three contiguous research topics. (i) "Climate control" that seeks to combine Regional Climate Model (RCM) simulations with permafrost-specific subsurface models for the projection of mountain permafrost evolution, (ii) "Spatio-temporal subsurface characteristics" within different substrates (debris, bedrock) to map and quantify the subsurface characteristics of permafrost-affected landforms and (iii) "Kinematics and instabilities" for the analysis of changes in landform geometry and process rates of permafrost creep phenomena. Research is conducted at different Universities in Germany and Switzerland. The interrelations and intersections between the individual projects are indicated by the interlaced illustration (Fig. 1.4).

The present thesis is integrated in project SPCC 3 on the spatial assessment of permafrost characteristics and dynamics in alpine periglacial environments. It focusses on unconsolidated sediments and debris, which show a distinct heterogeneity in terms of grain size and distribution of permafrost within the subsurface. Field work is implemented in recently deglaciated glacier forefields, whose areas were formerly (LIA) covered by polythermal glaciers and subsequently adapted to ice retreat and modified thermal conditions in the subsurface. Geophysical and geomorphological methods are combined with data from temperature measurements above, at, and below the ground surface and kinematic measurements to investigate the spatial pattern of permafrost distribution as well as temporal changes on a seasonal and annual basis.
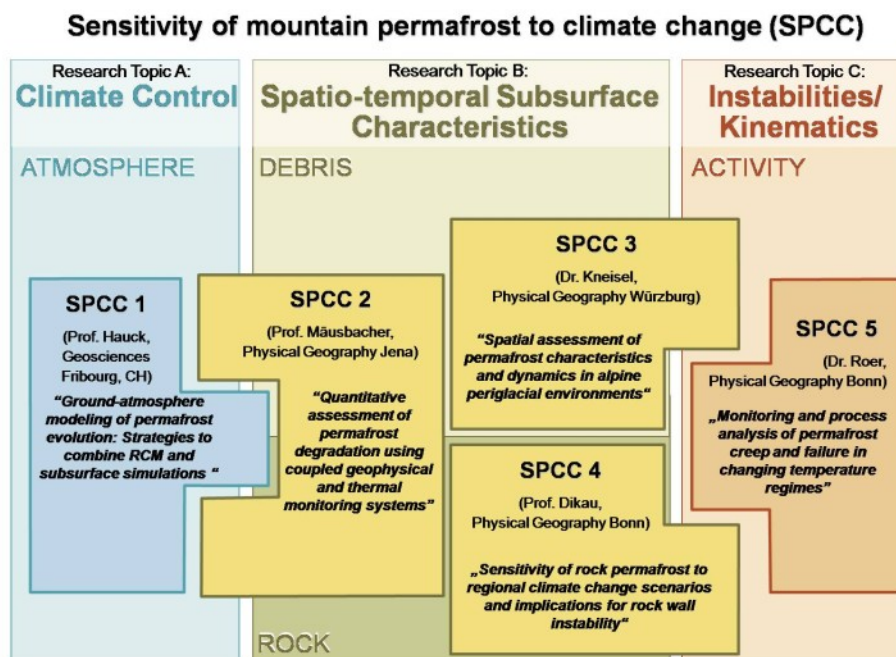
Figure 1.4: Structure and linkages of the SPCC project cluster and its five individual research projects.

1.5. Research goals and structure of the thesis

The small-scale heterogeneity of surface conditions and the patchy distribution of discontinuous mountain permafrost in alpine environments pose questions on the spatial presence of frozen ground and on the dominant influencing factors that cause this pattern. Moreover, the thermal state of discontinuous permafrost with internal temperatures only slightly below the freezing point necessitates the long-term observation of frozen ground. Most substantial changes in ground conditions occur at around 0°C, when the melting of ice-rich permafrost results in the settlement of formerly frozen ground, the supply of unconsolidated sediments for all kinds of mass movements, and the destabilization of rock walls caused by the deepening of the active layer. This study focuses on glacier forefields and thus allows to consider the possible aggradation of permafrost into the recently exposed debris. The main tasks of the present study are addressed by the observation of changes in the uppermost part of permafrost-affected landforms both in spatial as well as temporal direction, to finally increase the existing knowledge of site-specific processes in these environments. Therefore, a combination of complementary methods acting on the point scale (temperature measurements, boreholes, kinematic data)

as well as two-/three-dimensional measurements (logger transects, geophysical measurements, monitoring approaches for temporal integration) for the investigation of changes in areas of 10–100 m^2 is applied. Based on the general issues and the objective to characterize the subsurface internal structures of typical glacial and periglacial landforms, the following research issues are addressed:

- As key parameter for geomorphological studies in mountain environments, a detailed characterization of permafrost in unconsolidated sediments — spatial extent, thickness, and active layer thickness — is required beyond the very local information of existing boreholes

- The determination of spatio-temporal variability on permafrost dynamics including the presence or absence of permafrost within the investigated glacier forefields as well as changes in thermal conditions and ice contents over time

- The investigation of the influence of surface textural characteristics and annual snow cover conditions on the ground thermal regime by monitoring near-surface, ground surface, and subsurface temperatures

- High-resolution monitoring of active layer processes during the snow melt period by means of detailed temperature and geophysical observations

- Increase the process understanding of glacier-permafrost interactions in environments that were recently object to the transition from a glacial to a periglacial system as well as the outlook on a possible future development of the discontinuous permafrost

Questions are raised, which parameters determine the distribution of permafrost in unconsolidated sediments? Can temporal changes in the subsurface be observed with the methods applied? What processes occur at the transition zone between active layer and permafrost? To investigate these issues, three field sites were chosen where the recession of glaciers since the LIA has released wide areas of glacial till, glaciofluvial sediments, talus, and block fields. At these sites permafrost has already been observed or is expected (e.g. Hoelzle et al., 2002; Kneisel, 2010b). As key site, the Murtèl/Corvatsch area is selected that is known for its variety of periglacial landforms and its suitability for

permafrost research. Another field site in the southeastern Swiss Alps is Val Muragl that has already been investigated in terms of glacier–permafrost interaction since more than a decade by our research group (cf. Kneisel, 2010b, and references therein). In addition, the Zugspitzplatt was chosen as a third site with comparable glacial history but with different climatological conditions in terms of precipitation and snow cover.

The outline of this thesis is as follows: the Introduction (1) shortly summarizes the alpine permafrost system and presents the research environment, in which this study was embedded. Chapter 2 gives an overview on the geologic and climatologic conditions at the three investigation sites and reviews the existing knowledge from previous permafrost-related studies within these areas. The methods that were applied during field work are presented in chapter 3, together with a review of recent applications in permafrost research. Also, the present data basis and the analysis procedure addressed. Data and results from each of the three investigation sites, starting with the most extensive investigations at Murtèl/Corvatsch site are shown in chapters 4–6. The key site is followed by results from Val Muragl (5) and the Zugspitzplatt (6). Beyond the basic presentation of results a first interpretation of the data and their implications for permafrost is included in chapters 4–6. The discussion of these results is presented in chapter 7 in order to compare the recent findings and discuss them in the light of similar studies found in the literature. Therefore, the discussion chapter is separated in a section on methodological aspects and a section on general findings of the alpine permafrost system, complemented by short summaries of each investigation site. In a final chapter (8) the major findings and conclusions are summarized. In the appendices the present geophysical data basis is listed in tabular form (A-C). Temperature curves of all loggers placed at the ground surface are compiled in appendices D and E.

During the progress of the project, several tasks concerning the research questions outlined above could be addressed and partial results were already published. The descriptions of the field sites, the methods applied, and the key findings published in these articles are integrated in the present thesis based on the following articles:

- Kneisel, C.*, Rödder, T.*, Schwindt, D.*, 2014. Frozen ground dynamics resolved by multi-year and year-round electrical resistivity monitoring at three alpine sites in the Swiss Alps. Near Surface Geophysics–Special Issue on Geoelectrical Monitoring. 12, 117-132. DOI: 10.3997/1873-0604.2013067.
  * The authors contributed equally to this work.

- Kneisel, C., Rödder, T., Roth, N., Schwindt, D., 2012. Electrical resistivity monitoring for the detection of changes in mountain permafrost at different time scales. International workshop on geoelectrical monitoring, GELMON 30.11.–02.12.2011, Vienna. Extended abstracts. In: Supper, R. and Kauer, S.: Berichte der Geologischen Bundesanstalt, 92.

- Rödder, T., Kneisel, C., 2012a. Influence of snow cover and grain size on the ground thermal regime in the discontinuous permafrost zone, Swiss Alps. Geomorphology. Early online. DOI: 10.1016/j.geomorph.2012.07.008.

- Rödder, T., Kneisel, C., 2012b. Permafrost mapping using quasi-3D resistivity imaging, Murtèl, Swiss Alps. Near Surface Geophysics. 10, 117–127. DOI: 10.3997/1873-0604.2011029.

2. Investigation sites

The investigation of permafrost distribution and the characterization of frozen unconsolidated sediments at recently exposed ground (since about 1850 at the longest) are realized in two different areas in the European Alps (Fig. 2.1). Two glacier forefields are located in the southeastern part of Switzerland, in the inneralpine valley of the Engadin. The key site of this study is the Murtèl/Corvatsch area that has a large spectrum of permafrost-affected landforms and a long tradition (approx. 40 years) of periglacial research (Hoelzle et al., 2002). Data and results from investigations in another glacier forefield at the head of Val Muragl are analyzed complementary. In the last 15 years, numerous field visits and measurements were implemented at the latter site providing an extensive data base and a priori knowledge at Val Muragl. As comparison to the Engadin with a climate favorable for periglacial environments and a widespread distribution of discontinuous alpine permafrost, a third investigation area was selected.
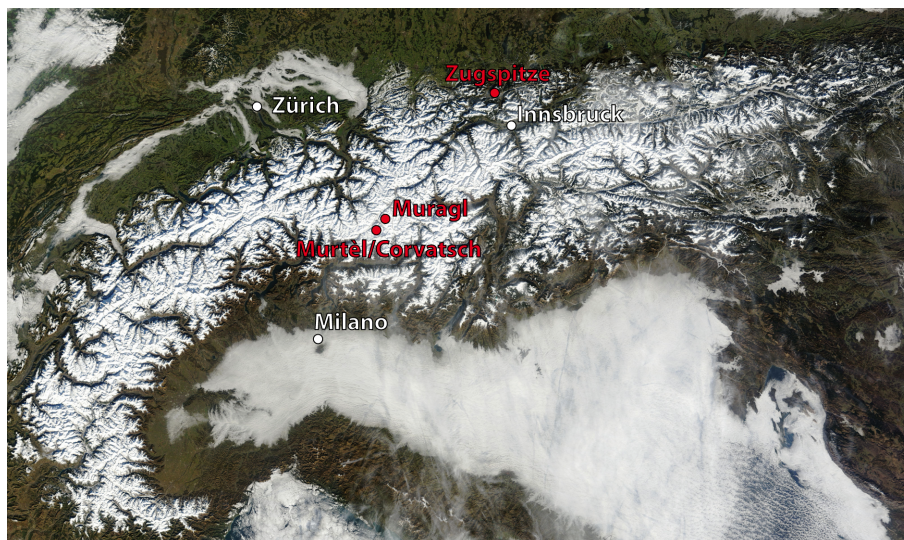
Figure 2.1: Satellite image of the European Alps (acquired January 17, 2011) with investigation sites marked by red dots (NASA, 2011).

The Zugspitze, Wetterstein Mountains, is located in the Northern Calcareous Alps (Fig. 2.1). It is characterized by much higher precipitation and lower altitude compared to the investigated areas in the Engadin. Permafrost is not as common in that area

but observations and measurements verified the presence of frozen bedrock along the summit crest (Krautblatter, 2010b; Bayerisches Landesamt für Umwelt, 2012). In the present study a focus is placed on the talus slopes and debris that accumulates on the Zugspitzplatt underneath the steep rock faces of the summit crest. In the following sections information on the geomorphology, geology, and climatology of the research sites as well as a review of previous permafrost-related studies is given.

2.1. Murtèl/Corvatsch area, Upper Engadin, Switzerland

The mountain crest extending from cable-car station Murtèl (2699 m) over the summits of Piz Murtèl (3433 m) and Piz Corvatsch (3451 m) to the Furtschellas ridge (2937 m) delineates the Murtèl/Corvatsch area (Fig. 2.2). While the eastward declivity is covered by several glaciers above Val Roseg, the area west of the crest is characterized by steep rock faces, large talus slopes, blockfields, and numerous rock glaciers of different age and activity. Periglacial research so far concentrated on the northern part of this area around rock glacier Murtèl. This study extends the investigation area to the southern part where the NW-exposed glacier forefield Murtèl is present. Field work was implemented in this glacier forefield, on rock glacier Rabgiusa, as well as on two solifluction lobes west of the Chastelets ridge.

The dominant geological units that construct the mountains of the Upper Engadin are the Austroalpine nappes of Grisons (Labhart, 2001, Fig. 2.3). They are part of the former African continent and were obducted up to 100 km toward north/northwest during the closure of the ancient Tethys Ocean. Regarding the lithology, the Murtèl/Corvatsch area consists mainly of crystalline, intrusive igneous rocks. These rocks form the Corvatsch unit as part of the Err-Bernina nappes (Carboniferous period). At the base of this unit sedimentary rocks (Permian period/Mesozoic) are intercalated (Chastelet unit). Typical rocks that are present in the investigation area are granite, granodiorite, gneiss, and mica schist (Spillmann and Trommsdorff, 2007a,b).

The climatic regime in the Engadin is characterized by rather dry conditions compared to the neighboring regions of the Alps. The shading effect of surrounding mountain chains protects the Engadin from moist air. Average precipitation is between 700–1000 mm/year at the valley floor: Samedan (1708 m), 700 mm/year; Pontresina (1774 m), 799 mm/year;
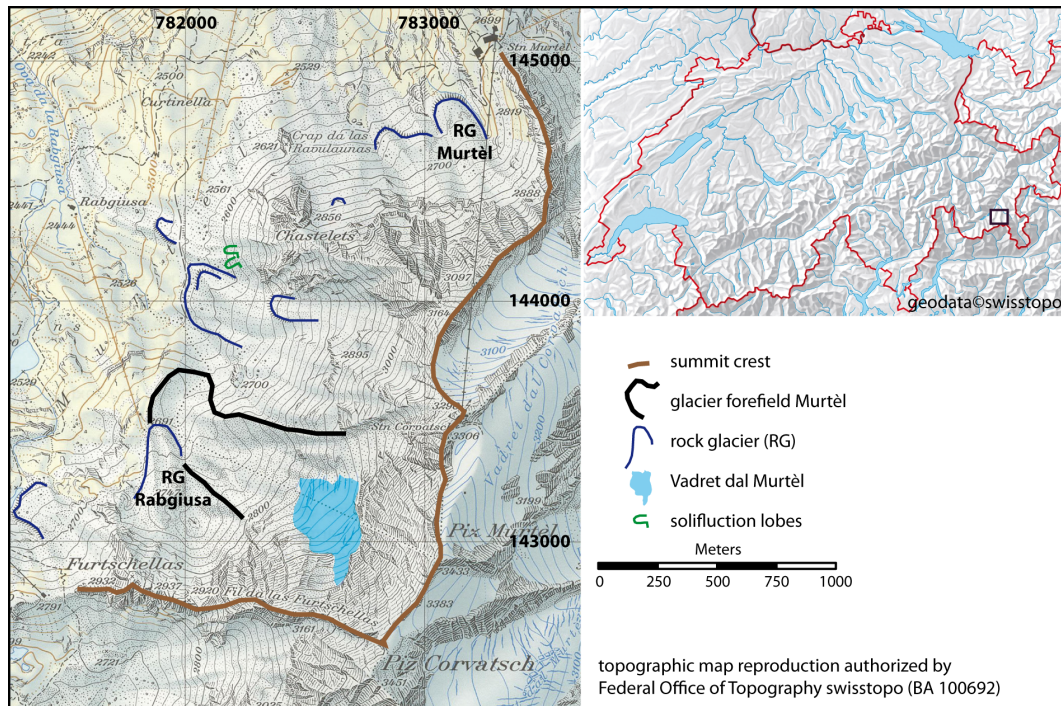
Figure 2.2: Investigation site Murtèl/Corvatsch with glacier forefield Murtèl highlighted
by lateral moraines (black lines).
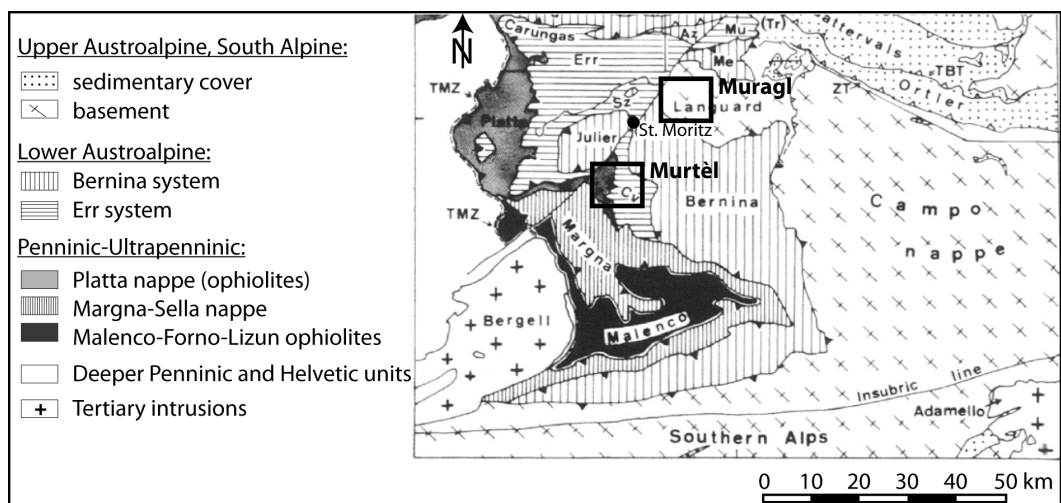
Figure 2.3: Tectonic map of the Penninic and Austroalpine nappes in the southern part of
Grisons. Cv = Corvatsch nappe, Me = Mezzaun unit, Mu = Murtiröl unit, Sz
= Samedan zone, TBT = Trupchun-Braulio thrust, TMZ = Turba mylonite
zone, ZT = Zebru thrust (modified after Froitzheim et al., 1994).

Segl-Maria (1798 m), 978 mm/year and 850 mm/year at Piz Corvatsch (3305 m) for the
reference period 1961–1990 (MeteoSchweiz, 2012). Dry air masses in this high alpine

valley enable a high incoming radiation during the day and vice versa a strong potential for outgoing long-wave radiation during cloud-free nights. As a consequence, the Engadin receives a large quantity of sunshine hours with 1732 h (= 53 % of potential sunshine duration) in Samedan and 2079 h (= 48 %) at summit station Piz Corvatsch. On the other hand, the number of freezing days, i.e., days with a minimum temperature below 0°C, is considerable. Climate station Samedan records on average more than 259 freezing days/year, summit station Piz Corvatsch even 318 freezing days/year. The exceptional large number at the valley station Samedan is caused by the frequent cooling at the valley bottom during cloudless nights that leads to days with temperatures below 0°C also during summer months ($\sim$ 20 days between June and August). MAAT at Samedan is 1.3°C, at Piz Corvatsch -6.0°C (MeteoSchweiz, 2012), and at the climate station on rock glacier Murtèl -1.8°C in 2670 m (data provided by PERMOS).

The climatic conditions as outlined above are an important factor for the predominance of periglacial processes and landforms in the Engadin as typical for cold nonglacial environments. The continental climate with low precipitation inhibits the formation of large glaciers as it is the case for the more southerly Bernina range that is characterized by higher altitude ($\sim$ 4000 m) and more precipitation. In the Murtèl/Corvatsch area only one small hanging glacier — Vadret dal Murtèl (not to confuse with the larger Vadret das Murtèl on the eastward face of Piz Corvatsch) — can be found west of the rock faces of Piz Murtèl and Piz Corvatsch. Typical landforms in the periglacial zone above 2400 m are rock glaciers, large moraine complexes representing former glacier extents, and talus slopes.

The abundance of these landforms, which can be accompanied by the presence of ground ice, promoted research on permafrost-related questions in this region since the early 1970s. A focus was placed on rock glaciers in the Upper Engadin — as the most-striking geomorphological landforms — using methods such as seismic refraction and photogrammetry to derive information on active layer thickness, differences between active, inactive, and relict rock glaciers, and dynamics of the landforms under survey (Barsch, 1973; Barsch and Hell, 1975).

A review of permafrost research that was conducted between the 1970s and 2002 in the Murtèl/Corvatsch-Furtschellas area is given by Hoelzle et al. (2002). The authors provide detailed information on realized investigations and compile results from borehole

observations, surface velocity measurements, geophysical investigations, energy flux measurements, and permafrost distribution modeling. Since new perspectives and questions arose from the early results (Hoelzle et al., 2002) research proceeded within the past 10 years and a summary of the most recent findings is given hereafter. During the last decade research focussed on the ground thermal regime within the active layer, the small-scale occurrence of permafrost, and the main parameters influencing its spatial pattern. Hanson and Hoelzle (2004) investigated the coupling between air temperature and temperatures at and below the surface of the rock glacier Murtèl with multiple thermistors and identified five main categories that show the thermal connection between the air and the active layer over an annual cycle. The investigations were extended into the shallow subsurface, using boreholes of 6 m depth, and to locations others than the rock glacier with different surface material (Hanson and Hoelzle, 2005). The relative importance of conduction and convection was displayed by the shape of the thermal envelope, while the size of the thermal offset in coarse debris highlighted the efficiency of the convective heat transfer in coarse material. The same borehole setup was analyzed using an 8-year data record by Schneider et al. (2012). The authors conclude that the type of subsurface material (bedrock, coarse material, fine-grained debris) is crucial for the site specific processes that control the thermal regime. Ice-rich, coarse-grained material buffers the thawing of permafrost due to the phase change from ice to water and at the same time enhance winter cooling because of a broken snow cover at the surface. Sites with fine material and less ice content are seen as more sensitive to a climate warming. Similarly, Hoelzle et al. (2003) determined differences between measured temperatures from 11 miniature ground temperature data loggers installed at and around rock glacier Murtèl related to variable surface characteristics. The question of scale-dependent measurements and analysis of ground temperatures in the Murtèl/Corvatsch area was recently addressed by Gubler et al. (2011). This study showed the variability in surface conditions and measured temperature parameters in an area of 16 km^2 stretching over an altitudinal range of 1200 m on the large scale as well as within plots (footprints) of 10 by 10 m on a small scale. The same data set was analyzed to infer snow pack ripening and melt out dates (Schmid et al., 2012).

In the last years, geophysical investigations concentrated on rock glacier Murtèl. Hauck and Vonder Muehll (2003b) tested the application of 2D electrical resistivity tomography

(ERT) for the detection of mountain permafrost, while the internal structure was investigated with additional geophysical techniques (time-domain electromagnetic system, seismic refraction, ground-penetrating radar, borehole radar) demonstrating the possibilities and limitations of these methods (Maurer and Hauck, 2007). Further studies investigated the resistivity–temperature relationship (Hilbich et al., 2008a) and the applicability of electrical resistivity tomography monitoring (Hilbich et al., 2009) on this ice-rich, coarse blocky landform, of which the structural composition is well known from direct borehole observations (Vonder Muehll and Holub, 1992; Hoelzle et al., 2002). Deformation measurements in the borehole and information on the internal structure of rock glacier Murtèl indicates a zone of massive ice between 3 and 28 m that represents the part of the rock glacier above a distinct shear zone where most of the displacement occurs (~ 60 %; Arenson et al., 2002).

2.2. Val Muragl, Upper Engadin, Switzerland

Val Muragl is a W/NW-exposed tributary valley of the Engadin that extends between 1733 m (Punt Muragl) and 3157 m (Piz Muragl). Its lower part turns toward southwest. The climatic regime corresponds to the one described in the section above, since Val Muragl is located only about 15 km northeast of the Murtèl/Corvatsch area. Most prominent geomorphological landforms are the glacier forefield of Vadret Muragl and the adjacent rock glacier Muragl (Fig. 2.4).

The rock formations that construct the Val Muragl with summits Piz Vadret (3199 m), Piz Muragl (3157 m) and Las Sours (3008 m), and the neighbouring valleys mainly consist of Ortho- and Paragneiss with magmatic and sedimentary origin, respectively (Peters, 2005). Tectonically, they belong to the Languard nappe, a unit of the Upper Austroalpine nappes (Fig. 2.3). The valley floor is covered by glacial and glacio-fluvial sediments and different glacier extents could be identified based on moraine ridges of lateglacial ages (Maisch et al., 2003). Holocene glacier variations occurred within the extremes of LIA conditions around 1850 and the recent situation.

In Val Muragl, this recent glacier forefield (2640–2900 m) is characterized by a thick sediment bed and distinct morphology with moraine complexes, ridges, run-off channels, and depressions. Small remnants of Vadret Muragl are located at the headwalls of the
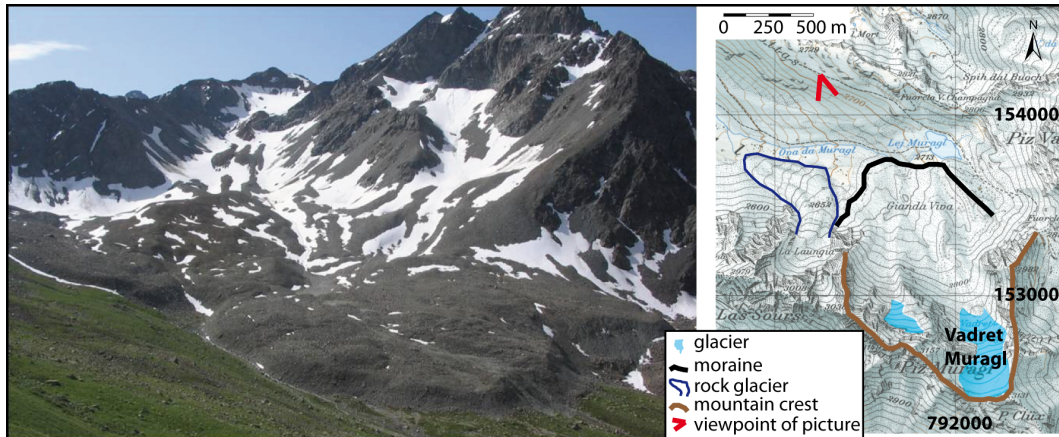
Figure 2.4: Photograph (July 24, 2009) and topographic map of the upper part of Val Muragl with rock glacier and glacier forefield Muragl. Topographic map is reproduced by permission of swisstopo (BA12008).

upper reaches of Val Muragl. The glacier has lost about 75 % of its area between 1850 and 1973 (Maisch, 1992) and another 68 % loss occurred between 1973 and 1988 (Kneisel, 1998). Today, the lower part of the glacier is debris-covered as visible from ice outcrops caused by debris flows of saturated sediments above the ice (active layer slides). The close proximity between glacier ice and permafrost occurrence at glacier forefield Muragl makes it a key site to investigate glacier–permafrost interaction, permafrost evolution, and dynamic behavior in this high alpine area. Present-day processes comprise recent glacier recession and contemporaneous aggradation and degradation of permafrost (Kneisel, 1999, 2010b).

Beside the mapping of lateglacial and Holocene glacier extents and the reconstruction of corresponding paleoenvironments, a variety of research was conducted in Val Muragl. As mentioned above the glacier forefield (within the limit of the 1850s moraine) was investigated in terms of permafrost dynamics. Permafrost occurrence was detected in detail using geophysical techniques by Kneisel (1998, 1999, 2003, 2006, 2010b). In addition to the mapping of permafrost, zones of maximal surface displacement in the glacier forefield were delineated using photogrammetric methods and geomorphological observations (Kääb and Kneisel, 2006; Kneisel and Kääb, 2007). Based on the results of these integrative analyses the forefield consists of a push-moraine complex with high ice content and a slight horizontal displacement, a part with small ice content but moderate creep

rates, a part with thin permafrost and small-scale settlement structures, and finally of non-creeping parts that are most probably not underlain by permafrost (see Fig. 8 in Kneisel and Kääb, 2007). A detailed analysis of the resistivity distribution in the subsurface using 2D geoelectrical transects arranged in a 3D grid was conducted by Bast (2009) with a focus on small-scale heterogeneity of permafrost occurrence. Roth (2011) analysed the temporal behaviour of the thin permafrost close to the front of the forefield, while Kästl (2012) investigated the zone of highest horizontal displacement close to the rock glacier at the front of the forefield by means of combined geophysical methods.

Adjacent to the glacier forefield, rock glacier Muragl is located and equally well investigated. Photogrammetric analyses of surface kinematics started already in the first half of the 20th century (Salomon, 1929; Domaradzki, 1951). Investigations were extended using refraction seismics by Barsch (1973). Arenson et al. (2002) gives a detailed description of the internal structure of the rock glacier derived from four boreholes: ~ 70 m deep, drilled in 1999. Compared to e.g., rock glacier Murtèl the ice content is more heterogeneous at depth and is in general comparably low with 40–70 % by volume. Temperatures are slightly below the freezing point (minimum at -0.5°C) and the permafrost base was detected in about 20 m depth. Slight temperature oscillations in 25 m depth and the registration of air voids during drilling led to the conclusion that air circulation exists between that depth and the atmosphere (Vonder Muehll et al., 2003). A distinct shear zone where most of the deformation takes place is observed between 14 and 18 m depth (Arenson et al., 2002). Annual average surface horizontal displacement is up to 0.5 m/a, with maximum rates observed in the steeper central part (Kääb and Vollmer M., 2000). Arenson et al. (2002) observed seasonal variations in the creep rate with velocities up to three times higher during winter months. This pattern is attributed to the attenuation and phase lag of the temperature signal with depth. In general, the vertical displacement is rather small with ± 0.1 m/a. A surface lowering of up to 0.5 m/a was observed at the higher parts of the rock glacier provoked by a loss of ice in perennial ice patches (Kääb and Vollmer M., 2000).

2.3. Zugspitze, Wetterstein Mountains, Germany

The Zugspitze (2962 m) is the highest mountain in Germany located in the Wetterstein Mountains (Lechtal nappe, Upper Austroalpine nappes) at the national border between Germany and Austria (Fig. 2.5). Massive Triassic limestone (Wetterstein limestone) of about 800 m thickness builds up the rugged mountain crest. The marly claystone of the Partnachschichten (thickness of 300–400 m) has a low hydraulic conductivity and acts as an aquiclude at the base of the Wetterstein limestone (Wetzel, 2004, Fig. 2.6). South of the Zugspitze and enclosed by the c-shaped summit crest the eastward dipping Zugspitzplatt is located. The latter is a plateau-like area that is subject to karstification processes since the Tertiary and shows numerous dissolution forms of a typical karst landscape (karren, dolines, sink holes, karstic spring at 1430 m).

At the Zugspitze summit a meteorological observatory of the German Weather Service (DWD) is operated since 1900. During the climate normal period (1961–1990) mean annual temperature was -4.8°C, annual precipitation summed up to 2003 mm (DWD, 2012).

Through the mapping of moraine ridges on the Zugspitzplatt the retreat of the glaciers within the Wetterstein mountains (today: Southern and Northern Schneeferner, former: Plattachferner) was documented (Hirtlreiter, 1992, cf. Fig. 7a) and recently continued using geodetic measurements (Hagg, 2010). Accordingly, the Plattachferner covered an area of about 2.6 km^2 in 1820 (Hera, 1997) before it split up in two parts at the end of the 19th century. In 1892, Northern and Southern Schneeferner covered an area of 1.89 km^2 while in 2009 their extend is no more than 0.33 km^2 (Fig. 2.5). The most prominent reduction of ice-covered area within the past 117 years is observed at the Southern Schneeferner (96 %) owing to the lack of surrounding rock faces that deliver avalanche snow in winter or shading in summer (Finsterwalder and Rentsch, 1973). About 72 % of the glacier area was lost at the Northern Schneeferner were modern snow farming techniques (snow depots, partial coverage with white tarps in summer around infrastructure) highly influenced the mass balances in the last decades. Figure 2.6 shows glacier extents since the Last Glacial Maximum at the Zugspitzplatt and the adjacent Höllental according to associated moraine ridges.

The well documented reconstruction of glacier retreat in the last century using pho-
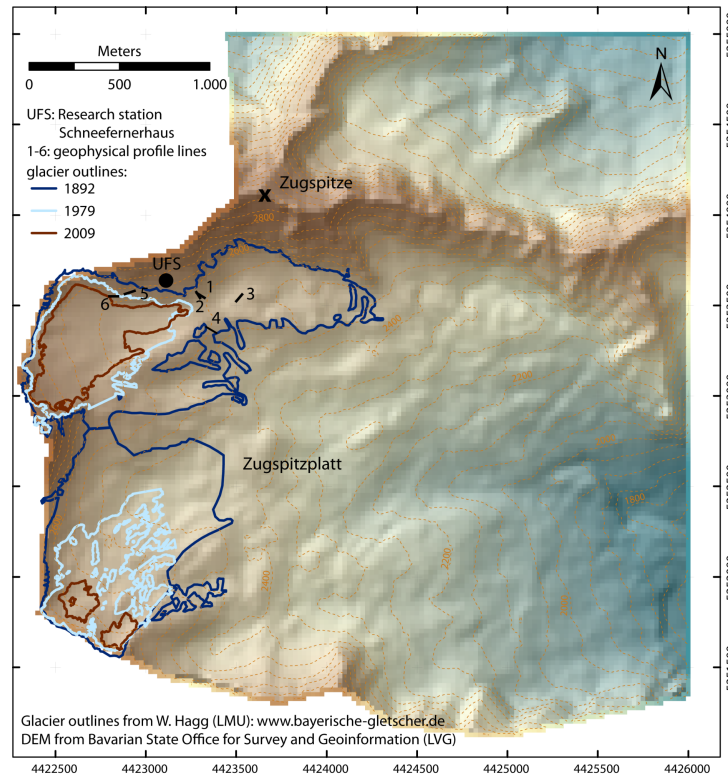
Figure 2.5: Digital elevation model of the Wetterstein Mountains with Zugspitze and Zugspitzplatt. Outlines of recent and former glacier extents are indicated by colored lines (Plattachferner in 1892, Northern and Southern Schneeferner in 1979 and 2009).

togrammetry and geodesy is supported by temperature observations. Data from the meteorological station Zugspitze provide information on a considerable warming trend in the last decades. At the beginning of the meteorological observations the MAAT was -5.0°C (1901–1930) (Verleysdonk et al., 2011). Between 1991 and 2007 the MAAT was -3.9°C at the observatory and thus another 0.9°C higher compared to the former normal period. Analyses of numerous alpine climate series have also shown this warming trend (e.g., Böhm et al., 2001) for the entire European Alps. This increase is about twice as high as the global average of 0.55°C warming between the 1970s and 2006 (Trenberth et al., 2007).

At the Zugspitze, an interest in permafrost and frozen ground conditions arosed when frozen rock and ice-filled clefts were detected during building operations at the summit crest. In 1961, during the construction of the cable car 'Eibsee-Zugspitze' perennially frozen weathered loam and up to 10 cm thick ice-lenses were found in the cleavages of the
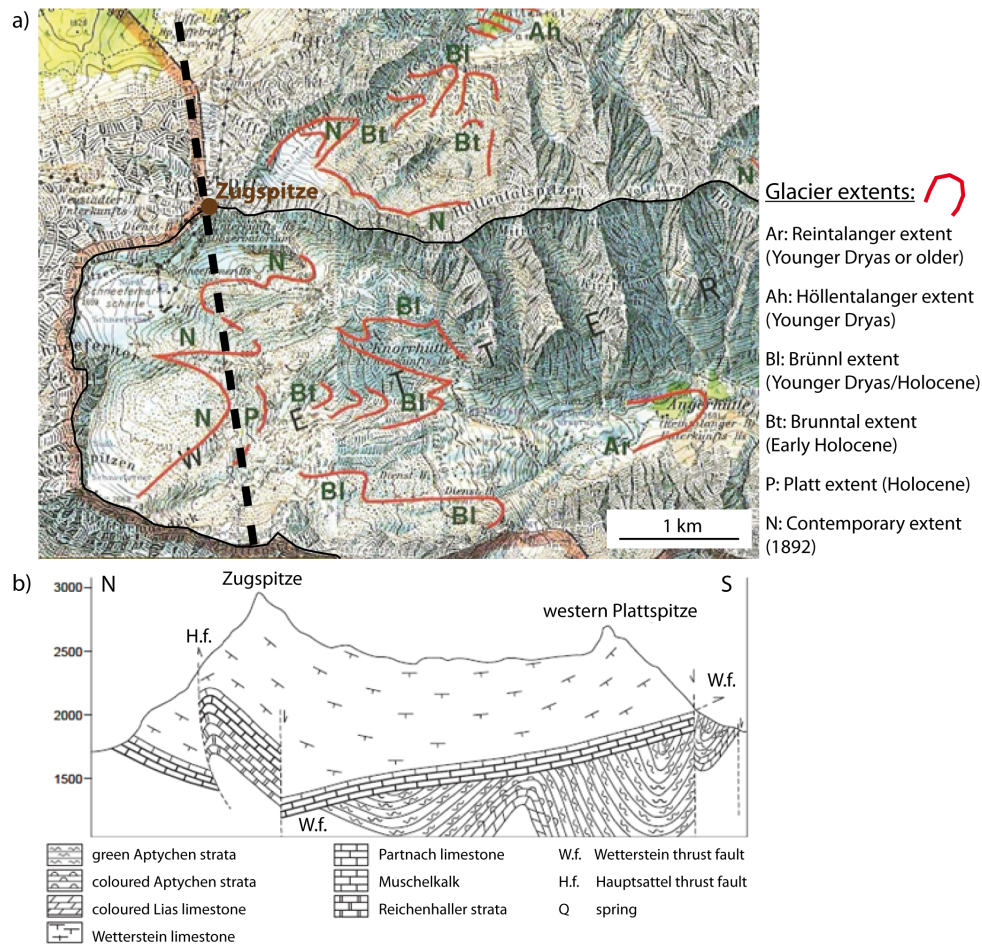
Figure 2.6: Topographical map of the western part of the Wetterstein Mountains and geological cross section along the black dotted line on the Zugspitzplatt. (a) modified from Meyer and Schmidt-Kaler (2002), after Hirtlreiter (1992), (b) in Wetzel (2004).

highly fractured crest (Körner and Ulrich, 1965; Ulrich and King, 1993). Similarly, ice-filled joints were observed in the shallow subsurface of the southern slope of the summit when another cable car ('Zugspitzplatt-Zugspitze') was constructed between 1991 and 1993 (Ulrich and King, 1993). Even at the Zugspitzplatt about 350 m below the summit, a massive ice body ($\sim$ 19 m in diameter) filled a sink hole that was hit during construction of a tunnel in 1985 (Ulrich and King, 1993). In the last decade, when a path leading from the research station Schneefernerhaus to the glacier Northern Schneeferner was bulldozed, ice outcropped in the upper zone of a talus sheet (H. Hiergeist, UFS, personal communication in July 2011). Further evidences of ground ice are collapsed sink holes that were formerly sealed with ice (Krautblatter and Verleysdonk, 2010).

Scientific investigation on permafrost distribution and its implication for the infrastructure of the summit station was implemented within the research project PACE (Permafrost and Climate in Europe, Harris et al., 2001). Based on results from temperature monitoring at the bottom of the winter snow cover and distribution modeling using the Swiss model PERMAKART the occurrence of permafrost at the Zugspitze crest was shown (Gude and Barsch, 2005). While the north-facing slopes are deeply frozen along the whole crest, cold BTS temperatures are sparse or inappropriate at the southern slope. Interpretation of the results is limited because of the shallow or even total lack of a considerable snow cover at the steep rock faces, which is a precondition for the BTS method. At the Zugspitzplatt ground ice was found in several places, which are interpreted as relict ground ice. In summer 2007, a roughly 50 m long borehole was drilled through the Zugspitze summit and equipped with 25 temperature sensors. The thermal regime is recorded within the summit crest from its south-facing slope to the north-facing slope. Permafrost conditions are evident from the center of the borehole ($<$-3°C) toward the north face (Bayerisches Landesamt für Umwelt, 2012). This corresponds to modeling results from idealized summit crests (Noetzli et al., 2007). Recent studies on permafrost distribution and the temperature–resistivity relationship on the north face of the Zugspitze were conducted using electrical resistivity tomography. Krautblatter (2010b) showed seasonal changes in a permafrost rock wall by repeated ERT measurements between February and October. Resistivity changes were found to be in agreement with seasonal temperature changes and freezing and thawing processes could be observed by decreasing and increasing resistivity values. Field measurements were calibrated using laboratory tests in a freezing chamber. The whole mountain permafrost system Zugspitze was analyzed in terms of sensitivity and path dependence using multiple methods such as historical data (maps, reports, aerial photographs), meteorological data, and electrical resistivity monitoring to analyze the present state of this system (Verleysdonk et al., 2011).

3. Methods and data basis

In this chapter the four complementary methods that were applied during fieldwork are introduced. Major advantages and drawbacks are discussed together with present permafrost-related studies that showed the applicability of each method. Finally, the data basis of the present study and the methods of analyses are given in each section.

3.1. Electrical resistivity methods

Developed in the early 1900s electrical resistivity methods are widely used in all kinds of geophysical prospections and environmental investigations. A focus in this study is on direct current electrical resistivity. The basic principles of this technique along with the nowadays standardly used electrical resistivity tomography approach are shortly described before their use in selected alpine case studies and the existing data base are discussed.

3.1.1. Basic principles of current flow in the subsurface

The overriding aim of geoelectrical resistivity techniques is the reconstruction of structures in the subsurface based on the measurement of the voltage difference between two potential electrodes in response to a direct current (DC) injected into the ground by two current electrodes. Geological and structural units with different electro-physical properties alter the distribution of the conductivity and its reciprocal, the resistivity of the ground compared to a homogeneous half space. Electrical currents are dragged into more conductive parts of the subsurface while more resistive ones are bypassed by the currents resulting in a change of the electrical potential. The electrical conductivity that is found in natural substances extends over a range of 25 magnitudes from Diamond (resistor) to Copper (conductor), which is beside the viscosity the second most dynamical physical property (Berktold et al., 2005). Consequently, this method enables the differentiation of subsurface materials (e.g., bedrock, sediment, water, air) because of the varying electrical conductivity/resistivity. However, typical resistivity ranges of naturally occurring materials overlap to some extent and thus the implications of the geoelectrical study may be

non-unique in terms of a geological or sedimentological interpretation (Table 3.1). Additional information from boreholes, outcrops, or other geophysical investigation techniques help to constrain the subsurface image.

Table 3.1: Range of electrical resistivity ρ and P-wave velocity V_p for materials relevant for permafrost-related studies (excerpt from Reynolds, 1997; Berktold et al., 2005; Kneisel and Hauck, 2008).

Material	ρ **[kohm.m]**	V_p **[m/s]**
Air	non-conductor	330
Water	10–300	1450–1530
Ice	$5*10^4$–$1.2*10^8$ [a]	3000–4000
Soil	8–1000	100–500
Snow	$>10^5$	350–3000
Sand and gravel	30–1400	400–2300
Glacial moraine	10–5000	1500–2700
Permafrost (Quaternary sediments)	10^3–$>10^4$	1500–4900
Limestone	50–10^7	2800–7000
Dolomites	350–5000	2500–6500
Granites (weathered)	300–10^6 (30–500)	4600–6200
Gneiss	100–10^3	3500–7600

[a] strongly dependent on temperature.

Three different kinds of mechanisms are responsible for current flow to occur in subsurface material. The transport of charge through the mineral grains itself (electronic conduction) is restricted for stones and bedrock. Similarly, the conductivity along the surface area of rock particles (dielectric conduction) is of minor importance for investigations that apply electrical resistivity methods. It may be of relevance for material with high clay content where the interaction between pore liquid and particle surfaces allow a current flow at the boundary of the clay particles. The dominant process that determines the conductivity of the mineral subsurface is the electrolytic conduction by means of ion transport within the pore fluids of the ground matrix. Already a thin (several molecules) interconnected layer of moisture at the surface of ground particles is able to increase the

conductivity by four to five magnitudes (Berktold et al., 2005). Beyond the simple avail-ability of a pore fluid, the saturation of pores, the chemical properties of pore water, the absolute pore volume and the temperature in the subsurface are of critical importance to the resistivity of ground material and explain the wide range of resistivity values as given in Table 3.1.

The effective resistivity (ρ) of a porous medium can be described with an empirical formula according to Archie (1942). This relationship takes into account the porosity (ϕ), the fraction of the pores containing water (s), and the resistivity of the water (ρ_w),

$$\rho = a * \phi^{-m} * s^{-n} * \rho_w. \tag{3.1}$$

Parameters a, m and n are empirical constants (see list of abbreviations). The formula indicates the importance of the proportion of pore fluids for the resistivity of the ground that is much more relevant than the electronic conduction in the host material. Be-side the saturation, anisotropic effects (e.g., parallel bedding of sediment structures) are responsible for the range of resistivity values that are registered in common geological materials.

3.1.2. DC resistivity tomography

Most measurements that are made with geoelectrical resistivity methods are based on the arrangement of four electrodes at the ground surface. The electrodes are usually inserted along a linear profile. Square arrays are also common and especially suitable for surveys of steeply dipping structures. An artificial power source injects a direct current through two current electrodes (A^+ and B^- in Fig. 3.1) into the subsurface. An electric current (I), which is defined as the direction of flow of positive charge, develops and induces a potential field perpendicular to the current lines. The resulting potential difference (δV) — as the energy needed to move a unit charge from one point to another in the electric field — is measured with two additional electrodes (M and N). On the basis of Ohm's Law the apparent resistivity of the investigated part of the subsurface can be calculated (eq. 3.2).

$$\rho_a = K * \frac{\delta V}{I}. \tag{3.2}$$

Dependent on the applied electrode arrangement the geometric factor (K) has to be considered. This factor depends on the geometry of the electrode configuration and can be calculated according to the equation given in Fig. 3.2. Because the investigated ground is a heterogeneous medium with different lithologies, geological structures, and variable contents of the phases water (and/or ice and vapor), air, and mineral grains, the resistivity obtained by this measurement is called the apparent resistivity ρ_a, which is not regarded as a physical property of the subsurface. Measurement results are given as apparent resistivity of an equivalent uniform half-space. Thus, all measured field data are considered as apparent resistivity whereas those derived from inversion and interpretation techniques are called "true" or "specific" resistivity.
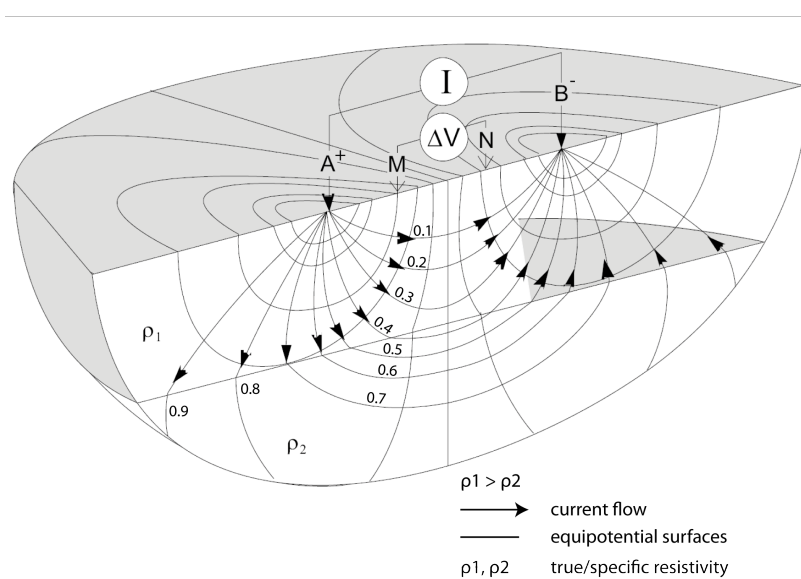
Figure 3.1: Cross section through a four-electrode arrangement with a positive (A^+) and a negative (B^-) current electrode and a pair of potential electrodes (M and N). Electric lines diverge from the positive point charge and converge at the negative point charge with potential difference between these two points as indicated by the equipotential surfaces. Numbers on the current lines indicate the fraction of current flowing above the line (modified from Berktold et al., 2005; Lowrie, 2011).

Depending on the objectives of the scientific problem and the logistical restrictions of the geoelectric study an appropriate electrode configuration has to be chosen. Most widely applied array types are Wenner (α), Schlumberger, Dipole-Dipole, Pole-Dipole, and Gradient arrays, with the first three (Fig. 3.2) as frequently applied configurations used for investigations in periglacial environments. For a comprehensive description of array types and their assets and drawbacks it is referred to relevant textbooks such as Telford et al. (1990), Reynolds (1997), or Berktold et al. (2005).

Differences between the electrode arrays comprise the amount of space needed for the installation in the field, the number of readings if measured with a multielectrode system, and above all the vertical and horizontal resolution of ground structures. The latter is expressed by the sensitivity to lateral and vertical heterogeneities and can be found in graphical form in Loke (2012, p. 28ff.). The Wenner array has a high vertical resolution and thus is most sensitive for horizontally layered structures. Comparable to the Wenner array is the Schlumberger array that has an almost similar resolution with depth. The vertical resolution of the Dipole-Dipole array is rather weak. However, it is well suited for the investigation of lateral inhomogeneities close to the surface. Another criterion for the appropriate choice of the electrode array for resistivity surveys is the signal to noise ratio. Since the signal strength is inversely proportional to the geometric factor of the applied array the Wenner array has the highest signal strength (cf. Table 2.1 in Loke, 2012, p. 27), whereas the Dipole-Dipole array has a low signal strength especially for large spacings between the two dipole pairs.

In the early days of electrical resistivity surveys one-dimensional vertical soundings using a simple four-electrode arrangement were applied. For the mapping of lateral inhomogeneity the four electrodes had to be moved along the surface, while an increase of the electrode spacing yielded data values from greater depth. With the continuous development of technical and computational capabilities electrical resistivity tomography has become the standard method for engineering and environmental studies. Today, multielectrode systems are used with a large number of electrodes, connected with a resistivity meter by a single multicore cable. A predefined measurement scheme is executed measuring all possible electrode combinations of the chosen array type. The available data set finally consists of numerous apparent resistivity measurements (so called pseudosection) that are inverted by efficient algorithms in commercial analysis software (e.g., Loke and
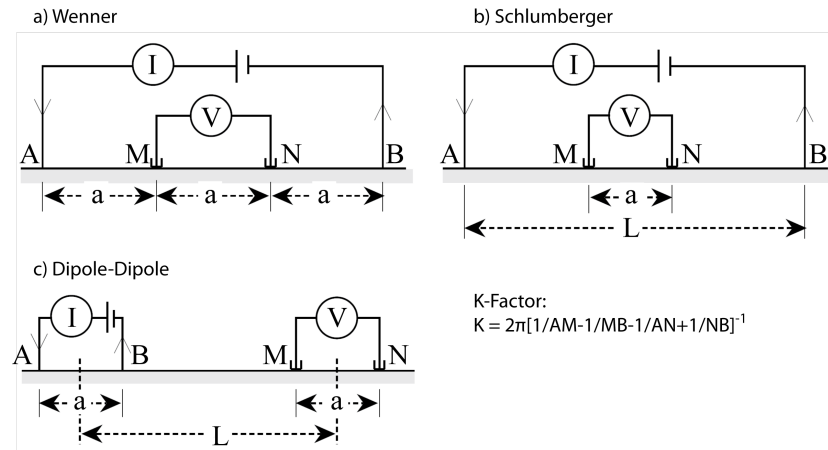
Figure 3.2: Geometric configuration of the array types (a) Wenner, (b) Schlumberger and (c) Dipole-Dipole. The general expression for the calculation of the geometric factor K is also given (modified from Lowrie, 2011).

Barker, 1996). The inversion computation seeks to find a plausible geological model with cell-based variable specific resistivity values that would yield a calculated pseudosection of apparent resistivities similar to the measured one. An iteration process aims at the minimization of the difference of the calculated and the measured data misfit by using either a blocky (robust) optimization method (L_1-norm, Claerbout and Muir, 1973) or a least-squares optimization equation (L_2-norm, deGroot Hedlin and Constable, 1990). While the former is suited for situations with homogeneous regions separated by sharp boundaries, the latter yields superior results in case of smooth resistivity variations. A study analyzing synthetic and field data by Loke et al. (2003) shows the advantages and problems of both optimization methods in resolving subsurface structures. The computation of the specific resistivity in a subsurface model enables the reconstruction of subsurface structures in complex terrain. However, resulting model sections of ERT surveys are not unique and additional information from geomorphological observation, borehole data, and/or additional geophysical methods are needed for a coherent interpretation of electrical resistivity data.

3.1.3. Electrical resistivity methods in permafrost-related studies

The applicability of electrical resistivity methods for periglacial environments with sporadic or (dis-)continuous permafrost is closely related to the drastic change in the physical

property (i.e., electrical conductivity) that is coupled with the phase change of water from liquid to solid. The general increase in resistivity during freezing of liquid water is well known (e.g., Scott et al., 1990, for a summary). Recently, Krautblatter (2009, 2010b) resolved the temperature–resistivity behavior of rock specimen of different lithology in a laboratory experiment with special focus on temperatures around the freezing point. Stepwise cooling of the rock sample yielded the following pattern: supercooling of the sample with slight resistivity increase between -0.5°C and -1.1°C, sudden freezing and release of latent heat (+0.6°C), and a new linear relationship between temperature and resistivity after the spontaneous freezing.

Because of the large contrast in resistivity between frozen and unfrozen material DC resistivity methods are widely applied to study permafrost-related problems. In alpine areas the use of electrical resistivity methods for the investigation of frozen ground was introduced in the 1970s and 1980s after the successful application in glaciological studies (i.e., determination of ice thickness Keller and Frischknecht, 1960; Röthlisberger, 1967). At first, the focus was placed on the detection and the examination of the permafrost thickness in Scandinavia (e.g., Østrem, 1964; King, 1982) and the European Alps (e.g., Fisch et al., 1977; King et al., 1987; Evin and Fabre, 1990; Vonder Muehll, 1993; Kneisel, 1998) using vertical electrical sounding, especially on landforms such as rock glaciers and ice-cored moraines. Surveys resulted in a sounding curve of the apparent resistivity and after inversion techniques were introduced the calculation of 1D models of the resistivity distribution with depth was possible. With the advent of more sophisticated resistivity meters and improved computational performance, 2D electrical resistivity soundings were developed. This technique was introduced at the turn of the century (Hauck, 2001) and is since then widely applied to investigate various landforms such as moraines (Hauck and Vonder Muehll, 2003b), rock glaciers (Ikeda, 2006; Hausmann et al., 2007), glacier forefields (Kneisel, 2003; Reynard et al., 2003; Kneisel, 2006; Kneisel et al., 2008; Kneisel, 2010a; Ribolini et al., 2010), talus slopes (Marescot et al., 2003; Kneisel and Schwindt, 2008; Scapozza et al., 2011), and rock walls (Sass, 2004; Krautblatter, 2010a,b; Verleysdonk et al., 2011). In recent years, further development is directed to the monitoring of dynamics and temporal changes in permafrost environments by multi-temporal ERT acquisitions (Hauck, 2002; Kneisel, 2006; Krautblatter and Hauck, 2007; Hilbich et al., 2008a,b) and the use of automated electrical monitoring systems (Hilbich et al., 2011;

Kneisel et al., 2014). Monitoring approaches enable to observe and detect long-term changes and/or time-dependent processes acting on different time scales within the active layer or within the permafrost-affected landform (Kneisel et al., 2012).

3.1.4. Data basis and method of analysis

Electrical resistivity measurements were performed at all three investigation sites to observe resistivity contrasts and thus infer subsurface structures in areas with potential permafrost occurrences. Each profile was measured with 36 electrodes connected to a resistivity meter (Syscal Junior Switch, Iris Instruments). Electrode spacing was chosen as tradeoff between spatial coverage of the investigated area (larger spacing for reconnaissance mapping and smaller spacing for in-depth sounding) and estimated depth of the anticipated target (e.g., active layer, permafrost thickness). To overcome the problem of bad electrode contact with the superficial coarse debris layer at some electrodes, wet sponges were clamped to reduce the contact resistance (Hauck and Kneisel, 2008). As best compromise between horizontal and vertical resolution, signal-to-noise ratio, and acquisition time Wenner and Wenner-Schlumberger arrays were chosen and yielded robust results in most cases. Tests with the Dipole-Dipole array gave less good results within the periglacial environments and thus were rejected. Only one electrical resistivity tomogram from the Zugspitzplatt based on a Dipole-Dipole array is presented and discussed (cf. chapter 6).

At Murtèl/Corvatsch site numerous ERT profiles were measured in August 2009 based on a reconnaissance mapping in 2008 that identified permafrost at the transition of lateral moraine and rock glacier (see Tables A.1 and A.2 in appendix A). Final goal was the establishment of a 3D subsurface resistivity model for the delineation of the ground ice body (3D ERT grid in Fig. 3.3).

The measurement grid consisted of 23 lines — 12 in x- and 11 in perpendicular y-direction — covering an area of about 120 m^2. Each profile was based on 36 electrodes leading to a total number of 826 electrode positions. An electrode spacing of 3 m and an inter-line spacing of 9 m has been chosen to reach a reasonable lateral and vertical resolution with 15–20 m median depth of investigation (depending on electrode array, cf. Edwards, 1977; Loke, 2012). Owing to steep and unstable terrain, profile Gl11 was skipped

and longitudinal profiles (Gl7–Gl12) were shifted uphill by 12 electrode unit spacings (see Fig. 4.2, p. 64). Profile Gl6 consists of two single profiles across the borehole, measured in a roll-along technique where the cable is moved past one end of the profile. Both profiles were concatenated into one data set for subsequent analyses.

Measurements have been conducted with Wenner (198 data points per profile) as well as Wenner-Schlumberger (288 data points per profile) electrode arrays. The coupling of electrodes to the ground was sometimes difficult because the ground was in parts covered with coarse gravel and large boulders, more than 0.5 m in diameter. The acquisition time for all 23 2D profiles was 7 days. Because the arrangement of electrodes is not in agreement with a true areal (3D-)array as proposed by Loke (2012), this combination of several single 2D ERT profiles, which are measured one by one and inverted afterwards with a 3D algorithm, is referred to as quasi-3D technique. The final outcome of this technique can be regarded as 3D subsurface model.

Based on the results of the 3D geoelectric study, borehole temperature data, and findings from refraction seismic tomography a monitoring system with buried electrodes and connection cables was installed at Murtèl/Corvatsch site in August 2010 (ERTM-Mrt, Fig. 3.4). Thin copper cables connect the electrodes with a switch box that is stored in a water resistant aluminum case. During the following six months the monitoring was measured five times manually with the Syscal Junior Switch (see Fig. A.1 in appendix A). In February 2011 a Geotom 100 (Geolog) was installed at the field site and since March 2011 the ERT monitoring was measured automatically on a daily basis (Table 3.2). The measured data is transferred wireless via directional antennae from the field site to the summit station of the Piz Corvatsch cable car. Here, a computer enables the communication with the resistivity meter and stores the incoming data. Power supply is obtained from 12 V batteries that are recharged by a solar panel. A detailed description of the Geotom measurement system with technical details is given by Hilbich et al. (2011) who use an identical system. During implementation of the automated monitoring system some problems arose and caused longer data gaps. Problems were caused by power failure in the summit station and subsequent breakdown of the control unit (lightning), abrupt termination of the measurement during data acquisition, and damage at the connection between electrodes and cable during winter.

Four permanent ERT monitoring profiles were installed in 2004 at glacier forefield
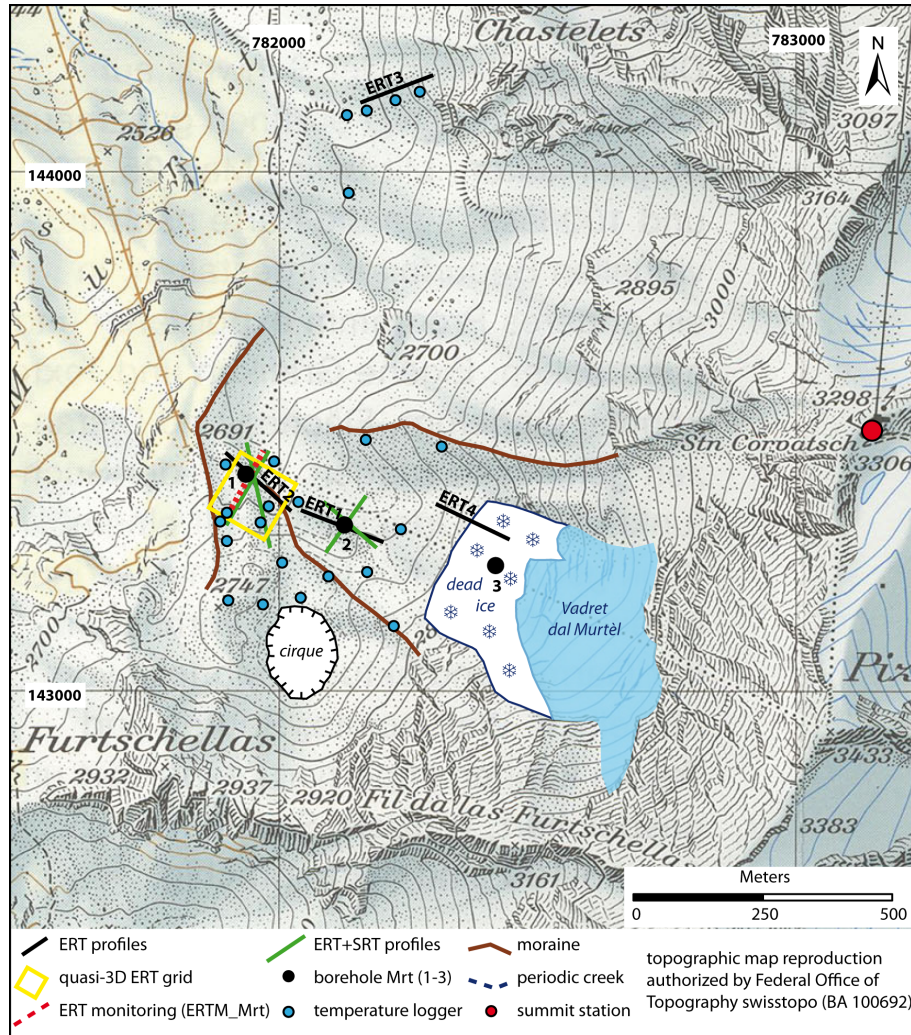
Figure 3.3: Glacier forefield Murtèl with position of the most important measurement
locations of ERT, RST, and temperature monitorings.

Muragl (Fig. 3.5). At both sites electrodes with a fixed spacing of 1 m and 2 m were
inserted into the ground and measurements were repeated several times during snow free
months (July–September) each year (see Table B.1 in appendix B). Different survey de-
signs aim at a detailed observation of active layer changes (1 m electrode spacing) and
general permafrost behavior (2 m), respectively. Because these monitoring sites were not
equipped with fixed cables access to the monitoring was only possible during summer
months. The 1 m profiles were disassembled in 2009 while the 2 m profiles were perpetu-
ated. Profile ERTM-Mgl1 close to the front of the glacier forefield monitors a permafrost
body beneath coarse blocky openwork whereas the other monitoring ERTM-Mgl2 was
constructed at a ridge with deep permafrost and fine- to medium-grained substrate at the
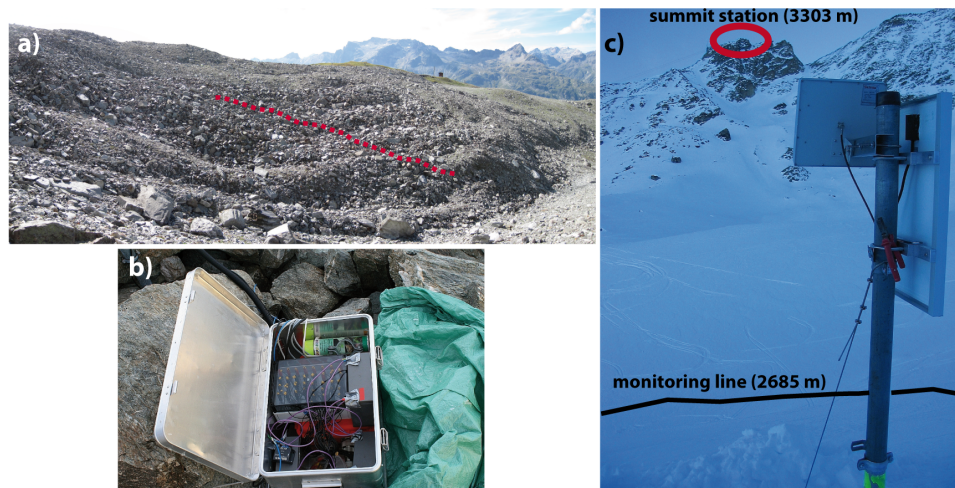
Figure 3.4: Photograph of the ERT monitoring installation at glacier forefield Murtèl. (a) position of the monitoring, (b) resistivity meter stored in a water resistant aluminum case, (c) winter situation with solar panel and antenna for communication with remote computer at station Corvatsch.

surface.

In 2009 and 2010 the profiles were equipped with a fixed cable and connection plug for year-round accessibility. Because of heavy snow load as well as harsh climate and surface conditions these setups were prone to damage, and data quality of measurements in September 2010 was greatly reduced compared to the years before. Consequently, these data set could not be utilized in this study. A summary of the ERT data base from all monitoring sites is given in Table 3.2.

Table 3.2: Data base of ERT monitoring data from glacier forefields Muragl and Murtèl.

ID	Electrode spacing [m]	Array type	No. of data sets	Measurement period	Acquisition mode
ERTM-Mgl1	1	Wen, WenSL, Dip*	21	July 28, 2005–Sept. 27, 2009	Manual (fixed el.)
ERTM-Mgl1	2	Wen, WenSL, Dip*	29	Aug. 5, 2004–Sept. 12, 2010	Manual (fixed el.)
ERTM-Mgl2	1	Wen, WenSL, Dip*	21	July 28, 2005–Sept. 27, 2009	Manual (fixed el.)
ERTM-Mgl2	2	Wen, WenSL, Dip*	28	Aug. 4, 2004–Aug. 10, 2010	Manual (fixed el.)
ERTM-Mrt1	2	Wen, WenSL	5	Aug. 24, 2010–Feb. 11, 2011	Manual (fixed el.)
ERTM-Mrt1	2	Wen, WenSL	58	Mar. 17, 2011–Sept 17, 2011	Automatic

* only few measurements implemented with Dipole-Dipole array in 2004 and 2006.

Because of bad weather conditions and snow fall in summer 2010 at the Zugspitzplatt
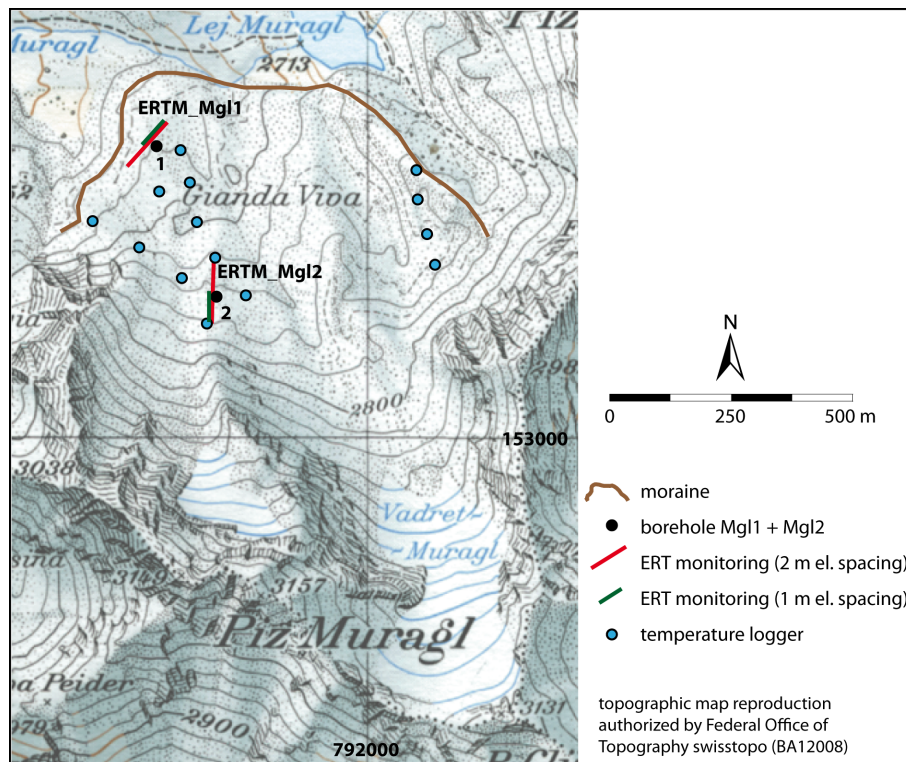
Figure 3.5: Glacier forefield Muragl with position of the most important measurement locations of ERT and temperature monitoring.

geoelectrical measurements were restricted to five days of field work in July 2011 (see Table C.1 in appendix C). During that period, which was also characterized by regular snowfall at night, in total 6 ERT profiles could be measured (see Fig. 2.5, p. 26). The profiles Zug-ERT1 and Zug-ERT2 were measured on a large talus cone directly underneath the Zugspitze crest. On the glacial till of the Zugspitzplatt two measurements (3 and 4) were conducted, bearing in mind that this area is highly influenced by constructional work for infrastructure and operation of ski runs. Along a path from the research station Schneefernerhaus toward the Northern Schneeferner two profiles were measured (5 and 6) above and beneath a distinct debris slide. All ERT profiles had an electrode spacing of 2 m with 36 electrodes in use.

Pre-processing of all geoelectrical raw data was done using the software Prosys II, before data were exported for further analysis. The inversion process of apparent resistivity values into specific resistivities was conducted in Res2dinv for 2D profiles and in Res3dinv for the collated data set (Murtèl). The absolute difference between measured and calculated apparent resistivity values is given as absolute error and indicator for the quality

of the data. Resulting tomograms were finally edited (extraction of vertical 1D sections) and illustrated in Geoplot and Adobe Illustrator.

3.2. Seismic surveying

Evolved from pioneering earthquake studies in the mid-to-late 19th century, seismic surveys are today based on different kinds of artificial (active) seismic sources. There are two main seismic methods, refraction and reflection, from which the former is applied in this study for the investigation of the shallow subsurface. A short introduction of the general principles of seismology are given before the refraction seismic tomography (RST) method is described in more detail. This section ends with a discussion on permafrost-related seismic studies and the description of the present data set.

3.2.1. Seismic waves

The basic principle of applied seismology is the measurement of the velocity of a seismic wave travelling through an investigated medium. If the points in time of wave generation and the times of arrival of the returning signal (via reflection or refraction) are known, the resulting time difference is used to derive information on the subsurface structure and the physical properties of the material that was passed through by the seismic wave (e.g., Telford et al., 1990; Reynolds, 1997; Brückl et al., 2005).

There are two main types of seismic waves generated by and travelling away from a seismic source (Reynolds, 1997): body waves pass through the bulk of the subsurface, while surface waves are confined to the interface of structures with differing elastic properties. The latter occur particularly at the ground surface. Body waves can be further distinguished in two types with different directions in terms of particle motion. P-waves (primary, longitudinal, or compressional waves) travel parallel to the direction of wave propagation by compressional and dilatational strain (Fig. 3.6). In contrast, S-waves (secondary, transverse, or shear waves) are characterized by particle motion perpendicular to the direction of wave propagation.

The speed of seismic wave propagation depends on the elastic moduli and the density of the medium that is passed. Different elastic moduli (dimensionless) describe the
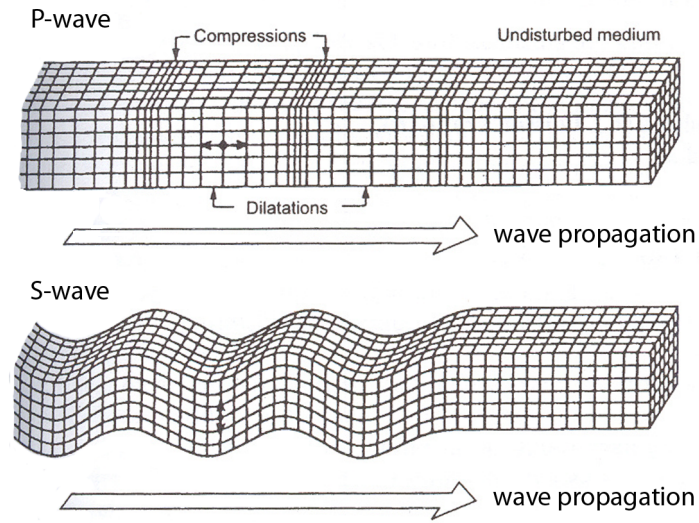
Figure 3.6: P-wave and S-wave propagation within elastic material. Black dots and arrows show ground particle motions in respect to the general direction of wave propagation (Reynolds, 1997).

stress-strain relationship that is linearly dependent for any material with elastic behavior according to Hooke's Law. Young's modulus E is valid in the case of triaxial strain and is a parameter for the resistance of the material against elastic deformation (incompressibility):

$$E = \frac{\sigma}{\epsilon},$$ (3.3)

with E=*Young's modulus*

σ=*longitudinal stress δ F/A*

ϵ=*longitudinal strain δ L/L.*

If the stress is applied from all directions (hydrostatic pressure) the volume is compressed without a change in the shape of the body (rigidity). This is described by the bulk modulus k:

$$k = \frac{\delta P}{\delta V/V},$$ (3.4)

with k=*bulk modulus*

P=volume stress

V=volume strain.

The shear modulus μ describes the change in shape of a body if tangential stress is applied:

$$\mu = \frac{\tau}{\epsilon},$$ (3.5)

with   *μ=shear modulus*

τ=shear stress

ϵ=shear strain.

The elastic moduli have to be considered if the deformation behavior of any material at a certain stress has to be described. In the elastic mode the body under stress reverts to its original shape and size when the imposed pressure is released. Above a critical threshold — the so called yield point — the deformation behavior changes from ductile to brittle and the body's shape is changed irreversible with a fracture as final consequence. In applied seismology the amount of energy (stress) that acts upon the investigated subsurface and the resulting strain is minimal and well within the range of an elastic behavior of the ground material. Exceptions occur very close to the seismic source.

As mentioned above, seismic wave velocities can be expressed by the elastic moduli and the densities of the rocks that are investigated (Reynolds, 1997). In general, the propagation velocity within an elastic material is

$$V = (appropriate\ elastic\ modulus/density)^{1/2}.$$ (3.6)

For P-wave propagation both the bulk (eq. 3.4) and the shear moduli (eq. 3.5) have to be considered leading to the following equation that describes the propagation velocity of primary waves V_P:

$$V_{\mathrm{P}} = \left(\frac{k + \frac{4\mu}{3}}{\rho}\right)^{\frac{1}{2}},$$ (3.7)

whereas S-waves are solely described using the shear modulus

$$V_{\mathrm{S}} = \left(\frac{\mu}{\rho}\right)^{\frac{1}{2}}. \tag{3.8}$$

In a first approximation the seismic velocity increases with increasing density of the host material. This is caused by the decreasing elasticity of the materials associated with an increase in density (Schrott and Hoffmann, 2008). Table 3.1 gives some exemplary seismic P-wave velocities for materials typically present in permafrost environments. The range of velocity values may be quite large since velocities are highly dependent on the type of measurement. In situ measurements can be significantly different compared to laboratory measurements (Reynolds, 1997). Parameters that have to be considered when comparing velocity values are the porosity of the investigated rock (number of joints, fractures, and clefts), the degree of saturation, the nature of the pore material (air, water, and/or ice), and the effect of anisotropy of the investigated material (stratification, mineral fabrics). A deeper introduction into the seismic theory, raypath geometry, source and receiver instruments, as well as the spectrum of the application of seismic methods can be found in standard textbooks (e.g., Berckhemer, 1990; Telford et al., 1990; Reynolds, 1997; Brückl et al., 2005; Lowrie, 2011).

3.2.2. Principles and raypaths in seismic refraction

One major task in refraction seismic measurements is the investigation of the refractor depth of layer interfaces and the determination of the seismic velocities of the investigated layers. Seismic refraction is especially well-suited for surveying the shallow surface (Brückl et al., 2005). These studies usually consider only P-waves, as the fastest moving body waves. According to Snell's Law seismic waves are reflected and/or refracted when they hit a stratigraphic boundary that separates two materials with different elastic properties (e.g., Reynolds, 1997). It explains the geometric behavior of waves at the interface between the two mediums. All incoming and outgoing waves lie in the same plane as the normal to the point of incidence. Furthermore, the ratio between the sine of the angle of incidence i and the sine of the angle of refraction r is equivalent to the ratio of the wave velocity of both mediums (eq. 3.10) passed by the wave:

$$\frac{\sin i}{V_1} = \frac{\sin r}{V_2} \tag{3.9}$$

$$= \frac{\sin i}{\sin r} = \frac{V_1}{V_2}. \tag{3.10}$$

In the case of an increasing seismic velocity with depth ($V_2 > V_1$) — a prerequisite for the principles of seismic refraction — the angle of refraction has to be larger than the angle of incidence ($r > i$) according to (eq. 3.10). As result, the wave is refracted away from the normal. At a certain angle of incidence (the critical angle i_c) the wave is refracted at an angle of 90°. While the refracted wave travels along the interface with the speed of propagation V_2, the material that is passed by the refracted wave is subject to an oscillating stress and constantly generates upward directed head waves (Fig. 3.7).

As stated above, the seismic velocity of deeper stratigraphic units has to be larger for the critical refraction of waves to occur. Otherwise the wave is bent toward the normal and cannot be recorded at the surface, which may be the case in several geological situations; for example if a so-called hidden layer with lower seismic velocity exists at depth. Similar problems arise in situations with a lack of sufficient velocity contrast at an interface. When a thin layer is buried at depth it cannot be resolved by seismic refraction if its thickness is smaller than the wavelength of the incident wave even though its seismic velocity might be higher than the one from the unit above. The same is true if the spacing between adjacent geophones is not appropriate to resolve thin layers (for further discussion on the hidden layer problem and the geometry of refracted raypaths for multilayer or dipping-layer cases it is referred to, e.g., Reynolds, 1997).

During seismic measurements, the signal is triggered by a seismic source (e.g., sledge hammer, drop weight, explosives, or vibrator) resulting in the generation of three types of waves: ground surfaces waves (direct waves), reflected waves, and refracted waves (Fig. 3.7a). Each of these wave types propagates at different speed through the ground and along layer boundaries. Geophones that are fixed to the ground along a profile register micromotion of the ground particles and thus are able to detect the arrival of the primary wave. The signals of all geophones along the profile (traces) corresponding to a single shot are registered at the seismograph (Fig. 3.7b). To increase the signal-to-noise-ratio multiple hits are implemented at each shot point and automatically stacked by the seismograph.

While the signal is in phase for all the shots, the noise cancels each other statistically and is reduced (Hecht, 2001). However, the rate of signal improvement corresponds to the square-root of the number of shots, i.e., a 10 % increase in the signal requires 100 hits per shot point (Reynolds, 1997).

For interpretation purposes, the first arrivals of P-waves and the corresponding travel-time is plotted on a time-distance graph (Fig. 3.7c). From the slope of each traveltime segment the seismic velocity of the corresponding layer can be calculated, which is done by time-term inversion for situations with simple 2 or 3 plane layers. At the crossover point, the gradient of the time-distance graph changes and indicates the distance, at which the refracted body wave precedes the direct wave. The latter is responsible for the P-wave signal registered at the geophones next to the seismic source. The third kind of wave — the reflected wave — is always slower and thus not resolved by the first signal at the geophones. At the critical distance, the arrival of the refracted wave coincides with the arrival from the reflected wave, however, both lag behind the direct wave.

Because of this time-distance pattern of seismic waves, only the direct and the refracted wave are commonly considered with this method. A detailed seismic refraction survey consists of multiple shot points along the profile together with some offset shots (from outside the geophone array) and enables the resolution of variations in seismic velocity in both directions — lateral and vertical. 2D refraction tomography as inversion method enables the analysis of data sets with complex subsurface structures and significant relief at the surface along the profile length. After picking the first arrivals of each geophone trace in the seismograms the traveltime curves can be computed. An initial velocity model has to be created before the analyses software models raypaths that produce calculated traveltimes. The so called inverse problem is non-linear and thus has to be resolved in an iterative way (Lanz et al., 1998). This procedure seeks to minimize the least-squares between the calculated and observed traveltimes leading to a ground model with certain physical properties constructed on the basis of observational data. The initial model is created either as a layered model with a constant increase in seismic velocity with depth or can make use of the time-term inversion or the generalized reciprocal method. In the latter case the model is based on information derived from the traveltime curves of the measured data. More details on the interpretation methods can be found in Reynolds (1997); Hauck (2001) or Schrott and Hoffmann (2008). The tomography method results in
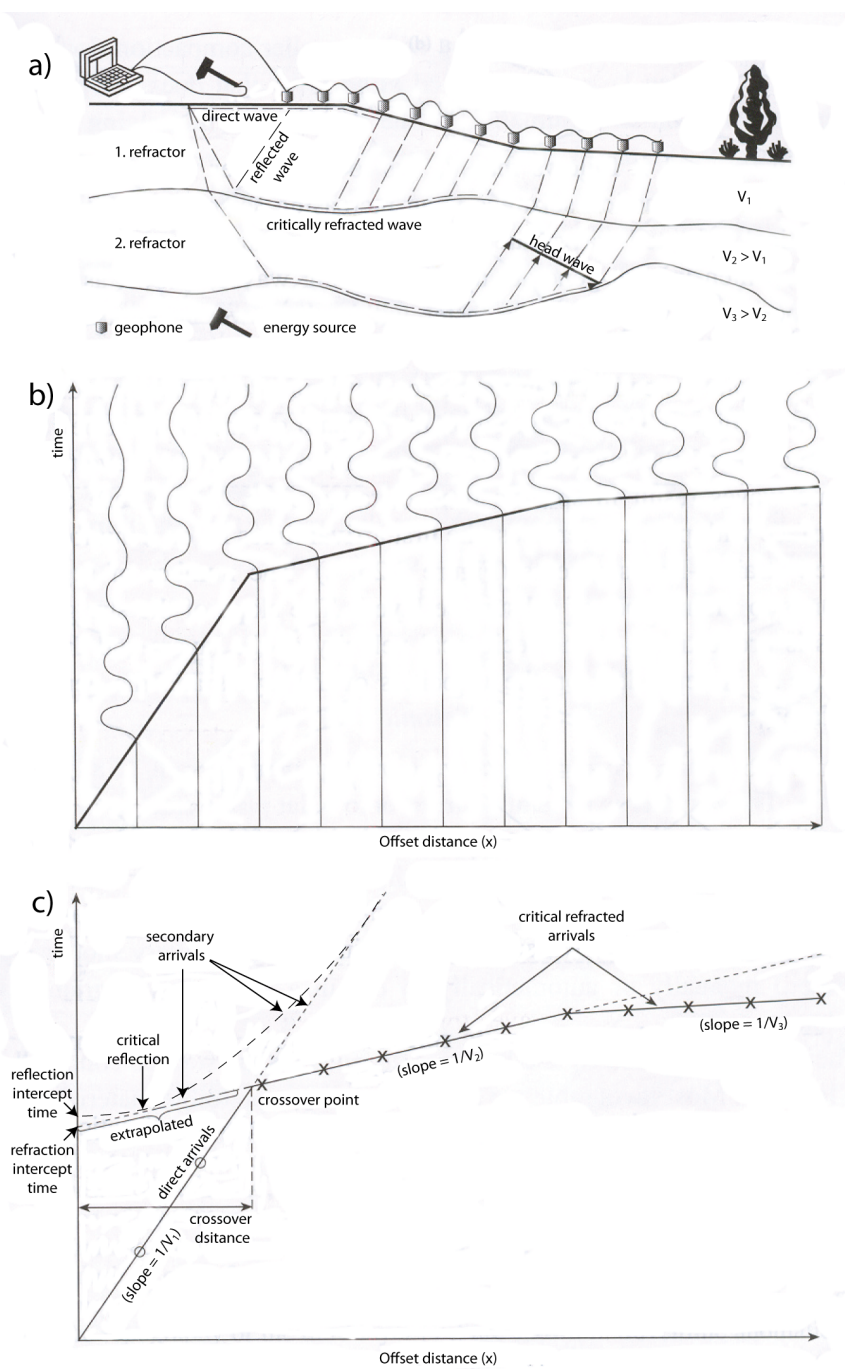
Figure 3.7: Principles of seismic refraction. (a) Schematic sketch of a seismic survey and raypath geometry for a three-layer case. (b) Example of a seismic refraction record. First arrivals are connected by the solid line. (c) Time-distance graph for the three types of waves generated by a seismic source (modified from Schrott and Hoffmann, 2008).

a 2D distribution of P-wave velocities plotted in a gridded model with single velocity data for each model block. Beside absolute values of velocity the raypaths can be displayed and therewith suggest the prominent refractors at depth. Also the region where physical parameters of the ground can be derived is constrained by the course of the raypaths. The tomographic interpretation method is especially well suited to investigate heterogeneous subsurfaces with limited a-priori knowledge and is able to resolve lateral variations in seismic velocities (Brückl et al., 2005), e.g., in mountainous terrain (e.g., Hauck, 2001; Musil et al., 2002; Schrott and Sass, 2008).

3.2.3. Refraction seismics in permafrost-related studies

Early work focused on the behavior of P-wave velocities above and below the freezing point in laboratory experiments of porous rocks (Timur, 1968; Carcione and Seriani, 1998) and showed the drastic increase in velocity during freezing of water-saturated rock samples. This change in velocity is used for the investigation of sites with ground-ice and frozen ground. Especially seismic refraction techniques are well-suited for the investigation of the shallow subsurface even in rough terrain. The upper limit of the permafrost table in rock glaciers was determined using the refractor depth based on a simple 2- or 3-layer assumption (e.g., Barsch, 1973; Vonder Muehll, 1993) as early refraction interpretation technique. This depth is usually easy to detect due to the large contrast between unfrozen sediments and the ice-rich permafrost body (Table 3.1). However, the heterogeneity within the alpine subsurface requires a more detailed analysis. With the progress in computational power, 2D and 3D tomography inversion schemes were developed and allow a more detailed imaging of the ground. Musil et al. (2002) showed the potential for resolving the structure of a rock glacier by way of refraction tomography. Often seismic refraction is used in combination with other geophysical techniques such as geoelectrics or georadar and has proven its ability to detect permafrost occurrences (Kneisel and Hauck, 2003; Hauck and Vonder Muehll, 2003a) and the structural composition of rock glaciers (Ikeda, 2006; Hausmann et al., 2007). The potential for monitoring the state of permafrost was recently shown by Hilbich (2010) using time-lapse seismic refraction tomography. Main advantages of seismic refraction investigation lies in the detection of permafrost, the determination of the active layer thickness, its lateral distribution, as

well as in the analysis of permafrost properties (Vonder Muehll et al., 2001; Hauck and Vonder Muehll, 2003a).

3.2.4. Data basis and method of analysis

For the present study, seismic refraction measurements were conducted at two of the three investigation sites. Each time, 24 geophones with 3 m geophone spacing and a Geode seismic recorder (Geometrics) were used. The seismic signal was produced by the strike of a sledge hammer on a rigid steel-plate. In some cases, where large boulders inhibited a proper fixation of the plate, the hammer was hit directly at the boulders.

In summer 2010, seven profiles (69 m each) were measured at Murtèl/Corvatsch (see Fig. 3.3, p. 38). Profile 1 and 2 as well as 3 and 4 were arranged in a roll-along procedure were the last geophone of the first profile was set as the first geophone of the second profile. Both lines cross the borehole location of borehole Mrt1 at the small rock glacier Rabgiusa. Two profiles (5 and 6) were placed across the second borehole at glacier forefield Murtèl, which indicated permafrost-free conditions. Another profile was measured outside of the forefield on a vegetated talus slope that has distinct bulges as expression of solifluction at its lower part. A proper measurement was inhibited owing to a broken seismic equipment. In summer 2011, three seismic surveys were implemented on the talus slopes surrounding the Zugspitzplatt using the same equipment and geometry as explained above. To increase the signal-to-noise ratio at each shot point, at least 10 hits were stacked to one data set. Offset shot points were implemented to enhance the raypath coverage at the edge of the geophone line. Basic parameters of the seismic profiles considered for this study are given in Table 3.3 and Tables A.2 and C.1 in the appendix.

Data processing and analysis was done with the software package Seisimager (Geometrics) and involved the following steps: (i) control of the profile geometry and picking of first arrivals in Pickwin, (ii) incorporation of topography (=relief along the profile) and offset shot points, generation of an initial model, and tomographic inversion of the data set in Plotrefa and (iii) visualization and extraction of data in GeoPlot. An estimate of the total performance of the tomographic inversion process is given by the RMS error. It shows the absolute time difference between observed and calculated traveltimes in ms.

Table 3.3: Data base of refraction seismic surveys at glacier forefield Murtèl (Mrt) and
Zugspitzplatt (Zug).

ID	Date	Spacing	No. of hit points	Setting
Mrt-RST 1+2	Aug. 18, 2010	3	11+11	roll-along across borehole Mrt1 (NE–SW)
Mrt-RST 3+4	Aug. 18, 2010	3	11+11	roll-along across borehole Mrt1 (N–S)
Mrt-RST 5	Aug. 18, 2010	3	10	across borehole Mrt2 (NW–SE)
Mrt-RST 6	Aug. 18, 2010	3	12	across borehole Mrt2 (E–W)
Mrt-RST 7	Aug. 18, 2010	3	4	solifluction (E–W), system broken after 4 hits
Zug-RST 1	July 19, 2011	3	14	talus slope beneath Zugspitze (NE–SW)
Zug-RST 2	July 19, 2011	3	11	talus slope beneath Zugspitze (N–S)
Zug-RST 1	July 21, 2011	3	13	path UFS to Northern Schneeferner (E–W)

3.3. Temperature data

The observation of temperatures above, at, and below the ground surface enables a better understanding of the thermal regime and the energy fluxes between the turbulent surface layer of the atmosphere and the shallow subsurface. This is important for investigations in periglacial environments because of the direct control of the local climate on (sub-)surface temperatures.

3.3.1. Possibilities and value of temperature monitoring for research on the ground thermal regime

Subsurface temperature data recorded in boreholes facilitate the ultimate confirmation of permafrost conditions at depth and thus are the only method to directly validate the thermal state of the ground. Since permafrost, in the proper meaning of the word, is defined as thermal condition of any ground material, borehole measurements can be regarded as final proof for the occurrence of permafrost. However, they yield only point measurements and other methods such as BTS or geophysical sounding facilitate the extension from the point scale to a larger area. Furthermore, drilling of boreholes in alpine environments with difficult logistics is expensive and so far mainly restricted to rock glaciers, bedrock, or exposed rock faces (cf. Gruber et al., 2003; Harris et al., 2009). Thus, beside the construction of four boreholes in both glacier forefields in the Engadin, further temperature measurements were conducted and numerous miniature temperature dataloggers were installed. The measurement of temperatures in various settings and

heights (above, at, or slightly below the surface) aims at the detailed characterization of the thermal regime and the observation of heat transfer near the ground.

The usage of the temperature at the bottom of the winter snow cover was introduced by Haeberli (1973) as a tool for the spatial assessment of permafrost occurrence in regions with a snow cover thickness of at least 0.5–1 m in February and March. In these months, the snow isolates the ground from air temperatures and the thermal regime at the surface is mainly controlled by the heat transfer from the uppermost ground layer (Hoelzle, 1992). Hence, the ground surface temperature (GST) in late winter provides an indication on the presence or absence of permafrost based on the so called rules of thumb that describe the probability of permafrost to occur as follows: BTS < -3 °C = permafrost likely, -3°C < BTS < -2°C = permafrost probable, and BTS > -2°C = permafrost unlikely. The intermediate class with a range of 1 K is an indication for the possible year-to-year variability of ground surface temperatures and the uncertainty of this method. However, this fast and easy approach has proven its suitability for a first approximation of permafrost conditions and for the purpose of permafrost probability maps and models in numerous studies in the Alps (Haeberli and Patzelt, 1982; Hoelzle, 1992; Hoelzle et al., 1993; Kneisel, 1999; Guglielmin et al., 2001; Gude and Barsch, 2005), Scandinavia (Isaksen et al., 2002; Heggem et al., 2005), Japan (Ishikawa and Hirakawa, 2000), and Canada (Lewkowicz and Ednie, 2004; Bonnaventure and Lewkowicz, 2008). Statistical analysis of BTS measurements have shown that autocorrelations of measured data may weaken the validity of regression models and that temporal variations have to be considered (Brenning et al., 2005). Thus, BTS is recommended as relative measure of the ground thermal state.

Technological developments have led to the employment of miniature temperature dataloggers for the continuous monitoring of ground surface temperatures (Hoelzle et al., 1999). They provide year-round information on the coupling of the ground with the atmosphere and enable the observation of heat exchange processes and convective heat transfer at the surface. Especially in winter during the snow cover period valuable information on the damping of ground surface temperatures and effects such as isolation of the ground or begin and end of the snow melt period (i.e., zero curtain effect) can be derived (Hoelzle et al., 2003; Hanson and Hoelzle, 2004). Ishikawa (2003) proposed four fundamental types of temporal changes in winter ground surface temperatures and inferred from these

pattern major factors that control the formation and preservation of permafrost: direct atmospheric cold heat penetration throughout winter, ground cooling before onset of snow accumulation, and cold air funneling along blocky surface material.

Additionally, the installation of snow poles with fixed temperature loggers in various heights enables the observation of temperatures above the ground surface and is of great value in the snow cover period (e.g., Lewkowicz, 2008; Farbrot et al., 2011). Recorded temperature data reflect the damping of the air temperature so that the timing of the coverage with snow can be estimated. Examples of snow cover reconstructions were based on several criteria such as a semi-quantitative fashion of comparing differences between air and snow logger temperatures (Lewkowicz, 2008), the timing of the zero curtain effect (Lundquist and Lott, 2008; Farbrot et al., 2011), the variance of daily temperatures (Danby and Hik, 2007; Schneider et al., 2012), or the height of the maximum drop of the diurnal temperature variance (Reusser and Zehe, 2010).

In general, the climate–permafrost system is described schematically by mean annual temperature regimes at three specific levels: air (MAAT), ground surface (MAGST), and permafrost table (TTOP) (Lachenbruch et al., 1988). These regimes are connected by varying positive or negative offsets (Fig. 1.1, p. 9). Degree-day factors for freezing (DDF) and thawing (DDT) are based on the sum of negative/positive mean daily temperature values and calculated for the hydrological year (October 1st – September 30th). They can be used as indices for the severity of each season, i.e., how cold a winter is at the ground surface (freezing index) or how warm a summer is (thawing index). Based on these indices the mean annual air temperature is expressed as:

$$MAAT = (DDT_a\text{-}DDF_a)/P, \tag{3.11}$$

with the subscript ($_a$) for air temperature data. A corresponding relation exists for ground surface ($_s$) temperatures:

$$MAGST = (DDT_s\text{-}DDF_s)/P. \tag{3.12}$$

For a description of the whole climate–permafrost system so called transfer functions (n-factors) were calculated (Lunardini, 1978; Smith and Riseborough, 2002):

$$MAGST = (n_T * DDT_a - n_F * DDF_a)/P. \qquad (3.13)$$

The use of these n-factors for parameterization of the surficial thermal regime based on more commonly available air temperatures has the potential for spatial modeling over larger areas (Klene et al., 2001). Originally they were educed within arctic lowlands (e.g., Lunardini, 1978; Jorgenson and Kreig, 1988) but recently were also introduced for mountainous regions, especially in Scandinavia (e.g., Juliussen and Humlum, 2007; Etzelmüller et al., 2008; Farbrot et al., 2011).

3.3.2. Data basis and method of analysis

In this study a large number of temperature dataloggers, four shallow boreholes each equipped with a thermistor string, snow pole temperatures, and BTS measurement points were used to observe and understand the thermal conditions at the ground surface and in the ground. At Val Muragl two 8 m deep boreholes were drilled in summer 2006 with temperature sensors at various depths. Additionally 15 temperature dataloggers were distributed in the glacier forefield between 2005 and 2010 to yield information on ground surface temperatures within different surface covers in terms of debris size. At that site temperature dataloggers were utilized already in the preceding years as shown in Kneisel and Kääb (2007).

In summer 2008, two boreholes (10 m) were drilled and equipped in glacier forefield Murtèl. Furthermore, 30 dataloggers were installed in 2008 and 2009, respectively, at different settings (ground surface, 2 m air, above and within the water of a small permafrost spring). BTS campaigns were conducted each winter between 2009 and 2011 at forefield Murtèl with a variable amount of measurement points (Table 3.4). The planned installation of temperature loggers at the Zugspitzplatt in 2010 had to be cancelled because several cold fronts with concomitant snow fall made a site visit and proper field work impossible. A summary of the available temperature data with information on the installation date, elevation, geomorphological setting, sensor depth/height, and data gaps is given in Tables 3.5, 3.6 and 3.7. The temperature curves from all loggers located in both glacier forefields in Switzerland are illustrated in Fig. D.1–D.3 and Fig. E.1–E.2 in appendices D and E.

Table 3.4: Information on BTS field work at glacier forefields Muragl and Murtèl.

Site	Date	Snow height [cm]	No. of data points	Measurement device	Comment
Muragl	Mar. 30, 2010	100–195	14	thermistor probe, multimeter	transect along Mgl2
Murtèl/ Corvatsch	Mar. 10, 2009	115–350	61	thermistor probe, multimeter	
	Mar. 29, 2010	70–320	146	thermistor probe, thermometer	
	Mar. 24./25, 2011	85-293	64	thermistor probe, thermometer	

Table 3.5: Borehole installations at glacier forefields Muragl and Murtèl.

Site	Elevation [m a.s.l.]	Depth [m]	Sensor depth [m]	Data record	Comment
Mgl1[a]	2660	8	0, -0.5, -1, -2, -3, -5, -7, -8	July 25, 2006– Sept. 11, 2011	coarse debris, near the front of the elevated sediment bed
Mgl2[a]	2765	8	0, -0.5, -1, -2, -3, -5, -7, -8	Sept. 28, 2006– Sept. 11, 2011	shallow ridge with finer till and overlying stones
Mrt1[a]	2685	10	-0.2, -0.4, -0.8, -1.2, -1.6, -2, -3, -5, -7, -10	Sept. 26, 2008– Sept. 9, 2011	moraine/rock glacier with coarse blocks, slight depression
Mrt2[a]	2715	10	-0.2, -0.4, -0.8, -1.2, -1.6, -2, -3, -5, -7, -10	Oct. 1, 2008– Sept. 9, 2001	central part of glacier forefield, finer till, flat area
Mrt3[a]	2783	10	0, -0.2, -0.4, -0.8, -1.2, -1.6, -2, -3, -5, -7, -8, -10	Aug. 21–Nov. 30, 2009	in debris-covered ice

[a] DALLAS sensor (Geoprecision): accuracy 0.25°C, resolution 0.065°C.

For the analysis of snow height derived from thermal measurements at the borehole sites, the diurnal temperature variances of each height (0, 25, 50, and 100 cm) were plotted in a contour plot and subsequently the 0.4 K contour line was extracted. That is, daily temperature amplitudes below that threshold are regarded as most suitable to indicate the coverage of the sensor with snow. Additional tests were also performed with 0.2, 0.3, and 0.5 K, but the best agreement with snow height data from the climate station at rock glacier Murtèl were yielded with the 0.4 K contour. This line is regarded as conservative estimation of the snow height based on the damping of diurnal temperature oscillations since the temperature logger observes higher variance when a very shallow snow cover is present. Owing to the maximum height of the snow poles (1 m) the snow cover evolution above that height cannot be estimated, which is less important for the determination of air-ground connectivity, snow cover duration at the ground, and isothermal snow conditions during the melting period.

Table 3.6: Information on temperature dataloggers at glacier forefield Muragl.

Logger-ID	Position	Elevation [m a.s.l.]	Installation date	Setting
ML1[a,b]	791571/153642	2670	Sept. 18, 2005	depression, close to Mgl1
ML2[a,b]	791522/153616	2672	Sept. 18, 2005	south end of ERTM-Mrt1
ML3[a,b]	791449/153489	2680	Sept. 18, 2005	moraine edge, fast moving/with data gaps
ML4[a,b]	791543/153427	2700	Sept. 18, 2005	large boulders, south part of forefield
ML5[a,b]	791712/153219	2770	Sept. 18, 2005	upper end ERTM-Mrt2/with data gaps
ML6[a,b]	791713/153279	2750	Sept. 18, 2005	lower end ERTM-Mrt2/with data gaps
ML7[a,b]	791776/153241	2750	Sept. 18, 2005	depression east of ERTM-Mrt2
ML8[a,b]	791616/153251	2690	Sept. 18, 2005	medium-grained, transect between ERTMs
ML9[b]	792170/153343[c]	2760[a]	Aug. 30, 2006	protalus rampart
ML10[b]	792100/153387[c]	2740[a]	Aug. 30, 2006	push moraine, depression
ML11[b]	792047/153612	2750	Aug. 30, 2006	push moraine, coarse
ML12[b]	792072/153658	2745	Aug. 30, 2006	push moraine, very coarse
ML13[b]	791547/153568	2680	Aug. 30, 2006	medium-grained, transect between ERTMs
ML14[b]	791630/153307	2736	Aug. 30, 2006	depression west of ERTM-Mrt2
ML15[b]	791503/153673	2655	2010	west of ERTM-Mrt1

[a] Onset Hobo sensor (UTL): accuracy 0.1°C, resolution 0.27°C.

[b] PT1000 sensor (Geoprecision): accuracy 0.1°C, resolution 0.01°C.

[c] estimated.

At each borehole location seasonal freezing and thawing indices (DDF/DDT) were calculated for a better understanding of the climate–surface–permafrost system. They are based on the cumulative sum of negative and positive mean daily temperatures in a hydrological year. Calculated n-factors represent the ratio between degree-day factors at the ground surface at each borehole and corresponding values from the climate station Murtèl, because no direct air temperature data are available from the logger positions. Furthermore, the thermal offset is calculated as the difference between MAGST and the mean annual temperature at the permafrost table. The calculation of n-factors in the extremely heterogeneous environment of glacier forefields can be regarded as attempt to assess the applicability of these factors for local or regional modeling schemes.

To investigate the influence of the substrate on the thermal regime it was classified according to the dominant grain size that prevails around the position of the boreholes and the temperature loggers, respectively. The grain size classification was implemented according to the German soil classification scheme with classes defined as follows: 1 = sand ($d < 0.2$ cm), 2 = gravel ($0.2 < d < 6.3$ cm), 3 = stones ($6.3 < d < 20$ cm), 4 = blocks

$(20 < d < 63 \,\text{cm})$ and $5 =$ boulders $(d > 63 \,\text{cm})$. The size of the particles is hereby related to its spherical equivalent diameter d. In the investigation areas, the presence of sandy sediments is limited to the river beds draining the glacier forefields. Since the thermal regime at these sites is highly influenced by running water and mechanical impact during melt no logger was installed in class 1. Information on each logger and its corresponding substrate class is given in Table 4.1, p. 84.

Table 3.7: Information on temperature dataloggers at glacier forefield Murtèl.

Logger-ID	Position	Elevation [m a.s.l.]	Installation date	Setting/Comments
A212[a]	782070/143250	2738	Oct. 05, 2009	left lateral moraine/with data gaps
A216[a]	781971/143277	2737	Oct. 05, 2009	furrow, coarse boulders
A218[a]	781946/143238	2745	Oct. 05, 2009	top of moraine-rock glacier-complex
A220[a]	782014/143208	2736	Oct. 05, 2009	cirque
A221[a]	781957/143324	2712	Oct. 05, 2009	on rock glacier, coarse blocks
A222[a]	781901/143351	2702	Oct. 05, 2009	fine-grained furrow
A223[a]	781920/143411	2687	Oct. 05, 2009	fine-grained moraine/with data gaps
A224[a]	781927/143421	2689	Oct. 05, 2009	on rock glacier, 5 m apart from A223
A225[a]	781966/143359	2699	Oct. 05, 2009	on rock glacier, steep slope
A227[a]	781920/143443	2695	Oct. 05, 2009	moraine ridge
A229[a]	781991/143359	2693	Oct. 05, 2009	coarse-grained furrow
A230[a]	781967/143437	2672	Oct. 05, 2009	next to spring in front of rock glacier
UTL20[b]	782237/144149	2616	Oct. 05, 2009	solifluction lobe, upper part
UTL21[b]	782203/143925	2609	Oct. 05, 2009	on relict rock glacier/failure
UTL22[b]	782227/144153	2600	Oct. 05, 2009	solifluction lobe, middle part
UTL23[b]	782200/144145	2595	Oct. 05, 2009	solifluction lobe, lower part
UTL24[b]	782169/144123	2585[c]	Oct. 05, 2009	boulders below solifluction lobe
UTL25[b]	782265/143507	2749	Oct. 05, 2009	right lateral moraine, coarse
UTL26[b]	782339/143475	2778	Oct. 05, 2009	right lateral moraine, fine/failure
UTL27[b]	782196/143308	2725	Oct. 05, 2009	central glacier forefield/failure
UTL28/UTL2[b]	782127/143271	2723	Oct. 05, 2009/ Oct. 10, 2010	depression above small lake/with data gaps
UTL29[b]	782180/143172	2745	Oct. 05, 2009	left lateral moraine
A418[a]	781967/143437	2672	Aug. 16–25, 2010	in and above water of PF spring
A211[a]	781967/143437	2672	Oct. 10, 2010	in water of permafrost spring
A217[a]	781944/143414	2685	Oct. 10, 2010	next to ERTM, ground surface
A219[a]	781944/143414	2685	Oct. 10, 2010	next to ERTM, 2 m height
A226[a]	781967/143437	2672	Oct. 10, 2010	60 cm height at permafrost spring
UTL4[b]	781992/143402	2683	Oct. 10, 2010	below rock glacier, fine material

[a] PT1000 sensor (Geoprecision): accuracy 0.1°C, resolution 0.01°C.

[b] Onset Hobo sensor (UTL): accuracy 0.1°C, resolution 0.27°C.

[c] estimated.

3.4. Kinematic measurements

The assessment of ground dynamics in the investigated areas necessitates sophisticated tools to document even slight displacement rates that are expected during the 3 years of measurements. Thus, a differential global positioning system (DGPS) and a terrestrial laser scanner are selected as suitable techniques for the detection of creep rates in the range of a few centimeters.

3.4.1. Differential global positioning system

In a recent compilation of rock glacier kinematics from six different regions of the European Alps (Delaloye et al., 2008), horizontal surface velocities were shown to vary over up to two orders of magnitude. While slow moving rock glaciers have creeping rates of about 0.1 m/year (e.g., Aget/Central Valais, Switzerland) others show velocities of up to 3 m/year (e.g., Reichenkar/Stubai Alps, Austria). Destabilized features may even exhibit surface velocities of 10 m/year and more (e.g., Graben Gufer/Bernese Alps, Switzerland) with distinct cracks at the rooting zone or close to the front (Delaloye et al., 2010). However, interannual variations have been very similar independent of the absolute velocity and thus are most likely attributed to external climatic factors (MAGST, winter ground freezing, and/or winter snow fall) (Delaloye et al., 2008). Long-term monitoring of rock glacier kinematics is ensured through the permafrost monitoring network in Switzerland (e.g., PERMOS, 2009, 2010). As the examples stated above have shown horizontal velocity rates can be very small and creep measurements demand for an accurate measurement system. Suitable resolutions can be achieved by terrestrial laser scanning, tachymetry, or differential global positioning system stations. To monitor the potential creep rates of the small rock glacier in glacier forefield Murtèl such a high-resolution positioning technique was required since creeping rates were expected to be in the range of several cm per year at most. Thus, a DGPS system was used in three consecutive years (August 23, 2009; August 22, 2010; September 09, 2011).

The basic principle of the DGPS technique is based on the use of two GPS receivers that are operated at the same time. While one receiver is placed on a known trigonometric point (reference/base station), the second receiver (moving/rover station) is used for the actual measurement. Most accurate results are obtained when at least four satellites can

be tracked simultaneously at both sites. For this study, corrections were made in a post-processing mode in a twofold manner. Differentiating the known position of the reference station from the calculated position yields the position corrections, which are subsequently applied to the data from the rover unit. Similarly, observed pseudoranges at the rover site can be corrected by applying pseudorange corrections of the reference station (Hofmann-Wellenhof et al., 2001). The reference station was placed on a marked surveying point close to the front of rock glacier Murtèl (position data were kindly provided by I. Gärtner-Roer). At the rock glacier surface four large blocks were surveyed on three individual points each (Fig. 3.8) to determine the 3D rotational movement of these blocks as well as the general direction and velocity of the rock glacier (Lambiel and Delaloye, 2004). Besides, individual points at and around the rock glacier were measured to determine the creep rates and reference values from the static surrounding. Based on position and pseudorange corrections, final accuracy of the position is given at the 1–5 cm level whereas the accuracy of the vertical component is at about ±10 cm.

Figure 3.8: DGPS rover and external antenna for measurement of the position of borehole Mrt1. The large block in the background (block1) was measured at three individual points (red dots) for the observation of its 3D movement.

3.4.2. Terrestrial laser scanning

Supplementary information on the kinematic behaviour of the investigation area Murtèl/ Corvatsch was achieved by the use of a terrestrial laser scanning system. Terrestrial laser scanning or LiDAR (Light Detection And Ranging) has become a very useful technique for the investigation of spatial mass movement processes. Nowadays, laser scanning techniques (terrestrial or airborne) create immense scatter plots and allow fast and accurate acquisition of topography and surfaces in high resolution. The vast amount of data is used to generate detailed digital elevation models of the investigation area (Bodin et al., 2008). Entire slopes, rock faces, or landforms that show surface dynamics can be seen as research targets focusing especially on field sites that are prone to geohazards.

In a typical periglacial environment Bauer et al. (2003) aimed successfully at the production of a 3D high-resolution surface deformation model of the front of an active rock glacier in Austria using terrestrial laser scanning. Other examples showed the applicability of this technique in permafrost-influenced surroundings for the generation of digital elevation models of rock glacier surfaces (Bodin et al., 2008) or alpine mass movements in permafrost areas in general (Kenner et al., 2013).

Colleagues from the University of Halle (Dr. D. Morche, A. Nicolay) provided the equipment and field assistance in August 2009 and 2010. This research group usually investigates sediment budgets, transfer rates, and mass movement processes in alpine catchments (e.g. Bimböse et al., 2011; Heckmann et al., 2012, and references therein).

The laser scanner system ILRIS-3_6D (Optech Inc.) enables the automatic acquisition of a high number of data points (see Bimböse et al., 2011, for detail). Based on a digital photograph obtained from the scanner the site of interest can be chosen and a fully motorized total station with pan tilt navigates during the data assimilation. Raw data were analyzed using the software IMAlign and IMInspect of the program package PolyWorks (InnovMetric Software). Based on a point cloud, an elevation model of the investigated surface is created. Results from the two surveys are subtracted from each other and thus kinematic changes at the surface (rock detachment, creep) can be obtained. Analyses of the data sets were implemented at the Institute of Geosciences and Geography at the University of Halle.

On August 19, 2009, 2.5 million data points were measured on rock glacier Rabgiusa

and the surrounding moraine at a resolution of 44 mm. The laser scanner was positioned at an elevated point in the central part of the forefield Murtèl to reach the best possible angle of incidence. Repeated data were gained on August 17, 2010 with 6.5 million data points at a resolution of 30 mm. Measurement accuracy is expected to be in the order of ±5 mm.

The increased data density of the laser scanning system gives more spatial information on deformation pattern compared to the point measurements of the DGPS system. The application of this technique aimed at the development of a more general model of surface displacement rates at the small rock glacier Rabgiusa. Some difficulties occurred with the choice of a proper stand point of the laser scanner system. Because of the rather planar terrain and the flat angle of incidence small areas that lie in a furrow of the rock glacier surface could not be covered with the laser adequately.

4. Results: Murtèl/Corvatsch area, Upper Engadin

This chapter presents results from the key site of this study — the Murtèl/Corvatsch area in the southeastern Swiss Alps. It is separated in the three sections of geophysical investigations, temperature observations, and kinematic measurements. Some interpretation of the results is already given for better understanding.

4.1. Geophysical investigations

Results from geophysical investigations comprise electrical resistivity (surveying, 3D mapping, and monitoring) and refraction seismic data. At some places ERT and RST were coupled along the same profile to increase and validate the significance of the findings.

4.1.1. Electrical resistivity tomography

Reconnaissance mapping of the glacier forefield

For large-scale geoelectrical surveying of the investigation site Murtèl/Corvatsch and the exploration of possible permafrost occurrences, several ERT transects were measured using a relatively large electrode spacing of 5 m. They allow for a good compromise between attention to details as well as depth and spatial coverage. Figure 4.1 summarizes results from four exemplary ERT soundings (out of several more) within or close to glacier forefield Murtèl (see Fig. 3.3, p. 38) to provide an impression on the resistivity ranges that are to be expected. Panels 4.1a–c have the same contour values ($\sim$1–40 kohm.m), whereas maximum resistivity values in Fig. 4.1d reach more than 2 Mohm.m and thus require an adjusted contour interval.

Profile Mrt-ERT1 is located in the centre of the recent glacier forefield characterized by fine- to medium-grained glacial till (sand/gravel with single stones on top). In the subsurface of this part of the investigated area resistivity values range between 1 and
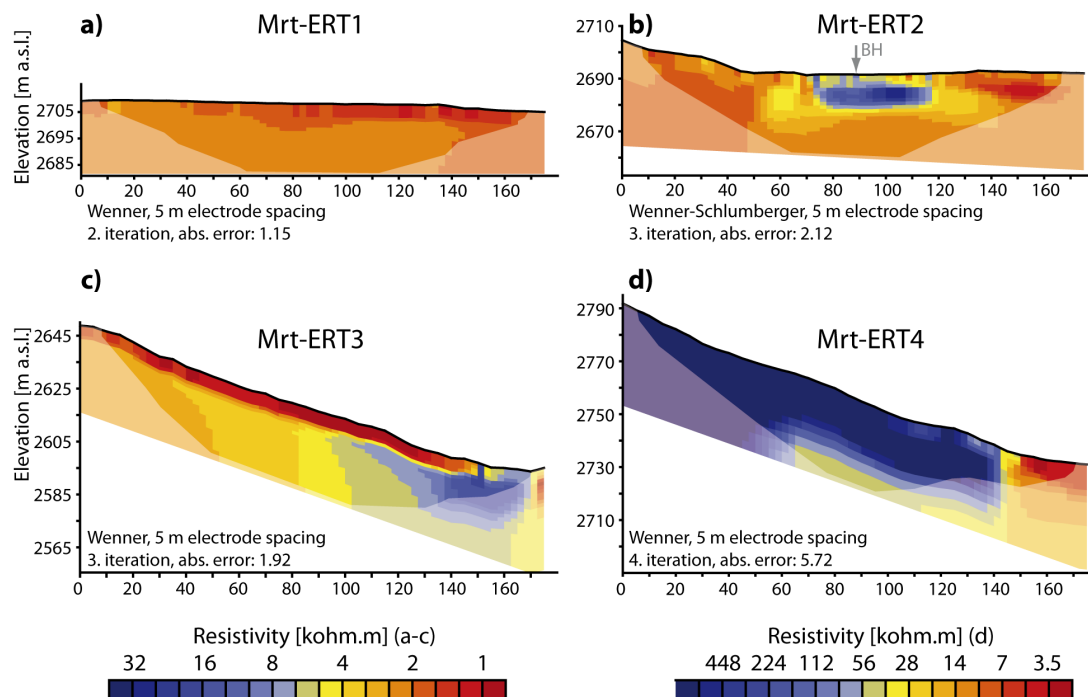
Figure 4.1: Exemplary ERT profiles from the investigation area Murtèl/Corvatsch.
(a) central glacier forefield, (b) lateral moraine and rock glacier Rabgiusa,
(c) solifluction slope, (d) debris-covered ice (note different contour values).

2.5 kohm.m without distinct resistivity contrast. Lowest values at the upper part of the tomogram are attributed to moist ground surface conditions. A profile at the southern lateral moraine (Mrt-ERT2) overlays parts of the moraine itself as well as coarse-grained boulders and blocks of the small rock glacier Rabgiusa in the central part of the line (horizontal distance 50–140 m). At horizontal distance 88 m of this profile, borehole Mrt1 is located. The subsurface in this central part has resistivity values as high as 30 kohm.m which is one order of magnitude higher compared to values obtained in the surrounding morainic material. First interpretations based on geoelectrical data together with temperature data from the adjacent borehole (see section 4.2) allow to denote the high resistive anomaly as permafrost body. More difficult is the assessment of Mrt-ERT3, a profile that was placed on a steep slope with several solifluction lobes above a relict rock glacier. Resistivity values immediately below the vegetated ground surface are at or below 1 kohm.m. The upper part of the slope has relatively low resistivity values (<4 kohm.m), whereas values increase toward the slope toe (15 kohm.m). At the transition between this lower part of the slope and the relict rock glacier large boulders are found at the surface

with air-filled voids in-between. The subsurface characteristics of this part are thus not easy to determine based on this profile that was designed to investigate the structure of the solifluction lobes. In tomogram Mrt-ERT4 most of the subsurface has resistivity values above 500 kohm.m and maximum values are above 2 Mohm.m. This profile extends from the central part of the glacier forefield in the direction of the present niche glacier Murtèl. Even though the surface is covered by coarse gravel and stones, the very high resistive anomaly as well as direct field observations of ice below a debris layer of several dm thickness reveal a massive (dead-)ice body. Weathering and debris accumulation from the upper rock faces produced a large zone of debris-covered glacier ice underneath the steep niche glacier. Only the lowermost part of this profile (145–175 m) shows reduced resistivity values (<10 kohm.m) and thus is most likely unfrozen.

Quasi-3D electrical resistivity survey

Based on the reconnaissance ERT soundings, further geophysical investigations focused on the area around profile Mrt-ERT2. This part of the glacier forefield where the orographic left lateral moraine intersects with the front of the rock glacier shows the most interesting surface and subsurface characteristics as well as a dynamic behavior expressed by a coarse debris cover with furrow–and–ridges topography.

It was therefore selected for an in-depth quasi-3D geoelectrical survey (see Fig. 3.3 for orientation). The aim was to test the applicability of this method under rough terrain conditions and to create a 3D ERT subsurface model of this permafrost-affected area.

The arrangement of 2D ERT profile lines – 11 profiles in x-direction and 12 profiles in y-direction – is shown in Fig. 4.2a. For evaluation of the influence of parallel and rectangular lines, the data set was inverted using three different modes. Panels 4.2b and c are based on profiles oriented either in x-direction or in y-direction. Image appraisals of the results, as shown by two horizontal depth sections (2.5–3 m and 4–5 m), indicate a distinct high resistivity anomaly extending from the southern corner to the central western side, outlined especially well at the deeper section. It is surrounded by a homogeneous area with resistivity values below 3 kohm.m, i.e., permafrost-free conditions. Differences in appearance between these two images are caused by the specific orientation of the ERT lines. Linear 2D electrode arrangements register resistivity changes along their axis. These changes are subsequently extrapolated between parallel profiles in the 3D

inversion. Therefore structures perpendicular to the profile direction are accentuated when parallel ERT profiles are concatenated (cf. Chambers et al., 2002) as it can be seen from the vertical appearance of structures in Fig. 4.2b and the horizontal appearance in Fig. 4.2c. Figure 4.2d is based on a data set consisting of all x- and y-lines. It confirms the general resistivity distribution in the subsurface as shown in the first two panels (Fig. 4.2b/c). However, it improves the model resolution, both at the transition between high resistive and low resistive model blocks as well as inside the anomaly. The high resistive structure is much better delineated and appears to be continuous already at a depth below 2.5 m, which is not definitely obtained from the x- or y-inversion. The presence of frozen ground at that depth is ascertained with borehole temperature data (see Fig. 4.16 and subsection 4.2.3).
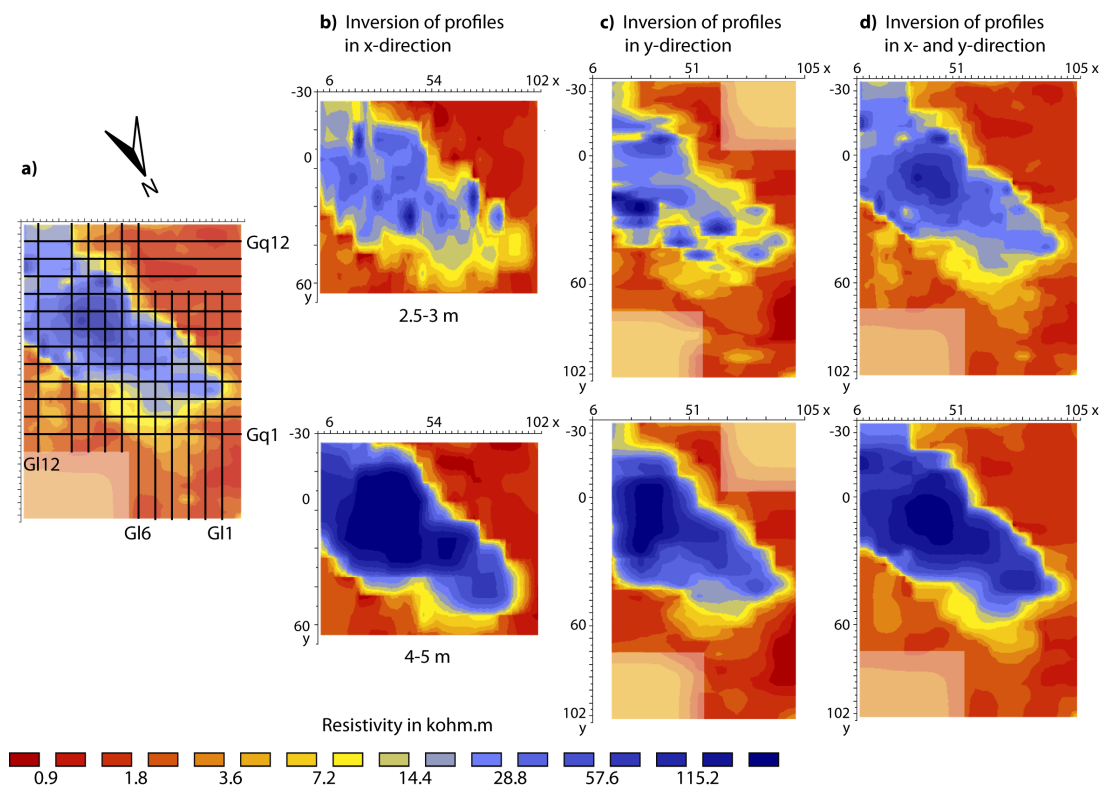
Figure 4.2: (a) Arrangement of ERT profiles with longitudinal profiles (Gl) and crossing profiles (Gq). Exemplary depth slices (2.5–3 m, 4–5 m) of the combined Wenner and Wenner-Schlumberger data set are given for x-inversion of parallel ERTs (b), y-inversion of parallel ERTs (c) and xy-inversion of parallel and orthogonal ERTs (d).

The gradient within the subsurface of the 3D measurement grid is steep, leading to a narrow transition from values of about 2 kohm.m to the high resistive area with >20 kohm.m. To check the subsurface model for true high/low resistive anomalies and potential artifacts, variations of the damping factor λ during the inversion process have been tested. An initial value λ_0 has been applied during the first iteration while this value has been reduced by 50 % in every subsequent iteration until a specified minimum value λ_{min} has been reached.

Figure 4.3 shows results where the damping factor is set to very low ($\lambda_0 = 0.05$) and high ($\lambda_0 = 0.4$) values, respectively, to determine the consistency of the computed models with measured data. The data set inverted with a low damping value (Fig. 4.3a) gives a data-consistent and noisier model with large resistivity variations. In contrast, larger damping parameters (Fig. 4.3b) produce a smoothed model of the resistivity distribution. While the structure of the high resistive anomaly is well-documented and equal in extent for both inversion settings, the resistivity range differs considerably with maximum values about 100 kohm.m higher in Fig. 4.3a. Especially in depth slice 2.5–3 m the resistive structure is poorly reproduced in Fig. 4.3b and does not convincingly indicate permafrost conditions. The small high resistivity anomaly at the southern side of the plot is less apparent when inverted with a larger damping factor and therefore may be a result of overfitting of the measured data. A mean value of $\lambda_0 = 0.15$ and $\lambda_{min} = 0.01$, as used in Fig. 4.2b-d, is regarded as a reasonable compromise between data-agreement and smoothing.

While structure and extent of the high resistive part are coincident for both inversion settings the absolute resistivity values, especially ρ_{max} varies considerably and thus impedes a quantitative interpretation of the data in terms of ice content or temperature without further constraints. The temperature information from the borehole enables a juxtaposition of resistivity and temperature values as shown in Fig. 4.4. Temperature values indicate frozen ground conditions below a depth of about 1.8 m up to the bottom of the borehole in 10 m depth. Resistivity values are extracted as 1D vertical sections from one lengthwise (Gl6) and one crosswise (Gq3, see Fig. 4.2a) ERT profile. Both lines cross the borehole position. A drastic increase in resistivity values occurs between a depth of 2–3.5 m. At about 5 m depth, maximum values reach as high as 26 kohm.m, before they drop to lower values below a depth of 8 m. Temperatures at the bottom of the borehole are only slightly below the freezing point (0.12°C). The frozen ground can be
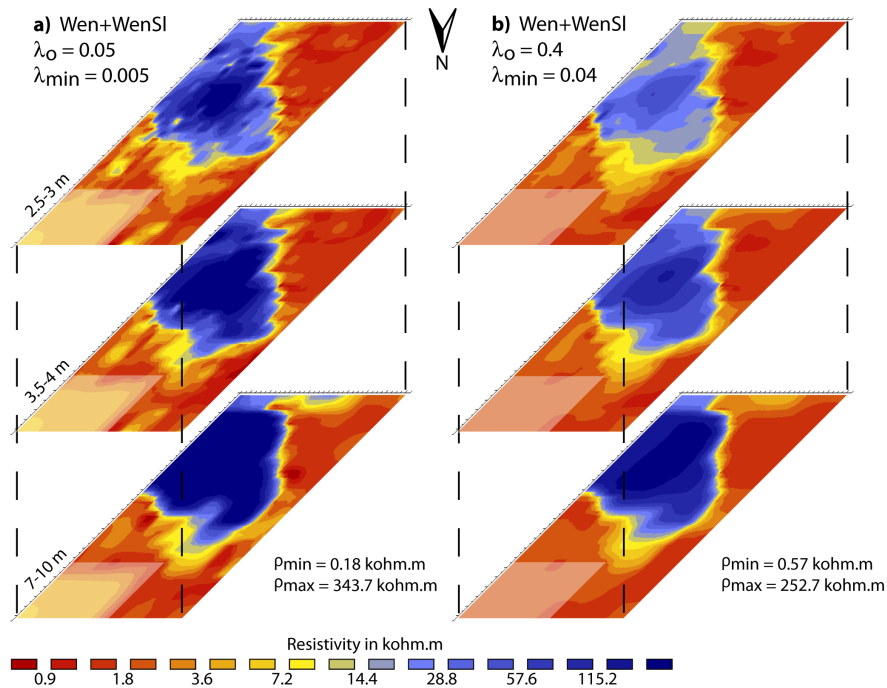
Figure 4.3: Three depth slices of the combined data set inverted with (a) low damping factor and (b) high damping factor.

estimated to be about 8–10 m thick in that part of the permafrost body. Considerably higher resistivity values south of the borehole suggest thicker permafrost with higher ice content.

Based on ERT data a distinct high resistive anomaly underneath the coarse surface layer of the rock glacier could be delimited. This permafrost core runs in south–north direction on the north-exposed slope at the orographic left side of glacier forefield Murtèl. It has a width of about 50 m and a length of more than 120 m. The upper limit of the rock glacier was not covered by the ERT grid and thus remains vague. Mapped permafrost extent in the subsurface is congruent with the distribution of coarse blocks at the surface, whereas the area covered with finer debris does not show any evidence for frozen ground conditions. The former findings point to the special microclimatic conditions that prevail in this kind of blocky environment (e.g., Harris and Pedersen, 1998; Juliussen and Humlum, 2008, and subsection 4.2.2).

ERT monitoring

Inspired by the results from the detailed 3D subsurface model and the availability of
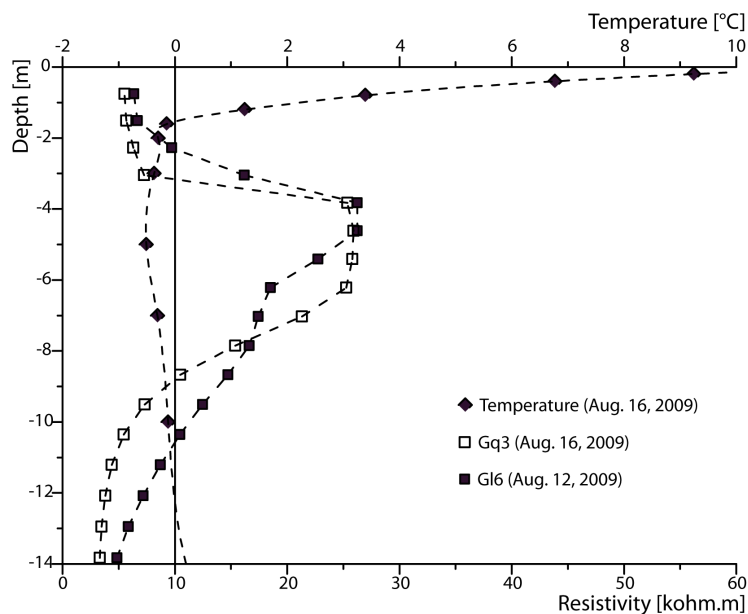
Figure 4.4: Temperature–resistivity diagram based on data obtained during the quasi-3D ERT acquisition and from borehole Mrt1.

borehole temperature data, a fixed ERT monitoring was installed in summer 2010. The monitoring line contains 36 fixed electrodes and muffled cables and crosses the borehole Mrt1 in the lower part of the rock glacier. ERT monitoring data were obtained in two phases using different acquisition modes. Between August 2010 and February 2011 the monitoring was measured manually (Syscal Junior Switch, Fig. 4.5a) before an automated resistivity meter (Geotom, Fig. 4.5b) with wireless data transfer to summit station Corvatsch was installed. The analyses are based on 63 measurements in total.

An overview of subsurface resistivity evolution between August 2010 and August 2011 is given in Fig. 4.5. The active layer — as seen in August and October 2010 by low resistive values — appears to be 2–3 m thick and uniform between horizontal distances 8 and 60 m. The high resistive subsurface that reflects the permafrost body as validated by former ERT results and borehole data is split in two parts: southwest of the 40 m mark resistivity values are higher than 100 kohm.m while toward northeast values reach at most 14 kohm.m. These values are slightly reduced until October 2010 before the active layer starts to dry/freeze until end of November 2010. Throughout winter and until the beginning of May 2011, subsurface resistivity values increase predominantly in the upper part of the ERT monitoring line (10–40 m) and in a depth between 2 and 10 m.
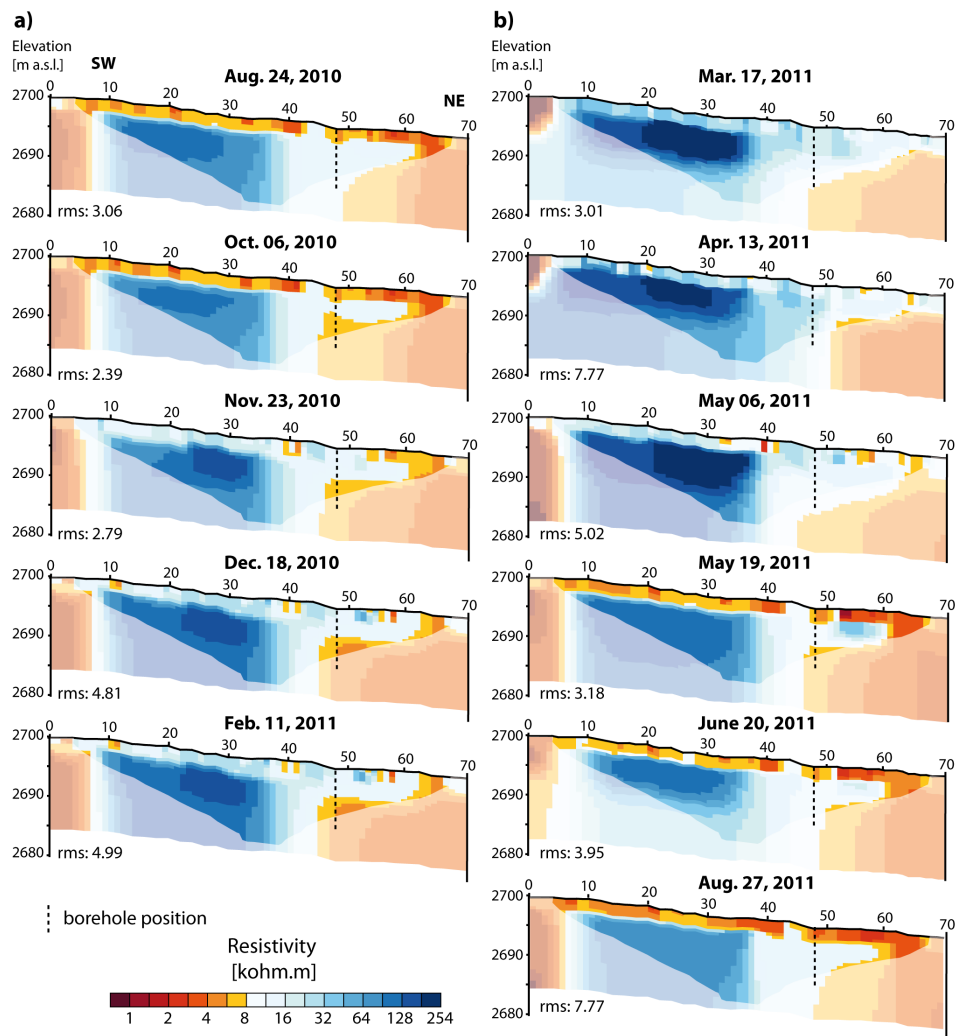
Figure 4.5: ERT monitoring results from Wenner array between August 2010 and August 2011 based on manual (a) and automated (b) measurements.

Finally, resistivity values exceed 290 kohm.m whereas the active layer remains constant at 10–30 kohm.m. As already shown by the 3D ERT subsurface model, the fine-grained morainic parts surrounding the permafrost body do not alter in terms of ground resistivity in a noteworthy manner. Except for the near-surface layer this part remains unfrozen at most probably stable moisture conditions. Care has to be taken because both ends of the monitoring line are not represented by measured data points at depth (faded part in all tomograms).

A drastic change occurs in the first half of May 2011 when resistivities in the active layer decrease to <7 kohm.m and in the permafrost body drop to about 120 kohm.m. These substantial modifications in the electrical properties of the ground are caused by

the onset of snow melt at that time and accompanied by the input of melt water into the subsurface. A detailed analysis of this most dynamic period is presented below (Fig. 4.6 and 4.7). Ongoing reduction in resistivity values within the permafrost body is confirmed by two subsequent data sets (about 85 kohm.m in summer 2011). The last tomogram in Fig. 4.5 matches very well with the data set recorded one year before. Only between 10 and 30 m horizontal distance and 2–8 m depth, the calculated resistivity values are slightly reduced.

Short-term changes were intended to be resolved with the automatization of the ERT monitoring in February 2011. The melting period in spring 2011 when subsurface resistivity variations occurred at a very fast rate is analyzed at higher temporal resolution. Air and ground surface temperature data with 20 minutes resolution recorded at the center of the monitoring line (25 m) as well as temperatures from a snow pole at 48 m for the period May 6 to May 19 are shown additionally (Fig. 4.6a). Around noon temperatures rise usually above 10°C (no shielded temperature measurements) and promote the melt of the snow cover from the top. Nocturnal cooling reaches down to -9°C but is almost totally absent between May 11 and May 15 when temperatures rarely fall below the freezing point. As indicated by the snow pole data, isothermal conditions at 1 m height were reached on May 7 and during the following days at the lower sensors. For the same period 1D vertical resistivity sections were extracted at horizontal distance 48 m (borehole location) from the 2D subsurface model and resolved by nine consecutive measurements (Fig. 4.6b). Additionally, subsurface temperature data from the beginning and the end of this 2-week period are plotted (Fig. 4.6c).

The snow cover that was well above 2 m at that time starts to melt in response to positive air temperatures and melt water percolates and potentially refreezes in the snow pack or at the ground surface. With the infiltration of melt water into the ground resistivity values are lowered, especially obvious in the uppermost 2 m (active layer). Most profound changes — i.e., either increase or decrease — in resistivity values occur between 2 and 3 m depth (grey shaded area in Fig. 4.6b). Here, values rapidly drop (May 10) or rise (May 5 and May 16). Below a depth of 8 m, resistivity values stay constant, which is related to the lack of many data points toward the bottom of the tomograms.

Temperature data from the borehole and the adjacent snow pole indicate frozen conditions during the whole investigation period. However, a continuous warming trend is
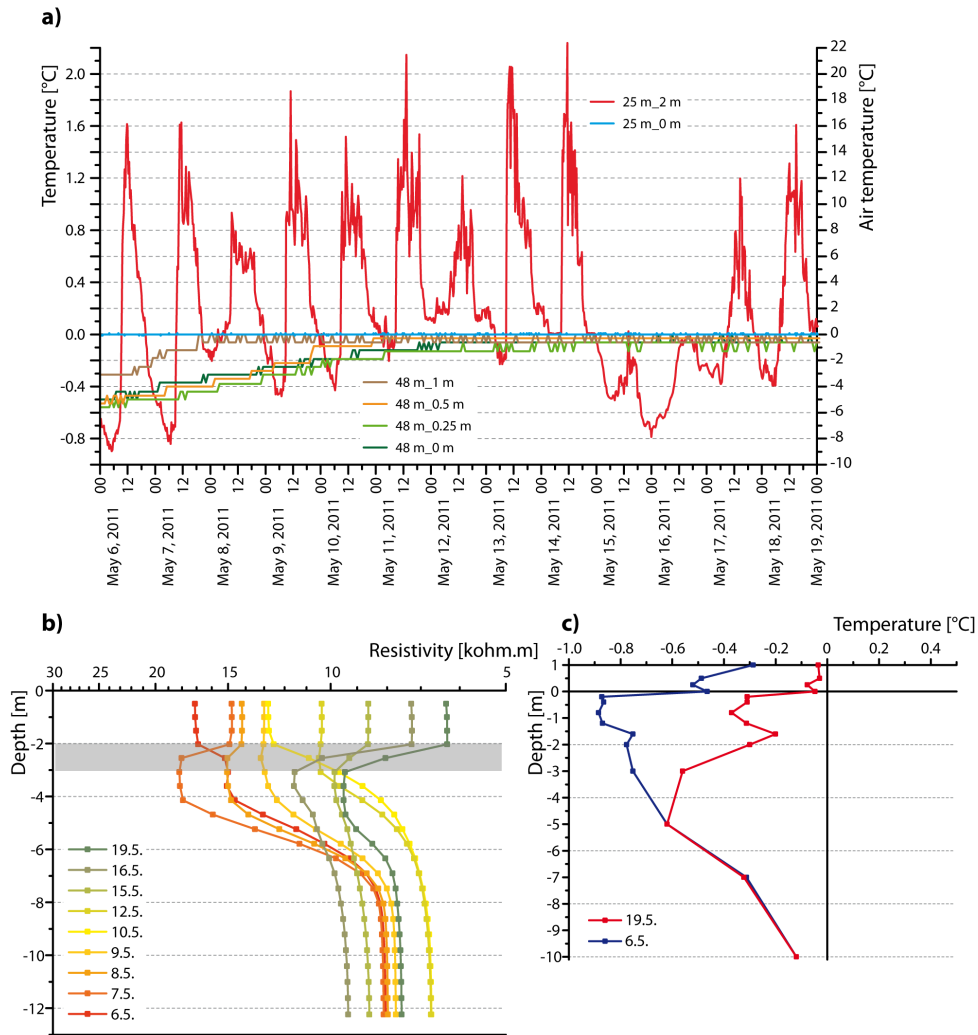
Figure 4.6: Temperature and resistivity conditions in May 2011. (a) Snow and GST (left axis) and air temperature (red line, right axis). 1D vertical sections of subsurface resistivities (b) and subsurface temperatures (c) at Mrt1.

obvious in the uppermost 5 m where a rise of about 0.5°C is recognized. Simultaneously, snow temperatures warm up to isothermal conditions close to the melting point, indicating the percolation of melt water. In the lower half of the 10 m borehole, no changes in temperatures are observed.

The sudden increase in resistivity values between 2 and 3 m may be related to the refreezing of percolated melt water or the lack of further melt water supply during a three day period of cold temperatures. The comparison with air temperature data (Fig. 4.6a) shows that the ERT pattern is a direct response to a halted snow melt and considerable nocturnal cooling (-8°C). On May 15, mean daily air temperature drop to -4°C and

maximum temperatures stay below 0°C. Thus, the percolation of melt water through the snow cover into the active layer is stopped and refreezing of the present liquid water at the permafrost table is ascertainable with the ERT data (Fig. 4.6b). Especially the last two data sets (May 16 and 19) show a distinct increase in resistivity values below a depth of 2 m. The phase transition from liquid water to ice is accompanied by a release of latent heat of fusion, which is responsible for an ongoing increase of active layer temperatures. This increase coincides with the progressive decrease in resistivity values in the uppermost 2 m where a considerable content of liquid water is constantly available during the snow melt.

A compilation of all analyzed data sets is given in Fig. 4.7. For this purpose, the subsurface is separated into three distinct areas, derived from the inverted tomograms. Based on the former findings, the active layer, the permafrost body, and the unfrozen morainic material are discerned. Specific resistivity values are shown as mean values to monitor the evolution of electrical properties for each of these three parts between August 2010 and June 2011.

Air and ground surface temperature loggers were installed in October 2010 shortly before the cooling of the active layer started. This is well documented by active layer resistivities that show a marked increase between October (5 kohm.m) and November (15 kohm.m). At the same time this increase is less pronounced for the permafrost area (40–45 kohm.m) and the unfrozen parts (3.5–4 kohm.m). During the following winter with mean daily air temperatures mostly below -8°C and constant ground surface temperatures at around -4°C, subsurface resistivities slightly increase to maximum values at the end of March. The permafrost body levels out at 100 kohm.m whereas the active layer (27 kohm.m) and the unfrozen material (6 kohm.m) reach much lower values.

The melting period is characterized by temperatures of 0°C at the ground surface. There is not much change in resistivity values at the beginning of this zero curtain period (dashed line 1 in Fig. 4.7). With the reduction of the snow height and positive air temperatures (∼2°C) a drop in resistivity values (line 2) of the active layer is registered. The most dominant increase in conductivity occurs a few days later during a warm period with mean daily air temperatures above the freezing point (line 3 and grey shaded area that highlights the 2-week period shown in detail in Fig. 4.6).

Together with data from the manual measurements prior to the automatization, the

evolution of subsurface resistivity can be analyzed in great detail. Especially the high temporal resolution of resistivity data in combination with temperature data provide deeper insights into subsurface thermal and hydrological processes at this permafrost site. During autumn and winter, resistivity data appear to increase at a slower rate except for the active layer. However, short-term processes cannot be assessed in detail until March. Cooling and freezing of soil moisture in the active layer had its largest impact between October and November when air temperature was well below the freezing point. In contrast, the infiltration of melt water in spring is suggested by a very rapid response of resistivity values within a period of two weeks (Fig. 4.6).
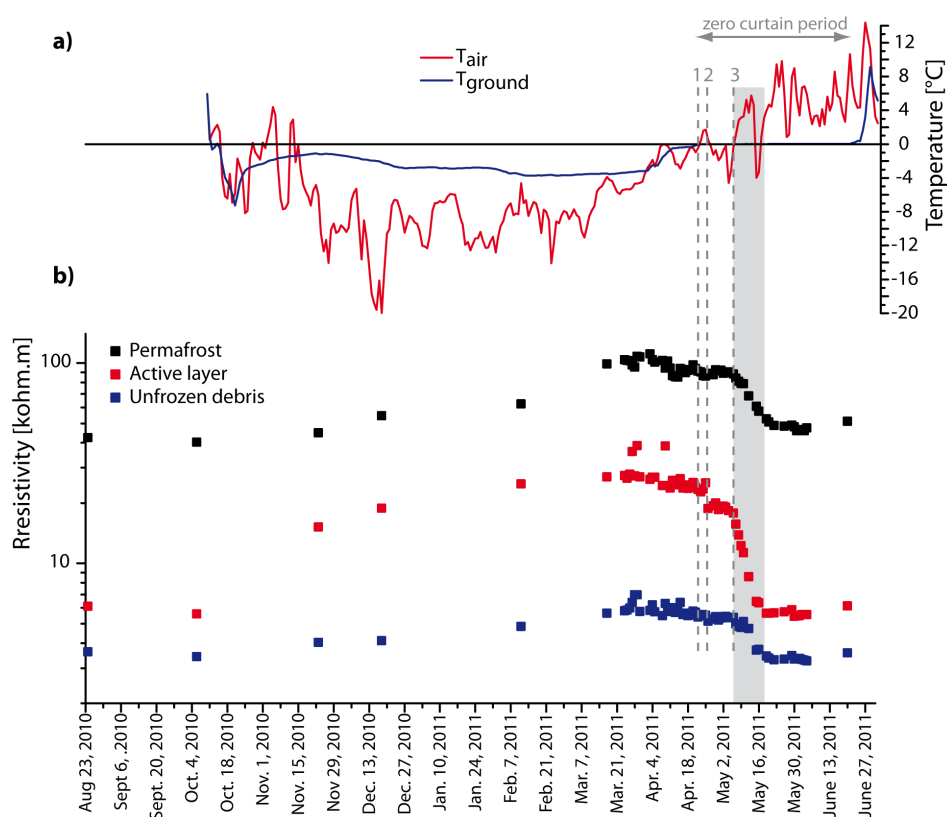
Figure 4.7: Compilation of temperature data (a) and ERT monitoring data from glacier forefield Murtèl (b), August 2010 to July 2011.

4.1.2. Refraction seismic tomography

To validate the information on the subsurface structure gained from electrical resistivity data with seismic velocity data, several RST profiles were measured in summer 2010 at the study site Murtèl. Four of those were arranged as two roll-along transects across

borehole Mrt1 and rock glacier Rabgiusa, the others were placed in the central part of the glacier forefield.

The difference between seismic refraction profiles measured along the rock glacier and the glacial till, respectively is already obvious from a comparison of the traveltime curves that result from the selection of first P-wave arrivals as registered by the geophones. Distinct break points in these traveltime curves indicate the presence or absence of refractors before the inversion process has started. In Fig. 4.8 the traveltime curves of two profiles (RST3 and RST5) are presented. The two profiles, measured with equal geophone setting and profile length, differ significantly from each other as obvious from the maximum traveltime recorded by the geophones. In Mrt-RST3 one distinct refractor can be recognized at about 24 ms at shot location 1.5 m and at about 4 ms at shot location 55.5 m. This discrepancy of the break point position along the traveltime–distance graph suggests the existence of a dipping layer, i.e., a seismic interface close to the surface at the right hand side of the profile and at greater depth toward the left side. Numerous bumps and cusps along the traveltime curves indicate a non-planar interface. Parts of this irregularity can also be attributed to the rough terrain conditions and inevitable noise that may lead to imprecise picks in the original data set. As a second example a smooth and linear traveltime–distance graph is shown from profile Mrt-RST5 (Fig. 4.8). Here maximum traveltimes are more than three-times longer than the ones in Mrt-RST3 and no refractor is apparent. Therefore, a uniform subsurface model with a gentle gradient of velocity increase with depth is to be expected from this data set.

Based on these traveltimes velocity sections of the subsurface are generated using an inversion routine. On the basis of RST profiles, the presence of permafrost is limited to the rock glacier Rabgiusa in glacier forefield Murtèl. Fig. 4.9 illustrates the P-wave velocity distribution beneath the two roll-along profiles. Profile Mrt-RST1+2 runs approximately parallel to the ERT monitoring line with the latter extending between 20 and 80 m horizontal distance in Fig. 4.9a.

The permafrost body — as resolved by ERT data — beneath the coarse surface debris is characterized by increased P-wave seismic velocities at shallow depth. Between horizontal distance 40 and 80 m velocity values around 3.5 km/s are recorded at about 5 m depth. In the lower (-10–40 m) and upper (80–150 m) parts of the transect a constant velocity gradient does not point to the existence of a distinct refractor. Here, P-wave velocities of
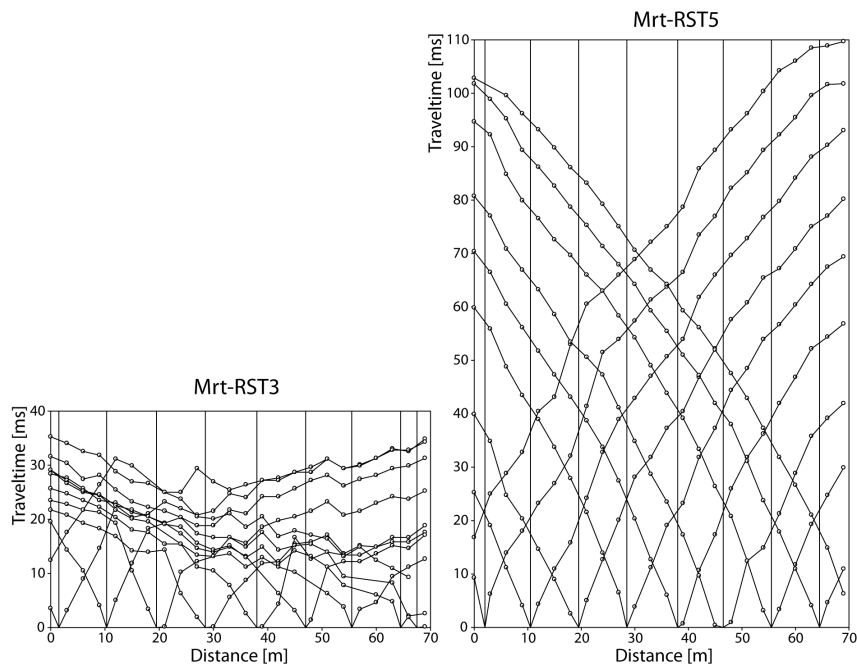
Figure 4.8: Traveltime–distance graphs from two refraction seismic profiles in glacier fore-
field Murtèl.

about 1.5-2 km/s are present at 15 m depth that are not representative for frozen ground conditions.

Profile Mrt-RST3+4 (Fig. 4.9b) is oriented along the central flowline of the rock glacier. Except for the lowermost part (10–15 m horizontal distance) that lies on morainic material this transect is placed between coarse blocks and boulders. A change in seismic velocity increase with depth occurs at horizontal distance 12 m, a pattern that reflects well the traveltime curves and the refractor depth as shown in Fig. 4.8. Toward south, the main reflector is slightly undulating at a depth between 3–5 m. It extends toward the upper part of the slope where no limit of the region with high velocity can be recognized. This is in agreement with the results obtained from the quasi-3D ERT approach with high resistivity values at the southern corner of the measurement grid.

To emphasize the contrast between these transects and a RST profile measured in the center of glacier forefield Murtèl the latter is shown in Fig. 4.10. For clarification the same color scale is used as in Fig. 4.9. In profile Mrt-RST5, P-wave velocity values increase to a maximum of 1.5 km/s. Neither in vertical nor in horizontal direction a distinct refractor appears in the subsurface, which is therefore regarded as very homogeneous. The vertical increase in velocity is attributed to the consolidation of the ground material with depth.
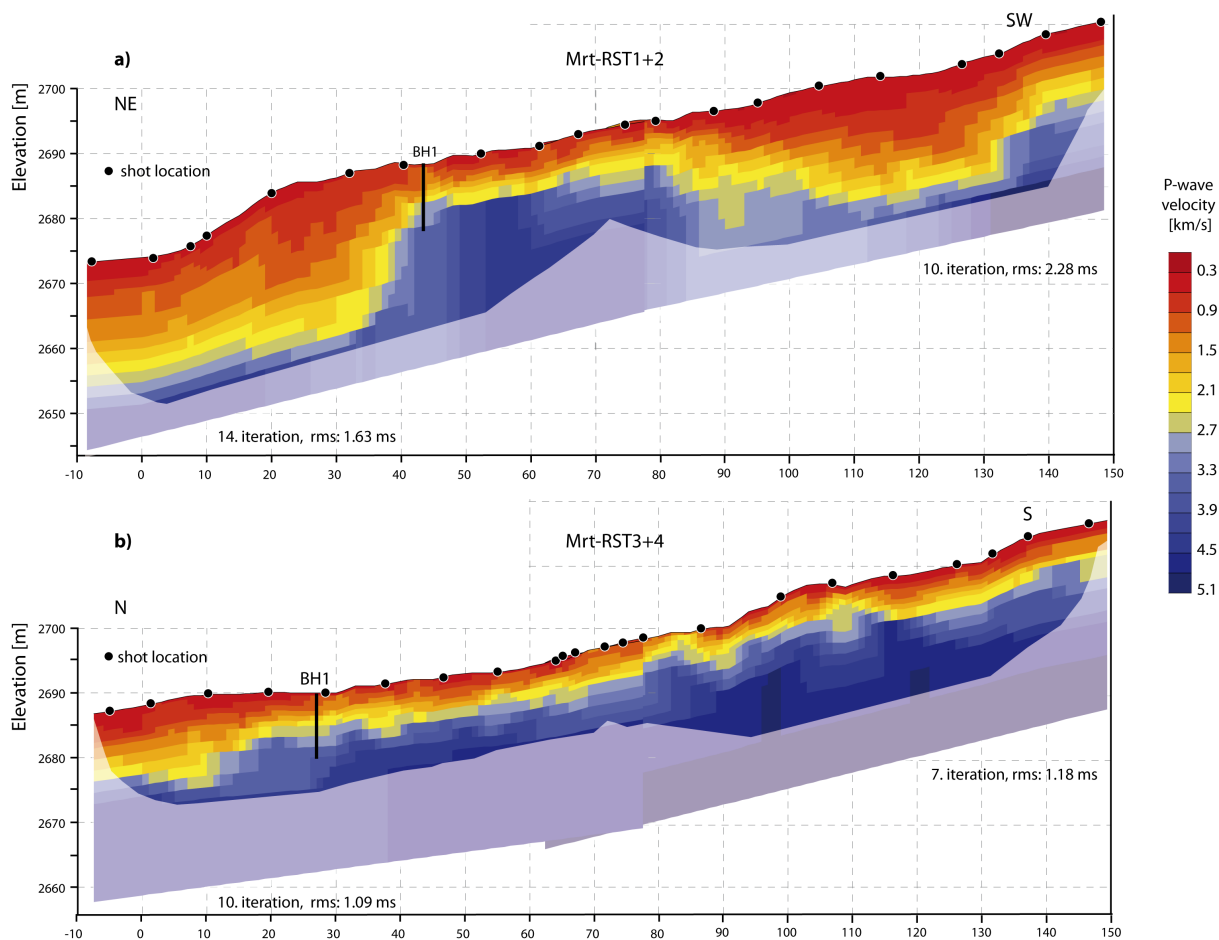
Figure 4.9: Refraction seismic tomograms across borehole Mrt1 and the rock glacier in glacier forefield Murtèl in NE-SW (a) and N-S (b) direction.
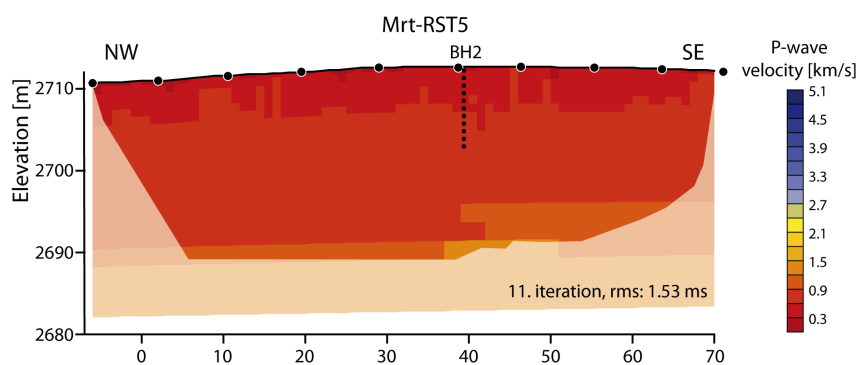
Figure 4.10: Refraction seismic tomogram in the central part of glacier forefield Murtèl across borehole Mrt2.

4.2. Air, surface, and ground temperature observations

Subsurface temperature evaluation is crucial to characterize and monitor permafrost conditions. The thermal state of the ground can either be directly assessed via temperature measurements in boreholes or estimated indirectly by temperature measurements in the air or at the ground surface. The latter are much easier to collect and are useful as upper boundary condition for the subsurface temperatures (Fig. 1.1, p. 9). In the following sections data from measurements at the bottom of the snow cover, air, ground surface, and ground temperatures are presented and analyzed in terms of the connectivity between air, surface layer, active layer, and permafrost/unfrozen ground. Borehole temperatures allow for an immediate assessment of the thermal state of the permafrost at Muragl (5 years) and Murtèl site (3 years).

4.2.1. BTS data

As a fast and low-cost method, the measurement of the temperature at the bottom of the snow cover (BTS) in winter (February/March) enables the estimation of the presence or absence of permafrost based on certain threshold values. As shown by Haeberli (1973) and Hoelzle et al. (1993) a temperature above -2°C at the ground surface underneath an insulating snow cover is indicative for permafrost-free conditions in the subsurface. If temperatures lie below -3°C the presence of permafrost is likely, whereas a margin of uncertainty exists between -3 and -2°C.

Interpolated temperature data from three BTS campaigns in March 2009, 2010, and 2011 in glacier forefield Murtèl are presented in Fig. 4.11. Similar patterns of temperature distribution are recognized in all years, while absolute temperature values differ considerably. In 2009, generally lower temperatures were recorded. Based on the mapping in 2009, most of the glacier forefield could be classified as area with probable permafrost occurrence. Nonetheless there are differences of more than 6 K between the area in front of the present glacier Murtèl (-9.6°C) as well as the rock glacier (red box, -6.7°C) and the central part of the forefield where borehole Mrt2 was drilled (-2.7°C). The measurement grid consists of 61 measured points and is rather coarse. A buffer zone of 50 m around each point was selected for the interpolation to display a general picture of surface temperature distribution. Temperature values at some distance from the actual measurement point

are error-prone and have to be interpreted with care because the heterogeneity between ground temperatures can be very immense as shown in subsection 4.2.2.

The cold temperatures in 2009 were not expected because snow cover at the time of data collection was between 180 and 350 cm, a height that definitely insulates the ground surface from cold air temperatures above. Regarding the snow thickness similar conditions prevailed in the two following winters with snow heights during data acquisition between 70 and 320 cm in 2010 and between 85 and 290 cm in 2011. The differences in absolute temperatures may be to some degree attributed to a change of the measurement device. In 2009, a multimeter was used and the measured resistivity had to be converted into temperature. A new BTS-probe was utilized since 2010, which directly displays temperature values. The latter is based on a standard avalanche probe, and hence, much smaller in diameter compared to the one previously used. As a consequence, the disturbance of the snow cover during the insertion of the probe is reduced and the circulation of cold air in the course of the measurement is limited. However, as already mentioned the general pattern with cold temperatures above the debris-covered ice in front of the glacier as well as around the rock glacier is confirmed by all three data series.

In 2010, the investigation was focussed on the area at and around the rock glacier at the western part of the forefield. The density of the measurement grid was increased to 147 points in total. The radius that is shown around each data point based on the spatial interpolation of temperatures is reduced to a circle of 30 m in diameter. The temperature pattern within the 3D ERT grid closely resembles the distribution of resistivity values as shown in Fig. 4.2. Cold surface temperatures are recorded from the center toward the southern corner of the grid and further extend in southward direction. This spatial extent of permafrost-indicative temperatures points to a much larger complex of frozen ground conditions south of the glacier forefield Murtèl itself. A transect that was measured crossing the central part toward borehole Mrt3 yielded ground surface temperatures of about -3 to -1°C suggesting the absence of permafrost. A sharp rise to values below -5°C represents the transition between the forefield and the debris-covered ice, which is not obvious from geomorphological evidence or relief in the field because of the thick debris layer.

In a repeated field campaign in 2011 with 65 measured points at and around the rock glacier the same pattern of temperature distribution was obtained. Temperature values

are slightly higher than in 2010 but still herald the occurrence of frozen ground in a small zone in that southwestern part of the forefield.
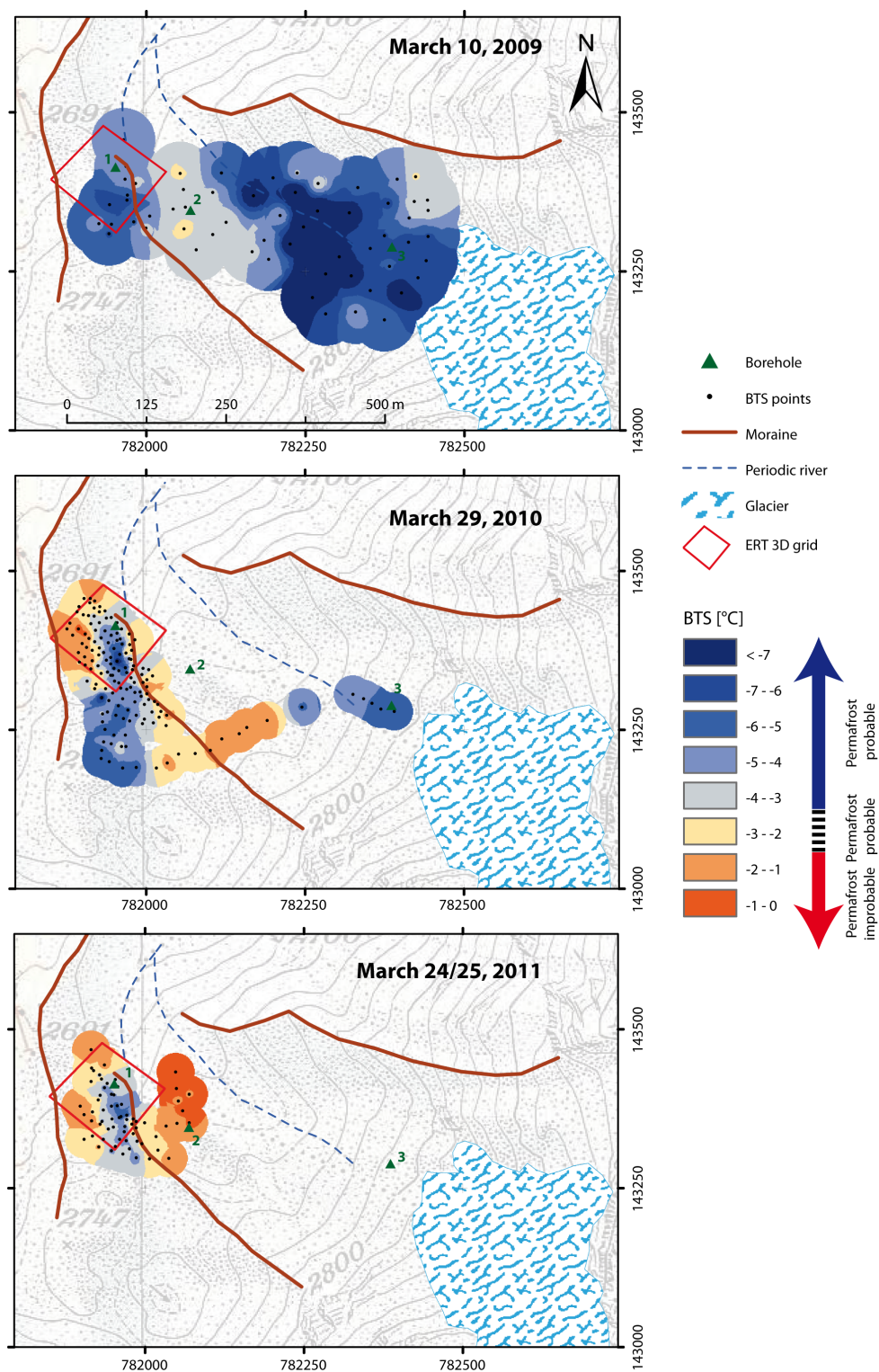
Figure 4.11: BTS data for three consecutive winters (2009–2011) based on point measurements in glacier forefield Murtèl.

The BTS campaigns can be summarized as suitable method in winter to get a fast overview of the ground surface temperature distribution in the investigation area. As the results in Fig. 4.11 show, the variability of surface temperatures might be large and years with cold temperatures such as 2009 may lead to an over-estimation of the presence of frozen ground if only one data set is considered. The repetition of measurements increases the degree of certainty: in this sample the pattern of relative temperature differences is confirmed each year between 2009 and 2011 even though absolute temperatures at the same point may vary by about 2 to 3 K. Based on these results, further investigations on the air–ground surface–subsurface coupling are essential.

4.2.2. Air and ground surface temperature data

An increased understanding of the connectivity between the air and the ground surface, especially in winter when a variable snow cover is present, can be gained by analysis of year-round temperature data. Air temperature and snow cover data from the nearby climatological station at rock glacier Murtèl (data were kindly provided by PERMOS) are used as reference data set (Fig. 4.12) because no air temperature recordings exist directly on site. Since 2008, additional information on snow cover evolution is available from temperature loggers installed in 0.25, 0.5, and 1 m height at two snow poles next to the boreholes. The reduction of the diurnal temperature oscillations due to the insulating snow cover in winter at borehole Mrt2 is used to infer the timing of snow coverage of a specific sensor. This method allows to compare snow height estimated at the borehole with snow cover data measured at the reference station (Fig. 4.12). For this purpose the best agreement was obtained by plotting the 0.4 K daily amplitude.

In 2010, one temperature logger could be installed at the solar panel pole of the ERT monitoring system in 2 m height. Additionally, numerous temperature loggers placed at the ground surface give insights on the thermal regime at multiple points with different surface characteristics.

The large variability in terms of annual ground cooling in winter is presented in Fig. 4.13 based on data from four temperature loggers. All loggers are located within a circle of about 50 m radius. In panel a the snow cover evolution is shown for comparison based on snow height data from climatological station Murtèl for 2009/2010 and reconstructed from
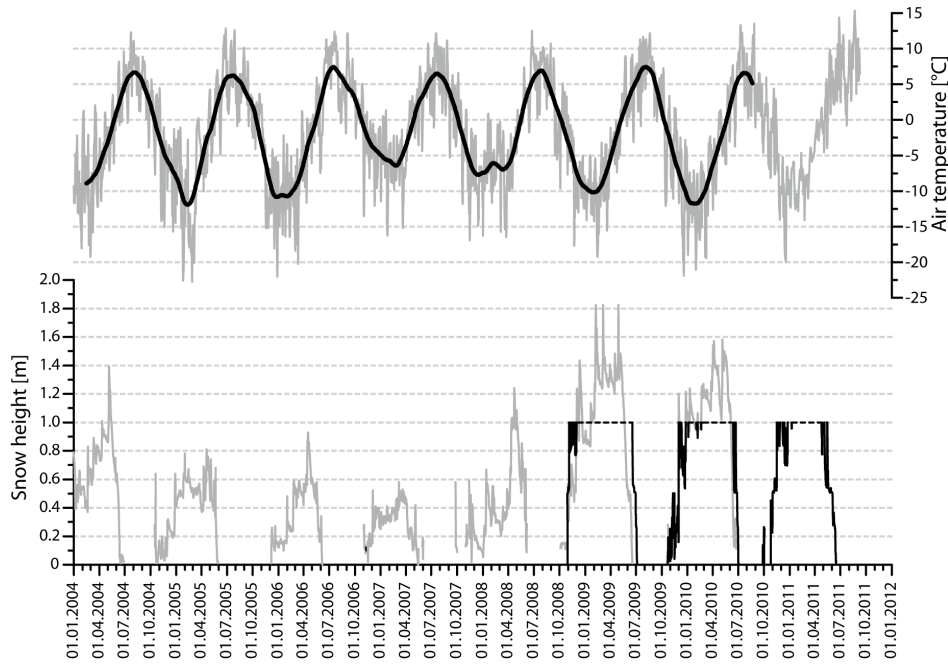
Figure 4.12: Mean daily air temperature and snow cover at meteorological station Murtèl 2004–2010 (data provided by PERMOS). The fitted temperature line is a seasonal running mean (90 days). Since October 10, 2010 own air temperature data measured at Mrt1 are available. 2008–2011 snow height is inferred from temperature data: black line ≤0.4 K daily temperature amplitude, dotted line represents snow height >1 m.

temperature measurements as explained above (2009–2011). The MAGST between sites differed by more than 4.2°C in 2009/2010 and about 3.4°C in 2010/2011, respectively. Capital letters A to E indicate categories for the connection between air and near surface temperatures based on an approach by Hanson and Hoelzle (2004). They suggest that air and ground temperatures together with the snow cover development reflect the main heat transfer processes toward the active layer. A description of the thermal processes behind each abbreviation can be found below Fig. 4.13.

Logger A221 is placed between stones in the upper part of the active rock glacier. In autumn, cold air penetrates through the shallow snow cover (period B) before the air temperature signal is highly damped as of November (C). During winter GST slightly decreases to a minimum value of -4.2°C (February 27, 2010) and -3.1°C (March 19, 2011). In May the release of latent heat is indicated by a sudden increase in temperatures. This sharp rise is attributed to melt water that percolates through the snow cover before
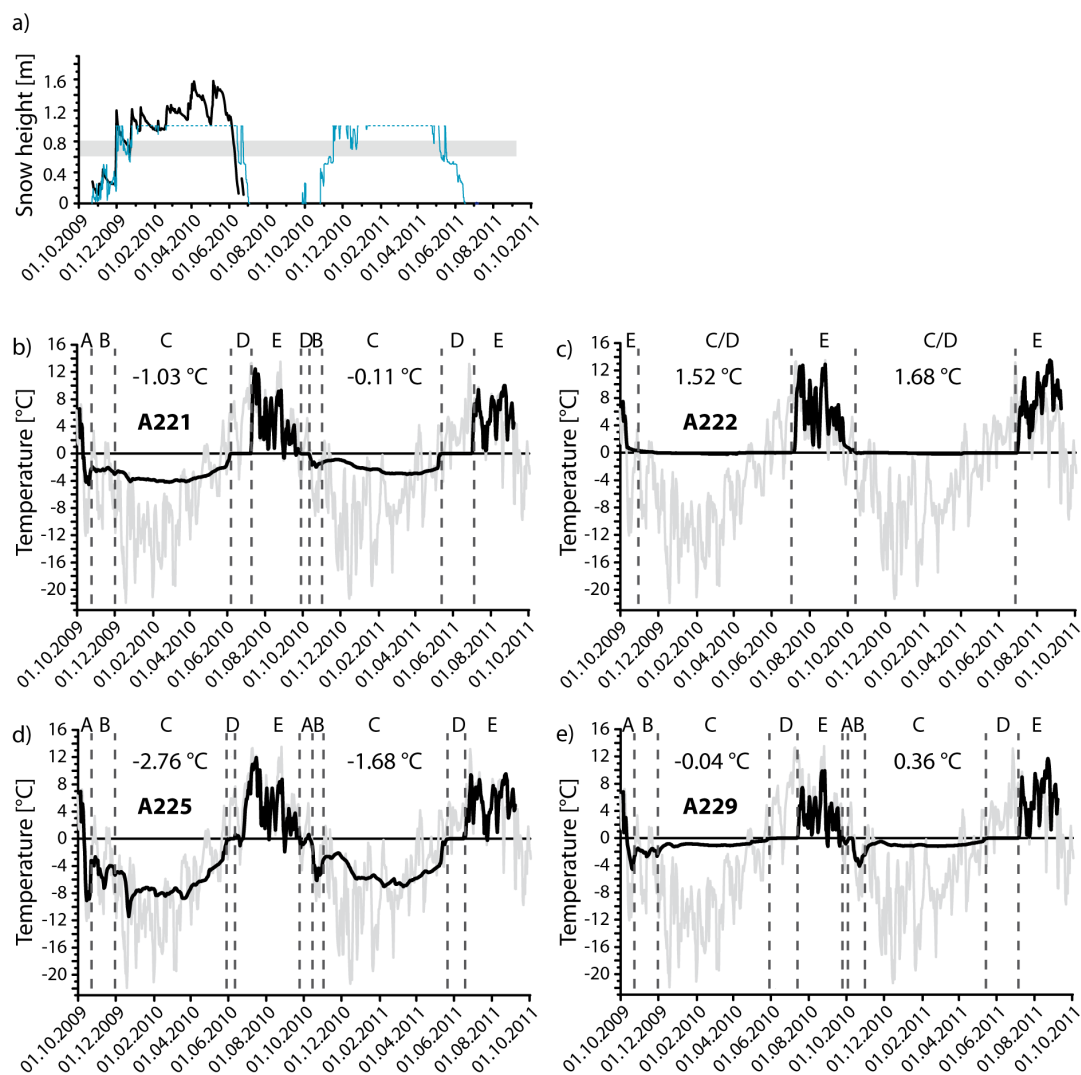
Figure 4.13: (a) Snow cover development at climate station Murtèl (PERMOS) (black) and at borehole Mrt2 (blue), as inferred from daily temperature oscillation; dotted line is snow height >1 m. (b–e) GST at 4 miniloggers placed in a 45 m-radius; grey line shows air temperatures from climate station Murtèl. A-active layer cooling before the onset of a lasting snow cover, B-shallow snow cover which allows connection between atmosphere and active layer in addition to negative active layer temperatures, C-lasting snow cover with no connection between the atmosphere and the active layer, D-zero curtain, E-active layer temperatures above zero; MAGST is denoted in period C.

it refreezes and therefore leads to a warming effect at the ground surface (latent heat of freezing). After this short period of temperature increase (7 days in 2010, 4 days in 2011) a zero curtain (D) develops at the surface whereas air temperatures are already well above the freezing point with daily means as high as 14°C. The zero curtain ends with the disappearance of the snow cover at that site and immediately GST follow closely the air temperature with a slight degree of damping (E). A second logger (A222) lies in a furrow of finer morainic material, sparsely vegetated with grass and vascular plants. In contrast to the other loggers plotted in Fig. 4.13 ground temperatures never fall significantly below the freezing point. Even at the beginning of winter the GST remains constant at 0°C, which indicates a fast buildup of the snow cover and/or a higher liquid water content at that site. In the following months the temperature signal is highly disconnected from the air temperature above the snow cover (C/D). GST do not indicate a substantial freezing of the ground below. With the end of the snow melt period temperatures increase and follow air temperatures.

Logger A225 is placed between large boulders on a slope at the rock glacier. Other than A221 and A222 the temperature signal at the surface follows the air temperature signal until end of January. Even in late winter there are still some peaks visible that correlate with cold spells (during period C). The increase in temperature caused by latent heat release appears approximately at the same time as at A221, whereas the zero curtain period is greatly reduced with 6 (2010) and 24 (2011) days, respectively. The temperature curve of logger A229 is affected by some peaks in autumn that reach down to -4.5°C in 2009 (October 20) and -4.1°C in 2010 (October 22). It is located within coarse stones and blocks, only about 20 m apart from A225. Instead of a cooling trend, as seen at A221, this site levels off at 1.1°C between December and May. In spring the temperature slowly approaches the freezing point without a pronounced rise at the beginning of the snow melt period.

The duration of the zero curtain period differs strongly between these four sites. The shortest period is observed at the slope that is covered with boulders (A225, Ø 15 days) while logger A222, placed in a depression, has on average 80 days of isothermal conditions in spring. An intermediate duration, with 42 days, is recorded at the two other loggers. In addition, a zero curtain period (D) is recorded at A221 in autumn 2010, when the temperatures stayed at the freezing point for two weeks during the melt of early snow.

At the site with fine grained material (A222), which is generally more susceptible to the release of latent heat during freezing caused by a higher water content the zero curtain period extends more or less through the whole winter season. Because of the moist sediment, only a marginal cooling of the ground is registered. In contrast, the sites with coarse boulders do not show lasting isothermal conditions at 0°C in autumn. The length of the zero curtain for all loggers is compiled in Table 4.1.

The exemplary analysis of four selected temperature loggers is underpinned by a summary of all loggers distributed within glacier forefield Murtèl (Table 4.1). The table lists the main thermal characteristics of each logger together with the specific elevation and the substrate class the logger was placed in (see subsection 3.3.2 for classification). The difference in MAGST at glacier forefield Murtèl (only 2 years of measurements compared to 6 years at Val Muragl) ranges from 0.14°C to 1.08°C with generally warmer values in 2010/2011. The increased MAGST in 2010/2011 can be attributed to the snow cover evolution as most important factor because corresponding MAAT from station Murtèl show similar values for both years with 2.82°C in 2009/2010 and 2.59°C in 2010/2011. On the one hand, an isolating snow height of more than 60–80 cm established at the end of November in 2009, whereas in 2010 this height has been measured already two weeks earlier and disconnected the ground from cold air temperatures in autumn/early winter. On the other hand, the snow cover fully disappeared on June 16, 2011 compared to July 2, 2010 and thus enabled the ground to warm up earlier in the second year. An indication for the duration of the snow melt period and thus indirectly for snow height at the beginning of the melt season is derived from the length of the zero curtain (Table 4.1).

Especially the loggers placed on morainic material (dominated by gravel, e.g., A222 or borehole Mrt2) observe very similar mean annual temperatures at the surface in both years. Larger differences are recorded at loggers installed between coarse boulders (e.g., A218, A221, A225). Because vegetation is mainly absent in the area the micrometeorological influences at the surface can be attributed fore and foremost to the dominant grain size of the superficial sediments. They are therefore investigated by plotting the MAGST recorded at the different temperature loggers versus the substrate class (Fig. 4.14). In 2009/2010 GST were only available from the two borehole locations Mrt1 and Mrt2. As seen in the following years the scattering in substrate class 2 (= gravel 0.2–6.3 cm) is much less compared to the one in class 5 (= boulders >63 cm).

Table 4.1: Characteristics of temperature loggers placed in glacier forefields Murtèl and
Muragl.

Logger	Substrate class	Elevation [m a.s.l.]	Data record	mean[a] [°C]	MAGST[b] [°C]	ΔMAGST [°C]	ZC (min/max)[c] [days]
Murtèl							
A216	4	2737	Oct.09–March11	-0.98	-	-	40
A218	5	2745	Oct.09–Sept.11	-0.12	-0.52/0.35	0.87	0
A220	5	2736	Oct.09–Sept.11	1.08	0.90/1.31	0.41	65 (63/67)
A221	4	2712	Oct.09–Sept.11	-0.59	-1.03/-0.11	0.92	42 (33/50)
A222	2	2702	Oct.09–Sept.11	1.60	1.52/1.68	0.16	80 (74/85)
A223	2	2687	Oct.09–Sept.11	1.25	1.24/1.50	0.26	54 (50/58)
A224	4	2689	Oct.09–Sept.11	1.73	1.59/1.84	0.25	36 (31/40)
A225	5	2699	Oct.09–Sept.11	-2.28	-2.76/-1.68	1.08	15 (6/24)
A227	2	2695	Oct.09–Sept.11	1.44	1.22/1.67	0.45	67 (61/73)
A229	4	2693	Oct.09–Sept.11	0.18	-0.04/0.36	0.40	42 (33/50)
A230	3	2672	Oct.09–Sept.11	-0.22	-0.52/0.11	0.63	29 (27/31)
Mrt1	4	2683	Oct.08–Sept.11	0.45	0.20/0.65	0.45	56 (49/69)
Mrt2	2	2713	Oct.08–Sept.11	1.40	1.85/1.99	0.14	62 (55/68)
Muragl							
ML1	4	2670	Sept.05–Sept.11	-0.42	-1.94/0.88	2.82	71 (29/88)
ML2	3	2672	Sept.05–Sept.11	0.28	-0.60/1.06	1.66	47 (38/60)
ML3	2	2680	Sept.05–Sept.11	1.13	0.56/1.79	1.23	37 (17/53)
ML4	3	2700	Sept.05–Sept.11	0.58	0.09/1.09	1.00	44 (31/66)
ML5	2	2750	Sept.05–Sept.11	0.75	0.25/0.97	0.72	40 (25/66)
ML6	3	2770	Sept.05–Sept.11	0.42	-0.69/1.35	2.04	45 (32/57)
ML7	3	2750	Sept.05–Sept.11	0.78	0.15/1.17	1.02	44 (31/63)
ML8	3	2690	Sept.06–Sept.11	0.93	0.30/1.27	0.97	45 (30/64)
ML9	4	2735	Sept.06–Sept.11	-1.03	-1.41/-0.61	0.80	89 (66/147)
ML10	4	2755	Sept.06–Sept.11	-1.42	-2.85/-0.34	2.51	46 (32/64)
ML11	3	2750	Sept.06–Sept.11	0.09	-0.64/0.53	1.17	36 (20/54)
ML12	5	2745	Sept.06–Sept.11	-0.46	-1.47/0.42	1.89	31 (12/43)
ML13	3	2680	Sept.06–Sept.11	1.09	0.55/1.34	0.79	48 (36/61)
ML14	3	2736	Sept.06–Sept.11	0.79	0.56/1.07	0.51	62 (48/79)
Mgl1	4	2660	July06–Sept.11	-0.10	-1.07/0.56	1.63	32 (24/47)
Mgl2	2	2763	Sept.06–Sept.11	-1.06	-2.37/-0.003	2.37	10 (0/16)

[a] mean value for the whole measurement period 2006–2011 (Muragl) and 2009–2011 (Murtèl).

[b] minimum and maximum MAGST from the data record is listed to indicate the range.

[c] minimum number and maximum number of days showing a zero curtain during the measurement period.
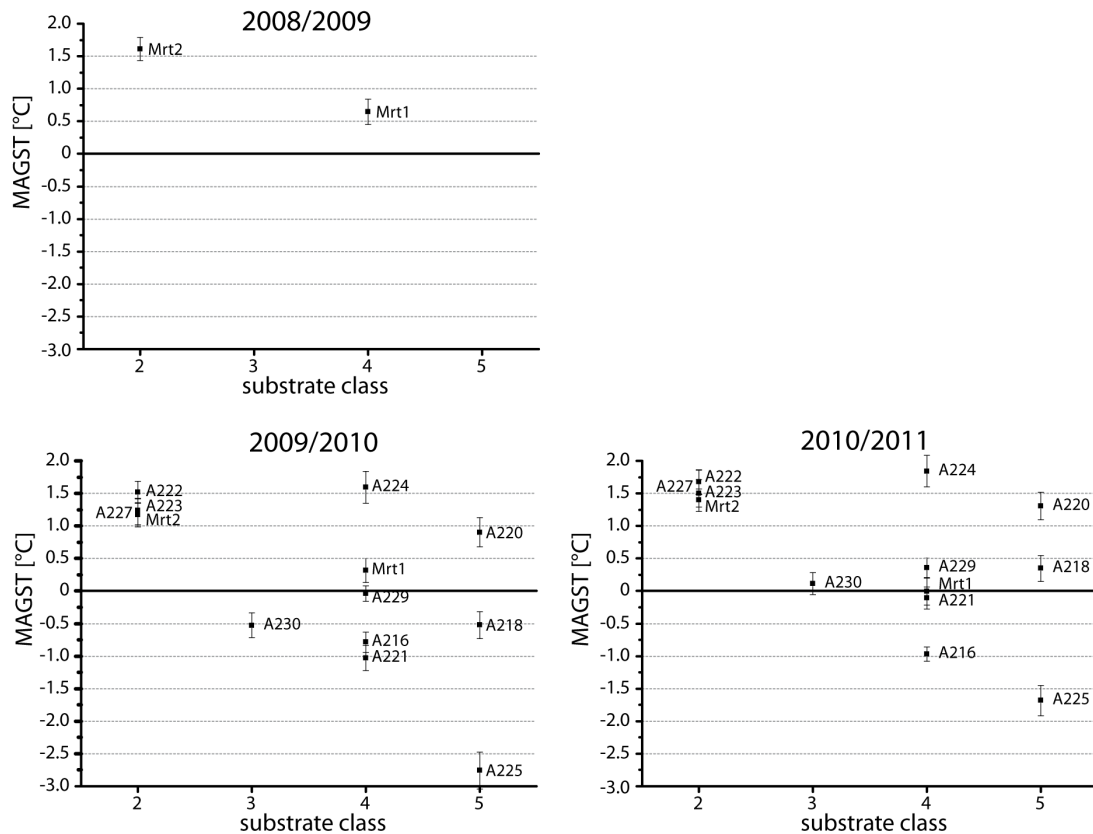
Figure 4.14: MAGST vs. substrate class for hydrological years (2008–11) at Murtèl site. Squares indicate mean values, bars the standard deviation.

A general trend toward lower MAGST with increasing grain size is recognizable in both years. Positive outliers are present in classes 4 and 5. A more reliable statement of the relation between MAGST and substrate can be deduced from analysis of temperature data from Val Muragl that are based on a 6-year record (see subsection 5.2.2).

Melting of the interstitial ice at the core of rock glacier Rabgiusa occurs during summer as visible at a small spring at its front. Temperature recordings show that water temperatures stay at 0°C in summer even though at 50 cm height above the water table values up to 18°C are recorded (Fig. 4.15). Thus, melt water from the rock glacier contributes to the discharge at the spring instead of percolated precipitation that would have higher temperatures. As derived from the daily ERT measurements during spring ice growth occurs at the bottom of the active layer and probably also within the permafrost body. Therefore, ice melt in summer is counterbalanced by refreezing of percolating snow melt in spring. Temperatures at the third sensor, which was installed slightly above the water
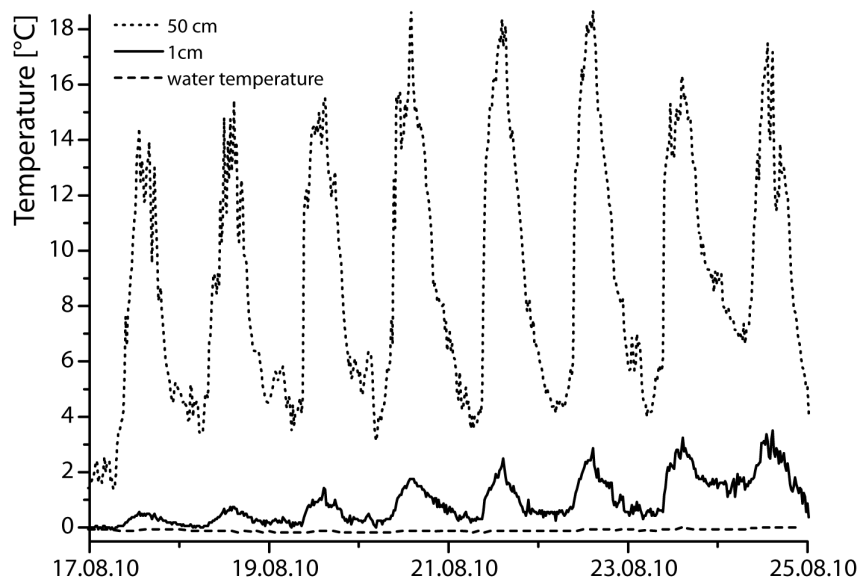
Figure 4.15: (Water-)Temperatures at the permafrost spring in front of rock glacier
Rabgiusa.

surface, fluctuate between 0 and 3°C and indicate a variable water level at the spring.

4.2.3. Borehole temperature data

An ultimate confirmation of the presence/absence of permafrost or information on its
thermal state and its mid- to long-term evolution is achieved by direct temperature ob-
servations within boreholes. That is why two shallow boreholes were drilled in glacier
forefield Murtèl in summer 2008 (by C. Kneisel), one in the rock glacier (Mrt1) and an-
other one in the fine-grained glacial till in the central part (Mrt2, cf. Fig. 3.3). A third,
10 m deep borehole was melted in the debris-covered lower part of glacier Murtèl in 2009.

The boreholes in glacier forefield Murtèl differ strongly from each other in terms of their
thermal conditions. While borehole Mrt1 has permafrost conditions down to more than
10 m depth, the second borehole Mrt2 is characterized by seasonal frost. Temperatures
below the permafrost table (Mrt1) are slightly below the freezing point with a minimum
temperature of -0.62°C in 5 m depth. Slow conduction of the cold temperature wave below
the active layer delays the downward propagation of temperatures. The active layer has
an average depth of almost 2 m for the past three years (Table 4.2) based on the linear
interpolation between adjacent temperature sensors. The inter-annual variation of active
layer depth is very small in spite of a rather variable length of zero curtain conditions and
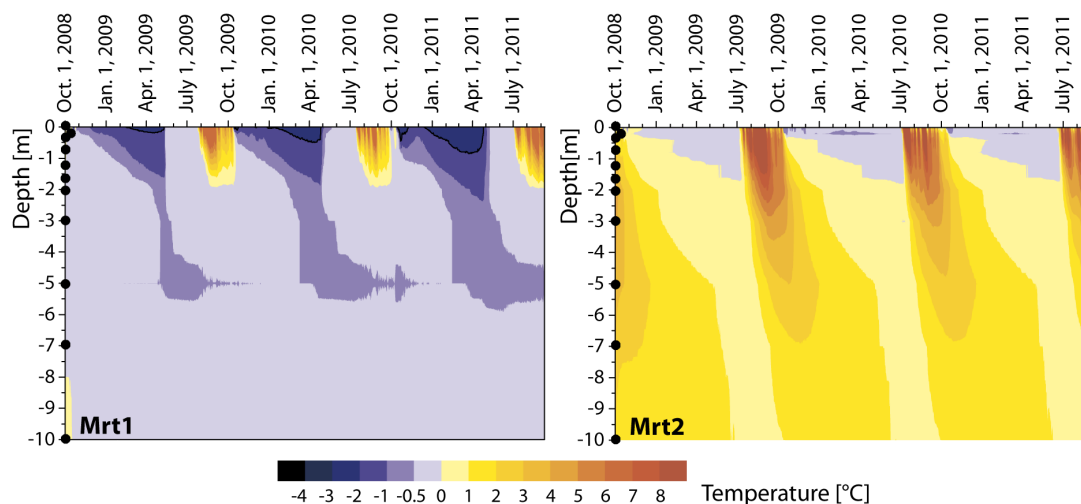
Figure 4.16: Borehole temperatures at glacier forefield Murtèl. Position of each sensor is indicated by black dots on the y-axis.

of subsequent snow free periods. Even though permafrost is present at Mrt1 MAGST was on average above 0°C. Since mean annual temperatures at the permafrost table (TTOP) are about -0.35°C a mean thermal offset of 0.74°C is registered between the ground surface and the permafrost table.

Summer temperatures at the ground surface and in the active layer at borehole Mrt1 are in line with air temperatures with increasingly damped amplitude with depth. The annual variation of summer temperatures, expressed as thawing degree-days (DDT), is relatively small within the past three summers as can be seen from Fig. 4.12 and Table 4.2. DDT has values between 503 and 531 cumulated positive ground surface temperatures. Much larger variations are seen from the cumulative sum of negative surface temperatures, expressed as freezing degree-days (DDF). The absolute values range from 293 to 463 at the permafrost-affected borehole in dependence of the effect of annual snow cover evolution.

At Mrt2, the freezing period lasts approximately from October/November to July. Temperatures as high as 2°C are registered down to a depth of 7 m in autumn. Thus, this location is far from having frozen ground conditions. The annual depth of the seasonal frost is approximately 1.75 m whereas the mean annual temperature at 2 m depth is clearly positive with 1.9°C, as is the MAGST with 1.4°C. Positive summer temperatures show little variation (DDT between 556 and 618) at Mrt2 and cumulative negative temperatures are much lower compared to Mrt1 (DDF between 30 and 130). The lat-

Table 4.2: Thermal characteristics of the subsurface at borehole sites Mrt1 and Mrt2.

	Year [01. Oct−31. Sept.]	ALT [m]	ZC [days]	MAGST [°C]	TTOP [°C]	Thermal offset [°C]	DDF	DDT	n_F	n_T
Mrt1	2008/2009	1.93	69	0.65	-0.25	0.90	292.95	528.78	0.20	0.63
	2009/2010	1.93	49	0.32	-0.36	0.68	387.61	503.07	0.22	0.69
	2010/2011	1.96	51	0.20	-0.45	0.65	462.92	531.30	0.30	0.89
	Ø	1.94	56.3	0.39	-0.35	0.74	381.16	521.05	0.24	0.74
		SF [m]		Temp. at -2 m [°C]						
Mrt2	2008/2009	1.72	68	1.61	1.88		30.13	618.46	0.02	0.74
	2009/2010	1.73	62	1.17	1.99		129.98	556.99	0.07	0.77
	2010/2011	1.80	55	1.41	1.85		88.09	572.30	0.06	0.96
	Ø	1.75	61.7	1.40	1.91		82.73	582.58	0.05	0.82

ALT = active layer thickness, as interpolated from adjacent temperature sensors; ZC = zero curtain; MAGST = mean annual ground surface temperature; TTOP = temperature at the permafrost table (i.e., 2 m at Mrt1); DDF = freezing degree days; DDT = thawing degree days; n_F = freezing n-factor; n_T = thawing n-factor; SF = depth of seasonal frost.

ter values reflect the considerable influence of the snow cover that isolates the ground from cold air temperatures as well as the importance of the zero curtain. The release of latent heat during most parts of the winter keeps the ground surface temperature at isothermal conditions without further cooling. The duration of the zero curtain as given in Table 4.2 corresponds to the melting period in spring. At borehole site Mrt2, a zero curtain is also present in autumn and because of the isolating snow cover in winter the ground surface does not register many subfreezing temperatures values, for example in 2008/2009 (DDF=30). In winter 2009/2010 (DDF=130) temperatures decrease slightly below -0.5°C down to 20 cm depth caused by a temporary reduction of the snow height to about 50 cm at the end of December.

The resulting n-factors show the correlation between air temperatures and ground surface temperatures at the borehole sites. Average thawing n-factors range between 0.74 and 0.82. The coupling between air temperatures and the ground surface is highly disturbed in winter as represented by small values for n_F. At borehole Mrt1 n_F averages to 0.24 whereas it is even smaller with 0.05 at Mrt2. This underlines the efficiency of the snow cover as buffer layer between the air and the surface.

An estimation of trends in the permafrost's thermal state is difficult to obtain from
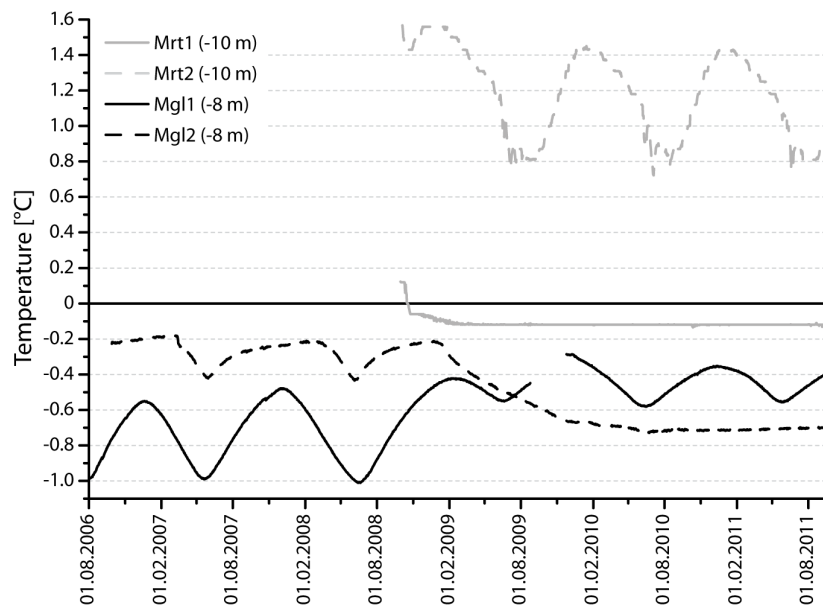
Figure 4.17: Mean daily temperatures at the deepest sensors in boreholes Mgl1, Mgl2, Mrt1 (permafrost), and Mrt2 (seasonal frost). Data gap at Mgl1 because of sensor failure.

the short temperature record at these two boreholes. Figure 4.17 shows the thermal conditions at the deepest sensor of each borehole (for discussion of boreholes Muragl see subsection 5.2.1, p. 106). Borehole Mrt2 has a distinct seasonal signal at 8 m depth without any values at subfreezing temperatures. Lowest temperatures are recorded between July and August, indicative for a time-lag of about 8 to 9 month compared to the lowest temperatures at the ground surface that are recorded in October before a significant snow cover has settled. Short after the installation of sensors at Mrt1 temperatures dropped within a few days to values slightly below the freezing point and are constant since then (-0.12°C). These isothermal conditions suggest that permafrost extents from about 2 m to the bottom of the borehole. Temperature observations confirm the results from 2D and quasi-3D ERT subsurface models that indicate a lower boundary of the permafrost body at about 11–12 m depth.

In 2009, a third borehole was drilled in the debris-covered part of Vadret dal Murtèl at the head of the glacier forefield. The drilling of a 10 m-deep borehole using hot water vapor (Heucke Ice Drill) was possible without hitting any obstacle. Thus, beneath a 20 to 40 cm thick debris cover massive glacier ice of more than 10 m thickness is present. Temperature recordings in the boreholes were difficult because the casing and the sensor
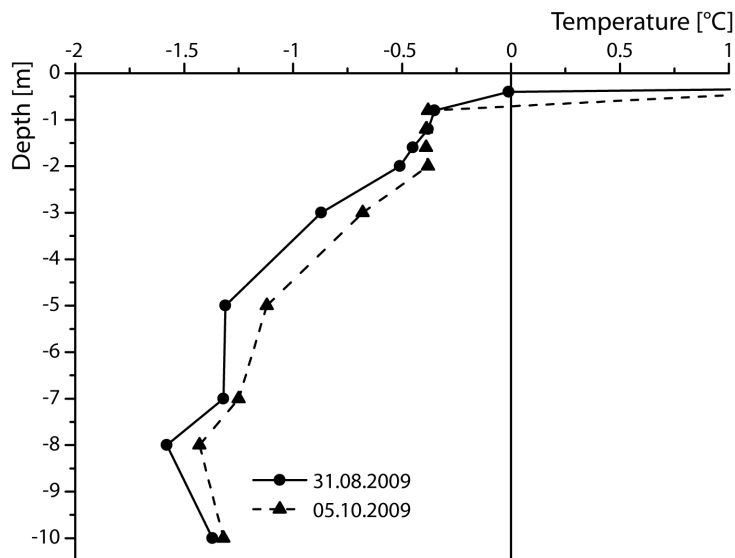
Figure 4.18: Temperatures in the debris-covered ice of Vadret dal Murtèl in 2009.

string was continuously lifted after installation and was sheared off at the surface in October 2009. Short after installation temperatures of about -1.5°C were measured in 8 m depth (Fig. 4.18). This value might be suggestive for cold-based conditions and potentially frozen ground beneath the ice. Observations during summer months, however, revealed that melt water of the glacier remnants above infiltrates along outcrops and crevasses. This water flows either beneath the debris-covered ice or englacial; in any case it disturbs the thermal regime at depth and makes the presence of a frozen bed less likely. The melt water reappears at the lower end of the glacier forefield at about 2620 m a.s.l.

4.3. Kinematic measurements

For the observation of ground motion in glacier forefield Murtèl, repeated DGPS surveys were conducted every summer since 2009. At or close to the rock glacier, four large blocks that are supposed to float within the matrix of the ground were chosen for detailed kinematic measurements to provide information on rock glacier creep (points DGPS 6–9). Furthermore, several distinct points — like the borehole sites — and stones were selected for reference. In Fig. 4.19 the creeping rates of some of the targets for the two years August 23, 2009–August 22, 2010 and August 22, 2010–September 09, 2011 are shown. As a third column, the total creep distance (2009–2011) is plotted. All values have to be

regarded as horizontal distances with the values for blocks 1–4 as arithmetical mean of three measurement points on each block (cf. Fig. 4.20).

The three points 'laser rock', 'laser moraine', and 'snowpole 2' are located in the central part of the glacier forefield and have displacement values for both years that lie within or very close to the accuracy of the measurement (1–5 cm). Thus, they can be considered as stationary without any creep pattern. The same will be most likely true for 'borehole 2' where annual displacements in the order of 10 cm are in opposite direction and therefore probably attributed to a positioning error of the DGPS antenna in the field in 2010. The measurement in 2011 yields a position that is very close (3.5 cm) to the first measurement in 2009, suggesting stationary conditions. Much larger displacement values are registered at the other points. Point DGPS 5 refers to the small spring at the front of the rock glacier, DGPS 10 is located on the lateral moraine very close to the margin of the rock glacier. Measurement points DGPS 6 to DGPS 9 are placed on top of the rock glacier and have displacement values between 12 and 48 cm per year. From points 'source', 'borehole1', and 'block1', all located in the lower part of the rock glacier, it seems that between 2010 and 2011 creep was at least twice as high as the year before. For 'block4' there might be also an inaccuracy of one measurement point that leads to a relative large motion (>20 cm in each year), while the total displacement does not correspond to the sum of both years.

The vertical component of the displacement for the period 2009–2011 as a whole is plotted at the upper graph of Fig. 4.19. DGPS points 1 to 4 show negligible values of the vertical movement that lie within the accuracy of the method. The same is true for the point at the spring even though a considerable horizontal movement is registered here. All points measured on the rock glacier are subject to a slight subsidence in the order of 11–20 cm per year. Maximum subsidence values of 35 cm for both observation years are registered at points DGPS 6, DGPS 8, and DGPS 9. This might be to a large part attributed to the downslope movement of the blocks.

As already mentioned the values of the four large blocks on the rock glacier were averaged from single measurements at three points marked on each block (cf. Fig. 3.8, p. 58). This approach allows to study the three-dimensional rotation and tilting of each block. The displacement vectors of the individual points are shown in Fig. 4.20 with the planar surface of the investigated blocks transferred into a coordinate system. Thus,
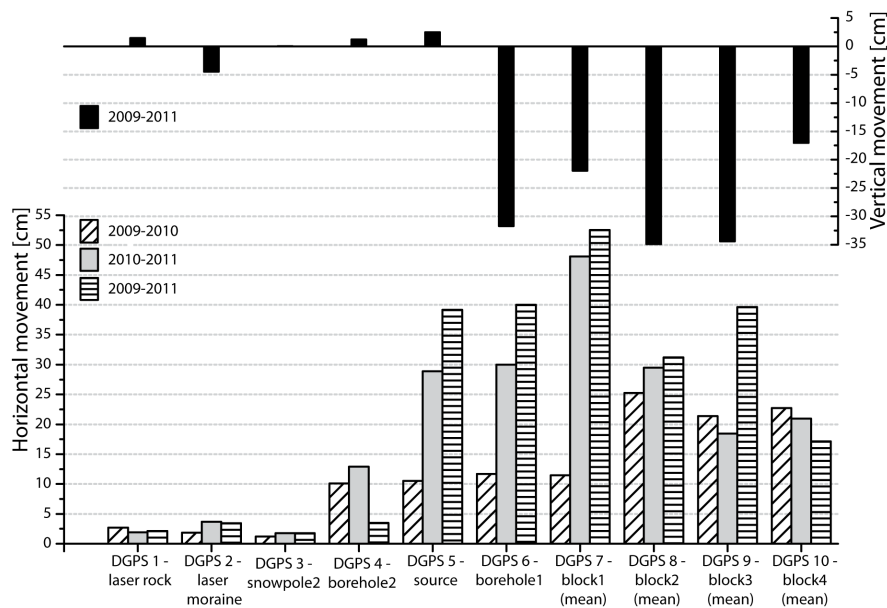
Figure 4.19: Vertical and horizontal movement at selected points at glacier forefield Murtèl measured annually using DGPS.

the measured points form a triangle with its center as origin of ordinates. The relative horizontal movement of each point is indicated by solid (2009–2010) and dotted arrows (2010–2011), respectively, while the vertical component is represented by thin lines. Lines directed upward refer to a lifting of the point, lines directed downward to subsidence (Fig. 4.20).

Block1 is moving in northeast direction with a slight tilting toward its left side in 2010 and toward its right side in 2011. This tilting is inferred from the lifting of point 2 and the simultaneous subsidence of point 3 as well as an opposite directed vertical movement of these two points in 2011. Point 1 constantly sinks at a rate of about 15 cm per year. The whole block is positioned at the front of a ridge structure on the rock glacier relief and moves toward a furrow. The direction of the horizontal movement of block2 between 2009 and 2010 was likewise toward northeast, while in the second year this block experienced a tilting toward its left side as apparent from points 2 and 3. This tilting is associated with a subsidence of up to 43 cm.

The most uniform horizontal displacement in the two years of measurements was observed at block3, which is located at the steepest part of the rock glacier. All points move in north/northeast direction with a creep rate of about 20 cm per year. A contemporary
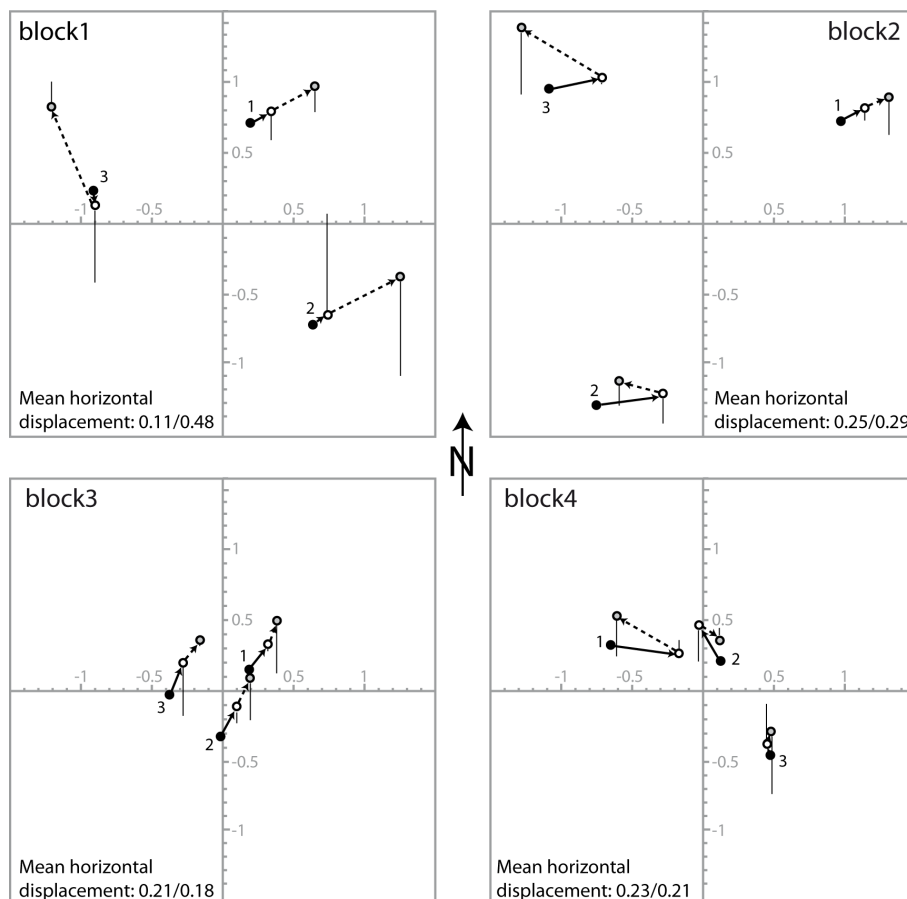
Figure 4.20: 3D displacement behavior of four selected blocks located at or close to the rock glacier for the period 2009–2011 as given by horizontal and vertical vectors (scale is in m).

subsidence of about 30 cm was registered at point 3 (in 2009) and points 2 and 3 (in 2010). In general, the direction of the movement of block4, located on morainic material nearby the rock glacier, is directed toward north. Only point 1 experienced a large displacement in 2010 and in the opposite direction in the following year. This might be because of a positioning error of the antenna in 2010 since vertical movements of points 1 and 2 in the first year are very small and a tilting of point 3 at the same time is also not very substantial. Comparing only the years 2009 and 2011 results in a relatively low horizontal displacement of about 18 cm toward north as shown in Fig. 4.19, which is about half the movement or less compared with the other blocks.

Based on the measurement of certain targets in the glacier forefield and of selected blocks that are supposed to move within the subsurface matrix the dynamic behavior of

the sediments with and without the influence of permafrost was estimated by means of DGPS. While the points located in the central part of the glacier forefield are regarded as more or less stationary the rock glacier creeps at a rate of 15–26 cm per year. Under the influence of this shear force the lateral moraine that lies in front of the rock glacier is consequently pushed forward at a rate of 9–19 cm per year as derived from the measurement points at the small spring and at block4.

Complementary laser scanner data acquired in summer 2009 and 2010 gave similar results with 15–25 cm of subsidence in the central part (rock glacier Rabgiusa) of the target area. It has to be mentioned that the data quality is of less accuracy in 2009 because of the lower number of data points (2.5 million) compared to 2010 (6.5 million). Furthermore, the inclination angle of the position of the laser scanner toward the rock glacier was not optimal. Therefore, results from the laser scanner survey are not discussed in more detail.

5. Results: Val Muragl, Upper Engadin

Based on profound knowledge on permafrost distribution and creep dynamics in Val Muragl (Kneisel, 2010b) this study analyzes data from geoelectrical monitoring sites (since 2004) and from temperature loggers (since 2005) as well as borehole temperature records (since 2006). The focus is on two sites with frozen ground present at depth.

5.1. Geoelectrical monitoring

After the implementation of intensive geoelectrical surveys in different parts of glacier forefield Muragl (see Kneisel, 2010b, for a review and references), two permafrost monitoring sites were equipped with buried electrodes in 2004. One site is located at the lower end of the glacier forefield on a blocky moraine (ERTM-Mgl1, see Fig. 3.5, p. 40) while the second one is on an elevated slope with fine- to medium-grained glacial till at the surface (ERTM-Mgl2).

The active layer at both monitoring sites is especially well resolved by the monitoring line with 1 m electrode spacing. As shown in Fig. 5.1a, the profile ERTM-Mgl2 is completely underlain by permafrost conditions. Maximum resistivity values up to 22 kohm.m are recorded at 5 m depth between 10 and 17 m horizontal distance on July 25, 2006. Until September, resistivity values decrease slightly in that part to about 18 kohm.m. The depth toward the higher resistive subsurface has a wavy pattern along the whole profile. This illustrates a variable active layer thickness between 2 and 5 m. While the active layer is highly variable in lateral direction only little change is registered over time. The time series from 2006 show that resistivity values in the uppermost layer stay well below 5 kohm.m during the two months of observations. No considerable thickening of the low resistive active layer is observed. Most drastic changes with more than 10 % reduction in ground resistivity are registered very locally between 10 and 15 m horizontal distance (Fig. 5.1b) with absolute values of 18 kohm.m still indicative for frozen ground. Over the summer resistivities in the permafrost body lower marginally by about -8 %. Changes close to the surface can only be assessed very carefully. The active layer is influenced

by meteorological conditions prior to and during data acquisition with changing ground coupling of the electrodes. In 2006, a slight resistivity increase (3–15 %) within this zone is recorded.

The profile presented in Fig. 5.2 runs parallel to the one in Fig. 5.1. Both profiles overlap in the upper part (0–35 m) of the slope. Based on the monitoring line with 2 m electrode spacing the resistivity evolution at the end of the thawing period is shown for each year (2004–2010), represented by the latest annual measurement in September. As seen from Fig. 5.2a, the permafrost is separated in two resistive anomalies between horizontal distances 8 and 26 m (upper) and 35 and 47 m (lower), respectively. The wavy pattern of the active layer is resolved in less detail compared to the tomograms obtained from the profile with 1 m electrode spacing. Significant changes in ground resistivity are mainly confined to the lower anomaly. A resistivity increase is observed in 2005 and 2006 before values decrease the following years. Inter-annual variability is large and can be in the order of ±30 % for several model cells especially within the active layer or close to the permafrost table (Fig. 5.2b).

Resistivity changes with reference to the first measurement in 2004 are documented in Fig. 5.2c to give an impression on the multi-annual evolution at this permafrost site. A slight increase can be observed in 2005 and 2006, whereas the following years are characterized by an ongoing lowering of ground resistivity. Almost the entire lower half of the profile is subject to resistivity changes in the order of -40 % in 2010 compared to the conditions in 2004. Only a small patch close to the upper anomaly (10–20 m) displays largely unchanged values (±5 %) compared to the reference year 2004.

This pattern is also illustrated in Fig. 5.3 based on three selected parts of the resistivity tomogram. These parts refer to the upper, higher resistive anomaly (8–26 m), the lower resistive anomaly (35–47 m), and the active layer (10–60 m) as denoted in Fig. 5.3a. The permafrost body is thus separated in an upper and a lower anomaly disconnected by a zone of resistivities of maximal 11 kohm.m. This zone is penetrated by the borehole Mgl2 that registers permafrost conditions below 5 m depth.

In Fig. 5.3b the evolution of specific resistivity values is shown based on all 29 measurements (3–5 data sets each year) conducted with the Wenner-Schlumberger array. Apart from the regular seasonal pattern, slightly different trends are obvious from this analysis of averaged resistivity values for isolated sections of the subsurface. As expected, little
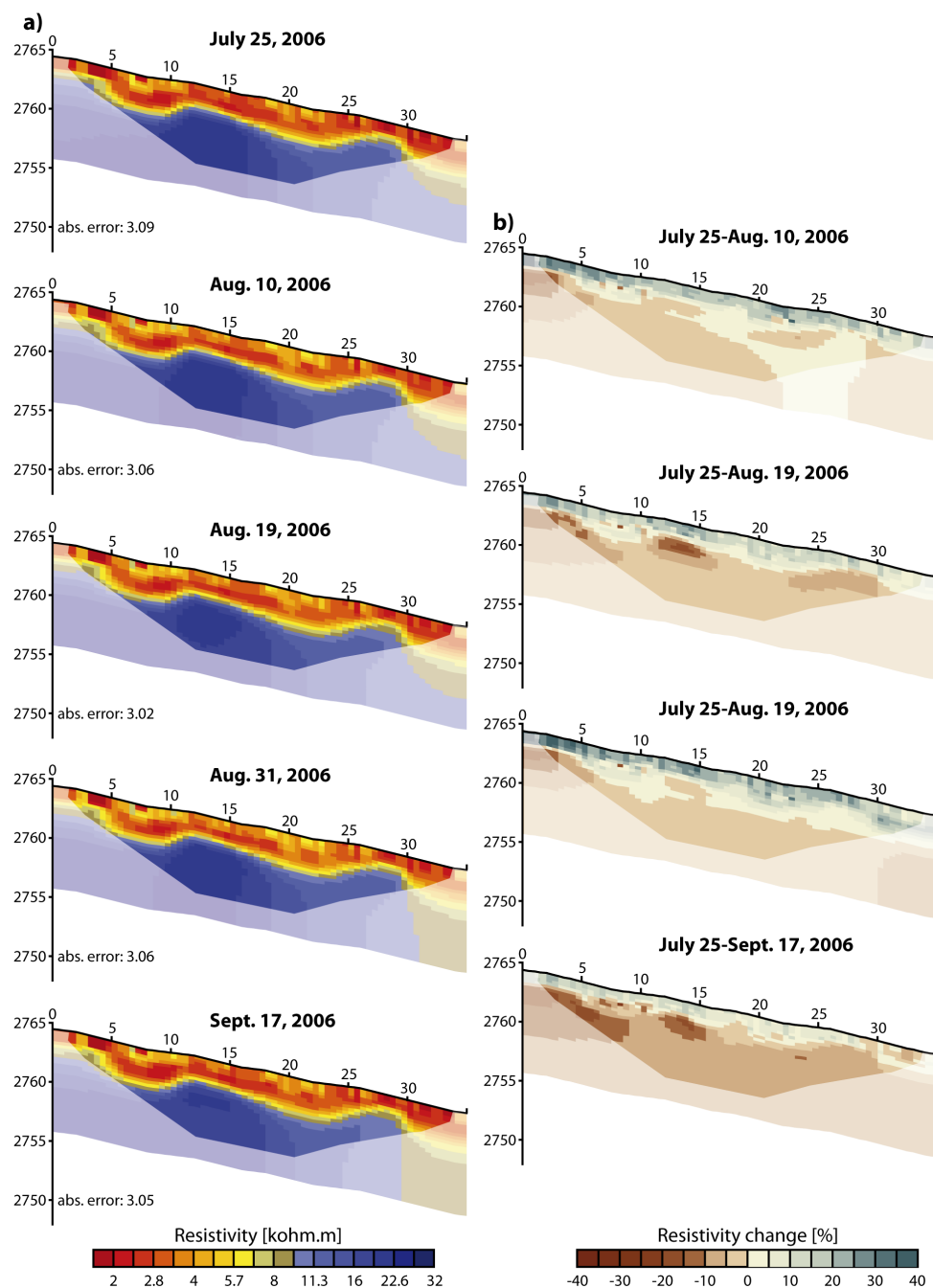
Figure 5.1: Annual evolution of ground resistivity at ERTM-Mgl2 (WenSL, 1 m electrode spacing, 3$^{\text{rd}}$ iteration). (a) Electrical resistivity tomograms between July and September 2006. (b) Time-lapse tomograms with resistivity changes between the July measurement and each consecutive measurement.
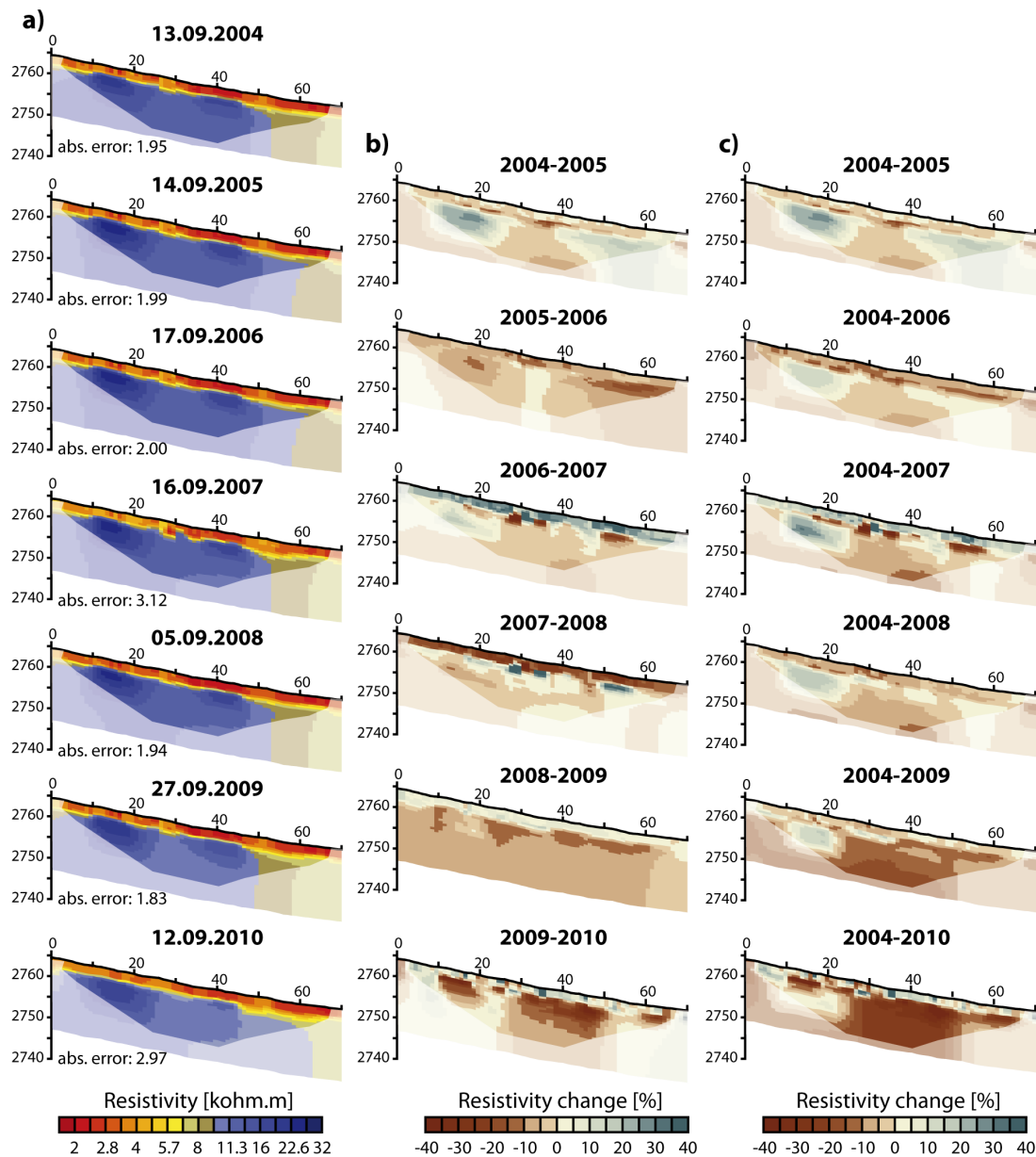
Figure 5.2: (a) ERTs from the end of the thawing period between 2004 and 2010 at the upper monitoring site, ERTM-Mgl2 (WenSL, 2 m electrode spacing, 3rd iteration). (b) Time-lapse tomograms showing resistivity changes between two consecutive years. (c) Time-lapse tomograms showing resistivity changes between 2004 and the following years.
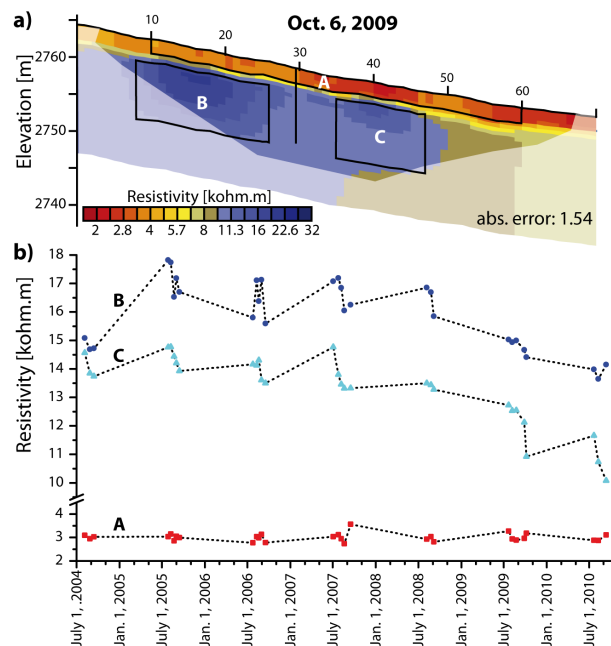
Figure 5.3: (a) Tomogram from the monitoring site ERTM-Mgl2 (October 06, 2009) with marked sections: A=active layer; B=upper permafrost area; C=lower permafrost area. (b) Specific resistivity evolution 2004–2010 plotted for each individual section.

variability is recognized within the active layer (A). A moderate increase in resistivity, e.g., recorded in September 2007 (see also Fig. 5.2b) can most likely be attributed to moisture conditions at the surface. The upper permafrost anomaly (B) rises from about 15 kohm.m on average in 2004 to about 17 kohm.m in 2005. Conditions appear to be stable until 2008, before a decline to about 15 kohm.m in 2009 and 14 kohm.m in 2010 is observed (cf. Fig. 5.2c). Thus, after a slight increase in resistivity the anomaly roughly regains its starting value in 2010. The resistivity increase in the first two years is not observed at the lower permafrost anomaly (C) where the mean values remain more or less at the same level until 2007 (14 kohm.m). Thereafter, the decline is similar to section B and finally an average value of 10 kohm.m in September 2010 is recorded. Permafrost conditions on the lower part of this slope are therefore most probably close to degradation. However, the inter-annual variations may be to a large extent a function of the snow cover conditions at the site because these conditions are responsible for the intensity of the ground cooling in winter. For a detailed discussion of this influence, see chapter 7.

For a comparison of ERTM data and borehole temperatures, ground resistivities were
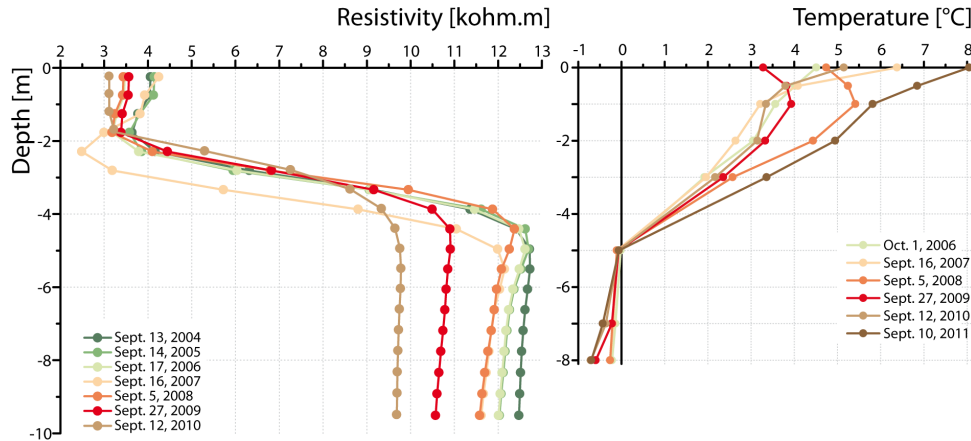
Figure 5.4: Ground resistivities in September 2004–2010 at a virtual borehole location (at 29.5 m horizontal distance of the 2 m monitoring ERTM-Mgl2) and borehole temperature data from the same location (2006–2011).

extracted at a virtual borehole position at 29.5 m, i.e. the location of borehole Mrt2 (cf. Fig. 5.3a). Similar to section C in Fig. 5.3b resistivity values stay relatively constant until 2008 before they drop in the following years with maximum values close to 10 kohm.m. The thickness of the active layer derived from ERT data as indicated by the drastic increase from 4 to >10 kohm.m remains constant at about 4 m. On the right hand side of Fig. 5.4, borehole temperature data from 2006 to 2011 are plotted. The thermal boundary between the active layer and the permafrost table can be set to about 5 m based on the linear interpolation between temperature sensors. Above that depth, the thermal regime is influenced by daily incoming radiation and temperatures in late summer are higher than 2°C in 3 m depth. Within the permafrost body the temperature conditions are inconsistent. Constant temperatures are recorded in the first three years. At the beginning of the year 2009 (cf. Fig. 5.5) temperatures in 8 m depth decrease from -0.22°C steadily to -0.7°C. Since 2010 they remain constant again. Similar in 7 m depth temperatures dropped from -0.15 to -0.42°C in 2009. This cooling trend at the bottom of the borehole is in contradiction to the lowered resistivity values that are recorded especially in 2009 and 2010. A thermal influence of the drilling in 2006, especially at this low porosity, fine- to medium-grained site, cannot be excluded but a period of adjustment until 2009 seems to be rather long. Cooling furthermore occurs in a year when the penetration depth of the cold wave is much less compared to the two previous winters (cf. Fig. 5.8). There might
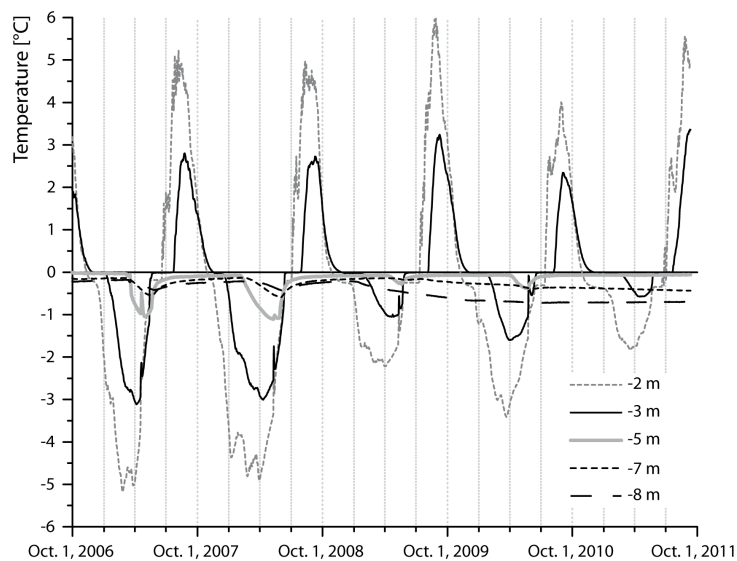
Figure 5.5: Borehole temperatures Mgl2, October 1, 2006–September 10, 2011.

be some degree of latent heat consumption in association with melting of interstitial ice at depth. This phenomenon could explain the simultaneous decrease in resistivity values (more liquid water) and lowering of temperatures (latent heat uptake). However, a drift of the sensors at 7 and 8 m depth caused by leakage cannot be excluded and has to be taken into account in further analyses. Finally, the reasons for this contradiction at the upper monitoring site remain unclear.

Time series of ERT monitoring data from the second monitoring site ERTM-Mgl1 in the lower part of the forefield are presented in Fig. 5.6 and 5.7. The monitoring line with 1 m spacing overlaps the northern half of the profile with 2 m electrode spacing and ranges from 35 to 70 m of the latter. In general, resistivity values close to the surface as well as within the permafrost body are more than one order of magnitude higher compared to ERTM-Mgl2. The high resistivities at the surface are attributed to the dominance of coarse blocks and large air-filled voids in that area, and especially between 30 and 70 m horizontal distance. Resistivities of several 100 kohm.m within the permafrost point to a higher content of ice (see Kneisel and Kääb, 2007) of the ice–air–water–debris mixture.

Results from the 1 m ERTM profile highlight the variability of the active layer thickness in lateral direction (Fig. 5.6a). It is about 2 m thick between 50 and 70 m horizontal distance and increases toward the southern side to about 4 m. Maximum resistivities within the permafrost body are recorded between 50 and 60 m. While its shape remains
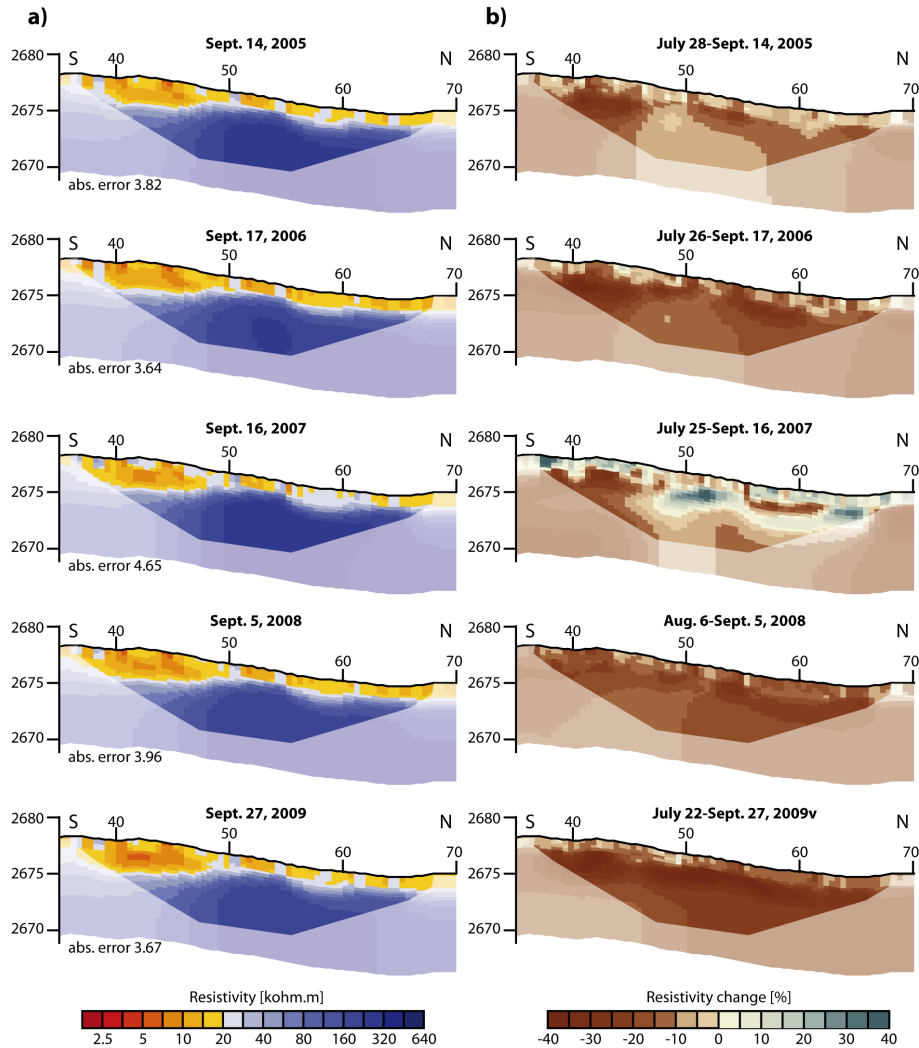
Figure 5.6: (a) Tomograms from profile ERTM-Mgl1 at the end of the thawing period
(WenSL, 1 m electrode spacing, 3rd iteration), (b) corresponding resistivity
changes (2005–2009).

stable, resistivity values in the resistive anomaly vary from year to year. After a slight
drop from 270 to 230 kohm.m between 2005 and 2006 maximum values rise again to about
280 kohm.m in 2007. In 2008 and 2009 maximum values at the end of the thawing periods
are lowered to about 200 kohm.m. These values still represent frozen ground conditions,
but the fluctuation in maximum resistivities highlights the variable amount of unfrozen
water and interstitial pore ice, respectively, in the permafrost itself. The volumetric frac-
tions of the components ice and water change on an annual cycle as a function of thermal
forcing (cold wave penetration, duration and strength of high summer temperatures) and
the infiltration of melt water and rain into the porous system in summer.

During the summer season, resistivity values of the permafrost at the monitoring site ERTM-Mgl1 decrease at a variable rate as shown in Fig. 5.6b. Tomograms refer to the resistivity change between the first (generally in July) and the last measurement (generally in September) at that site. A moderate decrease of mostly 10 % and higher values between 40 and 45 m is recorded in 2005. The resistivity change within the permafrost amounts to about -30 % in 2006, 2008, and 2009. An exception to this pattern is the marked increase in 2007. A rise in resistivity values (in parts >20 %) is observed between 47 and 66 m and at a depth of about 3–6 m, i.e., the upper part of the permafrost. An explanation could be a cold spell between September 4 and September 6 when daily mean air temperatures were as low as -5.3°C at climate station Murtèl. The general resistivity loss over the summer (also recorded in the measurement from August 31, 2007) was reversed by this short period of cold air temperatures. The simultaneous ground cooling was likely associated with freezing of parts of the liquid water present in the uppermost permafrost, thus leading to the resistivity rise in September 2007.

The spatial distribution of the permafrost at ERTM-Mgl1 and its temporal evolution was further explored by the profile with 2 m electrode spacing. This profile extends further south, where permafrost is continuously present in the subsurface, but with considerable lower resistivities (Fig. 5.7). Highest resistivity values are recorded between 50 and 65 m horizontal distance, as also shown in Fig. 5.6, with maximum values slightly higher (200–370 kohm.m) than those from the 1 m monitoring line. The general resistivity distribution and the thickness of the low resistive uppermost layer are well reproduced every year. No considerable thickening or thinning of the active layer is observable on the basis of the inverted tomograms. The resistivity of this unfrozen layer does not change considerably at this coarse-grained site, a situation that was observed at the fine- to medium-grained upper monitoring site (cf. 2007 in Fig. 5.2). In the permafrost body slightly different trends of resistivity evolution are evident. While the southern part of the subsurface (15–25 m) experiences an increase in resistivities, values at the northern part of the monitoring line (45–60 m) show a slight decrease. To analyze this behavior in more detail, two virtual boreholes were set at 20 m and 52 m as indicated in the 2004 tomogram. Vertical sections of subsurface resistivities are shown from the final measurement each year in Fig. 5.7b and c.

At 20 m horizontal distance, a steady increase in resistivity values is recorded between
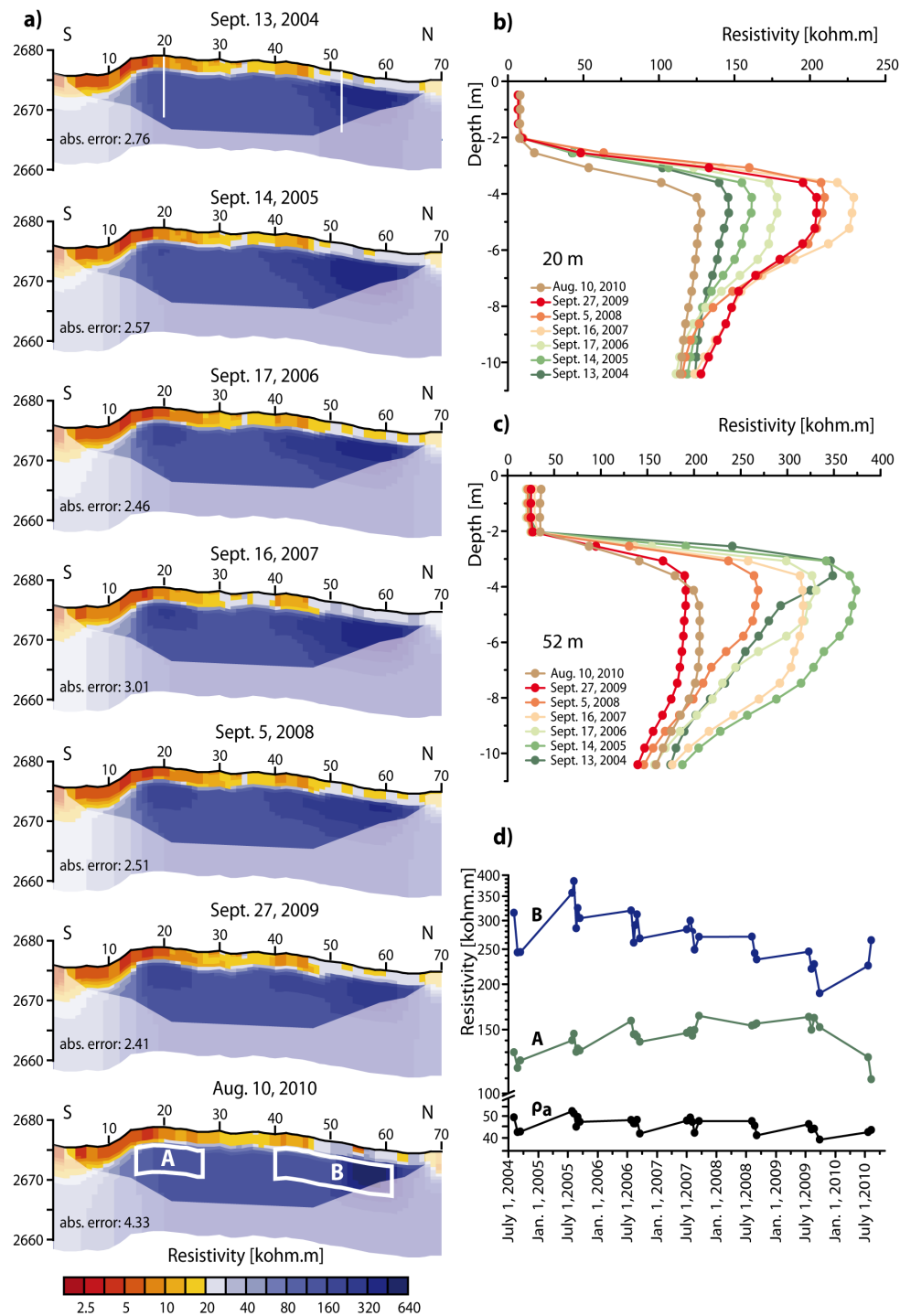
Figure 5.7: (a) Tomograms from ERTM-Mgl1 (WenSL, 2 m electrode spacing, 3rd iteration) between 2004 and 2010. (b) Vertical sections of ground resistivities at horizontal distance 20 m and (c) 52 m. (d) Specific resistivity evolution between 2004 and 2010 for two separate sections (as marked in a) and apparent resistivity values ρ_a.

2004 and 2007 at a depth of 4–6 m. Values stay the same in 2008 and 2009 before they considerably drop by about 75 kohm.m in August 2010 to values below the initial conditions in 2004. Consistent throughout the period under study is the drastic increase in resistivity values between 2 and 3 m depth of about one magnitude with maxima recorded in 4–6 m depth. Even though maximum values varied by about 100 kohm.m no changes in the thickness of the active layer can be derived from the ERT data. The second virtual borehole is set at 52 m horizontal distance. A sharp increase below 2 m depth indicates the thickness of the active layer, which is comparable to the virtual borehole at 20 m. After highest resistivity values are recorded in 2005, a constant decrease is registered until 2009. During that period, maximum values in 4 m depth decrease from 375 to 175 kohm.m. Especially between 2008 and 2009 the lowering of the ground resistivity is substantial. In 2010 a slight increase of maximum values is observed below 4 m depth.

This slightly contrary trend in resistivity evolution during the 6-year record of ERT monitoring data is summarized in Fig. 5.7d. Two parts of the tomogram were selected and averaged specific resistivities of these sections from 27 data sets are shown. In addition, apparent resistivity (ρ_a) data from the measurements (raw data without unambiguously erroneous data points) are shown as mean value. Apparent resistivity data can be used as reference data compared to the specific resistivity values that might be prone to inversion artifacts (Hilbich et al., 2011). The raw data show the expected seasonal variation with constantly decreasing values during the thawing period. As seen in 2007 (Fig. 5.7d), an early onset of winter accompanied by cold air temperatures may shift the time of maximum thawing to an earlier date (e.g., end of August instead mid or end of September as generally true for these alpine monitoring sites). Over the whole period there is no obvious trend whether the permafrost body at ERTM-Mgl1 degradates or aggradates.

Exploiting the full information of the two-dimensional data section as obtained from the ERT profile enables a more detailed analysis of the subsurface. As shown in the 2010 tomogram of Fig. 5.7a, two sections with approximately 300 and 150 kohm.m were selected. Similar to the results from the virtual boreholes in Fig. 5.7b and c, the trends in resistivity evolution are opposed. While section A indicates an increasing trend until 2009 that overlays the typical course over summer months, section B registers a slight increase in 2005 followed by a constant decrease of resistivities until 2009. The last measurement has to be analyzed with care because the 2010 measurements were implemented with a

buried cable that suffered from broken electrode contacts short after installation. Because it contained too many erroneous data points, the final data set from September 2010 is not further analyzed. Still, the trend seems to be reversed in 2010 with decreasing values at section A and a slight increase at section B. With this analysis of separate sections as well as with the virtual boreholes, the spatial variability of subsurface resistivity values in response to extrinsic (climatic) factors is illustrated and highlights the potential of ERT mapping for the decryption of spatio-temporal changes in permafrost conditions.

5.2. Temperature observations

At glacier forefield Muragl, the analysis of the climate–permafrost system and the influence of the substrate cover is based on temperature recordings at the surface and in two boreholes.

5.2.1. Borehole temperature data

Boreholes were drilled in summer 2006 down to a depth of 8 m at two sites where the occurrence of permafrost had been observed in previous studies. Borehole Mgl1 is located at the lower part of the glacier forefield in coarse debris; borehole Mgl2 was installed at the orographic left side in fine- to medium-grained glacial till (cf. Fig. 3.5, p. 40). Both boreholes were equipped with eight temperature sensors. Thermal conditions within the boreholes are documented in Fig. 5.8 (note failure of sensor at 7 m depth in Mgl1 after installation). At the Muragl site, the coldest temperatures are registered annually at the end of May/beginning of June in both boreholes at 8 m depth (Mgl1: -0.4 to -0.7°C and Mgl2: -0.5 to -1.0°C). The plots show that the downward propagation of temperatures is delayed because of the slow conduction of the cold temperature wave below the active layer.

The 5-year data record from Muragl indicates the high fluctuation in penetration depth of cold winter temperatures. In the first two winters, 2006/2007 and 2007/2008, temperatures as cold as -2°C were measured at Mgl1 in almost 4 m depth, while such values did not reach a depth of 1.5 m in the three following years. This pattern can be explained by snow cover data from meteorological station Murtèl (Fig. 4.12, p. 80) and own field obser-
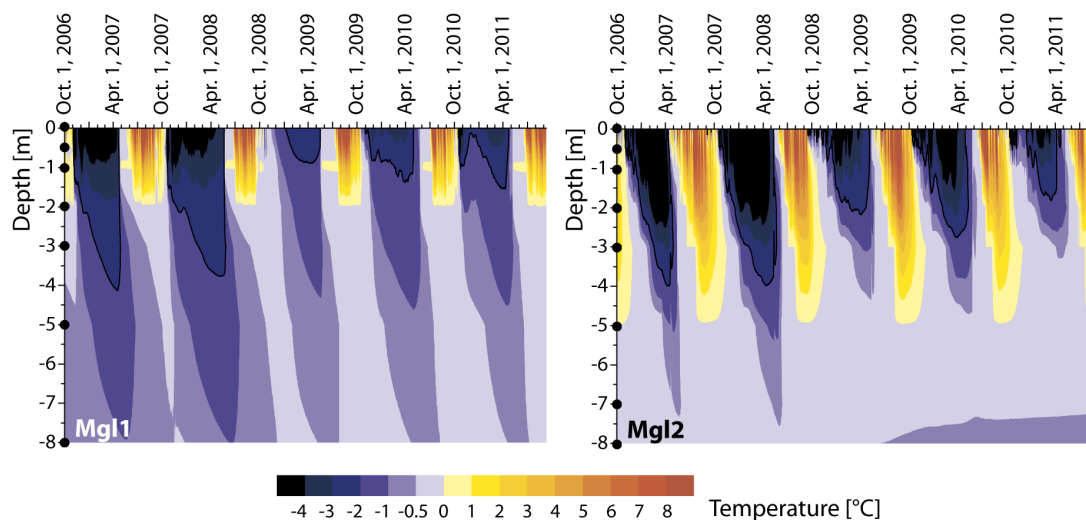
Figure 5.8: Borehole temperatures at glacier forefield Muragl. Position of each sensor is indicated by black dots on the y-axis.

vations that show a shallow snow cover in 2006/2007 and also during most of 2007/2008 (personal communication C. Kneisel). The following two winters are characterized by an insulating snow cover of more than 0.8 m already at the end of November.

Lower temperatures within the uppermost 2–3 m were observed at Mgl2 pointing to a more direct coupling between air temperatures and the ground surface. However, temperatures below a depth of about 5 m are not as cold as observed in Mgl1. In summer, the active layer reaches a depth of almost 5 m at the borehole with fine-grained substrate (Mgl2), whereas the borehole drilled in boulders shows an active layer depth of about 2 m (Mgl1). This is comparable with the active layer depth at the permafrost borehole Mrt1 in glacier forefield Murtèl. Between 2006 and 2011 the active layer depth stays constant with small fluctuations in the range of a few centimeters (Table 5.1).

The depth of zero annual amplitude cannot be derived from the temperature records in Val Muragl since a seasonal signal is still present in 8 m depth (Fig. 4.17, p. 89 and Fig. 5.8). The temperature trends at the bottom of both boreholes are contradicting. At Mgl1 the winter cooling was less pronounced following 2007/2008 and at the same time the amplitude has decreased by about 50 %. Instead, colder temperatures since 2009 and a lack of any annual signal were registered at Mgl2.

The duration of the zero curtain at both boreholes differs by a factor of about 3. While the zero curtain lasts on average 32 days at Mgl1 (24–47 days), its duration is considerably

Table 5.1: Thermal characteristics of the subsurface at boreholes sites Mgl1 and Mgl2.

	Year [01. Oct-31. Sept.]	ALT [m]	ZC [days]	MAGST [°C]	TTOP [°C]	Thermal offset [°C]	DDF	DDT	n_F	n_T
Mgl1	2005/2006	2.00								
	2006/2007	1.96	24	-0.17	-1.25	1.08	928.12	865.95	1.01	1.06
	2007/2008	1.97	26	-1.07	-1.42	0.35	1055.24	664.54	0.77	0.91
	2008/2009	1.98	47	0.56	-0.58	1.13	446.34	651.00	0.30	0.78
	2009/2010	1.98	27	0.07	-0.75	0.83	628.10	655.35	0.36	0.90
	2010/2011	1.98	37	0.13	-0.76	0.89	616.98	655.24	0.40	1.09
	Ø	1.98	32.2	-0.10	-0.95	0.85	734.96	698.42	0.57	0.95
Mgl2	2005/2006	4.99								
	2006/2007	4.93	0	-0.98	-0.22	-0.76	1143.13	786.31	1.25	0.96
	2007/2008	4.93	13	-2.38	-0.34	-2.04	1585.90	715.97	1.16	0.98
	2008/2009	4.96	8	-0.48	-0.10	-0.38	907.29	732.73	0.62	0.88
	2009/2010	4.95	16	-1.41	-0.11	-1.30	1154.01	637.87	0.66	0.88
	2010/2011	4.97	11	-0.00	-0.07	0.07	666.08	659.09	0.43	1.10
	Ø	4.96	9.6	-1.05	-0.17	-0.93	1091.28	706.39	0.82	0.96

ALT = active layer thickness, as interpolated from adjacent temperature sensors; ZC = zero curtain; MAGST = mean annual ground surface temperature; TTOP = temperature at the permafrost table; DDF = freezing degree days; DDT = thawing degree days; n_F = freezing n-factor; n_T = thawing n-factor.

shorter at borehole Mgl2 with 10 days on average. In fact, in winter 2006–2007 no zero curtain period was recorded at the ground surface, which highlights the reduced influence of the snow cover during winter at this more wind-exposed site.

This fact is also obvious if the freezing indices from both borehole sites are considered. At Mgl2 DDF reaches maximum values in winter 2007/2008 with little snow (Fig. 5.8 and Table 5.1). As already mentioned for data from boreholes Murtèl, the range in seasonal indices is much larger for DDF as for DDT because of variable snow cover conditions. At Mgl1 DDF varies between 446 and 1055 while at Mgl2 the range is even larger (666-1586).

MAGST was lower than MAAT in years when n_F-factors reach values above 1. This is true for both sites in 2006/2007 and for borehole site Mgl2 in 2007/2008. Within the following three years the influence of the snow cover is of much more importance. The lower the value for n_F the more the ground surface is decoupled from cold winter air temperatures. During summer time the connectivity between air and ground surface is higher, as expressed by values for n_T close to 1. These results were expected because both investigations sites lack of a considerable vegetation cover.

The temperature at the top of the permafrost corresponds to the year-to-year variability of the MAGST. Of special importance for the thermal condition at the upper boundary of the permafrost bodies is the annual cooling of the subsurface in winter as shown in Fig. 5.9. Here the annual freezing degree-days are plotted against the TTOP. The steeper gradients for both boreholes drilled in coarse-grained substrate (Mgl1 and Mrt1) point to a different heat transfer mechanism compared to borehole Mgl2. Conduction dominates in the finer glacial till at the latter site so that a cold winter with little snow results in a minor deviation of mean annual temperatures in 5 m depth (range of 0.27 K). A thinner active layer of 2 m as well as the influence of convective and advective transport mechanisms in the porous layer at Mgl1 and Mrt1 favors a wider range of TTOP according to the variability of the freezing degree-days at the surface. TTOP values at borehole Mgl1 were observed to range between -0.58 and -1.42°C. Values from Murtèl site are less representative because of the short time series (-0.25 – -0.45°C).
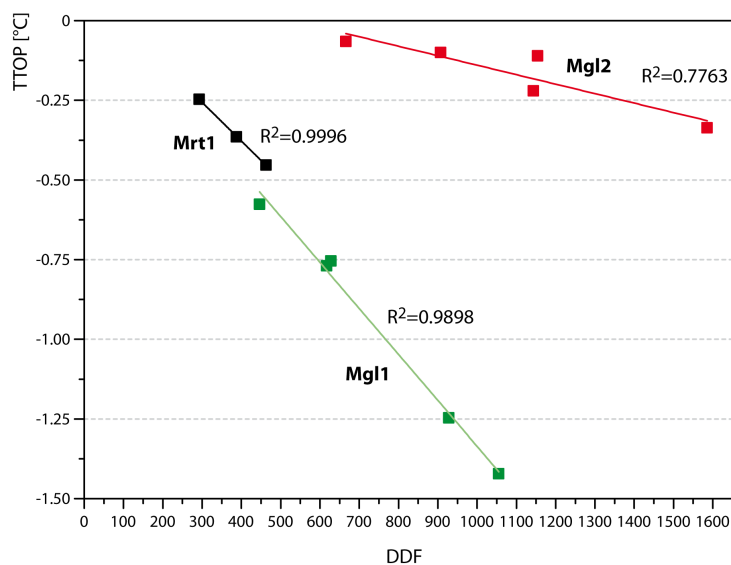
Figure 5.9: Relationship between freezing degree-days and the temperature at the permafrost table at borehole locations Mgl1, Mgl2, and Mrt1. TTOP is registered at 2 m depth for Mgl1 and Mrt1, and at 5 m depth for Mgl2.

These relationships are employed for spatial modeling of temperatures at the permafrost table at other sites in the glacier forefield. Four selected temperature loggers, which were placed on permafrost, based on BTS data and previous investigations (geoelectrics, photogrammetry, see Kneisel, 2010b), were selected to calculate TTOP. The freezing degree-

days are calculated based on the present temperature data record for each hydrological year. The temperature at the permafrost table beneath each of the selected loggers is modeled using the linear relationship shown in Fig. 5.9 with the correlation function from borehole Mgl1 for coarse-grained surfaces and the function from borehole Mgl2 for fine-grained surfaces (Table 5.2).

Loggers ML10 and ML11 are located at the push moraine complex in the north-western part of the glacier forefield. This area is characterized by large blocks and boulders at the surface and a high resistive massive ground ice body underneath (c.f., Kneisel and Kääb, 2007). Modeled TTOP lie between -0.62 and -1.89°C at ML10 and between -0.44 and -1.02°C at ML11. Values depend on the annual ground cooling at the surface that varies by a factor of 2 or more. Logger ML4 was installed between coarse-blocks at the orographic left side of the glacier forefield characterized by large horizontal surface displacements (0.55 m/year). Estimated TTOP are much lower compared to those of the push moraine complex and reach values between -0.08 and -0.50°C. In winter 2008/2009, the mean annual temperature at the permafrost table was close to the melting point, having almost no effect on the ground cooling in winter beneath the active layer. Even higher TTOP are calculated for logger ML3, placed about 100 m NW of ML4 at the orographic left front of the glacier forefield. Surface substrate in that part is composed of fine- to medium-grained glacial till, comparable to the material at borehole Mgl2. Therefore, TTOP is modeled for both functions ($TTOP_{c1}$ for coarse material and $TTOP_{c2}$ for fine material). Results can be regarded as minimum-maximum scenarios. Based on the latter function temperature values are at or slightly above 0°C; this points to thermal conditions that are not favorable for the preservation of permafrost in this part of the glacier forefield.

Reversely, the linear relationship in Fig. 5.9 can also be used to derive threshold values that are necessary for the conservation or aggradation of permafrost. For coarse surface material a freezing degree-day value higher than 73.7 is necessary to reach subfreezing temperatures at the permafrost table. For fine-grained substrate annual freezing degree-day values have to be 530.1 or higher in the long run for permafrost to exist. If the ground cooling at the ground surface in winter does not reach these values — either because of an insulating snow cover, or because of mild winter air temperatures — permafrost starts to thaw from the top. A sequence of several years with low DDF certainly leads to the degradation of permafrost.

Table 5.2: Measured freezing degree-days and calculated temperature at the top of per-
mafrost based on the linear relations as shown in Fig. 5.9.

Year	ML3			ML4		ML10		ML11	
	DDF	$TTOP_{c1}$	$TTOP_{c2}$	DDF	$TTOP_{c1}$	DDF	$TTOP_{c1}$	DDF	$TTOP_{c1}$
2005/2006	545.43	-0.68	-0.005	364.96	-0.42	-	-	-	-
2006/2007	488.71	-0.60	0.01	419.07	-0.50	1067.15	-1.43	692.89	-0.89
2007/2008	480.66	-0.59	0.01	408.73	-0.48	1385.41	-1.89	786.33	-1.02
2008/2009	155.52	-0.11	0.11	127.76	-0.08	502.88	-0.62	381.29	-0.44
2009/2010	-	-	-	205.91	-0.19	1068.33	-1.43	502.11	-0.62
2010/2011	132.89	-0.09	0.12	238.92	-0.24	776.83	-1.01	467.06	-0.57

$TTOP_{c1}$: calculated TTOP based on the function derived from Mgl1 for coarse-grained material.

$TTOP_{c2}$: calculated TTOP based on the function derived from Mgl2 for fine-grained material.

5.2.2. Ground surface temperature data

Analogous to glacier forefield Murtèl, 14 miniature temperature loggers were distributed
in glacier forefield Muragl to investigate the variability of the thermal regime at the ground
surface (Table 4.1, p. 84). The average temperature at the ground surface for the whole
measurement period lies between -1.42°C (ML10) and 1.13°C (ML3). At some dataloggers
the annual variability is even larger: e.g., ML10 recorded -1.94°C in 2005/2006 and 0.88°C
in 2008/2009, which can be in addition to different air temperatures attributed to variable
snow conditions (cf. Fig. 4.12, p. 80). As opposed to this, MAGST lie within a narrow
range of 0.51 K at ML14. The length of the zero curtain in spring varies between 10 and 89
days on average, ranging from years without any isothermal effect of the snow melt (Mgl2
in 2007) to years with a zero curtain duration of 147 days (ML9 in 2009). A prolonged
period of isothermal conditions at the surface until summer inhibits the warming of the
ground in response to higher air temperatures.

The influence of the dominating substrate grain size around the investigated temper-
ature loggers is illustrated in Fig. 5.10. Even though the absolute MAGST varies con-
siderably on an inter-annual basis, as described above, the relative distribution (trend)
remains consistent throughout the investigation period. In warm years (e.g., 2008/2009,
2010/2011) positive MAGST are recorded at almost all settings whereas in 2007/2008 con-
siderably lower MAGST are measured. The surface sensor at borehole Mgl2 represents an
outlier from the general trend toward lower temperatures at locations with coarse-grained
surfaces. As mentioned in subsection 5.2.1, the surface at Mgl2 is more directly linked
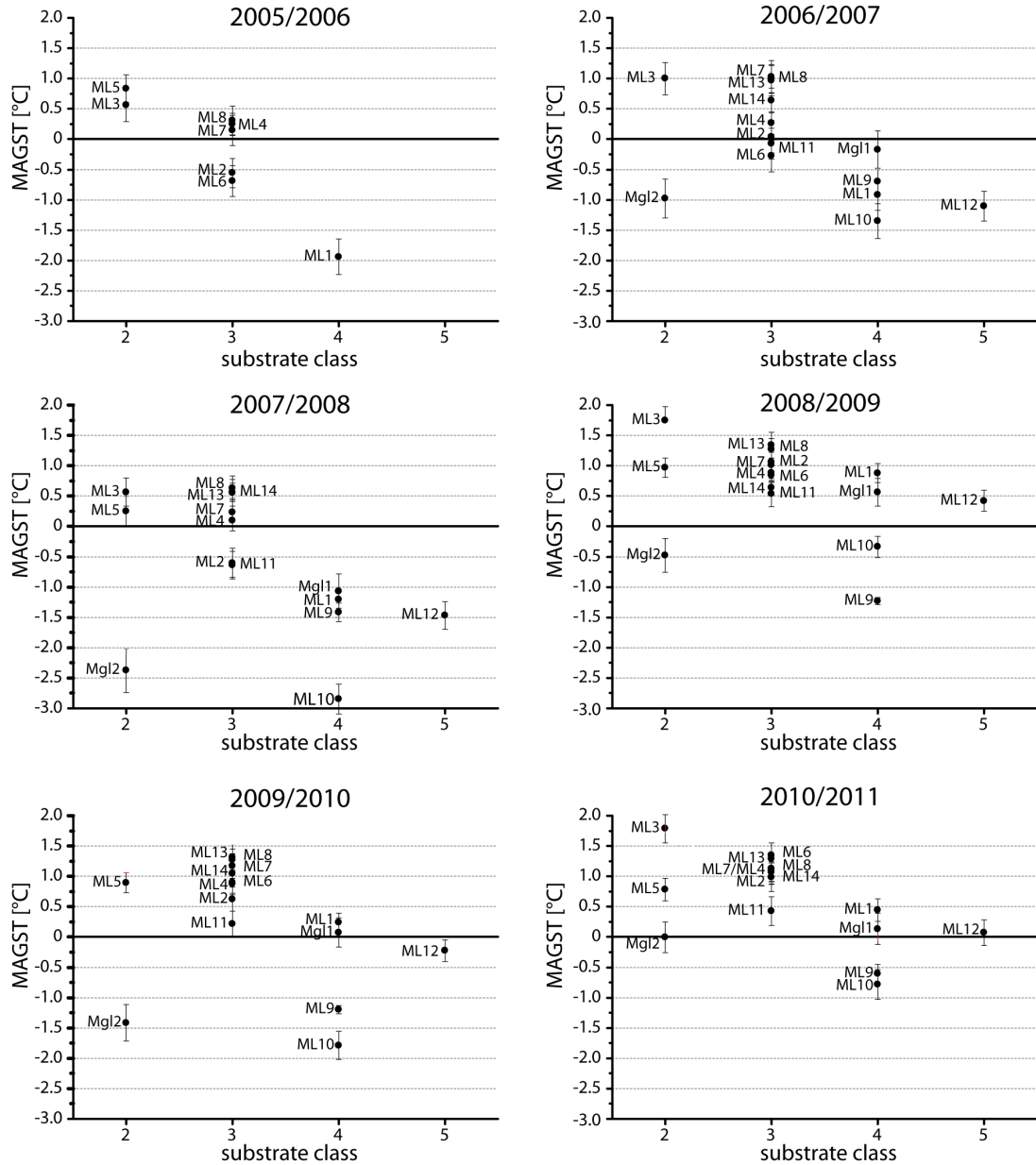
Figure 5.10: MAGST versus substrate class for individual hydrological years (October 1– September 30) at glacier forefield Muragl. Circles represent mean values, bars indicate the standard deviation.

with air temperatures during the entire winter season. The ground surface is subject to a pronounced cooling especially in early winter as well as in years with generally little snow. But in February and March, daily variations in ground surface temperature are still registered at borehole Mgl2 (Fig. 5.11).

In addition to Mgl2, the thermal regimes of ML3 and ML10 that are discussed in terms of their permafrost temperatures below the surface in subsection 5.2.1 are shown in Fig. 5.11. Logger ML3 is positioned at the orographic left side with permafrost probably close to degradation, while at logger ML10 (push moraine complex) massive ground ice is expected underneath. The different scale of the subfreezing temperatures on the y-axis as well as the freezing degree-day values indicate a fundamentally different exposure to cold winter air temperatures. The inter-annual variability in DDF is much larger compared to the thawing degree-days in summer. A 90-day moving average removes the high daily fluctuations and shows the seasonal trend in GST (Fig. 5.11). It accentuates the role of the annual snow cover for the ground cooling at the surface and thus for the upper boundary conditions of the cold wave in winter. Thermal conditions of the permafrost below are highly dependent on this cooling as emphasized as well in Tables 5.1 and 5.2.
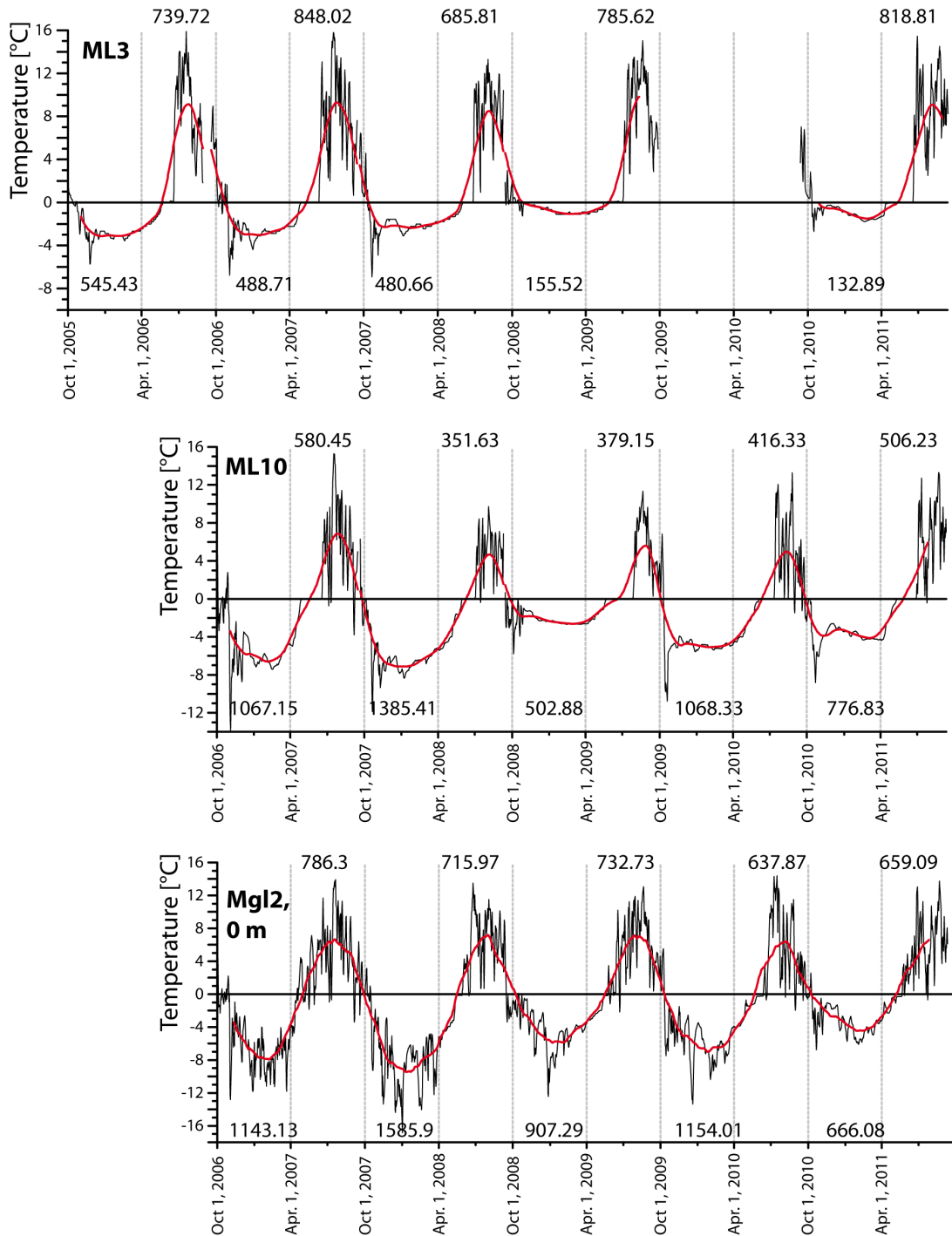
Figure 5.11: Mean daily temperatures for ML3, ML10, and the surface sensor at borehole Mgl2. Values above the line represent DDT, values below the line represent DDF. Red line is a 90-day moving average.

6. Results: Zugspitze, Wetterstein Mountains

Bad weather conditions at the Zugspitzplatt made it impossible to conduct field work in summer 2010 and hence the presented data and results in this chapter are based on the ERT and RST data recorded in late July 2011. In addition to the steep topography and loose scree at the mountainsides, measurement conditions were complicated by numerous snow fall events during the field visit. After snow-free conditions prevailed the days before the field work started, about 20 cm of fresh snow accumulated over night (cf. Fig. 6.1). The snow record of the past 3 years documents that maximum snow heights above 3 m and repeated summer snow fall events are common at the Zugspitze. Nevertheless, six electrical resistivity profiles and three seismic refraction profiles could be measured. Results are presented in Fig. 6.2–6.6.
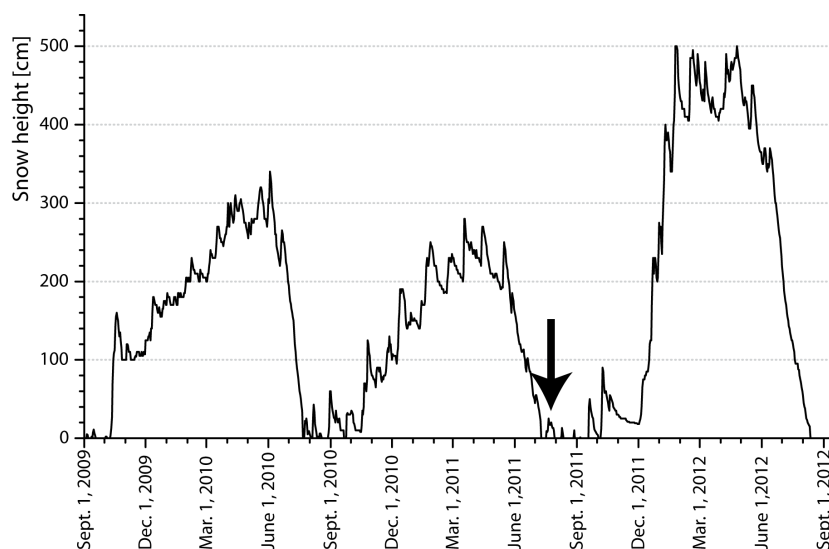
Figure 6.1: Snow height at the climate station Zugspitze (2962 m) between September 1, 2009 and September 1, 2012. Field work time in July 2011 is highlighted by the arrow (data from DWD, 2012).

6.1. Geophysical investigations on the Zugspitzplatt

To analyze the influence of former and present glacier extents on the distribution of potential permafrost occurrences, the geophysical profile lines were placed in the forefield of the present-day Northern Schneeferner. Profiles 1 and 2 were located on a steep talus slope, profiles 3 and 4 (not shown here) on the undulating glacial till, whereas profiles 5 and 6 were measured west of the research station Schneefernerhaus, directed toward the present glacier surface (Fig. 2.5, p. 26).
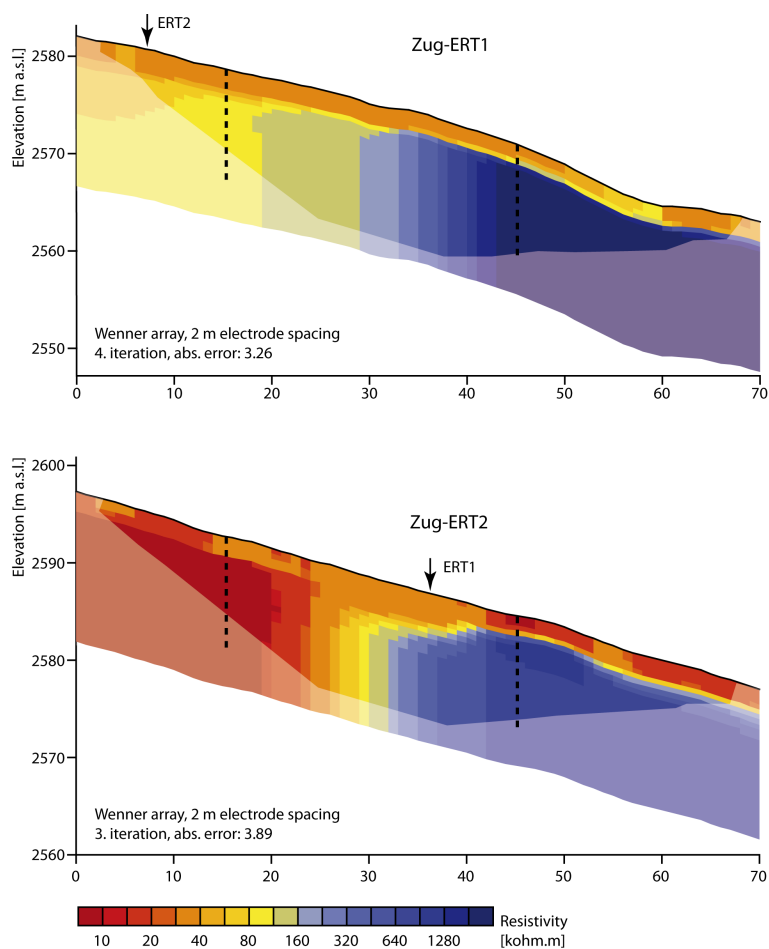
Figure 6.2: Electrical resistivity tomograms from the talus slope beneath the Zugspitze summit. Both profiles intersect at the position of the arrow (cf. Fig. 2.5, p. 26). Dotted lines indicate virtual boreholes.

Results from two profiles (Zug-ERT1 and 2) measured with the Wenner array and located at the talus slope beneath the Zugspitze summit are presented in Fig. 6.2. In general, ground resistivity is remarkable high with values rarely lower than 10 kohm.m.

This is a considerable difference to the results presented in chapters 4 and 5 from the investigation sites Murtèl and Muragl where the active layer generally was characterized by resistivity values lower than 5 kohm.m.

Both profile lines cross each other at about 5 m horizontal distance (in Zug-ERT1) and 35 m (in Zug-ERT2) and thus span a v-shaped area. In each tomogram resistivity values cover a range of more than two orders of magnitude and reach maximum values above 1 Mohm.m. Especially the lower parts of the profiles have distinct high resistive anomalies. These areas are underneath a near-surface zone with values of about 30 kohm.m, representing the dry, unconsolidated scree that was directly observed during field work. The upper parts of the profile lines, although not covered completely with measured data at greater depth, are characterized by a lower resistivity (90 kohm.m in Zug-ERT1 and 7 kohm.m in Zug-ERT2, respectively). Especially in Zug-ERT2 a substantial difference in subsurface resistivity exists between the upper and the lower part of the slope. The area of intersection in both tomograms features a rapid drop in resistivity values in horizontal direction.

For comparison and complimentary information, results from refraction seismic measurements are presented in Fig. 6.3 with the P-wave seismic velocity models of the subsurface. While the first tomogram has a relative consistent velocity increase with depth, there is much more variation in the horizontal direction within the second one. Only at the very lower end, profile Zug-RST1 (50–70 m) has a steeper gradient to velocities >3 km/s at about 4 m depth, a region that is not well covered with ERT data (Fig. 6.2). Profile Zug-RST2 likewise observes the largest gradient in the lower part of the talus. Here P-wave velocities are 3.5 km/s and even higher at about 5 m depth.

An integrated analysis and direct juxtaposition of the geophysical data obtained at the talus slope is done using vertical sections of the inverted specific resistivity as well as the P-wave velocity that were extracted as 1D vertical sections from the tomograms, one from the upper part (15 m) and another one from the lower part (45 m) of the slope. The results, presented in Fig. 6.4, show the vertical course of each of the geophysical parameters with depth. In Fig. 6.4a the most prominent feature is the steep rise in resistivity values over two orders of magnitude between 1 and 3 m depth at the lower end of the profile. There is much lower variation and especially considerable lower maximum values for the specific resistivity section taken at 15 m horizontal distance. These differences are mirrored in the
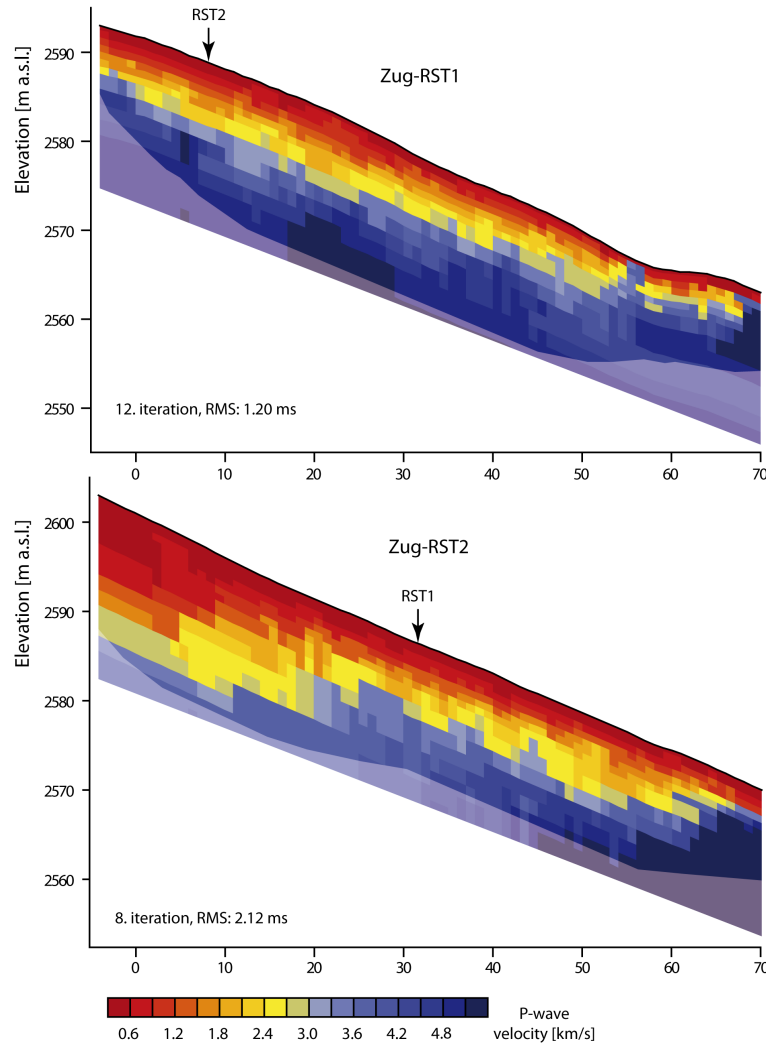
Figure 6.3: Refraction seismic tomograms from the talus slope beneath the Zugspitze summit. Both profiles intersect at the position of the arrow.

seismic velocity data. The gradient at the lower part of the slope (45 m) is larger within the upper 3 m than at the upper slope with seismic velocities in the order of 2 km/s and 1.2 km/s, respectively. A less apparent alignment consists at the second profile (ERT2 and RST2, Fig. 6.4b) where at 45 m horizontal distance the seismic velocity has a less distinct increase within the uppermost part of the 1D section. A considerable increase in velocity occurs between 4 and 5 m depth. The electrical resistivity shows a marked increase between 1 and 3.5 m, whereas at 15 m horizontal distance there is no steep gradient in the vertical profile. While the subsurface resistivity decreases below 2 m depth, the seismic velocity shows the expected gradual increase caused by the compaction of the underlying stratum. The lowermost meters of the specific resistivity sections can only be
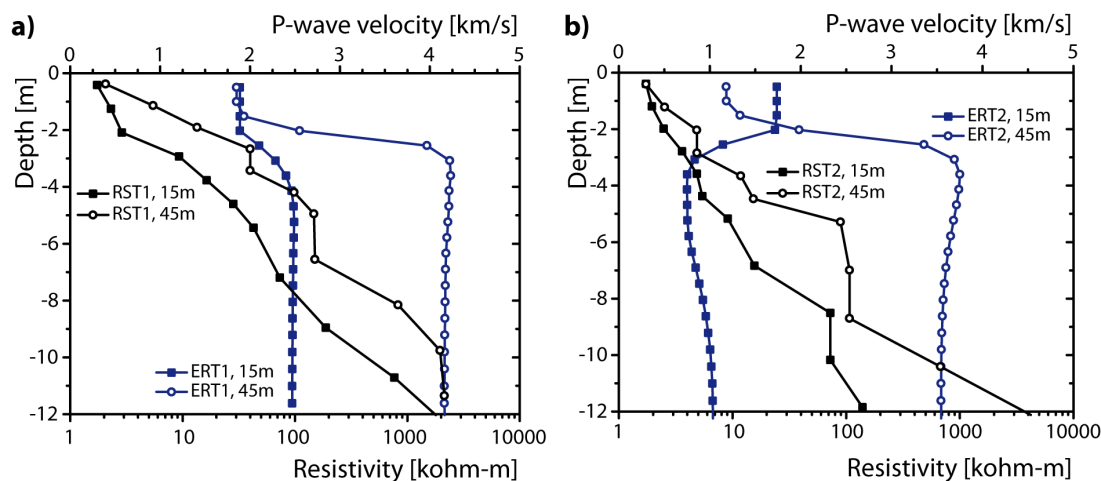
Figure 6.4: Vertical depth sections showing P-wave velocity and electrical resistivity data at the upper (15 m) and the lower (45 m) slope from profiles Zug-ERT1 (a) and Zug-ERT2 (b).

interpreted with care because they are not represented by measured data.

On the hummocky ground moraine of the Northern Schneeferner only one single ERT profile (Dipole-Dipole array) was measured. The insertion of the electrodes was partly difficult because of bedrock outcrops and glacial striated roche moutonnées at or very close to the surface. Only a shallow sediment cover of glacial till was present. At horizontal distance 15 m a few electrodes had to be inserted into crusted snow that led to a high contact resistance in that part. The inverted tomogram (Fig. 6.5) has a marked resistivity contrast between the uppermost 2 m (9–30 kohm.m) and the subsurface beneath (80–440 kohm.m). A prominent structure is obvious between horizontal distances 28 and 38 m, where the lower resistive surface layer reaches down to 5–6 m depth. Here, melt water of the fresh fallen snow flowed together and wet scree was present at the surface. The low resistive subsurface anomaly in the eastern part of the profile is based on a reduction of apparent resistivity values with depth but might be a result of overfitting during the inversion process. At the northeastern end of the profile line resistivity values close to the surface are already considerably high (ca. 50 kohm.m). A rock outcrop immediately next to the ERT profile indicates the presence of bedrock.

Two ERT profiles (Zug-ERT5 and Zug-ERT6) were measured atop of a narrow path leading from the environmental research station toward the present ice surface of the
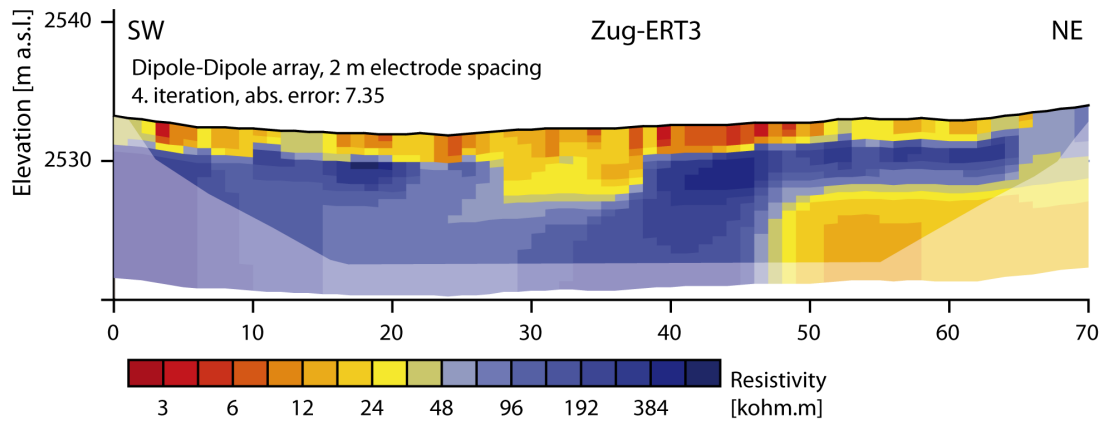
Figure 6.5: Electrical resistivity tomogram Zug-ERT3 measured on glacial till at the Zugspitzplatt.

Northern Schneeferner (Fig. 6.6a). During construction work and grading of this path in 2009, ground ice was observed. Halfway down the way a translational debris slide has occurred leaving a scarp of about 10 m diameter. Geophysical profiles were arranged upside and below the head scarp that was assessed as very steep and unstable with small gravels occasionally slipping off the slope.

Results from the upper transect indicate a rather uniform subsurface resistivity distribution (10–20 kohm.m) in most parts of the subsurface (Fig. 6.6b). A small anomaly appears around horizontal distance 30 m with maximum values of about 60 kohm.m. Toward east resistivity values suddenly rise with a very sharp gradient to maximum values of about 900 kohm.m (0–12 m). The lower transect (Fig. 6.6c) has significant higher resistivity values with most parts of the investigated subsurface in the range of several Mohm.m. These high values can be attributed to an electrical non-conductor very close to the surface. Only the uppermost 1–2 m of the depth section have lower resistivity values between horizontal distance 35 and 70 m. The field site conditions are able to explain this resistivity pattern. Between 0 and 16 m horizontal distance electrodes had to be inserted into ice of glacial origin and upward until 58 m, there was a mixture of ice-coated debris, snow, and ice at the ground surface. Thus, the high subsurface resistivity values can be associated with massive ice beneath a shallow surface layer of debris and scree material. Hidden underneath a layer of fresh snow and some scree the ice of the Northern Schneeferner was detected to extend until the position of the debris slide.

For comparison, the upper transect of the path was surveyed using the refraction seismic

method parallel to profile ERT5. The resulting seismic tomogram is displayed in Fig. 6.6d. While the eastern half of this profile does not show any pronounced anomaly, a prominent refractor is visible toward west at a depth of about 5–10 m. The seismic tomogram indicates a continuous structure between 0 and 35 m horizontal distance, whereas the ERT shows the strongest gradient in subsurface resistivity between 0 and 15 m (Fig. 6.6b). Still, there is a small anomaly at about 32 m in ERT5 that might be connected as single structure to the high resistive anomaly at the lower end as suggested by the seismic tomogram. Seismic velocity values of the refractor are between 3 and 4 km/s as indicative for ground ice (Fig. 6.6d). Since glacier ice could be directly observed along the ERT profile, no RST profile was measured parallel to Zug-ERT6.
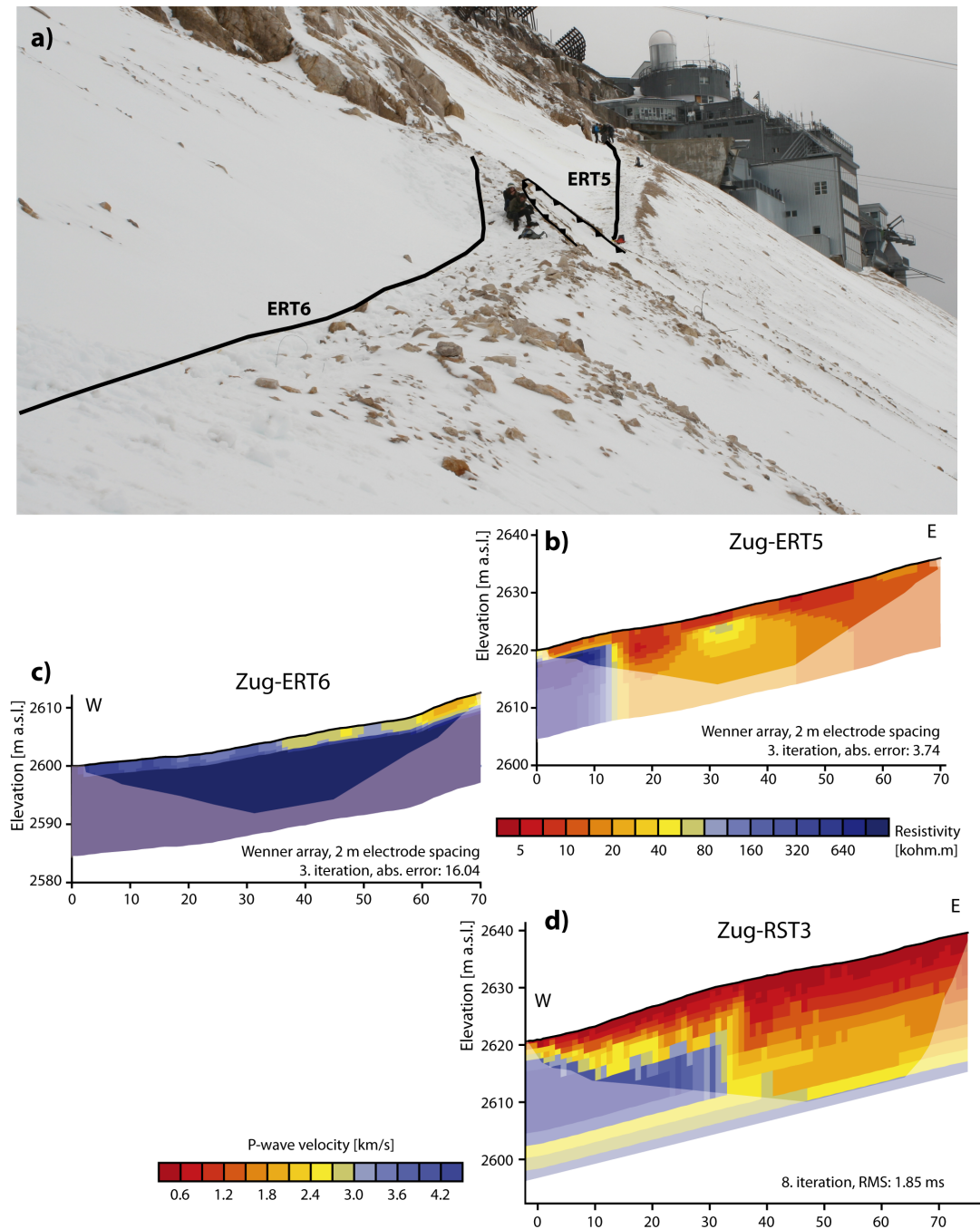
Figure 6.6: (a) View from the Northern Schneeferner toward research station UFS with marks for ERT survey lines and the debris slide between both profiles. (b) Upper section, Zug-ERT5. (c) Lower section, Zug-ERT6. (d) Refraction seismic tomogram measured parallel to Zug-ERT5.

7. Discussion

This study surveyed the occurrence of permafrost in unconsolidated sediments exposed since the end of the LIA with a combination of complementary methods. The investigations covered both, already identified permafrost sites with an existing knowledge on extent and depth and field sites in the forefields of recent niche glaciers that were examined for the first time. To achieve meaningful results and find answers to the research questions addressed in section 1.5 sophisticated methods were applied. Beyond the simple detection of frozen ground a main focus was placed on the observation of spatial and temporal changes in the state of the permafrost (in terms of temperature and relative ice content) as well as on the processes and controls that are responsible for these changes. The discussion is separated in two sections. At first, some methodological aspects that were gained during the implementation of the extensive field work (especially from quasi-3D ERT and ERT monitoring) are reviewed. More general findings of the investigated permafrost systems and implications for the process and system understanding are given afterwards. Possible future developments in consideration of changing environmental conditions are also addressed. Finally, the peculiarities for each of the investigation sites Murtèl, Muragl, and Zugspitzplatt are discussed.

7.1. Methodological aspects of the investigations

Here, some aspects of the detailed geophysical investigations are discussed in terms of the data analysis and the inversion routine. While the quasi-3D mapping yielded information on the spatial distribution of permafrost, temporal changes in the subsurface were observed with different monitoring approaches (multi-annual and diurnal, automatic ERTM). A detailed investigation of different inversion settings suitable for the quasi-3D data set is conducted and discussed in Rödder and Kneisel (2012b) and the aspect of temporal resolving power of manual and automated ERT monitoring systems is analyzed in Kneisel et al. (2014).

A comparison of resistivity inversion results based on the quasi-3D ERT data set at

glacier forefield Murtèl revealed only little variation. The main features are registered with both, the Wenner as well as the Wenner-Schlumberger array. At greater depth, however, the improved data coverage of the Wenner-Schlumberger array gives higher resolution. A comparison of the inversion types, least-squares (L_2-norm) and robust inversion (L_1-norm), revealed the advantages of the latter routine in this environment with mainly sharp resistivity contrasts. Temperature data from the borehole also supported the results obtained by the robust inversion scheme.

The variation of damping factors showed that results derived from the quasi-3D electrical resistivity tomography are reasonable and the extent of the permafrost body is reproduced with each configuration (Fig. 4.3, p. 66). Main differences are found in the range of resistivity values with substantially higher values inside the high resistive anomaly for the low damping parameters. A common interpretation of tomograms with different damping factors provides reasonable model results and helps identify possible artefacts. These findings confirm results from previous studies based on a synthetic model and 2D ERT measurements, conducted on an ice-cored moraine and two rock glaciers, respectively (Hauck et al., 2003).

By using parallel and orthogonal ERT profiles a fundamental improvement in the spatial resolution of the subsurface model is achieved compared to the combination of solely unidirectional profile lines (Fig. 4.2, p. 64). Because the collation of parallel profiles especially accentuates resistivity changes perpendicular to the profile, a combination of profiles in the x- and y-directions is recommended. A line spacing of three-times the electrode spacing gives satisfactory inversion results and is sufficient in areas with resistivity changes of at least one magnitude. Reasonable results have been shown from rock glacier Rabgiusa that creeps into a lateral moraine in glacier forefield Murtèl. For environments with a more heterogeneous resistivity distribution in the range of 1–3 m the grid layout has to be adjusted as described from the inversion of synthetic data by Gharibi and Bentley (2005), who showed the dependence of 3D ERT resolution power on array type, electrode and line spacing as well as relative size, depth, and location of the anomalous bodies. Improvements in grid geometry depending on ground conditions in periglacial environments can also be achieved using a forward modeling approach as recently shown by Schwindt and Kneisel (2011).

With this study it was shown that the quasi-3D technique enables a detailed imaging

of the resistivity distribution in three dimensions. It improves the spatial resolution and the delineation of subsurface structures compared to state-of-the-art 2D ERT that are limited to information gained along one profile or extrapolation between several single profiles. Owing to the time-consuming measurements of a dense grid of ERTs and the restrictions in cable length and electrode coupling with ground, it is challenging to apply this technique in periglacial environments. Its good resolution and promising results as shown in this study, however, demonstrate its value in the detection and 3D delineation of permafrost extent. In particular single landforms of small to medium size can be regarded as objectives and suggest the application of detailed quasi-3D or real 3D surveys. A major advantage of the quasi-3D technique is the larger extent on certain subjects of interest while 3D surveys with one cable are limited to a restricted area (e.g. small-scale areas for infrastructure in mountain permafrost or palsas). The depth of investigation is also more limited for the latter.

For environments with difficult ground coupling the Wenner-Schlumberger array is regarded as most suitable electrode configuration and as a good trade-off between accuracy and acquisition time. The strong resistivity contrast in the subsurface favors the application of the robust inversion scheme and relativizes the influence of the damping factor. Quantitative analysis solely based on ERT results are impossible as shown by the varying resistivity values obtained with different inversion settings or dependent on the setup (electrode spacing, orientation of profiles). Strong resistivity contrasts result in a loss of reliability in high resistive structures (Hilbich et al., 2009). Another source of inaccuracy is related to the imperfect and non-unique tomography resolution (Day-Lewis et al., 2005). Approaches to obtain quantitative results were recently proposed by Hausmann et al. (2007), Krautblatter (2010b), and Hauck et al. (2011). All of these studies make use of a combination of geophysical and thermal information of the ground to derive the fraction of the components of frozen ground (ice, water, rock, air). Presented results show the ongoing progress in the observation and characterization of frozen ground in mountain permafrost, but still this topic remains a major task for future studies.

A good overall agreement was achieved when electrical resistivity and refraction seismic data sets were measured at the same location, as was the case in glacier forefield Murtèl and on the Zugspitzplatt. The very marked increase in ground resistivities at the bound-

ary between the active layer and the permafrost body coincides with a large gradient of the seismic P-wave velocity (e.g., vertical section at 45 m in Fig. 6.4, p. 119). Typical P-wave velocity values for frozen sediments show a large range between 1.5–4 km/s (Table 3.1, p. 30). Concerning the thickness of the active layer, best matches between both methods are achieved, when P-wave velocities of about 1.5–2 km/s are set as lower limit for frozen ground conditions. For the electrical resistivity, a threshold of about 8–10 kohm.m is regarded as reasonable for the investigated environments in Switzerland as seen from a comparison with borehole temperature data (Fig. 4.4, p. 67). Maximum values vary considerably as a function of the availability of unfrozen water and of the ice content in the pore space (cf. Haeberli and Vonder Muehll, 1996). Values in the range of several 100 kohm.m are recorded at the quasi-3D grid and the ERT monitoring profile in forefield Murtèl, while measurements on the debris-covered glacier ice of Vadret dal Murtèl or in the surrounding of the present Northern Schneeferner reach maxima well above 2 Mohm.m. Indeed, the occurrence of pure glacier ice could be validated during field work at the latter sites. At the upper monitoring site in glacier forefield Muragl (ERTM-Mgl2) maximum values within the deep-seated permafrost body are only about 10–18 kohm.m. The formation of massive interstitial ice is prevented because of the limited pore space in the fine- to medium-grained substrate at this site.

A joint interpretation of electrical resistivity, refraction seismic, and temperature data was implemented by three SPCC research projects (SPCC 1, 2, and 3) in autumn 2011. In close collaboration with Christian Hauck, Christin Hilbich, and Sina Schneider (all from University of Fribourg, Switzerland) harmonized data from proximate sites in the Murtèl area were interpreted using uniform software settings. Especially ERT data from different rock glaciers measured in August 2011 could be compared by this approach. Results show that resistivity values of the frozen core vary in the order of more than one magnitude (Fig. 7.1). While rock glaciers Rabgiusa and Chastelets reach values of about 10 kohm.m at 5 m depth, rock glacier Murtèl show maximum values of 300 kohm.m at the same depth. The former rock glaciers could be also analyzed on a seasonal basis. Between August 2010 and September 2011 7 measurements were conducted at rock glacier Chastelets (7.5–25 kohm.m) while 10 data sets are available from rock glacier Rabgiusa (9–35 kohm.m). Variability at rock glacier Murtèl obtained from annual measurements in August (2009–2011) lies between 200–500 kohm.m. At all three sites temperature data

from boreholes could verify the existence of permafrost at a depth below 2–3 m with temperature values close to 0 °C at Chastelets and Rebgiusa and between -1 and -2°C at 10 m depth at rock glacier Murtèl. The latter shows a positive trend in temperatures over the past 20 years of continuous measurements (PERMOS, 2010).
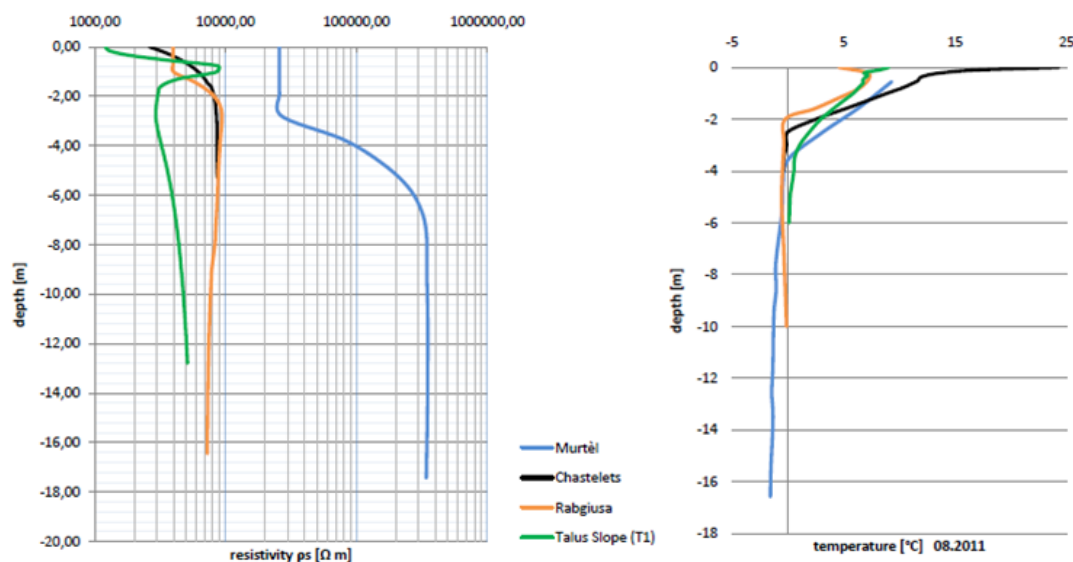
Figure 7.1: Vertical sections of specific resistivity and temperature obtained at four sites at research area Murtèl as presented at the working group Permafrost meeting in Bonn, 01.11.2011. Graphs were prepared by S. Schneider.

Refraction seismic data of all three sites match very well to each other. While rock glacier Chastelets shows values of about 2500 m/s in seismic velocity, the ranges of seismic velocity at rock glacier Rabgiusa (2500–3000 m/s) and rock glacier Murtèl (3000–3500 m/s) are slightly higher. All values underline the existence of a frozen part in the subsurface at all three sites.

Geophysical data from a fourth site, a talus slope with coarse surface material between rock glacier Murtèl and rock glacier Chastelets, were analyzed concurrently (Fig. 7.1). The seasonal variability of ERT data in 2011 lies within 5–7.5 kohm.m, seismic velocity lies between 2000–2500 m/s. These values already point to subsurface conditions that are hardly favourable for permafrost to exist. Temperature data from the talus slope show temperature values of 0°C at the bottom of the 6 m deep borehole. Relatively low values from geophysical data indicate very little ice during summer at that site that shows a seasonal regime of freezing and thawing.

More information and detailed results from these adjacent rock glaciers and talus slopes in the Murtèl area can be found for example in Hilbich et al. (2009), Schneider et al. (2012) or Schneider et al. (2013) and references therein.

Generally different resistivity ranges are recorded at the Zugspitzplatt where the lithology differs from the one found in the Upper Engadin. The Wetterstein mountains are constructed of massive calcareous bedrock of limestone and dolomite. Especially the latter has a comparably high electrical resistivity in an unfrozen state already. Laboratory data of several rock samples from the Zugspitze, tested in a freezing chamber for calibration purposes, give resistivity values at positive temperatures of more than 30 kohm.m. When the slightly depressed freezing point of the water within the saturated specimen was reached (supercooling), values increase at a very steep T–ρ gradient (Krautblatter, 2009, 2010b, see Fig. 7.2). Results obtained from field measurements at the Zugspitzplatt yield comparably high resistivities. At the surface, values for the unconsolidated scree are found to be in the order of 15–35 kohm.m, which is regarded as unfrozen material. The high resistive anomaly below (40–65 m in Fig. 6.2) with values up to 3 Mohm.m exceeds the range of resistivity values as observed in the laboratory and might be attributed to pure ice or an air-filled cavity (see discussion of the field site Zugspitzplatt in section 7.2).

Thus, the recognition of permafrost features in the subsurface depends among other things (thermal state, ice/liquid water content) on the lithology of the investigated site. The combination of ERT and RST (or other geophysical techniques) helps to pinpoint subsurface structures and to find threshold values valid for the individual environment (e.g., lithology). Laboratory measurements give relevant information on the physical parameters of the investigated rocks. Differences between laboratory conditions on single specimen and the situation in the field with unconsolidated sediments have to be considered.

The use of (automated) ERT monitorings enables the observation of changes in the subsurface that occur on different time scales. Annual data from Val Muragl have shown the stability of the active layer over seven years. Although measurements taken at the end of the thawing period did not indicate changes in the thickness of the active layer, resistivity values in the permafrost body do vary. Even along the same profile degrada-
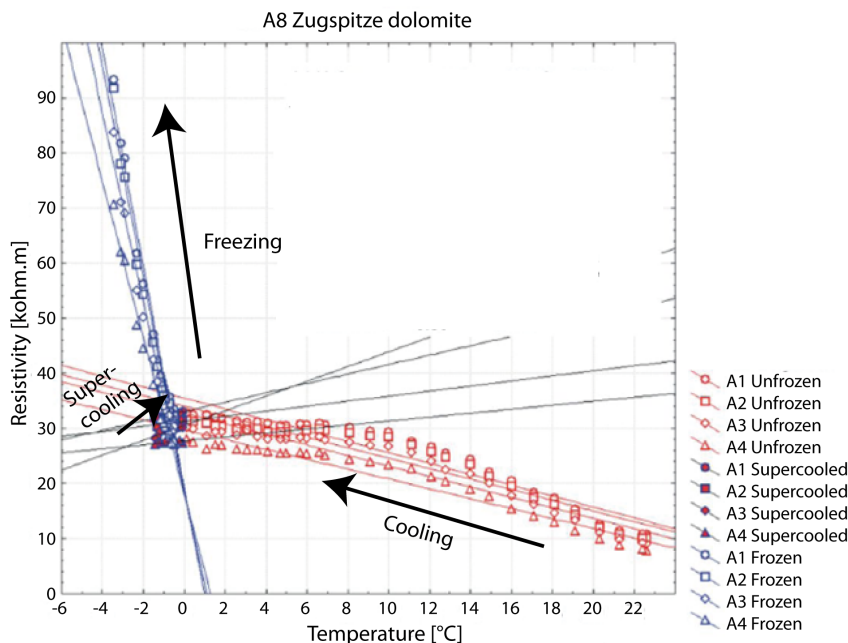
Figure 7.2: P-wave velocity path of Zugspitze dolomite during freezing as obtained from laboratory measurements (modified from Krautblatter, 2009).

tion and aggradation (in terms of positive/negative changes in subsurface resistivity) was observed. Ground coupling of the buried electrodes remained constantly good over the years. However, moisture conditions in response to the actual meteorological conditions have to be considered and limit the interpretability of the uppermost layer in the tomograms. In this regard, multi-annual ERT time series help to filter out years with outliers in the topmost layer.

With the installation of a fixed monitoring setup, the process understanding of melt water fluxes in spring or other short-term events (e.g., cold spells) is increased. Care has to be taken during the construction because of difficulties in the rough alpine terrain and to ensure the persistence of the system. Possible cable defects are easily caused by snow load, avalanches, tumbling stones, and corrosion. Data gaps and discontinuities in the recording of the automated monitoring and problems with the data transfer have shown that improvements have to be done concerning the robustness and stability of the monitoring system. Polarization effects as observed in clayey environments (Peter-Borie et al., 2011) are not expected in the coarse surface layer investigated in this study. In general, the good quality of the recorded data sets (manual and automated) over longer

time spans is to mention. Main problems are related to broken electrode contacts and result in a reduction of data points for the inversion. Thus, the maintenance of the monitoring system has to be ensured to avoid larger data gaps.

The application of these kinds of manual and automatic monitoring setups enables to address permafrost-related problems on different time scales. While annual and seasonal measurements are a valuable source for the observation of trends regarding the state of the permafrost, diurnal data sets resolve short-term changes in the ground resistivity. Hence, processes such as melt water infiltration, ice growth in the transient layer, or the influence of rain in summer can be observed. Both setups have proven their justification in the field and the application of such a monitoring system remains finally a question of the scientific problem to be explored, the field setting, the infrastructure facilities, and the available budget (Kneisel et al., 2014). Technical progress and advances in computational power promote the extended employment of automated monitoring systems especially at field sites where increased geomorphological activity in response to permafrost degradation is to be expected.

7.2. Process understanding of the discontinuous mountain permafrost zone

Trends in permafrost evolution and extent

Results from the ERT monitoring sites at glacier forefields Muragl and Murtèl allow to draw conclusions on the temporal behavior of the investigated permafrost bodies. The 7-year record from Val Muragl constitutes a valuable data set in terms of medium-term permafrost evolution with a seasonal to annual resolution. Information on active layer thickness is especially well resolved with the profile having 1 m electrode spacing. Based on annual measurements in September the active layer does not yet show any signs of a thickening. Instead, resistivity data indicate a remarkable stable thickness of about 3–5 m at ERTM-Mgl2 and 2 m at ERTM-Mgl1 throughout the measurement period (Fig. 5.1, p. 97 and Fig. 5.7, p. 104).

More differentiated is the picture regarding the resistivity development of the permafrost below. Except of a small area between 10 and 20 m (±5 %) resistivity values at ERTM-

Mgl2 have decreased considerably by up to 40 % between 2004 and 2010 (14 to 10 kohm.m, Fig. 5.3, p. 99). Similar signs of permafrost degradation are observed in the northern half of ERTM-Mgl1, although resistivity values are generally much higher at this site (200–350 kohm.m). In contrast, the ERTM data registered a reasonable resistivity increase of about 50 kohm.m between 2004 and 2009 at the southern half of the profile (Fig. 5.7d, p. 104). In 2010, values dropped back to conditions at the beginning of the measurements. These monitoring results show that permafrost aggradation and degradation (in terms of positive/negative changes in subsurface resistivity and thus, changes in liquid/frozen water content) may occur at the same time in the subsurface at a short distance of only about 30 m. This large variability of freezing and thawing processes in close proximity highlights the importance of measurement and analysis strategies that pay attention to a spatial characterization of the subsurface. In this respect, 2D and 3D monitoring approaches are valuable methods for the observation of changes over time and space. Measurements have proven to be robust in this rough terrain and that monitoring systems yield reliable data sets over a number of years.

As seen from the monitoring results, permafrost aggradation and degradation processes occur simultaneously. Such variable response of the ground to atmospheric forcing is verified by the differences in heat exchange processes as deduced from minilogger data (Fig. 4.13, p. 81). Cooling of the active layer may be limited or absent at locations where liquid water is present in fine-grained substrate or where a thick snow cover develops in autumn already (Fig. 4.13b). The former effect can be attributed to the release of latent heat, which acts to delay the penetration of the freezing front that advances from the surface downward and from the base of the active layer upward (Kane et al., 2001) until the liquid water has turned into ice and the cooling of the active layer starts. At sites with large blocks at the surface, the near-surface cooling may last until February when an insulating snow cover has finally accumulated (Fig. 4.13d). Hence, a direct coupling between air and subsurface allows for a distinctive cooling of the ground. As seen from these temperature series, thermal processes that are responsible for ground cooling and the preservation of permafrost in the subsurface differ on a local scale (<50 m) as a function of relief, snow cover evolution, snow height, and substrate.

Within the 3-year record from Murtèl, no temperature trend is obvious at the permafrost site or at the site with seasonal frost (Fig. 4.17, p. 89). In glacier forefield Muragl

(since 2006), the trends in 8 m depth are contradicting. At Mgl1 the winter cooling was less pronounced following 2007/2008, and at the same time the amplitude of the temperature signal decreased by about 50 %. However, lower temperatures since 2009 and a lack of any annual signal were registered at Mgl2. Permafrost conditions at Mgl2 are attributed to the geomorphological situation. The borehole itself was installed at the crest of a shallow ridge with reduced snow cover especially in early winter. As shown by Farbrot et al. (2011), three-dimensional effects in snow cover around the borehole location may lead to a different trend in MAGST and mean ground temperatures at depth. These effects could explain why temperatures at the bottom of the borehole decreased in 2009 while MAGST was lowest already in 2007/2008. However, the relatively short temperature records from both investigation sites do not yet allow the interference of climatically driven long-term trends or predictions for the near future. Instead, the year-to-year changes in the thermal regime at the ground surface and in the uppermost 10 m of the subsurface highlight the large annual variability of the main controlling parameters snow depth and winter air temperatures as a function of specific surface substrate and local relief.

Stability of the active layer

So far, all permafrost sites at Muragl and Murtèl show very stable conditions regarding the active layer depth with about 2 m at the blocky sites and about 5 m at the site with gravel and stones. While low winter temperatures are highly variable, duration and timing of the annual zero curtain seem to have no lasting impact on the thermal regime of the active layer in summer. Schneider et al. (2012) observed constant depths (about 3 m) of the active layer at shallow boreholes in coarse debris around rock glacier Murtèl, while two boreholes at a talus slope and within finer debris were characterized by a higher variability and active layer thickness between 3 and 6 m. An overview of the active layer depth at various boreholes throughout Switzerland is given in the PERMOS report (PERMOS, 2009). A rather stable depth is registered in the last decade for most of the boreholes, especially those with a high ice content. As an exception, the hot summer of 2003 had an immediate impact at the Schilthorn where the unfrozen layer almost doubled in size, attributed to the low ice content in the bedrock at that site. It is obvious that the reaction of the active layer to modified MAGST depends strongly on the ice content at the permafrost table caused by the uptake of energy (latent heat) that is required to

melt the ice. The transient layer acts as a buffer zone that imparts stability to permafrost under climatic fluctuations.

The relative stability of the active layer since 2004 therefore does not confirm the immediate response time of the active layer thickness to atmospheric warming as proposed by Haeberli (1992). Even without an increased thickness of the active layer in summer, ground temperatures in the permafrost body may change on a seasonal and inter-annual basis (Fig. 4.17, p. 89). It is therefore concluded that the thickness of the active layer alone is not indicative for variable hydro-thermal conditions at permafrost environments with an ice-rich transient layer.

The ice-rich layer at the transition between active layer and permafrost
The stability of the active layer suggested by multi-annual ERTM and temperature data as well as the findings on ice growth during the snow melt period in spring as observed by daily ERTM data confirm the concept of an ice-rich transient layer at the boundary between the active layer and the permafrost table as proposed by Shur et al. (2005). Although the total amount of ice in this zone varies throughout the seasons, its existence buffers the permafrost body below from energy fluxes from the ground surface. Hence, the response time of the permafrost system to changed climatic conditions is expected to be delayed because of the latent heat inherent in the transient layer and the recurring annual formation of ice during melt.

The concept of the ice-rich transient layer is supported by maximum values of subsurface resistivity in the uppermost part of the permafrost bodies (see Fig. 4.4, p. 67, Fig. 5.4, p. 100, and Fig. 5.7, p. 104). The reduced resolution of ERT data beneath high resistive structures has to be considered though (Marescot et al., 2003; Hilbich et al., 2009). Borehole stratigraphy information similarly indicates the presence of a supersaturated layer of ice at rock glacier Murtèl and an ice content of 40–70 % with decreasing trend toward depth at rock glacier Muragl (Arenson et al., 2002). A compilation of borehole geophysical data from global rock glacier data confirm an asymptotic decrease in ice content from about 100 % near the permafrost table to 50–70 % several meters below (Burger et al., 1999).

To increase the understanding of thaw-freeze processes in and the melt water influence on this zone, the automated ERT monitoring system is a suitable technique. The vast

amount of data sets generated with this method requires new automated data-processing approaches to filter the raw data for erroneous data points (cf. Hilbich et al., 2011). These computational tools are in the early stages of development. Therefore, the still manageable number of 58 data sets analyzed for this study was quality checked manually. On the basis of these diurnal measurements, the effect of snow melt input on the resistivity distribution in the uppermost part of the subsurface was investigated. The drastic reduction of ground resistivity as response to the impact of melt water at the surface was well resolved. Also, a cold spell lasting for several days during the thawing period had an immediate influence. Air temperature data at that time recorded values down to -8°C (Fig. 4.7, p. 72). While the input of new melt water from the snow cover was halted, resistivity values increased between 2 and 3 m depth. This indicates a depletion of the unfrozen water content and most probably a simultaneous ice accretion in the uppermost part of the permafrost body.

Influences of substrate and snow cover on ground thermal regime

As shown by the examples in Fig. 4.13, p. 81 the microclimate in mountainous environments is highly dependent on surface roughness, shadowing, relief, and snow. Consequently no simple zonation of possible permafrost occurrence according to elevation bands or air temperature proxies is justified if the presence of frozen ground has to be assessed on a local scale. The observed range in MAGST between the four sites in Fig. 4.13 (4.3°C in 2009/2010 and 3.3°C in 2010/2011) is similar to values reported from other studies. In a region with mountain permafrost in southern Norway, MAGST varied by 1.5–3.0°C over distances of 30–100 m (Isaksen et al., 2011). At mountain permafrost site Juvvass (Jotunheimen), MAGST between 1.9 and -2.6°C were obtained along an altitudinal transect (Farbrot et al., 2011). However, the altitudinal difference between sites is more than 500 m and therefore it is much more than the 20-m elevation difference between the loggers presented here. At research site Murtèl, Gubler et al. (2011) recently addressed the heterogeneity of surface characteristics on different scales using almost 400 low-budget miniloggers. The authors showed that within an area of 16 km^2 and a 1200-m altitudinal difference MAGST can vary by more than 9°C. The replication of GST was tested using 10 loggers placed in multiple 10 m × 10 m plots yielding a variability in MAGST between 0.16 and almost 2.5°C, a range that makes a validation or calibration of model results with ground measurements difficult (Gubler et al., 2011).

One of the most crucial factors for the annual evolution of the thermal state of permafrost bodies is regarded to be the winter snow cover. The effect of the snow cover on the ground thermal regime that is already evident from the multi-annual ERTM records is further investigated with the analysis of temperature data available from snow pole, ground surface, and borehole records (cf. Rödder and Kneisel, 2012a).

The borehole data presented in this study substantiate the importance of a critical snow depth and of the date of the first snow fall in autumn as shown in Fig. 4.16 (p. 87) and Fig. 5.8 (p. 107) for cold wave penetration in winter. An example for a reduced snow cover is the winter 2006/2007 when a threshold snow depth of 0.6–0.8 m was rarely exceeded. The lack of a thicker snow cover coincided with a mild winter and a temperature anomaly up to four standard deviations above the mean (Beniston et al., 2011). Even though winter temperatures were above the average in the altitudinal zone considered here (about 2700 m a.s.l.), air temperatures were still low enough for the ground to freeze. Generally, daily mean values between -5 and -20°C are regularly recorded at climate station Murtèl during winter and, hence, a substantial cooling of the subsurface especially in years with little snow is facilitated.

A very similar pattern in ground temperatures was observed in 2007/2008, whilst for the following years a less pronounced cooling was measured. Since 2008 a substantial snow cover of more than 1 m accumulated as early as November. Winter 2008/2009 in particular was characterized by its snow abundance in Switzerland and snow depth exceeded the long-term average in the southeastern Alps during winter months from November to April (Etter et al., 2011). Even though air temperatures were below the long-term average (Beniston et al., 2011), the corresponding ground temperatures at the boreholes in Val Muragl show a considerable reduction of the penetration depth of the cold wave compared to 2006/2007 and 2007/2008. At the lowest sensor in Mgl1 temperatures as low as -1°C were registered in winters with little snow, while a reduced amplitude with lowest temperatures around -0.55°C was observed for the subsequent three snow-rich winters. It is concluded that the snow cover development is the major factor for the ground thermal regime in this alpine environment.

Calculated values for the seasonal scaling factors (n_F/n_T) show a large range for n_F with values between 0.02/0.20 (Mrt2 without permafrost/Mrt1 with permafrost) and 1.25 (Mgl2). At the latter exposed site an average value close to unity points to the good

connectivity between air and ground surface that exists at least in early winter. The large range between sites and the high inter-annual variation at each site underlines the role of the snow cover. At Mgl1, n_F ranges between 1.01 (2006/2007) and 0.30 (2008/2009) for two winters with fundamentally different snow height patterns. In general, values for the thawing n-factor (n_T: between 0.63 at Mrt1 in 2008/2009 and 1.10 at Mgl2 in 2010/2011) have less variability between sites and between years. The lowest values are recorded at Mrt1 where snow can be present until late in July, while air temperatures are already positive. Comparable ranges are reported from discontinuous mountain permafrost sites in Norway (n_F: 0.14–1.04, n_T: 0.96–1.52) (Farbrot et al., 2011) and Iceland (n_F: 0.14–0.99, n_T: 0.87–1.15) (Etzelmüller et al., 2008), which is likewise attributed to variations in snow cover. However, n_F-values close to unity are more frequent because of a generally reduced snow cover and enhanced wind redistribution along slopes compared to the more gentle relief of the glacier forefields investigated here. Large fluctuations of surface temperatures indicate a good correlation between air and ground at exposed sites in subarctic mountain environments (see Fig. 3 in Kneisel, 2010a). From the comparison with these studies it is assumed that the snow cover is also an important factor for the heterogeneous response of permafrost to climatic signals in other alpine environments.

A potential parametrization of the scaling factors necessitates a continuation of ground temperature measurements at sites with different surface characteristics as well as additional on-site air temperature recordings for an increased understanding of the correlation between n-factors and snow depth. Scaling factors are regarded as a promising approach for ground temperature modeling in regions where only air temperature data are available.

Beside the snow cover, the substrate that dominates at the surface around the logger position influences the ground thermal regime with a trend toward lower MAGST for temperature loggers placed between blocks and boulders (Fig. 4.14, p. 85 and Fig. 5.10, p. 112). However, the absolute values of MAGST may vary considerably from year to year: e.g., 2.8°C at ML1 and 2.5°C at ML10. A higher variability exists at sites with larger debris, while the ranges in substrate classes 2 and 3 are somewhat smaller. This suggests that the strength of the ground cooling at blocky surfaces varies significantly depending on snow conditions. In general, the well-known negative thermal anomaly for openwork block fields (e.g., Harris and Pedersen, 1998; Juliussen and Humlum, 2008) is confirmed. The results highlight the small-scale variation in ground temperatures within a

larger geomorphological unit (glacier forefield) with various substrates, as opposed to the above-mentioned studies that were conducted exclusively in coarse-grained block fields or talus slopes. The coarse debris layer hinders the development of a closed snow cover in early winter, allows the internal circulation of cold air (convection/advection), and traps cold air masses between the large blocks during summer. This trend is less pronounced at Murtèl with one outlier in each of the classes 4 and 5. Borehole Mgl2 shows permafrost conditions below a depth of 5 m even though it is drilled in finer morainic till. The presence of permafrost at that site is possible because of the strong cooling of the ground surface in winter. The observed thermal offsets make it more difficult to predict the occurrence of permafrost solely based on MAGST. The locations at boreholes Mgl1 and Mrt1 have permafrost conditions, although MAGST can be above 0°C. In contrast, a negative thermal offset is able to preclude permafrost at sites with rather low MAGST. Burn and Smith (1988) gave values for the thermal offset in permafrost terrain of the Yukon Territory (USA) between 0.4 and 1.7°C, which they attributed to varying soil moisture contents. At the presented investigation sites, the thermal offset varies, beside different soil thermal properties, as a function of the winter cooling at the ground surface. It may even change sign at the same location as a function of snow height (an example is borehole Mgl2: -2.04°C in 2007/2008 and 0.07°C in 2010/2011).

A conceptual model of the active layer processes in coarse debris

A synthesis of the results from automated ERTM measurements as well as from temperature data at the ground surface and the borehole next to the monitoring system is developed in the form of a conceptual model of hydro-thermal processes in coarse debris (Fig. 7.3). Positive temperatures are recorded at and below the ground surface until the end of the thawing period (A). With the first cold surges in autumn and air temperatures as cold as -10°C the active layer starts to supercool (B). A lack of snow enables cold air to penetrate through the coarse substrate whereas the presence of a shallow snow cover actually favors the cooling of the surface (Keller and Tamás, 2003) because of the high emissivity of the snow (Zhang, 2005). Measured ground resistivities steadily increase during winter until maximum values are reached in February/March. After a sufficient snow cover of at least 60–80 cm has accumulated (e.g., Keller, 1994; Luetschg et al., 2008, for a discussion on the required snow depth for ground insulation), the coarse surface layer

is basically decoupled from cold air temperatures that regularly drop to -15 or -20°C in the Engadin (C). Energy transfer might be possible along funnels or large boulders that stick out of the snow cover (Bernhard et al., 1998), although during field visits in February, a smooth and gentle snow cover caused by wind-induced redistribution of the snow was found in most parts of the investigation areas (Fig. 3.4c, p. 39). Thus, only internal circulation and lateral heat transfer in the supercooled coarse substrate is to be expected beyond the restricted effect of thermal conduction (C). Because of the large voids that are mainly filled with air the moisture/ice content in this layer is estimated to be rather low. Thin layers of ice were observed during winter field work on top of some of the supercooled boulders.

In spring, the first temperature rise above 0°C induces the thick snow cover to melt from the top. Melt water percolates and eventually refreezes within the snow pack under release of latent heat. After the snow cover has gained isothermal conditions (Fig. 4.6c, p. 70) the melt water reaches the ground surface as highlighted by the beginning of the zero curtain period. The water infiltrates into the still frozen active layer and refreezes at the surface of the supercooled rocks. At the permafrost table ice aggregates whereas some melt water is expected to percolate into the permafrost (D). Because of the coarse granular matrix, the permafrost body is not regarded as well-defined aquiclude over the entire area even though the substrate gets finer with increasing depth. These conclusions are based on diurnal ERTM measurements (Fig. 4.7, p. 72) that show a rapid reaction of the resistivity values in the active layer and to an attenuated degree in the permafrost below after the snow melt has started in spring. Cold spells during that time are able to interrupt the snow melt. The effect of ice growth at the permafrost table could be observed (Fig. 4.6b, p. 70). After 1 to 2 weeks of snow melt active layer resistivity reaches values that are comparable with those registered at the end of the thawing period in September. Still, it takes more than a month for the snow cover to melt completely, which is obvious from the duration of the zero curtain period until late June (Fig. 4.7, p. 72).

Similar effects were studied by Scherler et al. (2010), who observed the infiltration of melt water by borehole temperature measurements and modeled the changes in ice and liquid water content during freezing in a fine-grained surface layer at the Schilthorn. Results could be verified using ERT data, however, no ERT data were available from the

critical thawing phase. The infiltration is described as oscillating process because of the presence of an impermeable frozen surface layer. Such an ice-rich layer immediately at the surface is not present at the coarse-grained site at rock glacier Rabgiusa so that the melt water can infiltrate into the frozen active layer without restrictions.
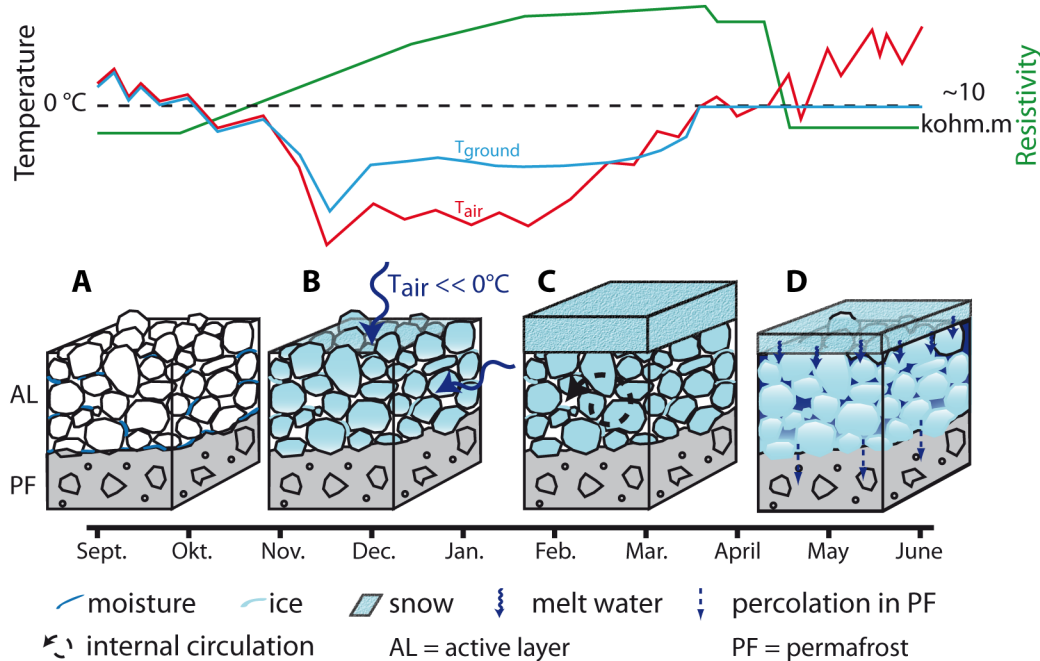
Figure 7.3: Schematic model of hydro-thermal processes at coarse-grained permafrost sites between autumn and the end of the thawing period. The sketch is based on diurnal ERTM data, GST, and borehole temperature data.

Consequences of future environmental changes

Several studies investigated the impact of climate warming on the snow cover in Switzerland. So far, a decrease in the number of snow days in winter is mainly observed at stations below 1300 m a.s.l. (Scherrer et al., 2004). Here, a temperature shift above the 0°C threshold can be recognized associated with a shift in the precipitation regime from snow to rain. Statistical analyses showed that alpine stations at about 1800 m were also affected by a step-like decrease of snow days at the end of the 1980s (Marty, 2008), but without a clear trend after this shift. Possible effects caused by a shift in the snow regime would have contrasting consequences. A general reduction in snow cover or a time delay in the date until an insulating snow cover accumulates could lead to an enhanced cold

wave penetration in the near surface and may be beneficial for permafrost occurrences in the discontinuous permafrost zone as long as low air temperatures prevail, on the one hand. Low temperatures at night caused by the high outgoing long-wave radiation in autumn and early winter are typical for the Engadin valley. If the warming of air temperatures coincides with an increased amount of precipitation (still as snow) in winter, on the other hand, the ground will experience a lack of substantial cooling with unfavorable consequences for the permafrost areas. Until now, the inter-annual variability of snow cover evolution is too high to determine a significant trend from the borehole temperature records investigated in this study.

The response of the ground thermal regime to modified climatic conditions was modeled by research project SPCC1 (Fig. 1.4, p. 13 and Scherler et al., 2013) using the one-dimensional COUP model (Jansson and Karlberg, 2001). This coupled heat and mass transfer model of the soil–snow–atmosphere boundary layer is able to simulate long-term ground temperatures based on an upper (calculated energy balance from global and regional climate model data) and a lower (geothermal heat flux) thermal boundary condition.

Climate change scenario data from the EU FP7 ENSEMBLES project are used to drive the subsurface model in order to simulate its impact on permafrost in the 21st century. For this study, the model is driven with Regional Climate Model data from the Danish Meteorological Institute (DMI) and the Max-Planck-Institute for Meteorology (MPI) and validated with temperature data from borehole Mrt1 (Fig. 7.4, Table 7.1). Details on the model structure and calibration techniques can be found in Scherler et al. (2013).

As shown in Fig. 7.4 the stability of the active layer thickness seems to persist for a while before it increases quickly. These two phases of reaction are characterized by a slow warming trend in the first phase and rapid permafrost degradation by gradually increasing active layer thickness in a second phase. The subsurface model forced with the DMI data set shows stable active layer conditions until about 2050. The reaction is much faster (at latest by 2025) if the MPI data are used as input. Little differences are visible comparing the two model runs from the same RCM but with different initial thermal conditions (Table 7.1) of the permafrost. Model runs DMI1 and MPI1 refer to the situation at the edge of the permafrost body at rock glacier Rabgiusa (borehole Mrt1) while DMI2 and MPI2 are more likely to represent initial thermal conditions in its center

beneath the ERT monitoring. For the latter cases permafrost is expected to degrade in 10 m depth about 5–10 years later (Fig. 7.4).

Sensitivity analyses of eight potentially influencing variables have shown that the ice content prior to thawing is statistically most significant (Scherler et al., 2013). This finding is in agreement with the importance of ice growth in spring as found in this study. When refreezing of melt water is not sufficient anymore to sustain the ice-rich transient layer, the thickness of the active layer increases at a rapid rate and finally leads to the disintegration of permafrost. Uncertainties in the results are associated with the lack of 2D or 3D heat and mass exchange processes (e.g., advection) in the model structure. The simulations presented here should therefore be regarded as a sensitivity study of the impact of climate change scenarios rather than a precise prediction of permafrost thaw.
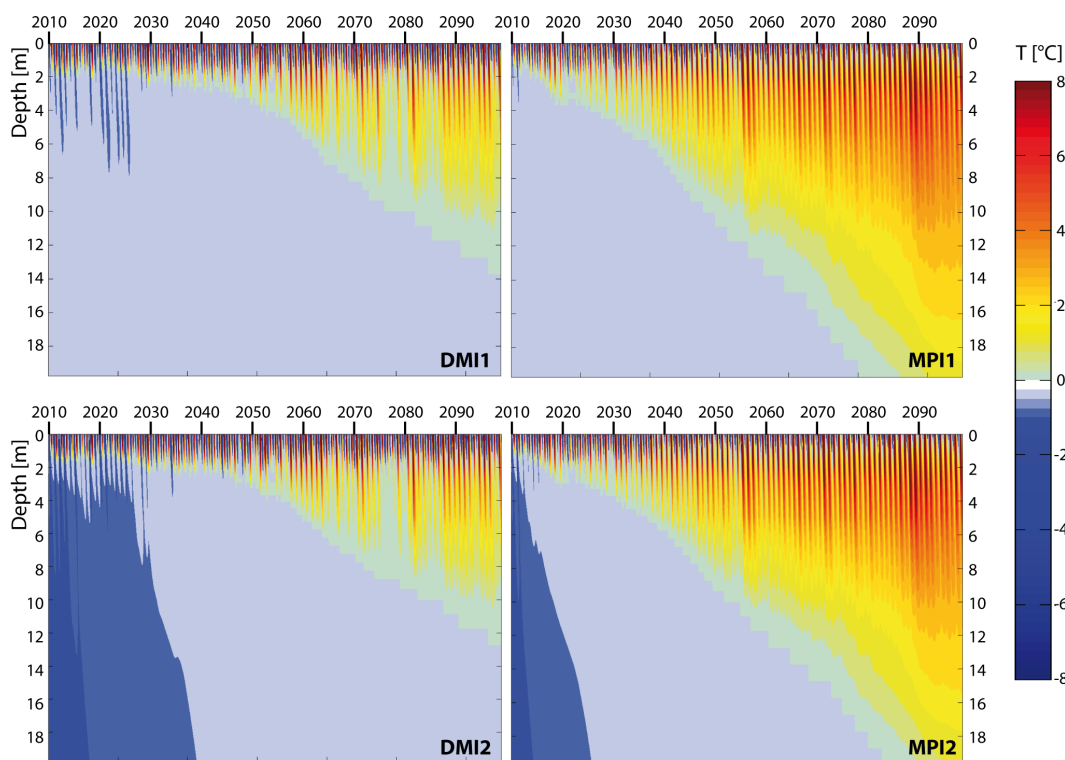
Figure 7.4: Projections of ground temperature evolution 2010–2100 at rock glacier Rabgiusa based on two RCMs and two different initial thermal conditions.

Associated with the degradation of permafrost is an anticipated increase in mass wasting processes. The potential of discontinuous permafrost zone as sediment supply largely depends on ice content and ground temperatures of the subsurface. Temperatures within the observed permafrost bodies are above -1°C and thus they can be classified as warm

Table 7.1: Input data for future permafrost simulations in Fig. 7.4.

Model run	GCM	RCM	T in 2 m/20 m[°C]	ice content [%]	porosity [%]
DMI1	ARPEGE	HIRHAM	-0.12 / -0.05	40	50
DMI2	ARPEGE	HIRHAM	-1 / -1	40	50
MPI1	ECHAM5-r3	REMO	-0.12 / -0.05	40	50
MPI2	ECHAM5-r3	REMO	-1 / -1	40	50

permafrost. Qi and Zhang (2008) showed for ice-rich soil that between -0.5 and -1°C mechanical properties (such as strain rate or compressive coefficient) of the ice–soil–water mixture change greatly if this temperature threshold is exceeded. Together with higher unfrozen water content the change in mechanical properties make the discontinuous mountain permafrost a highly temperature-sensitive environment. Further, permafrost areas are able to act as sediment magazines over longer time periods until they are mobilized during degradation (Etzelmüller et al., 2003). Changed mechanical properties and sediment storage capacity make degrading permafrost areas favorable for mass movements and act as a starting zone of debris flows and other kinds of gravitational sediment transport. The general disposition of the catchment is increased when more unconsolidated sediment is available for downslope transport (Zimmermann and Haeberli, 1992; Zimmermann et al., 1997). Beside the sediment availability, water input and slope gradient are crucial parameters and all of those have to be present in a critical combination for debris flows to occur (Rickenmann and Zimmermann, 1993).

Thus, the thawing of permafrost alone is not sufficient to increase the frequency of events when at the same time triggering factors such as precipitation or snow melt pattern change. Analyses of meteorological data and tree-ring records from historical times of the Ritigraben catchment (Valais, Swiss Alps) indicate a shift of debris flow events to occur later in the season (August/September) with long-lasting advective rainstorms as major trigger (Stoffel and Beniston, 2006; Stoffel et al., 2011). Sattler et al. (2011) recently argued that for the head area of the Schnalstal (South Tyrolean Alps) permafrost degradation is not necessarily associated with debris flow activity in permafrost environments. However, detailed field analyses are required if source areas for debris flows are located in the periglacial zone as the presence of permafrost is often restricted to small patches as shown in this study. Future projections favor an increase in magnitude of debris flows (Stoffel et al., 2011; Stoffel and Huggel, 2012) caused by (i) less frequent, but more intense

precipitation events, (ii) increased sediment accumulation in present channels, and (iii) the destabilization of permafrost bodies and the associated increase in material supply. On a longer perspective the complete wasting of permafrost could, in contrast, lead to a reduced disposition in debris flow source areas because of settling of the ground and ecological succession.

7.2.1. Glacier forefield Murtèl

Numerous geophysical mappings in the glacier forefield Murtèl restricted the presence of permafrost to an area at the western lateral moraine. Here, the small rock glacier Rabgiusa that is part from a larger rock glacier complex creeps into the lateral moraine at a rate of about 20 cm/year.

The upper part of the glacier forefield around borehole Mrt2 was still ice-covered in 1937 as documented in the geological atlas of Switzerland (Spillmann and Trommsdorff, 2007b, 1:25000). Even if the glacier was polythermal at that time, no permafrost has outlasted since then or could aggrade in the exposed debris after glaciation. The recession of the glacier has occurred relatively fast in the last century so that no favorable conditions prevailed for permafrost to develop under the margin of the ice. Likely, the lateral moraines do not contain any debris-covered ice or ice-core. Only at the steep uppermost part of the forefield debris-covered ice is present. Pure glacier ice was penetrated during borehole drilling and temperatures of about -1.5°C are registered in 8 m depth (Fig. 4.18, p. 90).

As obvious from BTS (information limited to the point of measurement) and geophysical data, permafrost extends further southwest from the investigated rock glacier. Here, coarse boulders dominate at the surface and construct a massive crest running toward the mountain ridge Furtschellas, which confines the Murtèl/Corvatsch area (Fig. 2.2, p. 19). The genesis of the frozen ground is expected to has proceeded according to the sketch in Fig. 7.5B. The deep cirque that is still present in front of the rock face might have been ice and snow filled for a considerable time following the LIA maximum ice extent. Rock fall and glacial thrusting have led to the build up of a moraine ridge/protalus rampart of frozen sediments that subsequently evolved in a rock glacier–moraine complex. One branch of this complex turned toward the glacier forefield. Here, it deformed the local

lateral moraine of Vadret dal Murtèl caused by applied push from the creeping rock glacier. Rough estimates when deformation of the lateral moraine has started can be done. The displacement of the lateral moraine sums up to about 15 m, while the actual creep rate of the rock glacier is 15–25 cm per year. These data reveal a minimum–maximum scenario of 60 to 100 years since both landforms have joined.
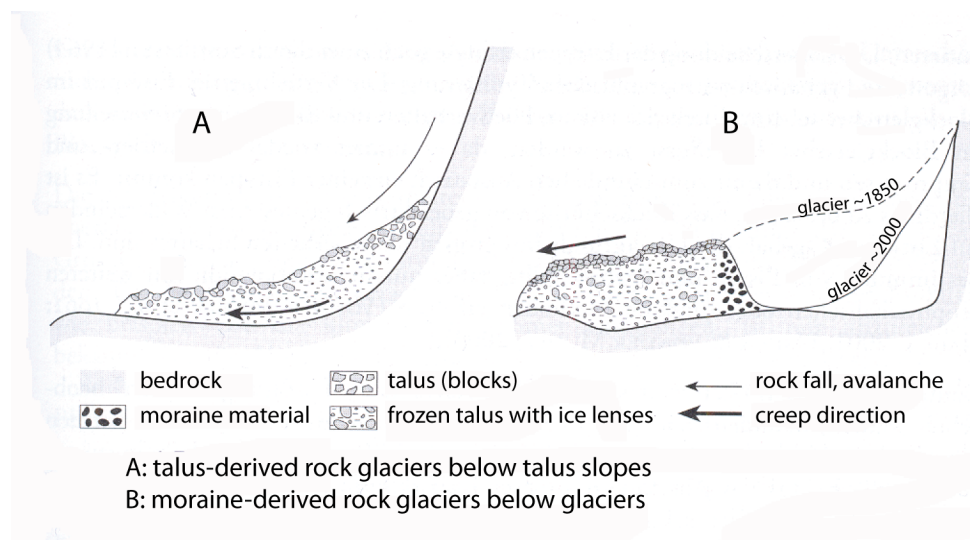
Figure 7.5: Rock glacier types and genesis, modified from Nyenhuis (2006) after Barsch (1996).

The well-developed solifluction lobes west of the glacier forefield (see Fig. 2.2) are most probably not underlain by frozen scree. As the ERT profile along the talus shows resistivities in the upper part are not indicative for frozen ground conditions. Only at the lower end resistivities above 10 kohm.m are recorded (Fig. 4.1c, p. 62). Temperature records at the ground surface (BTS of minimum -0.5°C) also do not support the idea of gelifluction on frozen ground at this site. One logger installed at the coarse openwork of the inactive rock glacier beneath the solifluction lobe gives BTS values of -2.98°C. Together with the ERT data this might indicate the presence of frozen ground within the inactive rock glacier. The latter has a dense vegetation and several large thermokarst structures from melt processes at the surface. A small seepage at the front (incised by a ski run) during summer corroborates the presence of relict ice in this formerly active permafrost landform.

7.2.2. Glacier forefield Muragl

Statements on the distribution of mountain permafrost and creep dynamics in glacier forefield Muragl were summarized recently by Kneisel (2010b). Detailed analysis at two permafrost sites were implemented in the present study. The analysis of ERT monitoring data since 2004 revealed the stability of the active layer at both monitoring profiles. Instead of significant changes in the thickness of the active layer, contrary trends of the permafrost evolution are recognized. Along the profile ERTM-Mgl1 changes in the liquid water content were observed (Fig. 5.7d, p. 104) between 2004 and 2009 as suggested by the calculated resistivity data. Long-term aggradation or degradation processes with corresponding ice growth or permafrost thaw have to be confirmed by repeated measurements in the upcoming years.

As a major factor for this heterogeneous ground resistivity development the annual snow cover conditions are considered. They show a large year-to-year variability and as a function of the total snow height the ground experiences different climate forcing especially in early winter. The fundamental role of the ground cooling in winter is illustrated by the response of the ground surface temperature as recorded by numerous temperature loggers. They show that GST vary considerably in time (annual snow fall pattern) and space (microtopography, wind redistribution, surface layer) and thus represent a highly variable upper boundary condition for the ground thermal regime.

Together with borehole temperature data the permafrost occurrence at borehole Mgl2 is regarded to be close to degradation. As the ice content is expected to be rather low at this site the effect of latent heat is reduced. The role of 3D effects because of the geomorphological situation are unclear and may be responsible for a cooling at the bottom of the borehole. Although, problems with the temperature sensor cannot be excluded.

7.2.3. Glacier forefield Zugspitze

Apart from visual observations during construction work no detailed investigations on ground ice has been conducted at the Zugspitzplatt. So far, research focussed on permafrost occurrences at the summit crest. Geophysical mappings were conducted to investigate the subsurface of the talus slopes and of the glacial till in the forefield of the present Northern Schneeferner. High resistivity values of several Mohm.m were calculated for the

profiles Zug-ERT1 and Zug-ERT6 that indicate the presence of ice of glacial origin. The later profile was located at the margin of the glacier where direct observations confirmed the existence of massive ice in the ground. At Zug-ERT1, an ice-filled sink hole could be the reason for the high resistive anomaly.

Permafrost in the sense of frozen unconsolidated sediments with interstitial congelation ice is hardly to expect based on the present results. This is because the debris layer is relatively thin at most sites and bedrock outcrops emerge frequently. Karstification processes may have been responsible for the generation of large sink holes that were filled with ice at the time of glacier coverage. After recession of the glacier these areas were covered with scree while they stayed sealed with ice of sedimentary origin. The considerably higher snow depth at the Zugspitzplatt (Fig. 6.1, p. 115) largely dampens the effect of cold winter air temperatures on the ground cooling. It is therefore expected to be less important compared to the sites in the Engadin. An issue that could be further validated with the use of ground temperature loggers or borehole recordings.

High resistivties of several kohm.m in the subsurface of Zug-ERT3 (Fig. 6.5, p. 120) with bedrock close to the surface may indicate the presence of frozen bedrock. This area could be investigated in more detail, e.g., by complementary geophysical measurements or the drilling of shallow boreholes.

8. Conclusions

The main objectives of the present study were related to the improvement of spatio-temporal observation techniques and the increase of the process understanding especially concerning the active layer–permafrost boundary in discontinuous alpine permafrost. Field work was concentrated at three investigation sites with similar surface characteristics but different climatological conditions.

The quasi-3D electrical resistivity approach has proven to be an appropriate and powerful tool for an improved investigation of the presence and extent of permafrost. Inspired from positive experiences in environmental sciences, this technique was applied at the small rock glacier Rabgiusa at Murtèl/Corvatsch site. It improves the spatial resolution and the delineation of subsurface structures compared to state-of-the-art 2D ERT that are limited to information gained along one profile or extrapolation between several single profiles. Owing to the time-consuming measurements of a dense grid of ERTs and the restrictions in cable length and electrode coupling with ground, it is challenging to apply this technique successfully in periglacial environments. Its good resolution and promising results as shown in this study, however, demonstrate its value in the detection and 3D delineation of permafrost targets. In particular single landforms of small to medium scale are regarded as objectives and favor the application of detailed quasi-3D or real 3D surveys.

Both, Wenner and Wenner-Schlumberger array yielded satisfactory results, with slight advantages for the Wenner-Schlumberger data set at greater depth. This is in analogy to 2D ERT mapping. The combination of both arrays in one data file did not considerably improve the resolution and therefore measurements using the Wenner-Schlumberger array are regarded as a good trade-off between accuracy and acquisition time for studies in environments with coarse debris at the surface. The robust inversion scheme showed better correlation with borehole temperature data and may be preferred in areas with well-delineated permafrost bodies and a clear contrast in resistivity values.

The well-observed demarcation of the high resistive subsurface anomaly beneath the rock glacier demonstrates the permafrost-favorable microclimate of coarse surface mate-

rial. Boreholes and temperature datalogger allow the investigation of the thermal connectivity between air, ground surface, and the subsurface at glacier forefields Murtèl and Muragl. The temporal evolution of ground temperatures enabled to estimate the importance of different heat transfer mechanisms, such as air–ground connectivity, advective heat transfer, or thermal insulation at these sites. Based on temperature data the influence of the annual snow cover (development and snow height) is considered as the major factor for the thermal regime on a local scale, where meteorological parameters such as air temperature, wind, precipitation, and incoming radiation are regarded as uniform.

Especially the timing of an insulating snow cover is fundamental for the penetration depth of the winter cold wave. It may be twice as deep in winters with a snow depth of <0.8 m even though air temperatures can be above the long-term mean at the same time (e.g., winter 2006/2007). Data from adjacent temperature loggers showed a difference in MAGST as large as 4.3°C with the lowest values registered in blocky material that favors a lasting exchange of cold air in early winter. Thus, the local grain size of the substrate is a second key parameter for the ground thermal regime and the negative thermal anomaly in coarse blocky surfaces because of cold air circulation between blocks and perforation of the snow cover. At Val Muragl, all loggers placed between debris of more than 20 cm in diameter recorded negative MAGST values between 2005–2011. The thermal conditions are furthermore modified by the local relief. A lasting connection between air and ground surface temperature in winter and 3D effects on shallow ridges facilitates the presence of permafrost also at sites with fine-grained substrate (e.g., Mgl2).

As shown with borehole temperature records at glacier forefields Murtèl and Muragl, the active layer thickness is stable over the past 7 years. This is attributed to the existence of an ice-rich transient layer at the bottom of the active layer, which exerts a considerable inertia on the thermal regime of permafrost systems owing to the inherent latent heat. However, reduced winter cooling caused by thicker snow cover since 2008/2009 and temperatures at the top of the permafrost at the fine-grained site Mgl2 close to the freezing point (-0.07°C) indicate a thermal state that is sensitive to degradation in the future. In general, active layer thickness alone is not regarded as a sufficient parameter for the characterization of the thermal state in the zone of discontinuous permafrost. While the former suggests little thermal disturbance during the period under study, borehole data indicate variations in permafrost temperatures. So far, no synchronous trends are

recognizable at the three permafrost boreholes. Similarly, multi-annual ERT monitoring results from Val Muragl verify the existence of permafrost degradation and aggradation processes (in terms of changes of the liquid/frozen water content) in a localized manner. Thus, alpine permafrost in unconsolidated sediments is subject to changes both in space and in time although the active layer thickness remains constant.

The existence of the transient layer and the increase of the ice content at the permafrost table was illustrated with data from an automated ERT monitoring. Diurnal resistivity data show at high resolution the impact of snow melt in spring. With the onset of snow melt a drastic decrease of resistivity values in the uppermost 2 m is registered. A cold spell in May, which interrupted the continuous infiltration of melt water enabled to monitor an increase in resistivity values that can most probably be attributed to the refreezing at the permafrost table. The repetitious cycle of ice growth during the infiltration of melt water into the frozen active layer is therewith demonstrated. Difficulties that appear during installation and operation of the ERT monitoring systems are related to harsh climatic conditions, snow load, avalanches, tumbling stones, corrosion of electrode contacts, and cable defects. Another source of defectiveness is the communication between the measurement system and the remote control unit and the maintenance of an autonomous power supply. Despite the error-proneness, the present findings highlight the large potential for automated ERT monitoring systems in periglacial environments. Together with information from ground surface and borehole temperature data it was concluded with a conceptual model of the active layer processes between autumn and early summer.

Possible consequence of the disintegration of frozen ground in the discontinuous mountain permafrost zone such as an increase in mass wasting processes might be inhibited as long as the repeated annual formation of ice in the transient layer continuous. Model simulations with long-term climatological input data indicate that there is a tipping point followed by rapid increase in active layer thickness. This effect is likely to be associated with the degradation of the ice-rich layer at the top of the permafrost.

Future investigations in this type of periglacial environments should be concerned in more detail with this transient layer and its stabilising effect on the permafrost system as a whole. As shown the application of modern geophysical techniques such as spatial 3D mapping and monitoring approaches is able to serve as appropriate tool for the mid- to long-term observation of permafrost in unconsolidated material. Especially, the

differentiated analysis of distinct parts of ERT tomograms makes a detailed investiga-
tion of a permafrost body possible. Technological progress will probably reduce current
problems and disadvantages such as longevity of the monitoring system, data transfer,
or power supply in remote areas. Together with temperature data but also soil moisture
measurements the knowledge about this crucial part in the subsurface of unconsolidated
sediments can be increased. Another aspect should be the transformation of results from
this local process study to regional modeling attempts of the distribution of permafrost.
Here, the consideration of the snow cover and of the grain size (n-factors) are valuable
starting points. Especially areas that are prone to mass wasting processes linked to the
degradation of permafrost and ground ice are regarded as important research sites.

Bibliography

Archie, G. E., 1942. The electrical resistivity log as an aid in determining some reservoir characteristics. Petroleum Transactions of AIME 146, 54–62.

Arenson, L., Hoelzle, M., Springman, S., 2002. Borehole deformation measurements and internal structure of some rock glaciers in Switzerland. Permafrost and Periglacial Processes 13 (2), 117–135.

Barsch, D., 1973. Refraktionsseismische Bestimmung der Obergrenze des gefrorenen Schuttkörpers in verschiedenen Blockgletschern Graubündens, Schweizer Alpen. Zeitschrift für Gletscherkunde und Glazialgeologie 9 (1-2), 143–167.

Barsch, D., 1996. Rockglaciers. Springer, Berlin.

Barsch, D., Hell, G., 1975. Photogrammetrische Bewegungsmessungen am Blockgletscher Murtèl I, Oberengadin, Schweizer Alpen. Zeitschrift für Gletscherkunde und Glazialgeologie 11 (2), 111–142.

Bast, A., 2009. Kleinräumige Permafrostverteilung in einem alpinen Gletschervorfeld. Val Muragl/Oberengadin, Schweiz. Ph.D. thesis, Universität Würzburg, Würzburg.

Bauer, A., Paar, G., Kaufmann, V., 2003. Terrestrial laser scanning for rock glacier monitoring. In: Phillips, M., Springman, S. M., Arenson, L. U. (Eds.), Proceedings of the 8th International Conference on Permafrost, Zürich, Switzerland. A.A. Balkema Publishers, Rotterdam and The Netherlands, pp. 55–60.

Bayerisches Landesamt für Umwelt, 2012. Permafrostmessungen an der Zugspitze. URL http://www.lfu.bayern.de/geologie/index.htm

Beniston, M., 2004. Climate Change and its impacts. An overview focusing on Switzerland. Vol. 19 of Advances in global change research. Kluwer Academic Publishers, Dordrecht.

Beniston, M., Uhlmann, B., Goyette, S., López-Moreno, J. I., 2011. Will snow-abundant

winters still exist in the Swiss Alps in an enhanced greenhouse climate? International Journal of Climatology 31 (9), 1257–1263.

Berckhemer, H., 1990. Grundlagen der Geophysik. Wissenschaftliche Buchgesellschaft, Darmstadt.

Berktold, A., Büttgenbach, T., Greinwald, S., Illich, B., Jacobs, F., Kolodziey, A. W., Lange, G., Maurer, H.-M., Prácser, E., Pfeifer, B., Pretzschner, C., Radic, T., Schaumann, G., Rezessy, G., Sebulke, J., Seidel, K., Szabadvary, L., Vértesy, L., Vogt, R., Weidelt, P., Weller, A., Wolff, U., 2005. Geoelektrik. In: Knödel, K., Krummel, H., Lange, G. (Eds.), Geophysik. Vol. 3 of Handbuch zur Erkundung des Untergrundes von Deponien und Altlasten. Springer, Berlin, pp. 71–387.

Bernhard, L., Sutter, F., Haeberli, W., Keller, F., 1998. Processes of snow/permafrost-interactions at a high-mountain site, Murtèl/Corvatsch, eastern Swiss Alps. In: Lewkowicz, A. G., Allard, M. (Eds.), Proceedings of the 7th International Conference on Permafrost, Yellowknife, Canada: Collection Nordicana No 55, Centre d'études nordiques, Université Laval, Saint-Foy (Québec), Canada. pp. 35–41.

Berthling, I., 2011. Beyond confusion: rock glaciers as cryo-conditioned landforms. Geomorphology 131 (3-4), 98–106.

Bimböse, M., Nicolay, A., Bryk, A., Schmidt, K.-H., Morche, D., 2011. Investigations on intra- and interannual coarse sediment dynamics in a high-mountain river. Zeitschrift für Geomorphologie, Supplementary Issue 55 (2), 67–81.

Bodin, X., Jaillet, S., Schoeneich, P., 2008. High-resolution DEM extraction from terrestrial LIDAR topometry and surface kinematics of the creeping alpine permafrost: the Laurichard Rock Glacier case study (Southern French Alps). In: Kane, D. L., Hinkel, K. M. (Eds.), Proceedings of the 9th International Conference on Permafrost, Fairbanks, AK, USA. Institute of Northern Engineering, University of Alaska, Fairbanks, pp. 137–142.

Boeckli, L., Brenning, A., Gruber, S., Noetzli, J., 2012a. A statistical approach to modelling permafrost distribution in the European Alps or similar mountain ranges. The Cryosphere 6 (1), 125–140.

Boeckli, L., Brenning, A., Gruber, S., Noetzli, J., 2012b. Permafrost distribution in the European Alps: calculation and evaluation of an index map and summary statistics. The Cryosphere 6 (4), 807–820.

Böhm, R., Auer, I., Brunetti, M., Maugeri, M., Nanni, T., Schöner, W., 2001. Regional temperature variability in the European Alps: 1760-1998 from homogenized instrumental time series. International Journal of Climatology 21 (14), 1779–1801.

Bonnaventure, P. P., Lewkowicz, A. G., 2008. Mountain permafrost probability mapping using the BTS method in two climatically dissimilar locations, northwest Canada. Canadian Journal of Earth Sciences 45 (4), 443–455.

Brenning, A., Gruber, S., Hoelzle, M., 2005. Sampling and statistical analyses of BTS measurements. Permafrost and Periglacial Processes 16 (4), 383–393.

Brückl, E., Dresen, L., Edelmann, H. A. K., Fertig, J., Gartner, H., Gelbke, C., Kirchheimer, F., Krummel, H., Liebhardt, G., Orlowsky, D., Sandmeier, K.-J., Schneider, C., Utecht, T., Witka, T., 2005. Seismik. In: Knödel, K., Krummel, H., Lange, G. (Eds.), Geophysik. Vol. 3 of Handbuch zur Erkundung des Untergrundes von Deponien und Altlasten. Springer, Berlin, pp. 425–726.

Burger, K., Degenhardt, J., Giardino, J., 1999. Engineering geomorphology of rock glaciers. Geomorphology 31 (1-4), 93–132.

Burn, C. R., Smith, C. A. S., 1988. Observation of the Thermal Offset in near-surface mean annual ground temperature at several sites near Mayo, Yukon Territory, Canada. Arctic 41 (2), 99–104.

Carcione, J. M., Seriani, G., 1998. Seismic and ultrasonic velocities in permafrost. Geophysical Prospecting 46 (4), 441–454.

Chambers, J. E., Ogilvy, R. D., Kuras, O., Cripps, J. C., Meldrum, P. I., 2002. 3D electrical imaging of known targets at a controlled environmental test site. Environmental Geology 41 (6), 690–704.

Claerbout, J. F., Muir, F., 1973. Robust modeling with erratic data. Geophysics 38 (5), 826–844.

Danby, R. K., Hik, D. S., 2007. Responses of white spruce (Picea glauca) to experimental warming at a subarctic alpine treeline. Global Change Biology 13 (2), 437–451.

Day-Lewis, F. D., Singha, K., Binley, A. M., 2005. Applying petrophysical models to radar travel time and electrical resistivity tomograms: Resolution-dependent limitations. Journal of Geophysical Research 110, B08206.

deGroot Hedlin, C., Constable, S., 1990. Occam's inversion to generate smooth, two-dimensional models from magnetotelluric data. Geophysics 55 (12), 1613–1624.

Delaloye, R., Lambiel, C., Gärtner-Roer, I., 2010. Overview of rock glacier kinematics research in the Swiss Alps. Geographica Helvetica 65 (2), 135–145.

Delaloye, R., Perruchoud, E., Avian, M., Kaufmann, V., Bodin, X., Hausmann, H., Ikeda, A., Kääb, A., Kellerer-Pirklbauer, A., Krainer, K., Lambiel, C., Mihajlovic, D., Staub, B., Roer, I., Thibert, E., 2008. Recent interannual variations of rock glacier creep in the European Alps. In: Kane, D. L., Hinkel, K. M. (Eds.), Proceedings of the 9th International Conference on Permafrost, Fairbanks, AK, USA. Institute of Northern Engineering, University of Alaska, Fairbanks, pp. 343–348.

Domaradzki, J., 1951. Blockströme im Kanton Graubünden. Ergebnisse der wissenschaftlichen Untersuchung des schweizerischen Nationalparks: Kommission der Schweizerischen Naturforschenden Gesellschaft. III/24. 177-235.

DWD, 2012. Deutscher Wetterdienst - Klimadaten online.
URL www.dwd.de

Ebohon, B., Schrott, L., 2008. Modeling mountain permafrost distribution. A new permafrost map of Austria. In: Kane, D. L., Hinkel, K. M. (Eds.), Proceedings of the 9th International Conference on Permafrost, Fairbanks, AK, USA. Institute of Northern Engineering, University of Alaska, Fairbanks, pp. 397–402.

Edwards, L. S., 1977. A modified pseudosection for resistivity and IP. Geophysics 42 (5), 1020–1036.

Engelhardt, M., Hauck, C., Salzmann, N., 2010. Influence of atmospheric forcing parameters on modelled mountain permafrost evolution. Meteorologische Zeitschrift 19 (5), 491–500.

Etter, H.-J., Zweifel, B., Dürr, L., 2011. Schnee und Lawinen in den Schweizer Alpen. Hydrologisches Jahr 2008/09. WSL-Institut für Schnee- und Lawinenforschung SLF, Davos and Switzerland.

Etzelmüller, B., 2013. Recent advances in mountain permafrost research. Permafrost and Periglacial Processes 24 (2), 99–107.

Etzelmüller, B., Berthling, I., Sollid, J. L., 2003. Aspects and concepts on the geomorphological significance of Holocene permafrost in southern Norway. Geomorphology 52 (1-2), 87–104.

Etzelmüller, B., Hagen, J. O., 2005. Glacier-permafrost interaction in arctic and alpine mountain environments with examples from southern Norway and Svalbard. In: Harris, C., Murton, J. B. (Eds.), Cryospheric Systems: Glaciers and Permafrost. Vol. 242. Special Publications, London, pp. 11–27.

Etzelmüller, B., Ødegård, R. S., Berthling, I., Sollid, J. L., 2001. Terrain parameters and remote sensing data in the analysis of permafrost distribution and periglacial processes: Principles and examples from southern Norway. Permafrost and Periglacial Processes 12 (1), 79–92.

Etzelmüller, B., Schuler, T. V., Farbrot, H., Gudmundsson, A., 2008. Permafrost in Iceland: thermal state and climate change impact. In: Kane, D. L., Hinkel, K. M. (Eds.), Proceedings of the 9th International Conference on Permafrost, Fairbanks, AK, USA. Institute of Northern Engineering, University of Alaska, Fairbanks, pp. 421–426.

Evin, M., Fabre, D., 1990. The distribution of permafrost in rock glaciers of the Southern Alps (France). Geomorphology 3 (1), 57–71.

Farbrot, H., Hipp, T. F., Etzelmüller, B., Isaksen, K., Ødegård, R. S., Schuler, T. V., Humlum, O., 2011. Air and ground temperature variations observed along elevation and continentality gradients in southern Norway. Permafrost and Periglacial Processes 22 (4), 343–360.

Finsterwalder, R., Rentsch, H., 1973. Das Verhalten der Bayerischen Gletscher in den letzten zwei Jahrzehnten. Zeitschrift für Gletscherkunde und Glazialgeologie 9, 59–72.

Fisch, W. s., Fisch, W. j., Haeberli W., 1977. Electrical D.C. resistivity soundings with long profiles on rock glaciers and moraines in the Alps of Switzerland. Zeitschrift für Gletscherkunde und Glazialgeologie 13 (1-2), 239–260.

French, H. M., 2007. The periglacial environment, 3rd Edition. Addison Wesley Longman Limited, Essex.

Froitzheim, N., Schmid, S. M., Conti, P., 1994. Repeated change from crustal shortening to orogen-parallel extension in the Austroalpine units of Graubünden. Eclogae Geologicae Helvetiae 87 (2), 559–612.

Gharibi, M., Bentley, L., 2005. Resolution of 3-D electrical resistivity images from inversion of 2-D orthogonal lines. Journal of Environmental and Engineering Geophysics 10 (4), 339–349.

Gruber, S., Haeberli, W., 2007. Permafrost in steep bedrock slopes and its temperature-related destabilization following climate change. Geophysical Research Letters 112, F02S18.

Gruber, S., Hoelzle, M., Haeberli, W., 2004. Rock-wall temperatures in the Alps: modelling their topographic distribution and regional differences. Permafrost and Periglacial Processes 15, 299–307.

Gruber, S., Peter, M., Hoelzle, M., Woodhatch, I., Haeberli, W., 2003. Surface temperatures in steep alpine rock faces - a strategy for regional-scale measurement and modelling. In: Phillips, M., Springman, S. M., Arenson, L. U. (Eds.), Proceedings of the 8th International Conference on Permafrost, Zürich, Switzerland. A.A. Balkema Publishers, Rotterdam and The Netherlands, pp. 20–25.

Gubler, S., Fiddes, J., Keller, M., Gruber, S., 2011. Scale-dependent measurement and analysis of ground surface temperature variability in alpine terrain. The Cryosphere 5 (2), 431–443.

Gude, M., Barsch, D., 2005. Assessment of geomorphic hazards in connection with permafrost occurrence in the Zugspitze area (Bavarian Alps, Germany). Geomorphology 66 (1-4), 85–93.

Guglielmin, M., Cannone, N., Dramis, F., 2001. Permafrost–glacial evolution during the Holocene in the Italian Central Alps. Permafrost and Periglacial Processes 12 (1), 111–124.

Haeberli, W., 1973. Die Basis-Temperatur der winterlichen Schneedecke als möglicher Indikator für die Verbreitung von Permafrost in den Alpen. Zeitschrift für Gletscherkunde und Glazialgeologie 9 (1-2), 221–227.

Haeberli, W., 1992. Possible effects of climate change on the evolution of alpine permafrost. In: Boer, M., Koster, E. (Eds.), Greenhouse-Impact on cold-climate ecosystems and landscapes. Catena Supplement 22. Catena-Verlag, Cremlingen-Destedt, pp. 23–35.

Haeberli, W., Beniston, M., 1998. Climate change and its impacts on glaciers and permafrost in the Alps. Ambio 27 (4), 258–265.

Haeberli, W., Hallet, B., Arenson, L. U., Elconin, R., Humlum, O., Kääb, A., Kaufmann, V., Ladanyi, B., Matsuoka, N., Springman, S., Vonder Muehll, D., 2006. Permafrost creep and rock glacier dynamics. Permafrost and Periglacial Processes 17 (3), 189–214.

Haeberli, W., Noetzli, J., Arenson, L., Delaloye, R., Gärtner-Roer, I., Gruber, S., Isaksen, K., Kneisel, C., Krautblatter, M., Phillips, M., 2010. Mountain permafrost: development and challenges of a young research field. Journal of Glaciology 200, 1043–1058.

Haeberli, W., Patzelt, G., 1982. Permafrostkartierung im Gebiet Hochebenkar-Blockgletscher, Obergurgl, Oetztaler Alpen. Zeitschrift für Gletscherkunde und Glazialgeologie 17, 127–150.

Haeberli, W., Vonder Muehll, D., 1996. On the characteristics and possible origins of ice in rock glacier permafrost. Zeitschrift für Geomorphologie, Supplementary Issue 104, 43–57.

Hagg, W., 2010. Bayerische Gletscher.
    URL `www.bayerische-gletscher.de`

Hanson, S., Hoelzle, M., 2004. The thermal regime of the active layer at the Murtèl rock glacier based on data from 2002. Permafrost and Periglacial Processes 15 (3), 273–282.

Hanson, S., Hoelzle, M., 2005. Installation of a shallow borehole network and monitoring of the ground thermal regime of a high alpine discontinuous permafrost environment, eastern Swiss Alps. Norsk Geografisk Tidsskrift - Norwegian Journal of Geography 59 (2), 84–93.

Harris, C., Arenson, L. U., Christiansen, H. H., Etzelmüller, B., Frauenfelder, R., Gruber, S., Haeberli, W., Hauck, C., Hoelzle, M., Humlum, O., Isaksen, K., Kääb, A., Kern-Luetschg, M. A., Lehning, M., Matsuoka, N., Murton, J. B., Noetzli, J., Phillips, M., Ross, N., Seppälä, M., Springman, S., Vonder Muehll, D., 2009. Permafrost and climate in Europe: monitoring and modelling thermal, geomorphological and geotechnical responses. Earth-Science Reviews 92 (3-4), 117–171.

Harris, C., Haeberli, W., Vonder Muehll, D., King, L., 2001. Permafrost monitoring in the high mountains of Europe, the PACE project in its global context. Permafrost and Periglacial Processes 12 (1), 3–11.

Harris, S. A., Pedersen, D. E., 1998. Thermal regimes beneath coarse blocky materials. Permafrost and Periglacial Processes 9 (2), 107–120.

Hartmeyer, I., Keuschnig, M., Schrott, L., 2012. A scale-oriented approach for the long-term monitoring of ground thermal conditions in permafrost-affected rock faces, Kitzsteinhorn, Hohe Tauern Range, Austria. Austrian Journal of Earth Sciences 105 (2), 128–139.

Hauck, C., 2001. Geophysical methods for detecting permafrost in high mountains. Ph.D. thesis, Versuchsanstalt für Wasserbau, Hydrologie und Glaziologie der Eidgenössischen Technischen Hochschule Zürich, Zürich.

Hauck, C., 2002. Frozen ground monitoring using DC resistivity tomography. Geophysical Research Letters 29 (21), 2016.

Hauck, C., 2013. New concepts in geophysical surveying and data interpretation for permafrost terrain. Permafrost and Periglacial Processes 24 (2), 131–137.

Hauck, C., Böttcher, M., Maurer, H., 2011. A new model for estimating subsurface ice content based on combined electrical and seismic data sets. The Cryosphere 5 (2), 453–468.

Hauck, C., Kneisel, C. (Eds.), 2008. Applied geophysics in periglacial environments. Cambridge University Press, Cambridge.

Hauck, C., Vonder Muehll, D., 2003a. Evaluation of geophysical techniques for application in mountain permafrost studies. Zeitschrift für Geomorphologie, Supplement Volume 132, 161–190.

Hauck, C., Vonder Muehll, D., 2003b. Inversion and interpretation of two-dimensional geoelectrical measurements for detecting permafrost in mountainous regions. Permafrost and Periglacial Processes 14 (4), 305–318.

Hauck, C., Vonder Muehll, D., Maurer, H., 2003. Using DC resistivity tomography to detect and characterize mountain permafrost. Geophysical Prospecting 51 (4), 273–284.

Hausmann, H., Krainer, K., Brückl, E., Mostler W., 2007. Internal structure and ice content of Reichenkar rock glacier (Stubai Alps, Austria) assessed by geophysical investigations. Permafrost and Periglacial Processes 18 (4), 351–367.

Hecht, S., 2001. Anwendung refraktionsseismischer Methoden zur Erkundung des oberflächennahen Untergrundes. Vol. 131 of Stuttgarter geographische Studien. Institut für Geographie der Universität Stuttgart, Stuttgart.

Heckmann, T., Bimböse, M., Krautblatter, M., Haas, F., Becht, M., Morche, D., 2012. From geotechnical analysis to quantification and modelling using LiDAR data: a study on rockfall in the Reintal catchment, Bavarian Alps, Germany. Earth Surface Processes and Landforms 37 (1), 119–133.

Heggem, E., Juliussen, H., Etzelmüller, B., 2005. Mountain permafrost in central-eastern Norway. Norsk Geografisk Tidsskrift - Norwegian Journal of Geography 59 (2), 94–108.

Hera, U., 1997. Gletscherschwankungen in den Nördlichen Kalkalpen seit dem 19. Jahrhundert. Vol. 25 of Münchener Geographische Abhandlungen, Reihe B. GEOBUCH-Verlag, München.

Hilbich, C., 2010. Time-lapse refraction seismic tomography for the detection of ground ice degradation. The Cryosphere 4 (3), 243–259.

Hilbich, C., Fuss, C., Hauck, C., 2011. Automated time-lapse ERT for improved process analysis and monitoring of frozen ground. Permafrost and Periglacial Processes 22 (4), 306–319.

Hilbich, C., Hauck, C., Delaloye, R., Hoelzle, M., 2008a. A geoelectric monitoring network and resisivity-temperature relationships of different mountain permafrost sites in the Swiss Alps.

Hilbich, C., Hauck, C., Hoelzle, M., Scherler, M., Schudel, L., Völksch, I., Vonder Muehll, D., Mäusbacher, R., 2008b. Monitoring mountain permafrost evolution using electrical resistivity tomography: A 7-year study of seasonal, annual, and long-term variations at Schilthorn, Swiss Alps. Journal of Geophysical Research 113, F01S90.

Hilbich, C., Marescot, L., Hauck, C., Loke, M. H., Mäusbacher, R., 2009. Applicability of electrical resistivity tomography monitoring to coarse blocky and ice-rich permafrost landforms. Permafrost and Periglacial Processes 20 (3), 269–284.

Hirtlreiter, G., 1992. Spät- und postglaziale Gletscherschwankungen im Wettersteingebirge und seiner Umgebung. Vol. 15 of Münchener Geographische Abhandlungen, Reihe B. GEOBUCH-Verlag, München.

Hoelzle, M., 1992. Permafrost occurence from BTS measurements and climatic parameters in the eastern Swiss Alps. Permafrost and Periglacial Processes 3 (2), 143–147.

Hoelzle, M., Haeberli, W., Keller, F., 1993. Application of BTS measurements for modelling mountain permafrost distribution. In: Proceedings of the 6th International Conference on Permafrost. Vol. 1. South China University of Technology Press, Beijing, pp. 272–277.

Hoelzle, M., Haeberli, W., Stocker-Mittaz, C., 2003. Miniature ground temperature data logger measurements 2000–2002 in the Murtèl-Corvatsch area, Eastern Swiss Alps. In: Phillips, M., Springman, S. M., Arenson, L. U. (Eds.), Proceedings of the 8th International Conference on Permafrost, Zürich, Switzerland. A.A. Balkema Publishers, Rotterdam and The Netherlands, pp. 419–424.

Hoelzle, M., Mittaz, C., Etzelmüller, B., Haeberli, W., 2001. Surface energy fluxes and distribution models of permafrost in European mountain areas: an overview of current developments. Permafrost and Periglacial Processes 12 (1), 53–68.

Hoelzle, M., Vonder Muehll, D., Haeberli, W., 2002. Thirty years of permafrost research in the Corvatsch–Furtschellas area, Eastern Swiss Alps: a review. Norsk Geografisk Tidsskrift - Norwegian Journal of Geography 56 (2), 137–145.

Hoelzle, M., Wegmann, M., Krummenacher, B., 1999. Miniature temperature dataloggers for mapping and monitoring of permafrost in high mountain areas: first experience from the Swiss Alps. Permafrost and Periglacial Processes 10 (2), 113–124.

Hofmann-Wellenhof, B., Lichtenegger, H., Collins, J., 2001. Global positioning system: theory and practice, 5th Edition. Springer, Wien.

Ikeda, A., 2006. Combination of conventional geophysical methods for sounding the composition of rock glaciers in the Swiss Alps. Permafrost and Periglacial Processes 17 (1), 35–48.

Isaksen, K., Hauck, C., Gudevang, E., Ødegård, R. S., Sollid, J. L., 2002. Mountain permafrost distribution in Dovrefjell and Jotunheimen, southern Norway, based on BTS measurements and 2D tomography data. Norsk Geografisk Tidsskrift - Norwegian Journal of Geography 56, 122–136.

Isaksen, K., Ødegård, R. S., Etzelmüller, B., Hilbich, C., Hauck, C., Farbrot, H., Eiken, T., Hygen, H. O., Hipp, T. F., 2011. Degrading mountain permafrost in southern Norway: spatial and temporal variability of mean ground temperatures, 1999-2009. Permafrost and Periglacial Processes 22 (4), 343–360.

Ishikawa, M., 2003. Thermal regimes at the snow-ground interface and their implications for permafrost investigation. Geomorphology 52 (1-2), 105–120.

Ishikawa, M., Hirakawa, K., 2000. Mountain permafrost distribution based on BTS measurements and DC resistivity soundings in the Daisetsu Mountains, Hokkaido, Japan. Permafrost and Periglacial Processes 11 (2), 109–123.

Jansson, P.-E., Karlberg, L., 2001. Coupled heat and mass transfer model for soil-plant-atmosphere systems. Ph.D. thesis, Royal Institute of Technology, Department of Civil and Environmental Engineering, Stockholm.

Jones, P. D., New, M., Parker, D. E., Martin, S., Rigor, I. G., 1999. Surface air temperature and its changes over the past 150 years. Reviews of Geophysics 37 (2), 173–199.

Jorgenson, M. T., Kreig, R. A., 1988. A model for mapping permafrost distribution based on landscape component maps and climatic variables. In: Senneset, K. (Ed.), Proceedings of the 5th International Conference on Permafrost. Vol. 1. Tapir Publishers, Trondheim, pp. 176–182.

Juliussen, H., Humlum, O., 2007. Towards a TTOP ground temperature model for mountainous terrain in central-eastern Norway. Permafrost and Periglacial Processes 18 (2), 161–184.

Juliussen, H., Humlum, O., 2008. Thermal regime of openwork block fields on the mountains Elgahogna and Solen, central-eastern Norway. Permafrost and Periglacial Processes 19 (1), 1–19.

Kääb, A., Kneisel, C., 2006. Permafrost creep within a recently deglaciated glacier forefield: Muragl, Swiss Alps. Permafrost and Periglacial Processes 17 (1), 79–85.

Kääb, A., Vollmer M., 2000. Surface geometry, thickness changes and flow fields on creeping mountain permafrost: automatic extraction by digital image analysis. Permafrost and Periglacial Processes 11 (4), 315–326.

Kane, D. L., Hinkel, K. M., Goering, D. J., Hinzman, L. D., Outcalt, S. I., 2001. Non-conductive heat transfer associated with frozen soils. Global and Planetary Change 29 (3-4), 275–292.

Kästl, J., 2012. Räumliche Heterogenität und zeitliche Variabilität der Permafrostverbreitung im Gletschervorfeld des Val Muragl. Ph.D. thesis, Universität Würzburg, Würzburg.

Keller, C. V., Frischknecht, F. C., 1960. Electrical resistivity studies on the Athabasca Glacier Alberta, Canada. Journal of research of the National Bureau of Standards 64 (5), 439–448.

Keller, F., 1994. Interaktion zwischen Schnee und Permafrost: Eine Grundlagenstudie im Oberengadin. Ph.D. thesis, Versuchsanstalt für Wasserbau, Hydrologie und Glaziologie der Eidgenössischen Technischen Hochschule Zürich, Zürich.

Keller, F., Tamás, M., 2003. Enhanced ground cooling in periods with thin snow cover in the Swiss National Park. In: Phillips, M., Springman, S. M., Arenson, L. U. (Eds.), Proceedings of the 8th International Conference on Permafrost, Zürich, Switzerland. A.A. Balkema Publishers, Rotterdam and The Netherlands, pp. 531–536.

Kenner, R., Bühler, Y., Delaloye, R., Ginzler, C., Phillips, M., 2013. Monitoring of high alpine mass movements combining laser scanning with digital airborne photogrammetry. Geomorphology (in press).

King, L., 1982. Qualitative und quantitative Erfassung von Permafrost in Tarfala (Schwedisch-Lappland) und Jotunheimen (Norwegen) mit Hilfe geoelektrischer Sondierungen. Zeitschrift für Geomorphologie, N.F., Supplementband 43, 139–160.

King, L., Fisch, W., Haeberli, W., Wächter, H.-P., 1987. Comparison of resistivity and radio-echo soundings on rock glacier permafrost. Zeitschrift für Gletscherkunde und Glazialgeologie 23 (2), 77–97.

Klene, A. E., Nelson, F. E., Shiklomanov, N. I., Hinkel, K. M., 2001. The n-factor in natural landscapes: variability of air and soil-surface temperatures, Kuparuk river basin, Alaska, U.S.A. Arctic, Antarctic and Alpine Research 33 (2), 140–148.

Kneisel, C., 1998. Occurrence of surface ice and ground ice/permafrost in recently deglaciated glacier forefields, St. Moritz area, eastern Swiss Alps. In: Lewkowicz, A. G.,

Allard, M. (Eds.), Proceedings of the 7th International Conference on Permafrost, Yellowknife, Canada: Collection Nordicana No 55, Centre d'études nordiques, Université Laval, Saint-Foy (Québec), Canada. pp. 575–581.

Kneisel, C., 1999. Permafrost in Gletschervorfeldern: Eine vergleichende Untersuchung in den Ostschweizer Alpen und Nordschweden. In: Trierer Geographische Studien. Vol. 22. pp. 1–156.

Kneisel, C., 2003. Electrical resistivity tomography as a tool for geomorphological investigations – some case studies. Zeitschrift für Geomorphologie, Supplementary Issue 132, 37–49.

Kneisel, C., 2006. Assessment of subsurface lithology in mountain environments using 2D resistivity imaging. Geomorphology 80 (1-2), 32–44.

Kneisel, C., 2010a. Frozen ground conditions in a subarctic mountain environment, northern Sweden. Geomorphology 118 (1-2), 80–92.

Kneisel, C., 2010b. The nature and dynamics of frozen ground in alpine and subarctic periglacial environments. The Holocene 20 (3), 423–445.

Kneisel, C., Hauck, C., 2003. Multi-method geophysical investigation of a sporadic permafrost occurence. Zeitschrift für Geomorphologie, Supplement Volume 132, 145–159.

Kneisel, C., Hauck, C., 2008. Electrical methods. In: Hauck, C., Kneisel, C. (Eds.), Applied geophysics in periglacial environments. Cambridge University Press, Cambridge, pp. 1–27.

Kneisel, C., Hauck, C., Fortier, R., Moorman, B., 2008. Advances in geophysical methods for permafrost investigations. Permafrost and Periglacial Processes 19 (2), 157–178.

Kneisel, C., Kääb, A., 2007. Mountain permafrost dynamics within a recently exposed glacier forefield inferred by a combined geomorphological, geophysical and photogrammetrical approach. Earth Surface Processes and Landforms 32 (12), 1797–1810.

Kneisel, C., Rödder, T., Roth, N., Schwindt, D., 2012. Electrical resistivity monitoring for the detection of changes in mountain permafrost at different time scales: Extended

abstract from the 1st International Workshop on Geoelectrical Monitoring - GELMON 2010.

Kneisel, C., Rödder, T., Schwindt, D., 2014. Frozen ground dynamics resolved by multi-year and year-round electrical resistivity monitoring at three alpine sites in the Swiss Alps. Near Surface Geophysics 12, 117–132.

Kneisel, C., Schwindt, D., 2008. Geophysical mapping of isolated permafrost lenses at a sporadic permafrost site at low altitude in the Swiss Alps. In: Kane, D. L., Hinkel, K. M. (Eds.), Proceedings of the 9th International Conference on Permafrost, Fairbanks, AK, USA. Institute of Northern Engineering, University of Alaska, Fairbanks, pp. 959–964.

Körner, H., Ulrich, R., 1965. Geologische und felsmechanische Untersuchungen für die Gipfelstation der Seilbahn Eibsee-Zugspitze. Geologica Bavarica 55, 404–421.

Krautblatter, M., 2009. Detection and quantification of permafrost change in alpine rock walls and implications for rock instability. Ph.D. thesis, Universität Bonn, Bonn.

Krautblatter, M., 2010a. Patterns of multiannual aggradation of permafrost in rock walls with and without hydraulic interconnectivity (Steintälli, Valley of Zermatt, Swiss Alps). In: Otto, J. C., Dikau, R. (Eds.), Landform - Structure, Evolution, Process Control. Vol. 115 of Lecture Notes in Earth Sciences. Springer, Berlin and Heidelberg, pp. 199–219.

Krautblatter, M., 2010b. Temperature–calibrated imaging of seasonal changes in permafrost rock walls by quantitative electrical resistivity tomography (Zugspitze, German/Austrian Alps). Journal of Geophysical Research 115, F02003.

Krautblatter, M., Hauck, C., 2007. Electrical resistivity tomography monitoring of permafrost in solid rock walls. Journal of Geophysical Research 112, F02S20.

Krautblatter, M., Verleysdonk, S., 2010. Felspermafrost an der Zugspitze. In: Götz, J., Schrott, L. (Eds.), Das Reintal. Pfeil, München, pp. 65–68.

Labhart, T. P., 2001. Geologie der Schweiz, 5th Edition. Ott Verlag, Thun.

Lachenbruch, A. H., Cladouhos, T. T., Saltus, R. W., 1988. Permafrost temperature and the changing climate. In: Senneset, K. (Ed.), Proceedings of the 5th International Conference on Permafrost. Vol. 3. Tapir Publishers, Trondheim, pp. 9–17.

Lambiel, C., Delaloye, R., 2004. Contribution of real-time kinematic GPS in the study of creeping mountain permafrost: examples from the western Swiss Alps. Permafrost and Periglacial Processes 15 (3), 229–241.

Lanz, E., Maurer, H., Green, A. G., 1998. Refraction tomography over a buried waste disposal site. Geophysics 63 (4), 1414–1433.

Lemke, P., Ren, J., Alley, R. B., Allison, I., Carrasco, J., Flato, G., Fujii, Y., Kaser, G., Mote, P., Thomas, R. H., Zhang, T., 2007. Observations: Changes in snow, ice and frozen Ground. In: Solomon, S., Qin, D., Manning, M., Chen, Z., Marquis, M., Averyt, K. B., Tignor, M., Miller, H. L. (Eds.), Climate Change 2007: the physical science basis. Contribution of working group I to the fourth assessment report of the intergovernmental panel on climate change. Cambridge University Press, Cambridge and United Kingdom and New York and NY and USA.

Lewkowicz, A. G., 2008. Evaluation of miniature temperature-loggers to monitor snow-pack evolution at mountain permafrost sites, northwestern Canada. Permafrost and Periglacial Processes 19 (3), 323–331.

Lewkowicz, A. G., Ednie, M., 2004. Probability mapping of mountain permafrost using the BTS method, Wolf Creek, Yukon Territory, Canada. Permafrost and Periglacial Processes 15 (1), 67–80.

Loke, M. H., 2012. Tutorial: 2-D and 3-D electrical imaging surveys.

Loke, M. H., Acworth, I., Dahlin, T., 2003. A comparison of smooth and blocky inversion methods in 2D electrical imaging surveys. Exploration Geophysics 34 (3), 182–187.

Loke, M. H., Barker, R. D., 1996. Rapid least-squares inversion of apparent resisitivity pseudosections by a quasi-Newton method. Geophysical Prospecting 44, 131–152.

Lowrie, W., 2011. Fundamentals of geophysics, 2nd Edition. Cambridge University Press, Cambridge.

Luetschg, M., Lehning, M., Haeberli, W., 2008. A sensitivity study of factors influencing warm/thin permafrost in the Swiss Alps. Journal of Glaciology 54 (187), 696–704.

Lunardini, V. J., 1978. Theory of n-factors and correlation of data. In: National Research Council of Canada (Ed.), Proceedings of the 3rd International Conference on Permafrost. Vol. 1. National Research Council of Canada, Ottawa, pp. 40–46.

Lundquist, J. D., Lott, F., 2008. Using inexpensive temperature sensors to monitor the duration and heterogeneity of snow-covered areas. Water Resources Research 44, W00D16.

Maisch, M., 1992. Die Gletscher Graubündens. Rekonstruktion und Auswertung der Gletscher und deren Veränderungen seit dem Hochstand von 1850 im Gebiet der östlichen Schweizer Alpen. (Bündnerland und angrenzende Regionen): Teil B: Verzeichnisse-Datenkataloge-Gletscherkarten. Vol. 33b of Schriftenreihe Physische Geographie. Zürich.

Maisch, M., Haeberli, W., Frauenfelder, R., Kääb, A., 2003. Lateglacial and Holocene evolution of glaciers and permafrost in Val Muragl, upper Engadine, Swiss Alps. In: Phillips, M., Springman, S. M., Arenson, L. U. (Eds.), Proceedings of the 8th International Conference on Permafrost, Zürich, Switzerland. A.A. Balkema Publishers, Rotterdam and The Netherlands, pp. 717–722.

Marescot, L., Loke, M. H., Chapellier, D., Delaloye, R., Lambiel, C., Reynard, E., 2003. Assessing reliability of 2D resistivity imaging in mountain permafrost studies using the depth of investigation index method. Near Surface Geophysics 1 (2), 57–67.

Marty, C., 2008. Regime shift of snow days in Switzerland. Geophysical Research Letters 35, L12501.

Maurer, H., Hauck, C., 2007. Geophysical imaging of alpine rock glaciers. Journal of Glaciology 53 (180), 110–120.

MeteoSchweiz, 2012. Klima Schweiz: Klimanormwerte.
URL `http://www.meteoschweiz.ch`

Meyer, R. K. F., Schmidt-Kaler, H., 2002. Auf den Spuren der Eiszeit südlich von München

- östlicher Teil. In: Wanderungen in die Erdgeschichte. Vol. 8. F. Pfeil, München, p. 144.

Musil, M., Maurer, H., Green, A. G., Horstmeyer, H., Nitsche, F. O., Vonder Muehll, D., Springman, S., 2002. Shallow seismic surveying of an alpine rock glacier: Case History. Geophysics 67 (6), 1701–1710.

NASA, 2011. Earth Observatory: Image of the day.
    URL `http://earthobservatory.nasa.gov/IOTD/view.php?id=48845`

Noetzli, J., Gruber, S., 2009. Transient thermal effects in Alpine permafrost. The Cryosphere 3 (1), 85–99.

Noetzli, J., Gruber, S., Kohl, T., Salzmann, N., Haeberli, W., 2007. Three-dimensional distribution and evolution of permafrost temperatures in idealized high-mountain topography. Journal of Geophysical Research 112, F02S13.

Nyenhuis, M., 2006. Permafrost und Sedimenthaushalt in einem alpinen Geosystem. Ph.D. thesis, Universität Bonn, Bonn.

Østrem, G., 1964. Ice-cored moraines in Scandinavia. Geografiska Annaler 46 (3), 282–337.

Paul, F., Kääb, A., Maisch, M., Kellenberger, T., Haeberli, W., 2004. Rapid disintegration of alpine glaciers observed with satellite data. Geophysical Research Letters 31, L21402.

PERMOS, 2007. Permafrost in Switzerland 2002/2003 and 2003/2004 Vonder Muehll, D., Noetzli, J., Roer, I., Makowski, K., Delaloye, R. (Eds.): Glaciological Report (Permafrost) No. 4/5 of the Cryospheric Commission of the Swiss Academy of Sciences, Zürich.

PERMOS, 2009. Permafrost in Switzerland 2004/2005 and 2005/2006. Noetzli, J., Naegli, B., Vonder Muehll, D. (Eds.): Glaciological Report (Permafrost) No. 6/7 of the Cryospheric Commission of the Swiss Academy of Sciences, Zürich: 100 pp.

PERMOS, 2010. Permafrost in Switzerland 2006/2007 and 2007/2008. Noetzli, J. and Vonder Muehll, D. (eds.): Glaciological Report Permafrost No. 8/9 of the Cryospheric Commission of the Swiss Academy of Sciences, Zürich.

Peter-Borie, M., Sirieix, C., Naudet, V., Riss, J., 2011. Electrical resistivity monitoring with buried electrodes and cables: noise estimation with repeatability tests. Near Surface Geophysics 9 (4), 369–380.

Peters, T., 2005. Erläuterungen Geologische Karte, Blatt 118: 1257 St. Moritz.

Qi, J., Zhang, J., 2008. Definition of warm permafrost based on mechanical properties of frozen soil. In: Kane, D. L., Hinkel, K. M. (Eds.), Proceedings of the 9th International Conference on Permafrost, Fairbanks, AK, USA. Institute of Northern Engineering, University of Alaska, Fairbanks, pp. 1457–1461.

Reusser, D., Zehe, E., 2010. Low-cost monitoring of snow height and thermal properties with inexpensive temperature sensors. Hydrological Processes 25 (12), 1841–1852.

Reynard, E., Lambiel, C., Delaloye, R., Devaud, G., Baron, L., Chapellier, D., Marescot, L., Monnet, R., 2003. Glacier/permafrost relationship in forefields of small glaciers (Swiss Alps). In: Phillips, M., Springman, S. M., Arenson, L. U. (Eds.), Proceedings of the 8th International Conference on Permafrost, Zürich, Switzerland. A.A. Balkema Publishers, Rotterdam and The Netherlands, pp. 947–952.

Reynolds, J. M., 1997. An introduction to applied and environmental geophysics. John Wiley & Sons Ltd., Chichester.

Ribolini, A., Guglielmin, M., Fabre, D., Bodin, X., Marchisio, M., Sartini, S., Spagnolo, M., Schoeneich, P., 2010. The internal structure of rock glaciers and recently deglaciated slopes as revealed by geoelectrical tomography: insights on permafrost and recent glacial evolution in the central and western Alps (Italy-France). Quaternary Science Reviews 29 (3-4), 507–521.

Rickenmann, D., Zimmermann, M., 1993. The 1987 debris flows in Switzerland: documentation and analysis. Geomorphology 8 (2-3), 175–189.

Rist, A., 2007. Hydrothermal processes within the active layer above alpine permafrost in steep scree slopes and their influence on slope stability. Vol. 57 of Schriftenreihe Physische Geographie. Zürich.

Rödder, T., Kneisel, C., 2012a. Influence of snow cover and grain size on the ground thermal regime in the discontinuous permafrost zone, Swiss Alps. Geomorphology Early online.

Rödder, T., Kneisel, C., 2012b. Permafrost mapping using quasi-3D resistivity imaging, Murtèl, Swiss Alps. Near Surface Geophysics 10 (2), 117–127.

Roth, N., 2011. Widerstands-Temperatur-Monitoring und thermal-offset Studien im alpinen Permafrost. Val Muragl/Oberengadin, Schweiz. Ph.D. thesis, Universität Würzburg, Würzburg.

Röthlisberger, H., 1967. Electrical resistivity measurements and soundings on glaciers: introductory remarks. Journal of Glaciology 6 (47), 599–606.

Salomon, W., 1929. Arktische Bodenformen in den Alpen. Sitzungsbericht der Heidelberger Akademie der Wissenschaften. Mathematisch-naturwissenschaftliche Klasse 5, Nr. 31.

Salzmann, N., Noetzli, J., Hauck, C., Gruber, S., Hoelzle, M., Haeberli, W., 2007. Ground surface temperature scenarios in complexe high-mountain topography based on regional climate model results. Journal of Geophysical Research 112, F02S12.

Sass, O., 2004. Rock moisture fluctuations during freeze-thaw cycles: preliminary results from electrical resistivity measurements. Polar Geography 28 (1), 13–31.

Sattler, K., Keiler, M., Zischg, A., Schrott, L., 2011. On the connection between debris flow activity and permafrost degradation: a case study from the Schnalstal, south Tyrolean Alps, Italy. Permafrost and Periglacial Processes 22, 254–265.

Scapozza, C., Lambiel, C., Baron, L., Marescot, L., Reynard, E., 2011. Internal structure and permafrost distribution in two alpine periglacial talus slopes, Valais, Swiss Alps. Geomorphology 132, 208–221.

Scherler, M., Hauck, C., Hoelzle, M., Salzmann, N., 2013. Modeled sensitivity of two alpine permafrost sites to RCM-based climate scenarios. Journal of Geophysical Research 118 (2), 780–794.

Scherler, M., Hauck, C., Hoelzle, M., Stähli, M., Völksch, I., 2010. Meltwater infiltration into the frozen active layer at an alpine permafrost site. Permafrost and Periglacial Processes 21 (4), 325–334.

Scherrer, S., Appenzeller, C., Laternser, M., 2004. Trends in Swiss alpine snow days: the role of local- and large-scale climate variability. Geophysical Research Letters 31, L13215.

Schmid, M.-O., Gubler, S., Fiddes, J., Gruber, S., 2012. Inferring snow pack ripening and melt out from distributed ground surface temperature measurements. The Cryosphere Discussion 6 (1), 563–591.

Schneider, S., Daengeli, S., Hauck, C., Hoelzle, M., 2013. A spatial and temporal analysis of different periglacial materials by using geoelectrical, seismic and borehole temperature data at Murtèl–Corvatsch, Upper Engadin, Swiss Alps. Geographica Helvetica 68 (4), 265–280.

Schneider, S., Hoelzle, M., Hauck, C., 2012. Influence of surface and subsurface heterogeneity on observed borehole temperatures at a mountain permafrost site in the upper Engadine, Swiss Alps. The Cryosphere 6, 517–531.

Schrott, L., Hoffmann, T., 2008. Refraction seismics. In: Hauck, C., Kneisel, C. (Eds.), Applied geophysics in periglacial environments. Cambridge University Press, Cambridge, pp. 57–80.

Schrott, L., Sass, O., 2008. Application of field geophysics in geomorphology: Advances and limitations exemplified by case studies. Geomorphology 93 (1-2), 55–73.

Schwindt, D., Kneisel, C., 2011. Optimisation of quasi-3D electrical resistivity imaging - application and inversion for investigating heterogeneous mountain permafrost. The Cryosphere Discussion 5, 3383–3421.

Scott, W. J., Sellmann, P. V., Hunter, J. A., 1990. Geophysics in the study of permafrost. In: Ward, S. H. (Ed.), Geotechnical and Environmental Geophysics. Vol. 1. Tulsa and Oklahoma, pp. 355–384.

Shur, Y., Hinkel, K. M., Nelson, F. E., 2005. The transient layer: implications for geocryology and climate-change science. Permafrost and Periglacial Processes 16 (1), 5–17.

Smith, M. W., Riseborough, D. W., 2002. Climate and limits of permafrost: a zonal analysis. Permafrost and Periglacial Processes 13 (1), 1–15.

Spillmann, P., Trommsdorff, V., 2007a. Erläuterungen Geologische Karte, Blatt 119: 1277 Piz Bernina.

Spillmann, P., Trommsdorff, V., 2007b. Geologische Karte Blatt 119: 1277 Piz Bernina.

Stocker-Mittaz, C., Hoelzle, M., Haeberli, W., 2002. Modelling alpine permafrost distribution based on energy-balance data: a first step. Permafrost and Periglacial Processes 13 (4), 271–282.

Stoffel, M., Beniston, M., 2006. On the incidence of debris flows from the early Little Ice Age to a future greehouse climate: a case study from the Swiss Alps. Geophysical Research Letters 33, L16404.

Stoffel, M., Bollschweiler M., Beniston, M., 2011. Rainfall characteristics for periglacial debris flows in the Swiss Alps: past incidences-potential future evolutions. Climate Change 105 (1-2), 263–280.

Stoffel, M., Huggel, C., 2012. Effects of climate change on mass movements in mountain environments. Progress in Physical Geography 36 (3), 421–439.

Telford, W. M., Geldart, L. P., Sheriff, R. E., 1990. Applied geophysics, 2nd Edition. Cambridge University Press, Cambridge.

Timur, A., 1968. Velocity of compressional waves in porous media at permafrost temperatures. Geophysics 33 (4), 584–595.

Trenberth, K. E., Jones, P. D., Ambenje, P., Bojariu, R., Easterling, D., Klein Tank, A., Parker, D., Rahimzadeh, F., Renwick, J. A., Rusticucci, M., Soden, B., Zhai, P., 2007. Observations: surface and atmospheric climate change. In: Solomon, S., Qin, D., Manning, M., Chen, Z., Marquis, M., Averyt, K. B., Tignor, M., Miller, H. L. (Eds.), Climate Change 2007: the physical science basis. Contribution of working group I to the

fourth assessment report of the intergovernmental panel on climate change. Cambridge University Press, Cambridge and United Kingdom and New York and NY and USA.

Ulrich, R., King, L., 1993. Influence of mountain permafrost on construction in the Zugspitze mountains, Bavarian Alps, Germany. In: Proceedings of the 6th International Conference on Permafrost. Vol. 1. South China University of Technology Press, Beijing, pp. 625–630.

van Everdingen, R., 2005. Multi-language glossary of permafrost and related ground-ice terms. National Snow and Ice Data Center/World Data Center for Glaciology, Boulder and CO.

Verleysdonk, S., Krautblatter, M., Dikau, R., 2011. Sensitivity and path dependence of mountain permafrost systems. Geografiska Annaler 93 (2), 113–135.

Vonder Muehll, D., 1993. Geophysikalische Untersuchungen im Permafrost des Oberengadins. Ph.D. thesis, Versuchsanstalt für Wasserbau, Hydrologie und Glaziologie der Eidgenössischen Technischen Hochschule Zürich, Zürich.

Vonder Muehll, D., Arenson, L., Springman, S. M., 2003. Temperature conditions in two alpine rock glaciers. In: Phillips, M., Springman, S. M., Arenson, L. U. (Eds.), Proceedings of the 8th International Conference on Permafrost, Zürich, Switzerland. A.A. Balkema Publishers, Rotterdam and The Netherlands, pp. 1195–1200.

Vonder Muehll, D., Haeberli, W., 1990. Thermal characteristics of the permafrost within an active rock glacier (Murtèl/Corvatsch, Grisons, Swiss Alps). Journal of Glaciology 36 (123), 151–158.

Vonder Muehll, D., Hauck, C., Gubler, H., McDonald, R., Russill, N., 2001. New geophysical methods of investigating the nature and distribution of mountain permafrost with special reference to radiometry techniques. Permafrost and Periglacial Processes 12 (1), 27–38.

Vonder Muehll, D., Holub, P., 1992. Borehole logging in alpine permafrost, Upper Engadin, Swiss Alps: Short Communication. Permafrost and Periglacial Processes 3 (2), 125–132.

Waller, R. I., Murton, J. B., Kristensen, L., 2012. Glacier–permafrost interactions: Processes, products and glaciological implications. Sedimentary Geology 255-256, 1–28.

Wetzel, K.-F., 2004. On the hydrology of the Partnach area in the Wetterstein Mountains (Bavarian Alps). Erdkunde 58, 172–186.

Zemp, M., Haeberli, W., Hoelzle, M., Paul, F., 2006. Alpine glaciers to disappear within decades? Geophysical Research Letters 33, L13504.

Zhang, T., 2005. Influence of the seasonal snow cover on the ground thermal regime: an overview. Reviews of Geophysics 43, RG4002.

Zimmermann, M., Haeberli, W., 1992. Climate change and debris flow activity in high-mountain areas - a case study in the Swiss Alps. In: Boer, M., Koster, E. (Eds.), Greenhouse-Impact on cold-climate ecosystems and landscapes. Catena Supplement 22. Catena-Verlag, Cremlingen-Destedt, pp. 59–72.

Zimmermann, M., Mani, P., Gamma, P., 1997. Murganggefahr und Klimaänderung - ein GIS-basierter Ansatz: Schlussbericht NFP 31. vdf Hochschulverlag AG an der ETH Zürich, Zürich.

A. Geophysical investigations Murtèl/Corvatsch

Table A.1: Basic information on geophysical profiles measured in 2008 and 2009.

Date	Name	Array	spacing [m]	Coordinates	Elevation [m]	Comment
Sept. 10, 2008	ERT1	Wen	5	782312/143291–782440/143206	2741–2819	on debris-covered ice
Sept. 10, 2008	ERT2	Wen	5	782095/143443–782186/143296	2703–2723	central glacier forefield
Sept. 10, 2008	ERT3	Wen	5	782023/143348–782186/143296	2705–2723	central glacier forefield
Sept. 10, 2008	ERT4	Wen	5	782058/143269–781958/143269	2687–2733	across RG Rabgiusa
Aug. 10, 2009	ERT1	Wen+WenSL	5	781896/143464–782014/143346	2692–2705	across RG Rabgiusa
Aug. 10, 2009	ERT2	Wen+WenSL	3	781908/143450–781977/143380	2693–2694	across RG Rabgiusa
Aug. 10, 2009	ERT3	Wen+WenSL	5	781937/143474–781958/143311	2676–2718	across RG Rabgiusa
Aug. 11, 2009	Gl1	Wen+WenSL	3	781947/143478–781897/143399	2669–2698	quasi-3D grid
Aug. 11, 2009	Gl2	Wen+WenSL	3	781950/143473–781897/143391	2672–2699	quasi-3D grid
Aug. 11, 2009	Gl3	Wen+WenSL	3	781953/143456–781910/143391	2667–2698	quasi-3D grid
Aug. 11, 2009	Gl4	Wen+WenSL	3	781966/143460–781915/143384	2670–2699	quasi-3D grid
Aug. 12, 2009	Gl5	Wen+WenSL	3	781973/143460–781923/143379	2664–2696	quasi-3D grid
Aug. 12, 2009	Gl6	Wen+WenSL	3	781981/143459–781928/143374	2665–2696	quasi-3D grid
Aug. 13, 2009	Gl6-2	Wen+WenSL	3	781 /143 –781909/143341	2679–2708	quasi-3D grid
Aug. 13, 2009	Gl7	Wen+WenSL	3	781971/143428–781917/143342	2683–2714	quasi-3D grid
Aug. 13, 2009	Gl8	Wen+WenSL	3	781982/143422–781923/143336	2682–2714	quasi-3D grid
Aug. 14, 2009	Gl9	Wen+WenSL	3	781982/143412–781927/143334	2675–2710	quasi-3D grid
Aug. 14, 2009	Gl10	Wen+WenSL	3	781982/143412–781927/143334	2675–2710	quasi-3D grid
Aug. 14, 2009	Gl12	Wen+WenSL	3	781984/143403–781937/143327	2680–2716	quasi-3D grid
Aug. 16, 2009	Gq1	Wen+WenSL	3	781929/143450–782006/143389	2690–2695	quasi-3D grid
Aug. 16, 2009	Gq2	Wen+WenSL	3	781923/143443–782007/143375	2694–2694	quasi-3D grid
Aug. 16, 2009	Gq3	Wen+WenSL	3	781920/143436–782003/143371	2695–2695	quasi-3D grid
Aug. 16, 2009	Gq4	Wen+WenSL	3	781913/143429–781997/143366	2696–2699	quasi-3D grid
Aug. 16, 2009	Gq5	Wen+WenSL	3	781905/143419–781984/143361	2697–2699	quasi-3D grid
Aug. 17, 2009	Gq6	Wen+WenSL	3	781900/143414–781982/143356	2698–2702	quasi-3D grid
Aug. 17, 2009	Gq7	Wen+WenSL	3	781896/143409–781978/143347	2701–2708	quasi-3D grid
Aug. 18, 2009	Gq8	Wen+WenSL	3	781888/143402–781967/143345	2704–2710	quasi-3D grid
Aug. 18, 2009	Gq9	Wen+WenSL	3	781888/143393–781971/143336	2705–2713	quasi-3D grid
Aug. 18, 2009	Gq10	Wen+WenSL	3	781880/143388–781960/143330	2706–2718	quasi-3D grid
Aug. 18, 2009	Gq11	Wen+WenSL	3	781885/143376–781963/143320	2710–2722	quasi-3D grid
Aug. 18, 2009	Gq12	Wen+WenSL	3	781883/143372–781952/143318	2715–2724	quasi-3D grid
Aug. 19, 2009	ERT4	Wen+WenSL	5	782303/143358–782428/143283	2731–2795	on debris-covered ice
Aug. 19, 2009	ERT5	Wen+WenSL	5	782156/144131–782297/144182	2595–2678	solifluction lobe
Aug. 19, 2009	ERT6	Wen+WenSL	5	782171/144091–782258/144217	2599–2662	solifluction lobe

Table A.2: Basic information on geophysical profiles measured in 2010.

| Date	Name	Array	spacing [m]	Coordinates	Elevation [m]	Comment
Aug. 18, 2010	RST1	refr. seismic	3	781938/143410–781978/143441	2674–2694	RG Rabgiusa
Aug. 18, 2010	RST2	refr. seismic	3	781938/143410–781894/143342	2694–2722	extension of RST1
Aug. 19, 2010	RST3	refr. seismic	3	781955/143436–781955/143370	2688–2697	RG Rabgiusa
Aug. 19, 2010	RST4	refr. seismic	3	781955/143370–781959/143313	2697–2713	extension of RST3
Aug. 19, 2010	RST5	refr. seismic	3	782063/143389–782093/143318	2711–2720	central glacier forefield
Aug. 19, 2010	RST6	refr. seismic	3	782053/143339–782113/143360	2716–2712	central glacier forefield
Aug. 19, 2010	RST7	refr. seismic	3	782177/144130–782222/144116	2595–2610	solifluction lobe, failed
Aug. 23, 2010	ERT1	Wen+WenSL+Dip	2	782060/143390–782088/143326	2711–2718	central glacier forefield
Aug. 23, 2010	ERT2	Wen+WenSL+Dip	2	782057/143343–782117/143361	2713–2709	central glacier forefield
Aug. 23, 2010	ERT3	Wen+WenSL+Dip	2	781980/143445–781945/143380	2676–2685	RG Rabgiusa
Aug. 23, 2010	ERT4	Wen+WenSL+Dip	2	782945/143380–781894/143347	2685–2710	extension of ERT3
Aug. 24, 2010	ERT5	Wen+WenSL+Dip	2	781951/143441–781953/143373	2681–2693	RG Rabgiusa
Aug. 24, 2010	ERT6	Wen+WenSL+Dip	2	781953/143373–781949/143314	2693–2733	extension of ERT5
Aug. 24, 2010	ERT7	Wen+WenSL+Dip	2	781949/143314–781942/143252	2733–2744	extension of ERT6
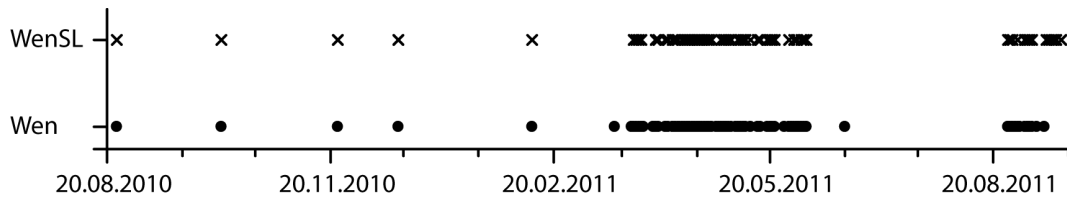
Figure A.1: Data base from ERT-monitoring at rock glacier Rabgiusa, Murtèl

B. Geophysical investigations Val Muragl

Table B.1: Data base from ERT-monitoring at glacier forefield Muragl.

Date	ERTM-Mgl1		ERTM-Mgl2	
	WenSL–1 m	**WenSL–2 m**	**WenSL–1 m**	**WenSL–1 m**
Aug. 05, 2004		x		x
Aug. 27, 2004		x		x
Sept. 09, 2004		x		x
July 28, 2005	x	x	x	x
Aug. 08, 2005	x	x	x	x
Aug. 22, 2005	x	x	x	x
Sept. 01, 2005	x	x	x	x
Sept. 14, 2005	x	x	x	x
July 25/26, 2006	x	x	x	x
Aug. 10/11, 2006	x	x	x	x
Aug. 19, 2006	x	x	x	x
Aug. 31, 2006	x	x	x	x
Sept. 17, 2006	x	x	x	x
July 03, 2007		x		x
July 25, 2007	x	x	x	x
Aug. 07, 2007	x	x	x	x
Aug. 20, 2007	x	x	x	x
Sept. 16, 2007	x	x	x	x
Aug. 06, 2008	x	x	x	x
Aug. 24, 2008	x	x	x	x
Sept. 05, 2008	x	x	x	x
July 22, 2009	x	x	x	x
Aug. 07, 2009	x	x	x	x
Aug. 24, 2009	x	x	x	x
Sept. 27, 2009	x	x	x	x
Oct. 06, 2009				x
July 22, 2010		x		x
Aug. 10, 2010		x		x
Sept. 12, 2010		x		x

C. Geophysical investigations Zugspitzplatt

Table C.1: Basic information on geophysical profiles measured in 2011.

| Date	Name	Array	spacing [m]	Coordinates	Elevation [m]	Comment
July 19, 2011	ERT1	Wen+Dip	2	4423330/5253539–4423278/5253570	2563–2590	talus slope
July 19, 2011	ERT2	Wen+Dip	2	4423302/5253535–4423276/5253578	2577–2603	talus slope
July 19, 2011	ERT3	Dip	2	4423536/5253565–4423495/5253517	2534–2534	glacial till
July 19, 2011	ERT4	Wen+Dip	2	4423391/5253346–4423333/5253381	2540–2563	till
July 19, 2011	ERT5	Wen+Dip	2	4422877/5253560–4422943/5253582	2620–2640	talus slope
July 20, 2011	ERT6	Wen+Dip	2	4422791/5253525–4422852/5253550	2599–2616	talus slope, glacier
July 19, 2011	RST1	refr. seismic	3	4423330/5253539–4423278/5253570	2563–2590	talus slope
July 19, 2011	RST2	refr. seismic	3	4423302/5253535–4423276/5253578	2577–2603	talus slope
July 19, 2011	RST3	refr. seismic	3	4423536/5253565–4423495/5253517	2534–2534	glacial till

D. Temperature datalogger Murtèl/Corvatsch
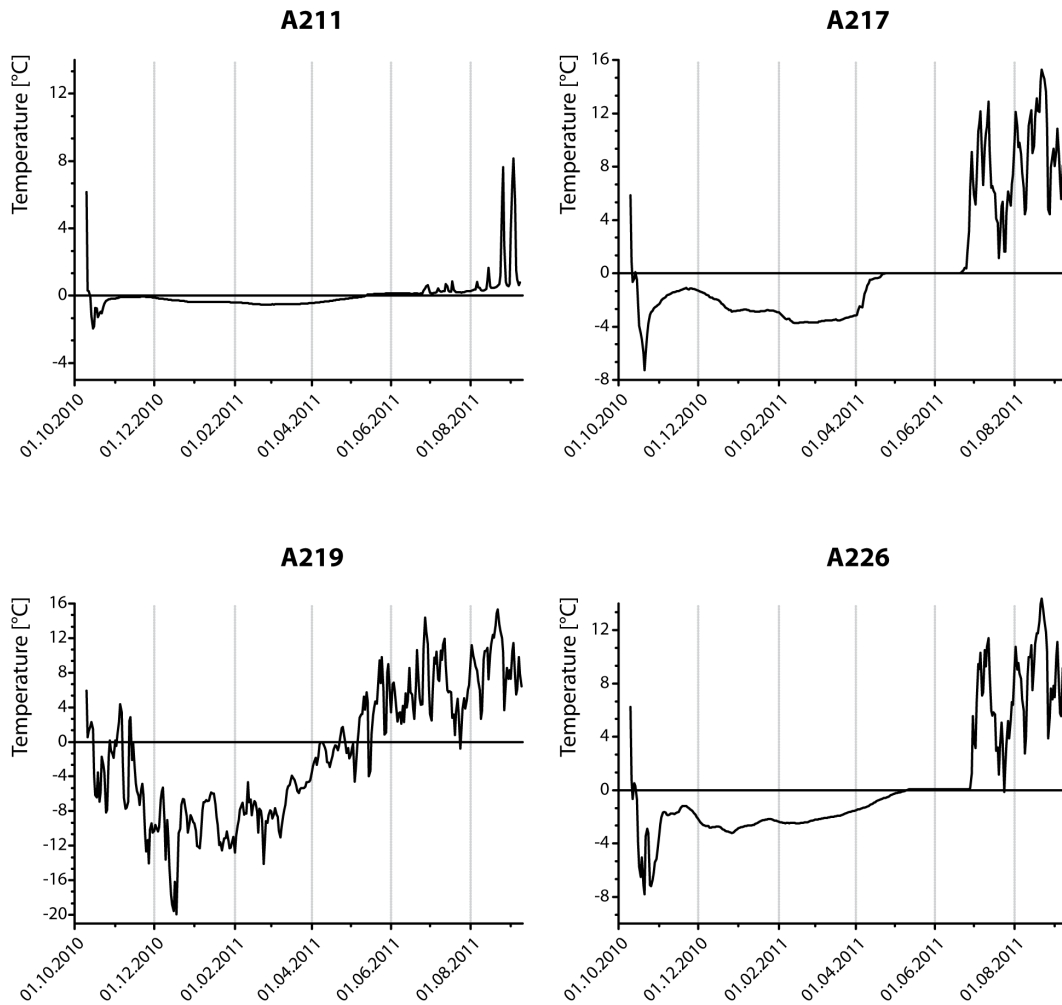
Figure D.1: Temperature profiles from data loggers Murtèl (I).
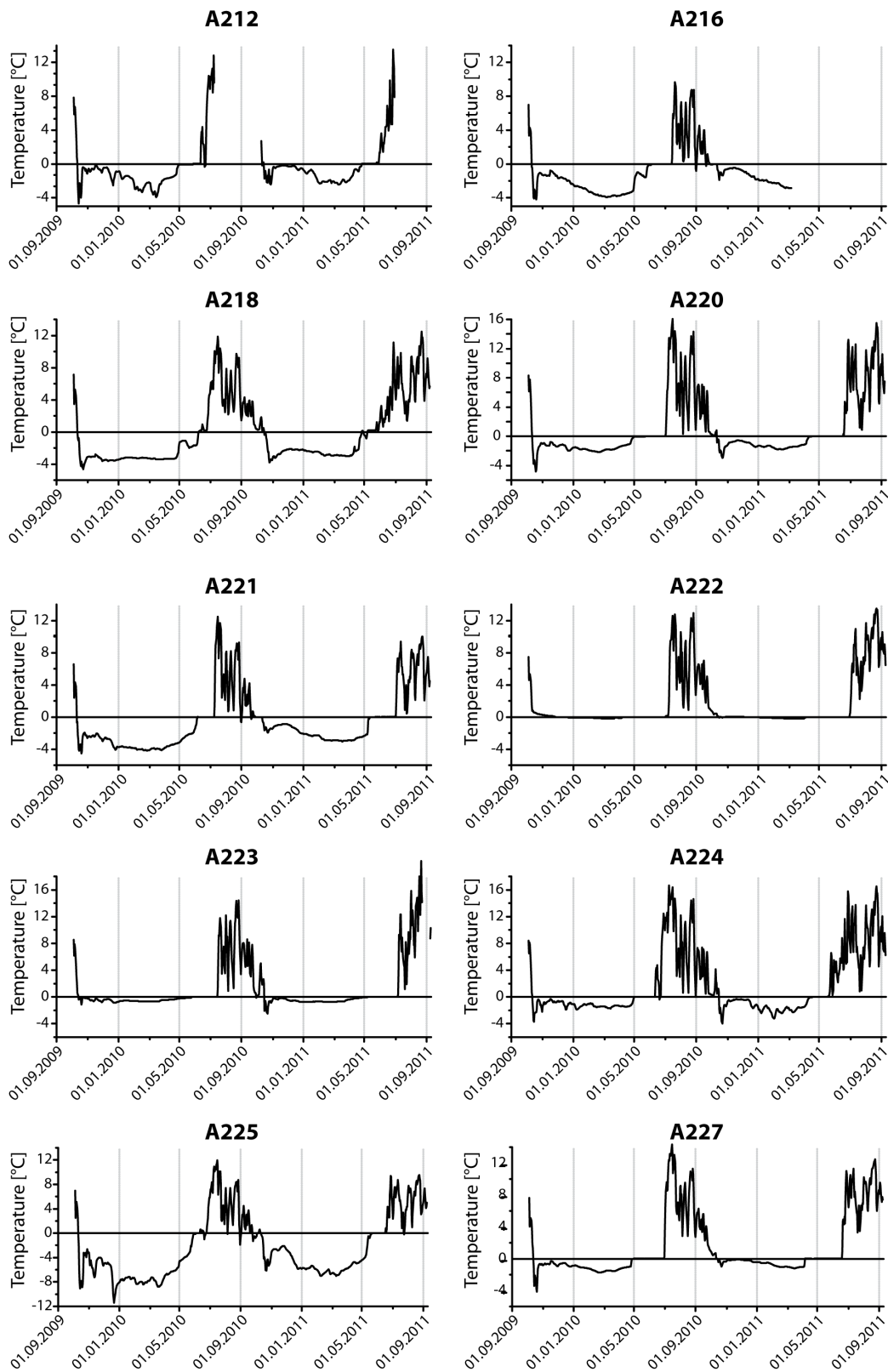
Figure D.2: Temperature profiles from data loggers Murtèl (II).
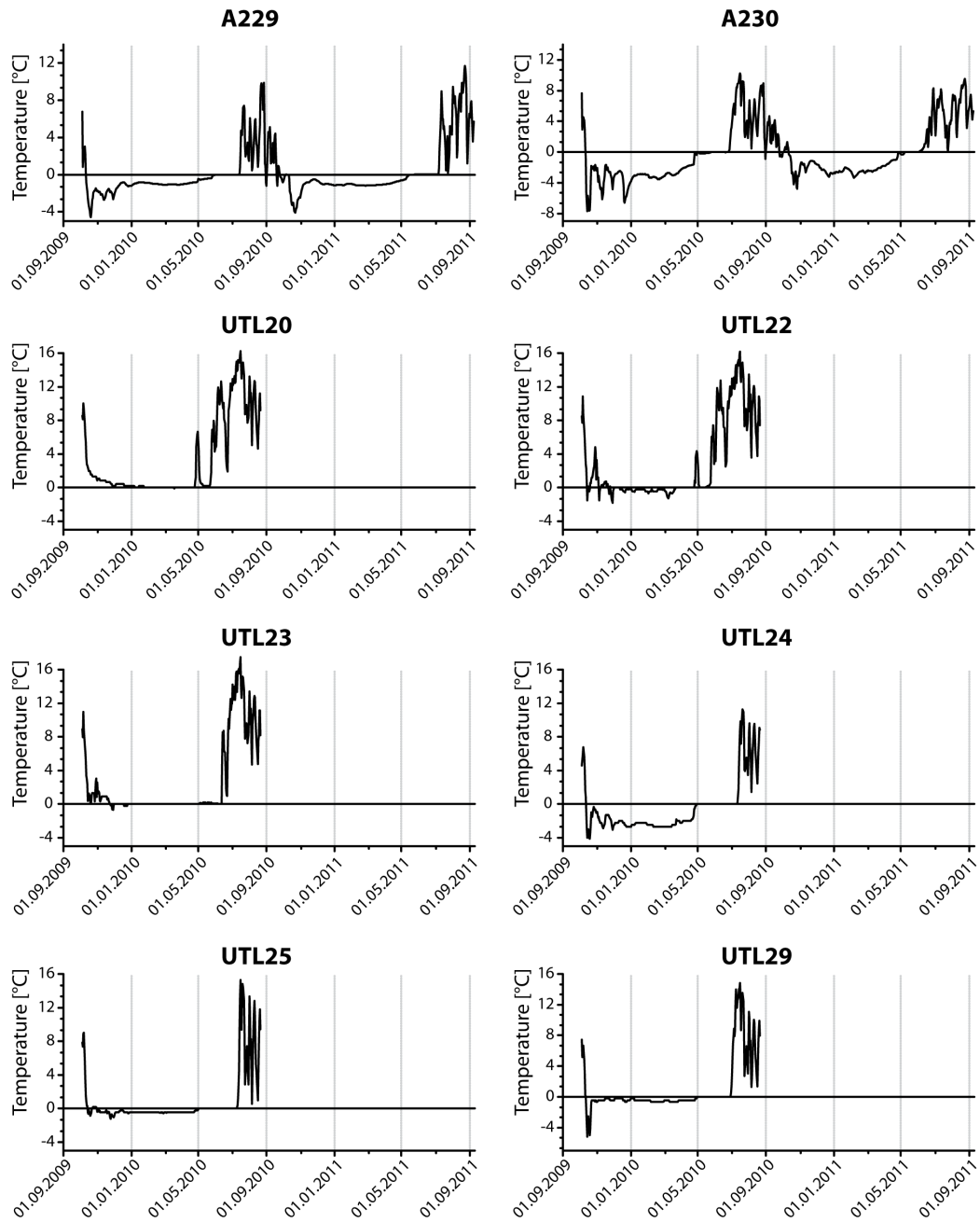
Figure D.3: Temperature profiles from data loggers Murtèl (III).
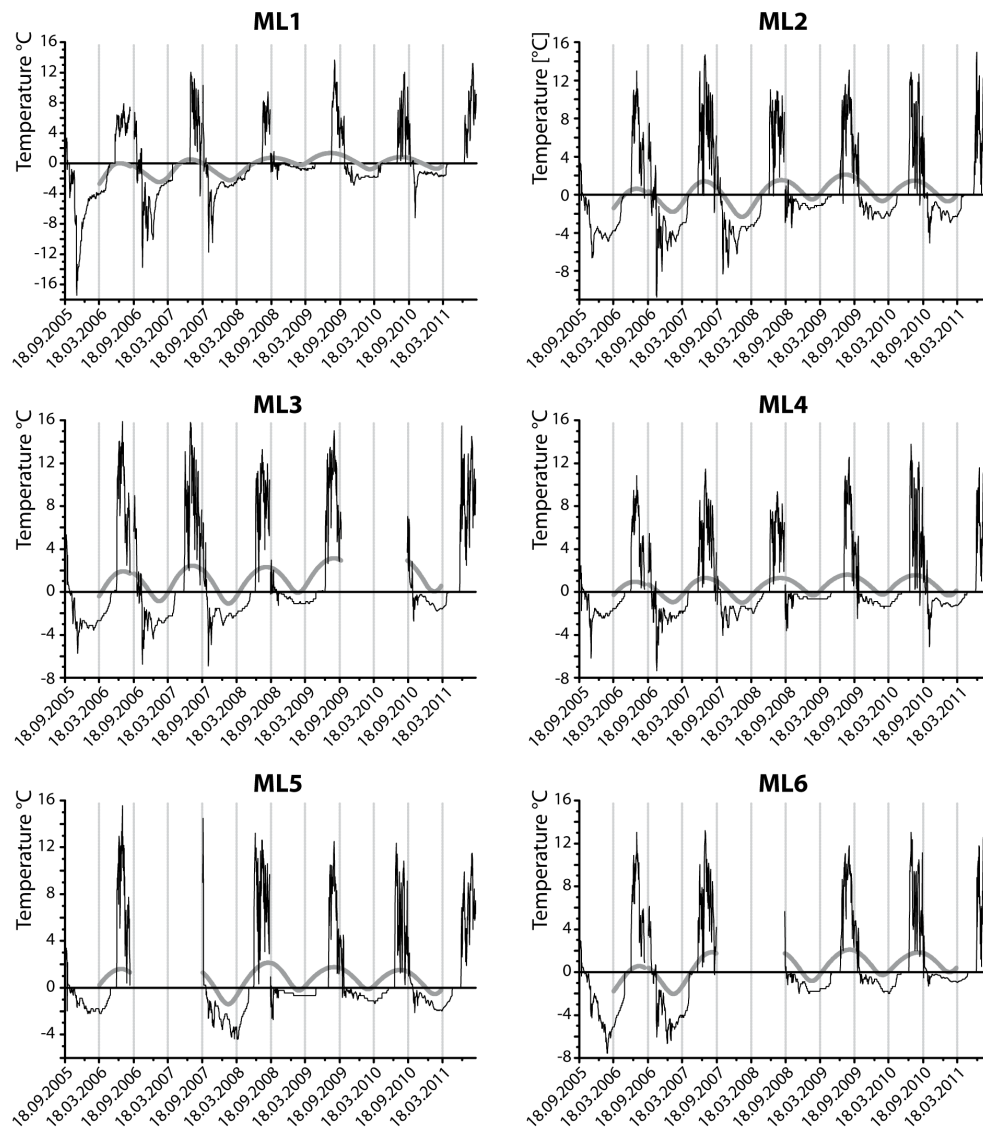
E. Temperature datalogger Val Muragl

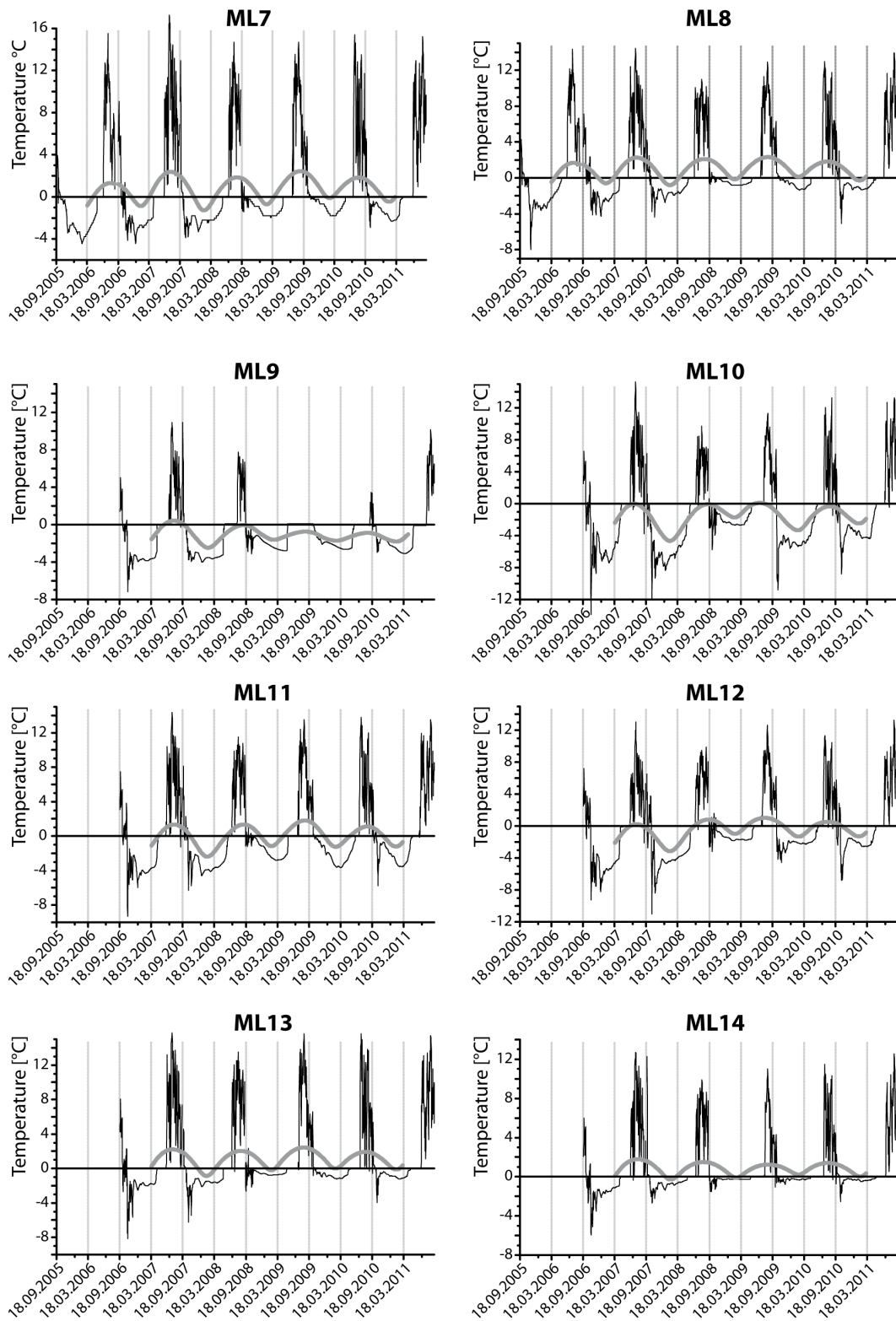Figure E.1: Temperature profiles from data loggers Muragl (I).

Figure E.2: Temperature profiles from data loggers Muragl (II).